Dynamic Analysis and Validation of Cantilever MEMS Subjected to Electro-Thermo-Mechanical Influences

Gino Rinaldi

A Thesis

in

The Department

of

Mechanical and Industrial Engineering

Presented in Partial Fulfillment of the Requirements
for the Degree of Doctor of Philosophy (Mechanical Engineering) at
Concordia University
Montreal, Quebec, Canada

April, 2006

Canada

Abstract

Dynamic Analysis and Validation of Cantilever MEMS Subjected to Electro-Thermo-Mechanical Influences

Gino Rinaldi, Ph. D.
Concordia University, 2006

Microsystem development and expansion to new applications requires modeling and simulation followed by rigorous testing in order to validate the performance of microscale devices. The effect of combined influences such as electrostatic, thermal, and mechanical, for example, on microsystem structures needs to be quantified in a systematic manner in order to obtain a synthesized performance profile of the microsystem. The feedback obtained through the validation process will not only serve to enhance the theoretical model but also establish a basis for microsystem design and optimization based on a set of predefined input parameters.

Micro-electro-mechanical-systems (MEMS) integrate, by definition, both electrical and mechanical components onto a microscale silicon substrate. Hence, in this regard it is often difficult to differentiate between mechanical and electrical influences on the microsystem. The inclusion of thermal gradients, as can be expected in harsh environments, for example, further tempers an already diluted microsystem response. Hence, the various combined input parameters need to be discretized, analyzed, and finally synthesized in order to obtain a systematic evaluation of microsystem performance.

The main influences investigated here that will affect the elastic properties of MEMS cantilevers are microfabrication tolerances at the support boundary, applied electrostatic potentials used to deflect the microcantilever, thermal loads that mimic harsh environments and alter the physical dimensions of the microcantilever, structural geometry used to optimize and tune, for example, the dynamic response, and cutouts along the microcantilever used for mass reduction and also for tuning capabilities. Artificial springs are used to model boundary support conditions and electrostatic influences. These influences are investigated first separately and then in a synthesized manner in which they are all combined.

The theoretical model is based upon the Rayleigh-Ritz energy method. This method is suitable for MEMS cantilevers under various applied influences, however, it is limited to microcantilevers without cutouts due to discontinuities created along the length of the cantilever by the cutouts. Hence, a *segment* Rayleigh-Ritz energy model was developed, in order to improve the theoretical formulation, based on a segmental approach in which the microcantilever is divided into segments that are a function of the number of cutouts.

This work presented herein attempts to synthesize the influence of electro-thermo-mechanical constituents of microsystems in a unified way so that it could fulfill the inverse design dream of MEMS engineers.

Acknowledgments

The author would like to express his sincere thanks and gratitude to his thesis supervisors Dr. Ion Stiharu and Dr. Muthukumaran Packirisamy for their unwavering encouragement and support. I am grateful to Dr. Stiharu for his willingness to *meet sometime and discuss something* and I am also very grateful that Dr. Packirisamy's office door was *always open*. Their genuine enthusiasm for this research topic created at atmosphere that was truly instrumental in the success of this present work. It was a pleasure and privilege to carry out research under them.

It is also my pleasure to extend my gratitude to Dr. R. B. Bhat for his incite, help and encouragement in the course of my studies.

I would also like to thank Dr. S. Rakheja for his technical support at CONCAVE, and for his concern and help shown in the progress of my thesis.

I owe debt of gratitude to Dr. P. Tzenov and Dr. M. Frank (Physics) for the TA appointments I received while pursuing my research studies.

The author extends thanks to Mr. Dan Juras for his help and friendly discussions. I would also like to thank Mr. John Elliot, Mr. Gilles Huard, Mr. Tainhe Wen, Mr. Jose Esteves, Mr. Mostafa Showleh, and Mr. Brad Luckhart for their technical expertise. The

I would like to express my thanks to my parents and relatives

for their love and encouragement.

This thesis is dedicated to them.

Discovery consists of seeing
what everybody else has seen,
and thinking what nobody
else has thought

A. von Szent Gyorgyi

Table of Contents

List of Acronyms

AC	Alternating-Current
AFM	Atomic-Force-Microscope
AutoCAD	*Auto*desk-Computer-Aided-Drafting
BEM	Boundary-Element-Method
CAD	Computer-Aided-Design
CMC	Canadian-Microelectronics-Corporation
CONCAVE	Concordia-Center-for-Advanced-Vehicle-Engineering
DC	Direct-Current
DXF	Data-EXchange-File
FEA	Finite-Element-Analysis
FEM	Finite-Element-Method
FEMLAB	Finite-Element-Method-LABoratory
GDS	Generalized-Data-Stream
HeNe	Helium-Neon
IC	Integrated-Circuit
IR	InfraRed
LinkCAD	*Linked*-Computer-Aided-Design
LDV	Laser-Doppler-Velocimetery (Vibrometry)
MATLAB	MATrix-LABoratory
MEMS	Micro-Electro-Mechanical-System
MicraGeM	Micralyne-Generalized-MEMS

MOEMS	Micro-Opto-Electro-Mechanical-System
MUMPs	Multi-User-MEMS-Processes
μMasch	**Mikro**(Masch)
NEMS	Nano-Electro-Mechanical-System
OW	Optical-Waveguide
RISO	**RI**gid-**SO**ft
RPM	Rotations-Per-Minute
RTD	Resistance-Temperature-Detector
SCSi	Single-Crystal-Silicon
SEM	Scanning-Electron-Microscope
SOI	Silicon-On-Insulator
SORI	**SO**ft-**RI**gid
SRS	Stimulated-Raman-Scattering
UV	Ultra-Violet (radiation)

List of Symbols

A	Area
A_i	i^{th} deflection coefficient
A_j	j^{th} deflection coefficient
$A.\ U.$	Arbitrary units
cm	Centimeter
C	Capacitance
$^{\circ}C$	Degrees centigrade
C_d	Damping factor
C_{dc}	Critical damping factor
d	Distance
d_0	Dielectric gap
E	Young's modulus of elasticity
$E^{(T)}$	Young's modulus of elasticity at temperature T
$E_{sg}^{(T)}$	Young's modulus of elasticity at temperature T of a particular beam segment
$Exp.$	Experiment
$Exp.\ Freq.$	Experimental frequency
f	Frequency
f_{Disc}	Frequency shift due to rotating disc
f_{Laser}	Optical frequency of laser source
f_{L1}	Focal length (lens $L1$)
f_{L2}	Focal length (lens $L2$)

F	Farrad
F_0	Force amplitude (at $t = 0$)
$F_E(x)$	Electrostatic force
GPa	GigaPascal
h	Material thickness
$h^{(T)}$	Material thickness at temperature T
$h_{sg}^{(T)}$	Material thickness at temperature T of a particular beam segment
H	Height
Hz	Hertz
I	Moment of inertia
$I^{(T)}$	Moment of inertia at temperature T
$I_{sg}^{(T)}$	Moment of inertia at temperature T for a given beam segment
I_n	Orthonormal condition for n^{th} mode shape
k	Boltzmann's constant
kg	Kilogram
kHz	kilohertz
k_E^*	Electrostatic spring stiffness (non-dimensionalized)
$k^{(T)}_E{}^*$	Electrostatic spring stiffness at temperature T (non-dimensionalized)
$k^{(T)}_E{}^*{}_g$	Electrostatic spring stiffness at temperature T for a given conditioning function Ψ and for a given beam segment (non-dimensionalized)
K	Kelvin
K_{APP}	Applied spring stiffness
K_b	Beam stiffness
K_C	Cantilever spring stiffness

K_E	Electrostatic spring stiffness
K_{ES}	Applied stiffness (electrostatic)
K_R	Rotational spring stiffness
K_R^*	Rotational spring stiffness (non-dimensionalized)
$K^{(T)}_R{}^*$	Rotational spring stiffness at temperature T (non-dimensionalized)
K_{RsgS}	Segmental rotational spring stiffness acting on side S
K_{R12}	Segmental rotational spring stiffness for segment 1 acting on side 2
K_{R21}	Segmental rotational spring stiffness for segment 2 acting on side 1
K_{R22}	Segmental rotational spring stiffness for segment 2 acting on side 2
K_{R31}	Segmental rotational spring stiffness for segment 3 acting on side 1
K_{RsgS}^*	Segmental rotational spring stiffness acting on side S (non-dimensionalized)
K_{STRU}	Structural spring stiffness
K_T	Translation spring stiffness
K_T^*	Translation spring stiffness (non-dimensionalized)
$K^{(T)}_T{}^*$	Translation spring stiffness at temperature T (non-dimensionalized)
K_{TsgS}	Segmental translation spring stiffness acting on side S
K_{T12}	Segmental translational spring stiffness for segment 1 acting on side 2
K_{T21}	Segmental translational spring stiffness for segment 2 acting on side 1
K_{T22}	Segmental translational spring stiffness for segment 2 acting on side 2
K_{T31}	Segmental translational spring stiffness for segment 3 acting on side 1
K_{TsgS}^*	Segmental translation spring stiffness acting on side S (non-dimensionalized)
KV	Kilovolt

L	Length
$L^{(T)}$	Length at temperature T
L_{sg}	Length of segment
$L_{sg}^{(T)}$	Length of segment at temperature T
$L_{D\text{-}C}$	Diverging-converging lens separation
$L1$	Diverging lens
$L2$	Converging lens
m	Meter
mm	Millimeter
m'	AFM microcantilever tip mass
mV	MilliVolt
M	Mass
MHz	MegaHertz
nm	Nanometer
$nat.\ Freq.$	Natural frequency
N	Newton
Pa	Pascal
q	Electrostatic charge
Q	Total electrostatic charge
r	Radius
s	Second
sg	Segment index
S	Segment side (= 1 or 2)

t	Time
T	Temperature
T_B	Kinetic energy
$T^{(T)}_B$	Kinetic energy at temperature T
T_{MAX}	Kinetic energy (maximum)
T^{*}_{MAX}	Kinetic energy (maximum) divided by cyclical frequency
Theo. Freq.	Theoretical frequency
U_B	Strain energy
$U^{(T)}_B$	Strain energy at temperature T
$U^{(T)}_B{}^{\Psi}$	Strain energy at temperature T for a given conditioning function Ψ
$U^{(T)}_B{}^{\Psi}_{sg}$	Strain energy at temperature T for a given conditioning function Ψ of a particular beam segment
U_E	Electrostatic potential energy
$U^{(T)}_E$	Electrostatic potential energy at temperature T
U_{ED}	Electrostatic *dynamic* potential energy
$U^{(T)}_{ED}$	Electrostatic *dynamic* potential energy at temperature T
U_{ES}	Electrostatic *static* potential energy
$U^{(T)}_{ES}$	Electrostatic *static* potential energy at temperature T
U_{MAX}	Maximum potential energy
$U^{(T)}_{MAX}$	Maximum potential energy at temperature T
U_n	n^{th} applied potential energy
U_{SP}	Potential energy of boundary support springs
$U^{(T)}_{SP}$	Potential energy of boundary support springs at temperature T
V	Voltage

V_0	Voltage amplitude (at $t = 0$)
$V_1{}^*$	Voltage (non-dimensionalized)
$V_1{}^{(T)*}$	Voltage at temperature T (non-dimensionalized)
$V_1{}^{(T)*}{}_{sg}$	Voltage at temperature T for a given beam segment (non-dimensionalized)
$V_2{}^*$	Voltage (non-dimensionalized)
$V_2{}^{(T)*}$	Voltage at temperature T (non-dimensionalized)
$V_2{}^{(T)*}{}_{sg}$	Voltage at temperature T for a given beam segment (non-dimensionalized)
V_{sg}	Voltage applied for a given beam segment
w	Material width
$w^{(T)}$	Material width at temperature T
w_{sg}	Material width of a particular beam segment
$w_{sg}{}^{(T)}$	Material width of a particular beam segment at temperature T
w_0	Material width (unconditioned)
$w(x)$	Positional width
$W(x)$	Flexural deflection
$W_S(x)$	Flexural deflection (static equilibrium)
$W'(x)$	Flexural deflection (first derivative)
$W''(x)$	Flexural deflection (second derivative)
$W_D(x)$	Dynamic deflections
$W_{Dsg}(x)$	Dynamic deflections for a given beam segment
x	Non-dimensionalized coordinate
$\hat{z}_n{}^*$	Virtual height
$4C$	Microcantilever cutout designation: 4 cutouts starting from "*clamped*" end

8C	Microcantilever cutout designation: 8 cutouts starting from *"clamped"* end
12C	Microcantilever cutout designation: 12 cutouts starting from *"clamped"* end
16C	Microcantilever cutout designation: 16 cutouts starting from *"clamped"* end
4F	Microcantilever cutout designation: 4 cutouts starting from *"free"* end
8F	Microcantilever cutout designation: 8 cutouts starting from *"free"* end
12F	Microcantilever cutout designation: 12 cutouts starting from *"free"* end
16F	Microcantilever cutout designation: 16 cutouts starting from *"free"* end

Greek Characters

α	Linear coefficient of thermal expansion
$\alpha^{(T)}$	Linear coefficient of thermal expansion at temperature T
α_c	Cutout width factor (0...1) of beam width
β	Width conditioning parameter
δ	Width conditioning offset parameter
Δh	Change in material thickness
ΔL	Change in material length
Δw	Change in material width
ε	Coefficient of thermal dependence for Young's modulus
ε_0	Permittivity of free space
ε_r	Relative permittivity of a given medium
$\phi_0(x)$	Parent polynomial in x
$\phi_i(x)$	i^{th} orthogonal polynomial in x
$\phi_j(x)$	j^{th} orthogonal polynomial in x

$\phi_i'(x)$	First derivative of ith orthogonal polynomial in x
$\phi_j'(x)$	First derivative of jth orthogonal polynomial in x
$\phi_i''(x)$	Second derivative of ith orthogonal polynomial in x
$\phi_j''(x)$	Second derivative of jth orthogonal polynomial in x
ϕ_L	Lens diameter
ϕ_{L2}	Laser spot size on lens $L2$
ϕ_{MEMS}	Laser spot size on lens MEMS surface
Φ_n	n^{th} mode shape
θ_{L1}	Laser beam divergence angle from lens $L1$
λ	Eigenvalue
$\lambda^{(T)}$	Eigenvalue at temperature T
$\lambda^{(T)}_{sg}$	Eigenvalue at temperature T for a given beam segment
λ_{Laser}	Laser source wavelength
λ_n	n^{th} eigenvalue
$\lambda^{(T)}_n$	n^{th} eigenvalue at temperature T
$\lambda^{(T)}_{n\,sg}$	n^{th} eigenvalue at temperature T for a given beam segment
Λ	Normalized eigenvalue
μm	Micrometer
π	Pi
ρ	Material density
$\rho^{(T)}$	Material density at temperature T
$\rho_{sg}^{(T)}$	Material density at temperature T for a given beam segment

ρ_G		Geometry conditioning width ratio
Σ		Sum
ω		Cyclical frequency
ω_n		n^{th} cyclical frequency
	$\omega^{(T)}_n$	n^{th} cyclical frequency at temperature T
	$\omega^{(T)}_{n\,sg}$	n^{th} cyclical frequency at temperature T for a given beam segment
ω_N		Natural cyclical frequency
ξ		Axis coordinate
ξ_d		Damping ratio
Ψ		Width conditioning function
	$\Psi_0(x)$	Width conditioning function *outer*
	$\Psi_C(x)$	Width conditioning function *cutout*
	$\Psi_S(x)$	Width conditioning function *soft*
	$\Psi_{S\,R}(x)$	Width conditioning function *soft-rigid*
	$\Psi_R(x)$	Width conditioning function *rigid*
	$\Psi_{R\,S}(x)$	Width conditioning function *rigid-soft*

Miscellaneous

dz/dx	Derivative of z with respect to x
$\partial z(x,\,y)/\partial x$	Partial derivative of $z(x,\,y)$ with respect to x
$\hat{z}^{*}_n$	Virtual height
$\dfrac{Z^{*2}_2}{Z^{*2}_1}$	Virtual deflection
$\ddot{x}$	Second time-derivative of x

~	Approximate
$\forall$	For all
kilo	10^3 (thousand)
mega	10^6 (million)
giga	10^9 (billion)
centi	10^{-2} (hundredth)
milli	10^{-3} (thousandth)
micro	10^{-6} (millionth)
nano	10^{-9} (billionth)

List of Figures

Chapter 3

Chapter 6

Appendix II

List of Tables

Chapter 1

INTRODUCTION TO MICROSYSTEMS

In this introductory chapter, microsystems will be introduced along with the basic concepts of micromachining. The rationale and objectives for the research will be presented. A literature review of microsystem analysis, modeling and characterization is given. An overview of microsystem synthesis and its implications to microsystem development is also included. Finally, the thesis layout is presented at the end of the chapter.

1.1. INTRODUCTION

One may argue philosophically that *infinity* is the definition of the limitless frontier on the large scale, while another may contend that the very small can be made infinitely smaller. In the year 1960, Richard Feynman put forth a challenge of stepping into the infinity of the *very small* by hypothesizing the reduction of the entire Encyclopedia Britannica onto the head of a pin [67]. In the year 2006 the German laser engineering journal, LTJ [264], reports that microengineering is on the threshold of new technological breakthroughs in many microengineering applications such as microfluidics, bio-medical imaging, microscopy, and microphotonics to name but a few. This trend continues the challenge put forth by Feynman and continues the miniaturization towards the infinitely small.

In the course of human technological advancement there has been no material more versatile and effectively exploited than silicon. Its versatility is due to a combination of three factors: it has good mechanical properties as its Young's modulus of elasticity is comparable to that of steel, it can be shaped to a high degree of precision, and it can be sensitized to many physical properties [73, 83, 186]. Petersen [186] states that the mechanical properties, high strength and high reliability, of silicon can be exploited for miniaturized mechanical devices and that these devices can be integrated with electronic components. Frühauf [73] has commented on the low thermal expansion, high heat conductivity and high elasticity of silicon, and that these properties can be exploited to fabricate miniaturized electro-mechanical sensors and actuators. Without the advent of silicon as a viable engineering material there would not be the vast gamut of electronic equipment and appliances so common today. From an engineering perspective, it is a material that lends itself into many fields through its mechanical, microfabrication, optical, and electrical properties. It is the multidisciplinary properties that are exploited to develop the field of Micro-Electro-Mechanical-Systems (MEMS) for vast applications.

MEMS could help to realize the integration of mechanical, electronics, optical and other elements on a common silicon substrate through the utilization of a specific microfabrication technology. By using similar micromachining tools initially developed for the silicon integrated circuits (IC) and semiconductor industry, MEMS engineers are microfabricating miniature structures from silicon and other materials. The IC component along with the software can be thought of as the *decision making* center of microsystems, and MEMS enhances this control capability with electro-mechanical or

opto-electro-mechanical sensing, for example, to enable microsystems to control their surrounding environment. Since MEMS devices are manufactured using batch fabrication techniques, high levels of functionality, reliability, and sophistication can be placed on a small silicon chip at a relatively low cost. Historically, sensors and actuators have been and continue to be the parts that are cost intensive and that need high reliability in an integrated sensor-actuator-electronics system. By comparison, MEMS technology allows these complex electro-mechanical systems to be manufactured using batch microfabrication techniques, and hence allowing the cost and reliability of the sensors and actuators to be comparable with that of IC.

MEMS microfabrication technology has enabled electrically actuated micromotors, capable of rotating at more than 10000 revolutions a minute, the size of a human hair for fans, pumps, or turbo generators [63, 75, 138, 161, 281]. Livermore [138] reports microturbine speeds in excess of 55000 revolutions per minute! However, although MEMS devices are *microsmall*, MEMS technology is not only about size and making things out of silicon, instead, MEMS should be thought of as a *new enabling* microfabrication methodology in which complex electro-mechanical microsystems are developed using *batch* microfabrication techniques in which a high volume of microdevices are fabricated in one process similar to the way IC are manufactured [53, 129, 185]. Already, MEMS are used for applications ranging from blood pressure and blood glucose monitoring to active suspension systems and airbag deployment sensors for automobiles [44, 115, 122, 160, 171, 230, 247, 253]. Within the next few years

MEMS accelerometers are expected to completely replace conventional devices in all foreign and domestic model cars [29, 82, 94, 123, 139, 146, 147].

Recently, micromachining methodologies have also been extended to optical microsystems, consisting, in general, of a combination of mirrors or electro-optical waveguides for light steering or sensing applications, where the microelectromechanical mirrors can be actuated to deflect light [32, 37, 39, 50, 52, 89, 119, 190, 224, 229, 231]. The mechanical motion of the mirrors or waveguides establishes *pathways* for a light beam. This allows one to steer, or direct the beam in a controlled manner as is required in microspectometer applications [199]. Micro-opto-electro-mechanical systems (MOEMS) are finding uses in such areas as fiber optic coupling, light emitting structures, optical scanners, photodetectors, and completely miniaturized optical systems such as spectrometers [41, 110, 118, 182, 199, 237, 261]. Kong [118] states that bulk micromachined silicon spectrometers, where silicon serves as a waveguide or optical path, are relatively simple to fabricate, and are compatible with standard IC microfabrication processes. These devices allow for the manipulation and interpretation of light signals as the sensing parameter through the analysis of a spectral or diffraction pattern that is characteristic of the changes in the sensed environment.

The MEMS technology evolution, in general, is greatly dependent upon the current capabilities of silicon foundry processes, especially as microscale devices are further miniaturized. An important process limitation of MEMS microfabrication technology is the increased need for tighter micromachining tolerances especially at boundary and

support surface interfaces as the trend continues towards smaller and smaller microstructures.

From an engineering point of view there are several advantages to having smaller components. Smaller systems have fast response times due to small mass and inertia and have high natural frequencies making them relatively impervious to external vibrations as might be expected in harsh environments. Ford [71] reports a response time of $3\mu s$ for a fiber optic attenuator based on an electrostatically actuated suspended microdevice. MEMS are having an impact on many different areas including basic science, aerospace, environmental condition monitoring, consumer goods, and medicine. MEMS are a significant step forward toward the ultimate miniaturization of current macro-scale machines and devices.

1.2. RATIONALE AND OBJECTIVES OF THE THESIS

As the complexity of microsystems increases, there is an increasing need to systematically research the *linked* physical influences on MEMS systems. There is currently a substantial amount of work on individual influences. Mechanical: where the microdevice is expected to respond to a change in operating conditions, sensed through a change in resonance frequency, which itself is a function of the mechanical property of the device [83, 125, 186]; thermal: where the thermal loading will change the geometry of the device and material properties [31, 55, 84, 150, 170]; electrostatic: where suspended structures such as microcantilevers and micromirrors can be actuated through

5

the application of an electrostatic potential [27, 159, 180], and on coupled electro-thermal influences [145]. Jensen [101] has investigated the switch failure and self pull-in due to thermal loading and found that the self pull-in was a dominant failure mechanism for a given switch geometry and applied electrostatic potential. Hung [96] has achieved vertical displacements of 1.75μm over a 2μm gap for electrically actuated mirrors. Ollier [167] has investigated moveable optical waveguides driven by electrostatic actuation, where the driving voltage and the optical path confinement within the waveguide are a function of the device geometry, that is, the geometry should be as narrow as possible to minimize power requirements but wide enough to contain the light which would otherwise *leak* from the waveguide.

Coupled influences such as microfabrication, electrostatic, thermal, geometrical, and cutouts have not been investigated as a group. These specific influences are relatively common both from the design and applications aspects. However, all coupled problems associated with multiparameter MEMS designs have not been investigated, and there is very little literature on this subject, but there is a huge amount of literature that deals with a single influence at a time. Hence, there is a need for a systematic modeling and experimentation of such coupled influences on the behaviour of microsystems that may also be extended to other systems and influences. The experimental data will enable one to verify, and enhance the mathematical theory and to create a detailed model that can be reverse synthesized for future applications. In this manner a synthesized approach to microsystem integration will allow MEMS design engineers to *look forward.*

Microcantilevers are very versatile MEMS devices and are used in many different applications, such as, biological sensors that can sense through variations in the frequency response of various biological agents, chemicals, and DNA factors [148, 195, 235, 245, 273]. Hence the frequency response of the microcantilever is very important to properly sense these parameters. McFarland [148] investigates the use of plastic microcantilevers of various geometries for chemical sensing in which changes to the resonance frequencies, due to a chemical reaction involving a specific coating on the microcantilever and a targeted reactant in the surrounding environment, are used for the sensing parameter. Datskos [50] reports that microcantilevers were found to respond to chemical stimuli even when only a small number of molecules adsorb on their surface, hence, there suitability to real time in-situ chemical sensing of hazardous materials.

Special polymer coatings, such as polyimide, can be applied to the surface of microcantilevers. The polyimide material is very sensitive to humidity [174], hence it can be used to measure the ambient humidity through changes to resonance frequency of the microcantilever, for example, due to the adsorption of water molecules which will change the overall mass of the system. Other examples of sensing applications include microscopy [215, 251, 286] where the surface features are scanned by microcantilever probes. Sader [216] and Pedersen [184] emphasize the importance of determining the spring constants of atomic force microscope cantilever probes and that the design of microcantilever beams for atomic force microscope applications should be optimized with respect to the first eigenfrequency by keeping the stiffness of the beam constant in order to properly scan the surface features of a given structure. Microcantilever based

actuators are also an important application, [228] where the displacement of the microcantilever under an applied stimulus is used to activate microswitches [38, 62, 144], where in maintaining a stable contact force between the switch and an electrode is of importance. Povinelli [190] has investigated optical microswitches based on a microcantilever geometries where the applied actuation voltage drops significantly with microcantilever length, for example, a $10\mu m$ cantilever requires $100V$ to actuate and a $14\mu m$ cantilever requires only $30V$, keeping all other parameters constant. This again shows the sensitivity of geometry considerations when designing microscale structures.

The main objective of this research presented here is to provide insight into the design of synthesized microcantilever beams through modeling with the Rayleigh-Ritz energy method [19], and experimentation. Other microcantilever modeling tools such as finite element method (FEM) models, for example, are limited by the type of mesh and element employed in the physical characterization of the microsystem which can affect the results obtained. Also, FEM methods are limited in the ability to systematically vary the boundary support stiffness in order to model microfabrication influences.

Hence, the theoretical formulation is best suited by a simplified approach, such as the Rayleigh-Ritz method, that can incorporate multiple influences into the model. Thermal influences are modeled solely by variations to the microcantilever geometry through the changes to the silicon microcantilever linear dimensions as a function of temperature.

The proposed research aims to synthesize the influence of coupled parameters on the behaviour of silicon microcantilevers through modeling and experimental verification.

1.3. MICROFABRICATION PROCESS

There are many different silicon foundry processes available today. Three such silicon foundry processes have been considered in the present work. They are: MUMPs technology [49] which is based on a 7 layer polysilicon-oxide-metal additive surface micromachining process, MikroMasch (μMasch) [153] that employs a bulk micromachining of silicon, and the Micralyne generalized MEMS (MicraGeM) [152] process using the silicon-on-insulator (SOI) bulk micromachining. The advantage of this particular process is that it allows MEMS designers to develop fully suspended structures with metal electrical contacts. Each of the above mentioned processes employ sets of fabrication steps that enable the realization of microstructures based on the original designs produced by multiple users.

The handling of silicon wafers for microfabrication purposes requires special attention to both the manner in which they are handled as well as to the environment in which they will be handled [7, 111, 272]. Kern [111] has demonstrated the effectiveness of hydrogen peroxide based solutions for cleaning bare silicon wafers, and reports that it will only negatively affect the surface quality of the silicon to a very negligible degree. These two issues are critical because dust and other contaminants will interfere with every microfabrication process step. All micromachining and microsystem fabrication

9

involves a lithography step in which the pattern of the microsystem design is transferred onto the silicon chip for processing and shaping.

1.4. COUPLED EFFECTS IN MICROSYSTEM INTEGRATION

The ever increasing need for miniaturization drives the design and microfabrication to limit the current tolerances. Often in the design process the coupling of microsystem parameters is unavoidable. MEMS designers must take into consideration the coupling between mechanical, electrical, thermal and geometrical effects.

1.4.1. *Micromachining influence on microcantilever performance*

Micromachining is a term that *usually* implies the machining of crystalline silicon or silicon products at the microscale through an appropriate mask design and etch process [90, 114, 141, 223, 239, 252, 265, 268]. Seidel [222] has reported on adding isopropyl alcohol to potassium hydroxide etchant solution in order to decrease the etch rate, and to increase the uniformity of the etch. One of the main challenges in the microfabrication of microstructures on a single silicon chip design layout is to control in a quantifiable manner the end support boundaries, and component interfaces within the design. These boundaries are the intersections of the crystalline planes of silicon where, for example, the intersection of the {111} and {100} planes is in the (110) direction. Each set of these planes is inclined at an angle of 54.74 degrees with respect to the surface [109, 222]. Unfortunately, with the current microfabrication limitations it is not possible to fully

control these parameters hence, a certain amount of undercutting of the structure occurs [30, 142]. Madou [142] states that undercutting is a function of etch time and hence related to the final etch depth. When etching rectangular corners, deformations occur due to undercutting and this is an unwanted effect where total symmetry and perfect 90 degree corners are required. This is of important consequence for the fabrication of suspended microcantilever beams used for a variety of applications such as atomic force microscope (AFM) probes [23, 60, 128] and optical applications [16, 28, 218]. Both Sader [216] and Pedersen [184] investigate the influences of final structure geometry on the performance characteristics of AFM probes. The final geometry, especially at the boundary support will in part determine the mechanical characteristics of the device. The static and dynamic mechanical behaviour of these types of devices are closely tied to the material used in the fabrication process, the geometry of the device, the environment in which they are to be employed, thermal and electrostatic influences and the microfabrication limitations resulting in *non-classical* support boundary conditions.

For the fabrication of microsmall devices *highly controllable* silicon etch processes are generally used [1, 22]. Boisen [22] describes a method based on an aluminum metal masking technique in which suspended silicon have been fabricated using reactive ion etching process. The aluminum is not affected by the reactive ion etching and hence forms a good mask for the silicon structure. However, the inherent nature of etching silicon and silicon based materials commonly used in microtechnology, results in small deviations to the effective support boundary geometry, and unfortunately as the size of the devices are reduced, there is in many cases not a corresponding reduction in the

microfabrication limitations for that particular foundry process. Intensive research activities have been undertaken throughout the world for newer microfabrication methods and also for nanofabrication methodologies in which the scaling of the micro-to-nano plays a significant role and which are currently beyond established microfabrication methods. Brugger [26] indicates that the current advancements in micromachining methods are slowly enabling access to the nano-scale, and that AFM microcantilevers with ultra sharp tips have been successfully fabricated using both wet and dry silicon etching processes. Further miniaturization will entail the need for improved high-resolution (<1 µm) micromachining methods such as with lasers or x-rays [100, 226]. It is reported by the Industrial News Room [100] that laser based micromachining will be able to micromachine *very small* parts with feature sizes of the order of 1/1000 of an inch with tolerances of ± 1/5000 of an inch.

Microcantilever silicon beams have a great potential for sensing and actuation at the microscale level in many different fields ranging from bio-medical to space exploration [176]. These types of sensing applications have increased difficulty due to the fact that support boundary effects at the ends of the beam play a significant role on the properties that are being measured, thus changing the *elastic* properties of the entire microsystem. The elastic characteristics of the microstructure define the mechanical limitations and operational quality of a given device and must be properly quantified. In most cases it is not possible to gauge the microfabrication influences beforehand, and one can only simulate these effects through mathematical modeling. However, these hypothetically imposed boundary conditions in the theoretical model may either over emphasis the

microfabrication influence or not take it adequately into account. Hence, a strong experimental initiative should be undertaken to augment and compliment the theoretical model for a given silicon foundry process.

AFM microcantilever probes are one type of application of silicon microsystem technology and are used to characterize surface features by measuring the displacement at the tip of a microfabricated cantilever with a given spring constant, K [107, 162]. Kawakatsu [107] reports typical mechanical characteristics of cantilevers measuring 10μm in length and thicknesses of 20nm were spring constants of a few mN/m and a natural frequency of 0.5 MHz. Therefore, in order to accurately quantify the surface topography of a given substance, the deflection properties, stiffness parameters, boundary conditions, and specifically the vibrational response of an AFM cantilever must be well understood. In this regard, there have been several published reports, [98, 107, 130, 162, 184, 216, 217], in which it is stated that the AFM spring constants as indicated by the manufacturers are inaccurate due to various reasons. Hence, the AFM cantilever manufacturers apply a wide range of tolerances in the specified values of the spring force constant because of the inaccuracies resulting mainly from inherent inconsistencies associated with manufacture of microcantilevers, for example, the variation in cantilever thickness, or end support conditions, etc. from one cantilever to the next. This fabrication specific anomaly has led to several different methods for estimating the AFM cantilever spring constant [98, 107, 130, 162, 184, 216, 217]. Gibson [78] proposes both static deflection by added mass and dynamic resonance response, test methods for the calibration of the AFM spring constants in order to obtain a mechanical characterization

that is *independent* of the geometry of the devices. Hence, micromachining is a contributing source of error when determining the microcantilever spring constant, K. One of the important possibilities is the influence of non-classical end support conditions on the elastic properties of the microcantilever.

Boundary conditioning is used in order to quantify the influence of non-classical support conditions and operating conditions on both static and dynamic behavior of micro-cantilever beams. The dynamic behavior of the micro-system is affected by varying the elastic properties of the entire system. By using this approach, it is possible to quantify the support influence through boundary support stiffnesses. In addition, the stiffness conditions at the boundaries allow the manipulation of the structural natural frequencies in a favorable fashion [179].

1.4.2. *Electrostatic influence on microcantilever performance*

The static and dynamic characteristics of MEMS microcantilevers can be influenced through the application of an electrostatic potential, which will also change the elastic properties of the entire microsystem. Interestingly, it is the mechanical property of the microcantilever that limits the amount of applied electrostatic potential. This is a consequence of the applied electrical load having an upper limit beyond which the mechanical restoring force of the microcantilever can no longer resist the applied electrostatic force and is *snapped* onto the substrate. This critical voltage is called the *pull in voltage, threshold voltage, snap voltage* or *touch down voltage* depending on

which nomenclature one prefers [2, 54, 69]. Flores [69] defines the *pull in voltage* as the voltage at which steady state solutions cease to exist for the electrostatic elastic model. Shown in Figure 1.1 is an illustration of a microcantilever and electrode combination.
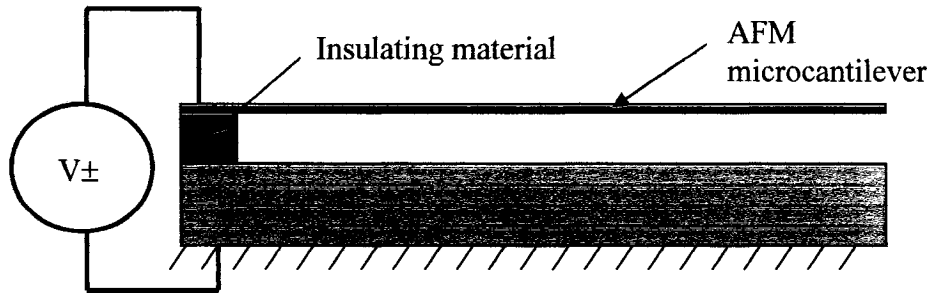
Figure 1.1. Schematic representation for the electrostatic influence.

The application of an electrostatic field can be seen as providing an electrostatic *softening* stiffness which can be used to selectively tune [96, 172] the microcantilever thereby improving resolution in AFM microcantilever probes [27]. Park [180] has reported that the stiffness of the microstructure can be reduced by providing an electrostatic negative stiffness that serves to improve the resolution of the sensing element. Yao [274] has demonstrated electrostatically actuated tunable microresonators where both the x and y flexural directions can be tuned simultaneously or independently and a typical tuning range of 60 kHz for a 0.96 MHz resonator.

1.4.3. *Thermal influence on microcantilever performance*

The nature of MEMS technology creates coupled behaviour where two or more energy domains such as mechanical, electrical, optical, or thermal, for example, combine and provide the static and dynamic characteristics of the device. The thermal energy domain is arguably the most influential in MEMS devices, either by intentional design or undesirable coupling. DeVoe [55] considers one of the main challenges in MEMS sensor applications is the limiting of sensor noise imposed by thermo-mechanical coupling. The unwanted coupling is a concern for MEMS applications where the device is to operate in harsh environments with large thermal gradients [44, 150]. Mehregany [150] is investigating silicon carbide as a MEMS material for harsh environments, owing to its excellent mechanical and electrical properties, and its high melting point of 2830 °C compared to 1415 °C for silicon. In this regard, the thermal *absorption* capabilities of a specific microsystem design and material need to be established in order to provide an adequate *thermal tolerance* for the microsystem so that the mechanical or electro-mechanical characteristics of the system not be negatively influenced to a great degree.

In general, thermal influences in MEMS micro-devices envelope a host of issues, from the efficient harnessing of thermal energy for actuation in bimorph structures to the reduction of thermal noise that is intrinsically imposed by thermo-mechanical coupling in microsensors and AFM microcantilevers [250]. Butt [31] reports that for AFM applications thermal fluctuations are the dominant source of unwanted noise and limit the resolution of the scanned surface and proposes quantifying the AFM spring constant as a

16

function of the thermal load. There currently exist numerous MEMS devices, such as thermal actuators, thermal flow sensors, micro-hot-plate gas sensors and tunable optical filters, that are based on thermal effects [40, 56, 133, 193, 242, 285]. Zine-El-Abidine [285] has designed a thermal bimorph actuator to vary the distance between two inductors for RF MEMS tuning applications where the tuning factor is a function of the thermo-mechanical actuation and reports a tuning capacity of 30% for a 5 GHz resonance. In thermal MEMS actuator applications, thermal loading causes mechanical stress and hence movement in the actuator, where the movement is a function of the applied thermal load and is not considered as a negative effect in this case. However, for the vast majority of MEMS applications thermal loading is considered undesirable and yet the problem remains to a large degree unavoidable.

Microcantilever based sensors have been used to monitor various physical and chemical processes by *processing* changes in temperature, mass, electromagnetic field, or surface stress, for example, into a micromechanical or nanomechanical response [13].

For increased sensitivity microcantilever arrays can be incorporated on a single chip [33, 59, 149] and coated with different reactant concentration for chemical or biological sensing. Calleja [33] incorporates polymer coatings on microcantilever arrays of up to 33 microcantilevers, where the polymer concentration differential will vary the frequency responses of the individual cantilevers within the array and can be used to target specific pathogen concentrations and DNA detection. Thermal devices such as sensors and actuators based on a bimorph (usually silicon-metal) platform have gained importance

due to their large actuation range and ease of fabrication [47, 77, 221]. Sehr [221], for example, reports thermal bimorph, silicon and aluminum structure, induced deflections of 4.5μm for a 1000μm long microcantilever and an input power of 3mW, and is one order of magnitude higher compared to a deflection of only 0.45μm for a similar non-bimorph structure.

1.4.4. *Geometrical influence on microcantilever performance*

Although humble in design, microcantilevers are versatile in sensor, actuator, or microphotonic waveguide applications. The durability and sensitivity of such microsystems is greatly dependant on the material, geometry and operating environment of the device. There are applications where a particular frequency response and mode shape is vital for a given microsystem sensing application. This condition is particularly true in the design of micro-accelerometers and gyroscopes, where sensing is accomplished through electrostatic, capacitance measurements that are inherently sensitive to geometry [125, 159]. Najar [159] investigated the influence of microcantilever beam thickness and width on the pull in voltages and static deflection range and found that increases to the beam width resulted in decreases to the pull in voltage and increases to the static deflection for a given voltage. The vibrations of thickness tapered, circular cross section microcantilevers have been investigated under various applied loads [106, 158, 269, 282, 283], where Zhou [282] investigated the dynamics of tapered beams with continually varying rectangular cross-sections, in order to optimize strength and weight distribution, and the dependence of the eigenfrequency

on the specific geometry. Lai [125] proposes an inverse mode shape approach for designing microcantilevers in which the geometry of the structure is designed for prescribed mode shapes using a given material and where the prescribed mode shape must be physically realizable based on a set of design criteria. One of the design criteria listed is that the mode shape and its four derivatives must be smooth and continuous.

There is currently considerable interest in integrated optical devices such as tunable optical filters, actuators, switches, and optical fiber aligners based on movable waveguides [20, 21, 51, 105, 164, 167]. Povinelli [190] has designed a microelectromechanical optical switch based on the horizontal deflection of an input waveguide with one of two output waveguides and states that the transmission losses due misalignment can be attributed, in part, to microfabrication limitations. These movable microcantilevers carry channel guides and have been demonstrated in silicon-on-insulator (SOI) and silica-on-silicon configurations. Since the waveguide can be moved by electrostatic deflection (Syms [238] reports static deflections of 500μm for cantilevers of 2mm length and 20V actuation), of the microcantilever, there are applications in switching, sensing and beam scanning.

The power attenuation can be achieved through the application of an electrostatic force [108, 136, 192, 236]. Liu [136] has developed an optical micromirror attenuator with an attenuation range of 45dB requiring only an 8V actuation voltage. The amount of static deflection depends upon the device geometry and applied electrostatic force. The characterization must also take into account the environment in which these types of

devices will operate. Harsh environments, such as high thermal gradients, for example, will require specialized MEMS packaging [36, 169, 271]. As for the optical mode converter (or isolator) applications, the contour width tapering will reduce the number of optical modes propagating down the waveguide [4, 34, 76, 181, 191, 241]. Almeida [4] proposes a nanotaper coupler consisting of a width tapered waveguide along the length, to a nanometer sized tip and where the optical mode isolation is a function of the width at the tip of the waveguide. These types of mode converters are especially useful for coupling with single mode fibers, for example, and find uses in telecommunication fields [46, 70, 256, 258].

Optical MEMS integrated with microfluidics find applications in biomedicine where the real time detection of pathogens is of critical importance [8, 81, 275]. Amritsar [8] has recently reported on optical detection methods based on static deflections of specially coated microcantilevers with enzymes for the detection of precursors to myocardial infarction, and where the amount of deflection is a function of the enzymatic reaction.

Recently it has been reported that SOI based waveguides, or microcantilevers, can be used to generate Raman lasing where the stimulated Raman scattering (SRS) in SOI waveguides is an attractive way of amplifying optical signals because it does not require the introduction of any dopants during fabrication of the SOI wafer [121, 182, 213]. Rong [213] has used a SOI waveguides of less than $5\mu m^2$ to achieve Raman lasing characteristics with optical wavelengths of 1542nm. The combination of lasing

capability on a MEMS SOI waveguide with width contouring on a microcantilever, and static deflection capabilities is an exciting, new area of research.

1.4.5. *Cutout influence on microcantilever performance*

There are surface microfabrication processes, such as the MUMPs process, for example, where etch holes or cutouts are incorporated into the top layer of the structure. These etch holes are needed for the passage of etchant to the underlying sacrificial layer or layers that need to be removed for the release of the surface structure [15, 24, 194] or for the minimization of squeeze film damping effects, Veijola [254] has reported that air damping can be minimized as a function of the radii of the circular cutouts incorporated onto the microstructure. Ford [71] has included *air passages* in the design of a microoptical attenuator in order to improve the response time of slow mechanical attenuators which were typically ~1s and improved to 3μs. Hence, the effect of cutouts on the static and dynamic characteristics of microcantilevers will be included in the investigations presented in this thesis.

1.5. MICROSYSTEM MODELING

The main objective for microsystem modeling and simulation is to facilitate and accelerate the transition from device conceptualization to device fabrication. The theoretical modeling allows MEMS designers to estimate and predict the static and

dynamic characteristics of the microsystem based on a set of input parameters: choice of material, geometry, and external influences.

1.5.1. *Boundary conditioning*

The mathematical modeling is carried out using the classical analytical tools used in the *normal size* world. The Rayleigh-Ritz energy method [124, 244], where the frequency of vibration is a function of the maximal strain and kinetic energies of the system comes with significant advantages as it may be readily applied to plates [19], triangular plates [18, 112] and plates with cutouts [126, 157]. In the Rayleigh-Ritz energy method, the flexural deflection shapes are assumed to be a linear combination of orthogonal functions satisfying at least the geometrical boundary conditions of the vibrating structure. The maximum strain and mass energies formulated using these shape function are used to acquire an expression for the natural frequency in the form of the Rayleigh quotient [17]. In this present work the approach as outlined in [19], but applied to a beam is employed for the dynamic analysis of a vibrating microcantilever. *Boundary conditioning* method is used to incorporate non-classical boundary support conditions, due to microfabrication influences, on the dynamic response of the structure [177] by incorporating artificial springs at the support boundary. In this approach it is possible to change the elastic properties of the microsystem by varying the boundary support conditions through the artificial support stiffnesses.

1.6. COUPLED ENERGY DOMAIN SYNTHESIS OF MICROSYSTEMS

Synthesis is a way of amalgamating distinct influences on a microsystem and studying their unified effect on the elastic properties of the microstructure. Haug [87] reports that the *structural optimization* for a small range of motion of the microcantilever, through the selection of an appropriate geometry, for a given application will form the basis for a conditioned output response profile that is a function of coupled input parameters. Hence, in this regard, a microsystem can be designed to give a distinct output response to a set of applied parameters and operating conditions such as electrostatic and thermal loading. This synthesis approach has been applied to beams under electro-thermal influences by Mankame [145] where the varied topology of the beam is synthesized into a quasi-beam element to facilitate the electro-thermal heat transfer along the surface of the beam.

The Oxford dictionary [173] defines synthesis as, *the combining of constituent elements of separate material of abstract entities into a single or unified entity*. This definition, as applied to microsystems, means that microfabrication limitations, electrostatic, thermal, and geometry influences, for example, can be unified through the output response, from which one may then use this information to design a microsystem for a given set of conditions, and based on this approximate, or estimate the performance of the microsystem [178]. Shown in Figure 1.2 is a conceptualized process flow for microsystem development and integration.

MEMS designers generally synthesize micromachined outputs by prototyping new microsystems based on existing physical phenomenon and principles [79, 104]. Kamalian [104] proposes a test-feedback strategy based on genetic algorithms for improving evolutionary synthesis as a function of test results obtained and the characterization of output. Through mathematical modeling it is possible to estimate the influence of the individual variables- mechanical, electrical, thermal, and geometry, for example, and it is also possible to predict the coupled parameter behaviour. In this regard multiple input parameters can be incorporated into the model and characterized as a whole with a *uniquely dependent* output response. Shown in Figure 1.3 is an overview of several input parameters investigated and synthesized in this thesis.
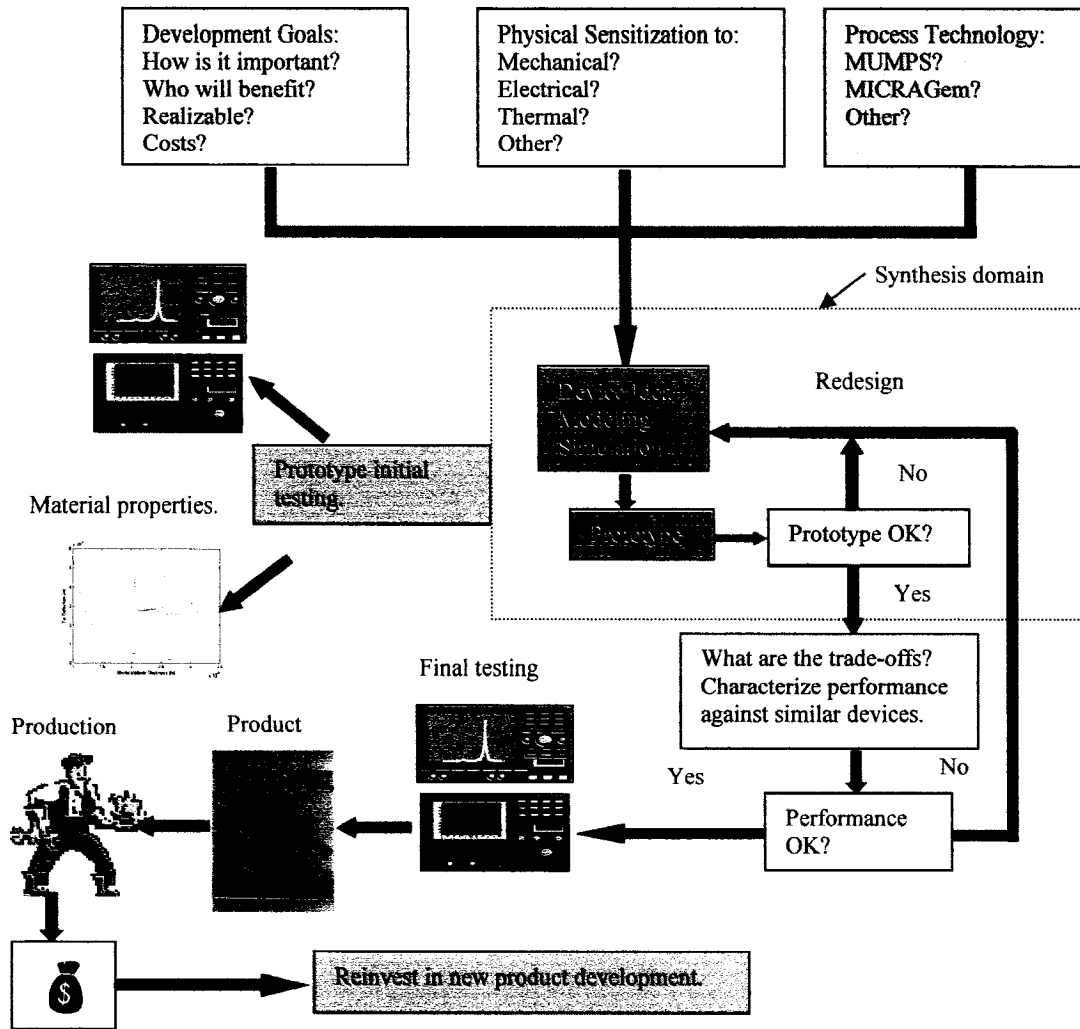
Figure 1.2. Process flow for microsystems: conceptualization to production.
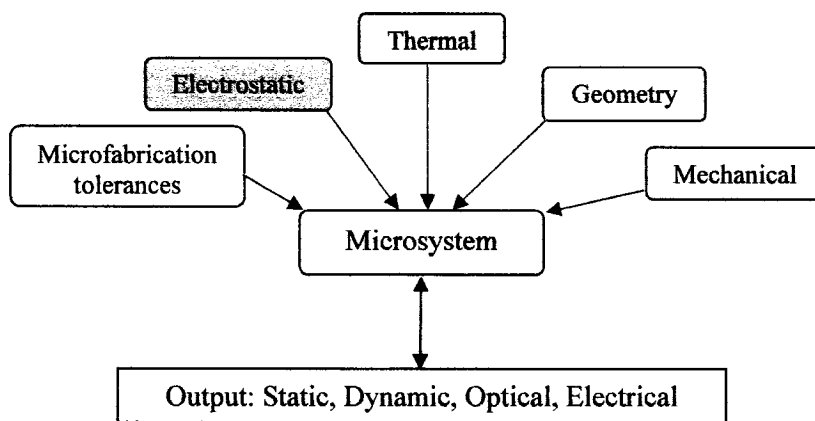
Figure 1.3. Physical phenomenon that can influence microsystems. The double arrow indicates the inverse design dream of MEMS engineers using synthesis.

1.7. DYNAMIC TESTING METHODS FOR MICROSYSTEMS

The testing of the static and dynamic behavior of MEMS micromachined components and integrated microsystems is vital in order to gain the needed performance characterization of these devices [117]. Lately, companies involved in testing of micro-electronic circuits have developed commercially available instruments to measure the mechanical performance of microstructures. Theoretical modeling forms only the basis for the performance characterization, and should be followed up with rigorous testing before these devices can be cleared for production in commercial quantities. However, due to their inherent small size, these structures pose a problem regarding the method of testing especially that their mechanical properties can vary significantly due to microfabrication tolerances and conditions [175, 214, 233, 234, 259, 284].

1.7.1. *An overview of some MEMS test methods*

Although MEMS are based on IC semiconductor technology, standard IC test methods do not fully address the mechanical features and environmentally dependent characteristics [61, 66], micromachining defects [48], and faults such as cracks due to packaging [248], and the reliability of the MEMS packaging process [92].

Optical profiling [86, 197, 198, 255, 260, 267], also known as white light interferometry, has long been used as a standard test method for characterizing surface topography of MEMS devices. Hart [86] incorporates this method by passing white light through a

26

beam splitter, where part of the light is directed to the sample and part to a reference surface. When the light reflected from these two surfaces recombines a pattern of interference *fringes* forms. During a measurement, a series of these interference patterns is collected, from which the height of each point on the surface can be determined. In most cases, test measurements have been made relatively early in the manufacturing process, before the MEMS device is packaged. Although these *early* tests are a normal step in the microfabrication procedure, most devices will perform differently once encased in their final packages [85, 279]. Hsu [92] emphasizes the need for cost effective packaging and *robustness reliability* in order to successfully commercialize MEMS products and to gain consumer confidence in these products.

1.7.2. *Laser Doppler velocimetry*

Laser Doppler velocimetry (LDV) is a testing method that enables the user to perform non-contact testing on microsystems. The sensing principle is based on the Doppler effect. Non-contact vibration measurements are thus possible with such a testing system that can lead to significant improvements in the accuracy and precision of MEMS testing [163, 220].

The proposed test method discussed herein offers a relatively simple and cost effective way to measure the mechanical behavior of MEMS structures. The resulting spectral response of the microstructure may then be detected by the LDV method. While this method is simpler than, for example, electrical output signaling in the form of capacitive

27

variations [27] it can only measure single-point velocities on the microstructure. For multi-point dynamic analysis, a sampling of many different points on the microstructure is required. This allows one to obtain a mode shape profile of the vibrating microsystem [189].

1.8. SUMMARY

MEMS require careful physical characterization and performance analysis due to the inherent cross-disciplinary nature they possess, as they provide wide range of possible applications. The *cross linked* features of these devices allows them to be manipulated in a variety of different ways, such as, mechanically through the variation of geometries and materials, electrostatically through the incorporation of electrodes either suspended over the device or incorporated on the substrate, thermally by designing bimetal or bimorph type structures, and optically through the incorporation of index sensitive silicon-silica waveguides. Also, the static and dynamic characteristics can be conditioned through the application of design parameters such as cutouts, and geometrical variations. However, the overall design synthesis must take into account all the parameters that will influence the operational characteristics of the microsystem. Hence, in this regard the most desirable qualities of microsystems, in general, are simplicity of design, compatibility with *batch* fabrication processes, excellent mechanical strength and ease of integration with peripheral devices such as optical fibers and/or microelectronics.

1.9. THESIS LAYOUT

The thesis layout is outlined below. The general format followed for each chapter includes a brief introduction to the content of the chapter being presented and summary at the end of the chapter.

Chapter 1: INTRODUCTION TO MICROSYSTEMS

This chapter introduces microsystems and microengineering by presenting an overview of the current microsystem technology and applications for MEMS devices. The rationale and objectives outline the need for the present research based on the lack of data on the cross-disciplinary nature of MEMS systems. Although there is a large amount of work that has been done on individual influences affecting a microsystem, no systematic studies have been carried out on coupled parameters. A literature review is given, and introduction to the individual influences such as microfabrication, electrostatic, thermal, geometry and cutouts investigated in this work is also presented. Microsystem modeling and test methods are discussed.

Chapter 2: MODELING OF ELECTRO-THERMO-MECHANICAL INFLUENCES

A brief overview of current microsystem modeling and simulation methods is given. The Rayleigh-Ritz energy method is introduced and applied to microsystems. Included in the modeling are, microfabrication, electrostatic, thermal and mechanical influences. Both static and dynamic modeling is given and the analytical results are also presented.

Chapter 3: SEGMENT RAYLEIGH-RITZ METHOD

The *segment* Rayleigh-Ritz method is introduced. This approach is used to model microcantilevers having etch holes, cutouts and boundary discontinuities. A comparison of FEM and *segment* Raleigh-Ritz results are presented. Also, included is a comparison of mode shapes, static deflections, and virtual deflections, of a microcantilever in terms of the number segments in order to validate this method. Finally, the synthesized analytical results that include all the influences such as, microfabrication, electrostatic, thermal, mechanical and cutouts, applied simultaneously are presented.

Chapter 4: MICROSYSTEM TESTING METHODS

An overview of current MEMS testing methods is presented. A detailed presentation of a non-contact optical testing method based on the Doppler effect and its suitability for testing microstructures is presented. Included is an overview of the optical test setup and measurement methodology established at the Optical Microsystems Laboratory at the CONCAVE research center for microsystem testing and analysis.

Chapter 5: SUPPORT BOUNDARY CHARACTERIZATION

The support boundary characterization of several microstructures fabricated using different technologies is investigated. The concept of thermo-mechanical microstructure support boundary characterization is also presented. The results are validated through experimental results obtained with the thermal loading. The experimental setup and procedure used for the thermal loading is given along with the results obtained. Electro-mechanical boundary support characterization is also presented as an alternate approach

to avoid thermal loading. The experimental results are presented and compared to those obtained for thermo-mechanical and electro-mechanical boundary characterization methods.

Chapter 6: SYNTHESIS OF MICROSYSTEMS

An experimental validation of the theoretical formulation presented in Chapter 3 is given. The investigation takes into account all the physical influences discussed in Chapter 3 for several microcantilever geometrical configurations. The results obtained experimentally are compared to that of the theoretical model.

Chapter 7: CONCLUSIONS AND EXTENSIONS

Concluding comments on the synthesis of microsystems and a summary of the aims and achievements of the work presented in this thesis are given. Future goals and directions are also discussed.

References

The numerated references are given here. They are listed in alphabetical order.

Appendix I: COMPUTER AIDED DESIGN OF GEOMETRICALLY DIFFICULT MICRO-MECHANICAL STRUCTURES FOR ACADEMIC ENVIRONMENT

The main steps involved in microsystem design using MATLAB to generate the microstructure geometry are given. Examples of geometrically difficult designs are presented along with microstructure mask layouts incorporating multiple structures.

Appendix II: MICRAGEM: SILICON-ON-INSULATOR BASED MICROMACHINING PROCESS

An overview of the MicraGeM technology with process steps is given.

1.10. PROMINENT CONTRIBUTIONS

- Microfabrication, electrostatic, thermal, geometry and cutout influences on cantilever MEMS have been successfully modeled.

- The segment Rayleigh-Ritz method has been developed in order to improve the theoretical analysis of cantilever MEMS with discontinuities along their length.

- The first successful experimental testing technique for MEMS in Canada has been developed.

- Boundary support characterization of MEMS cantilevers through experimental testing has been proposed.

- A method to design and characterize geometrically difficult microstructures has been developed.

- The design synthesis that has enabled the fine tuning of the static and dynamic behaviour of MEMS cantilever structures has been formulated.

32

Chapter 2

MODELING OF ELECTRO-THERMO-MECHANICAL INFLUENCES

Presented in this chapter is the mathematical formulation employed for the modeling of electrostatic, thermal and mechanical influences on a microcantilever. The Rayleigh-Ritz energy method is presented, and the concept of an elastic foundation is introduced.

2.1. INTRODUCTION

In recent times, microsystems draw a great deal of attention from mathematical modeling and simulation. Theoretical simulation of MEMS devices involves computing the deformations and stresses on particular microstructures subjected to electric fields, thermal loads, geometrical variations, and support boundary conditions. The MEMS structure can also include conductors, dielectrics and coatings which will need to be included in the model. For example, applied electrostatic fields produce forces on the surfaces of these structures and cause them to deflect and deform, as a function of the applied voltage [2, 54, 69, 96]. The resulting deformed shape alters the capacitance [27] of these structures and this, in turn, changes the forces on them. If thermal influences are also considered, then changes to capacitance as a function of thermal loading must also be included in the model. The behaviour of microsystems is very sensitive to geometry and applied voltages, and their response can be very non-linear. Hence, mathematical

33

modeling becomes a very important technique for gaining understanding of these physical systems [227].

2.1.1. *MEMS simulation methods*

Some of the past approaches to the simulation of MEMS have included capacitance modeling for electrostatics [91, 143], and hybrid boundary element method (BEM)-FEM for microscale simulations [3]. However, surface and volume mesh generation for MEMS is very demanding. For example, an electromechanical system involving coupled mechanical and electrostatic energy domains consists of a volume mesh for an electromechanical microstructure to perform finite element based elastic analysis and the surface mesh of the same device to perform exterior electrostatic analysis based on the boundary element method [6]. Finite element methods have been used for modeling and estimating the deflections and buckling characteristics of micromachined beams [14, 156, 168]. These methods are considered to be computationally intensive, requiring both a high level of skill and computing time [97]. They are also limited by the number and choice of mesh elements that can be used to model a system. Hence a simpler approach is needed to model microscale systems.

Meshless simulation techniques are becoming one of the most accepted and valuable methods of computer aided design (CAD) of MEMS structures [5]. They have gained such popularity in MEMS applications because of the multiphysics and multiscale analysis capabilities, which are fundamental requirements in MEMS simulation and

modeling. Neural network [132] based simulations consist of an interconnected assembly of simple processing elements or nodes, and the processing ability of the network is stored in the inter-nodal connection strengths, or weights, which are obtained by a process of adaptation, and can be used to make predictions on the functionality of MEMS devices.

2.2. RAYLEIGH-RITZ ENERGY METHOD

In the analysis of vibrating mechanical systems it is generally the fundamental frequency that is of greatest interest as opposed to higher frequencies because of its high response to a forced excitation at resonance. The Rayleigh method can be used to estimate the natural frequencies of elastic systems. In its fundamental form, the Rayleigh [196] method is a way to analyze a mechanical system through its potential and kinetic energies, and a single shape function. Ritz [278] improved on this method by introducing multiple shape functions multiplied by constant coefficients, and hence allowed for an improvement on the estimated natural frequencies of a vibrating system [244].

In the theoretical dynamic analysis of MEMS devices the Rayleigh-Ritz energy method is employed where the mathematical modeling of the MEMS microcantilevers is carried out by applying boundary characteristic orthogonal polynomials [19]. This approach is also adopted for the static deflections, where instead of an homogeneous eigensystem, one obtains a particular solution, for a set of linearly independent equations, for an applied electrostatic potential. This *approximate* numerical method is a simple way to analyze

the vibrational response of a variety of structures such as plates and beams [17, 18, 19, 112, 126, 157, 177] and is employed here for this reason.

The flexural deflection along the normalized length, x, of the microcantilever is estimated as,

$$W(x) = \sum_{i=1}^{n} A_i \phi_i(x) \qquad (2.1)$$

where, A_i are the deflection coefficients of the microcantilever, and $\phi_i(x)$, are the orthogonal polynomials satisfying the geometrical boundary conditions, x, is a non-dimensional *longitudinal* coordinate ranging from 0 to 1, and n is the total number of polynomials. The natural frequency of vibration of the microstructure is obtained from the Rayleigh quotient, and is defined as,

$$\omega^2 = \frac{U_{MAX}}{T_{MAX}^*} \qquad (2.2)$$

where $U_{MAX} = \Sigma U_n$ is the maximum potential energy and is the sum of the individual potential energies applied to the microcantilever.

$$T_{MAX} = \omega^2 T_{MAX}^* \qquad (2.3)$$

is the maximum kinetic energy of the microcantilever and, ω, is the cyclic natural frequency of the vibrating structure. The stationarity condition [17] of the Rayleigh quotient with respect to the undetermined deflection coefficients, A_i, given as,

$$\frac{\partial \omega^2}{\partial A_i} = 0 \quad \forall\ i = 1, \dots, n \qquad (2.4)$$

results in an eigensystem. The solution of the eigenvalue equation will provide the approximate natural frequencies and mode shapes for n number of modes.

2.2.1. Energy formulation

The energy formulation takes into account electro-thermo-mechanical influences. The thermal influences, however, are not directly energy based in this analysis. Their influence is brought into the model through changes in energy due to the influence on the geometry of the microcantilever. Shown in Figure 2.1 is a schematic representation of a microcantilever with electrostatic and geometrical influences.
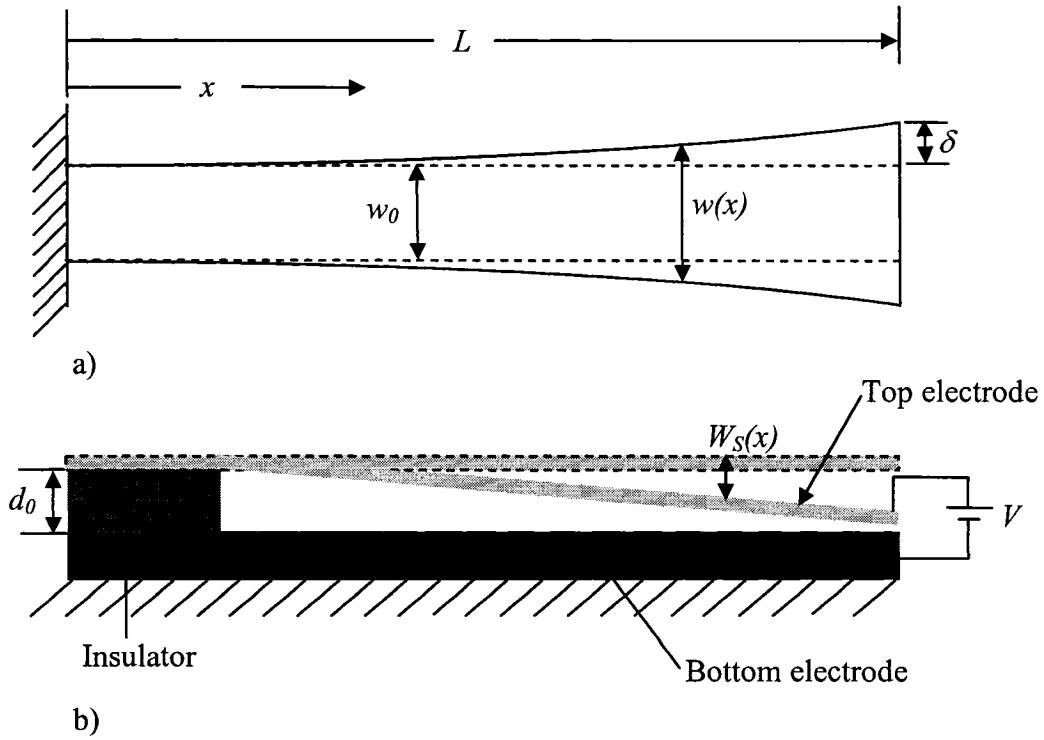
Figure 2.1. a) Schematic top view of microcantilever width contouring. b) Schematic side view of an electrostatically actuated microcantilever.

Where L is the length, x is the longitudinal coordinate, $w(x)$ the positional width, w_0 the unconditioned width, d_0 the dielectric gap (microcantilever-electrode spacing), V the applied voltage, and $W_S(x)$ the static deflection along the length of the microcantilever.

37

The electro-thermo-mechanical influences affecting a microcantilever are modeled with artificial springs as shown in Figure 2.2.

$$K_E = \int k_E(x)dx$$
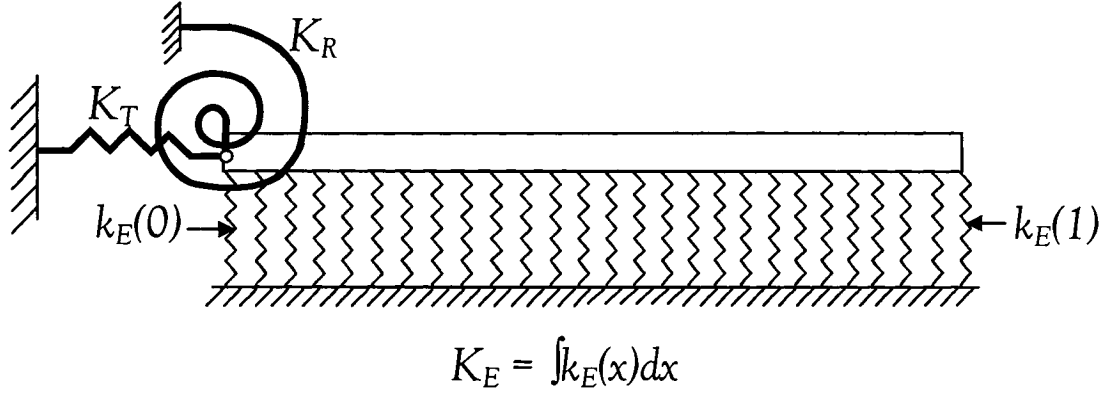
Figure 2.2. Equivalent microcantilever with artificial springs.

The maximum strain energy, $U^{(T)}_{MAX}$, of the microcantilever under electro-thermal influences is given by,

$$U^{(T)}_{MAX} = U^{(T)}_B + U^{(T)}_{SP} + U^{(T)}_E \tag{2.5}$$

where $U^{(T)}_B$, $U^{(T)}_{SP}$, and $U^{(T)}_E$ are the beam, boundary support springs and electrostatic potential energies, respectively.

The beam part of the microcantilever potential energy is given by,

$$U^{(T)}_B = \frac{E^{(T)}h^{(T)3}}{24L^{(T)3}} \int_0^1 w(x)(W''(x))^2 dx \tag{2.6}$$

and the maximum kinetic energy is given by,

$$T^{(T)}_B = \frac{1}{2}\omega^2 \rho^{(T)}h^{(T)}L^{(T)} \int_0^1 w(x)(W(x))^2 dx \tag{2.7}$$

38

where the following definitions apply, $L^{(T)}$ is the length, $h^{(T)}$, is the thickness, $E^{(T)}$, is Young's modulus of elasticity, $\rho^{(T)}$ is the material density, $w(x)$, is the positional width of the microcantilever, $W''(x)$ is the second derivative with respect to x, and ω is the rotational frequency. $W(x)$ will be $W_S(x)$ in the case of the static equilibrium estimation, and $W_D(x)$ in the dynamic equilibrium estimation. The superscript, (T), refers to temperature. The mechanical and electrostatic influences affecting the microcantilever response are presented below. In order to present the theoretical formulation in a seamless fashion all figures pertaining to microcantilever geometry and cutouts will be presented at the end of section 2.2.5.

2.2.2. Modeling of boundary support

The influence of the boundary support of the microcantilever on the potential energy is modeled by artificial boundary support springs given by,

$$U^{(T)}{}_{SP} = \frac{1}{2} K_T (W(0))^2 + \frac{1}{2} \frac{K_R}{L^{(T)2}} (W'(0))^2 \tag{2.8}$$

where, K_T (N/m) is the translation and K_R (Nm) is the rotational spring in non-normalized form, $W(0)$ and $W'(0)$ the deflection at the boundary support and the first derivative, respectively. By varying the values of K_R and K_T it is possible to vary the support boundary condition from *free* to *clamped*. In the modeling only K_R is varied, as there is no translational motion at the support, and one may model the support conditions as varying from *simply supported* to *clamped*. Hence, the microfabrication limitation influence at the support boundary is quantified through the rotational stiffness.

39

2.2.3. Geometrical modeling

One of the influences investigated in this work is the variation of geometry, namely the change in microcantilever width along its length. In this regard, the width, $w(x)$, of the microcantilever, is given by,

$$w(x) = w_0^{(T)}\Psi(x) \tag{2.9}$$

where $\Psi(x)$ defines a particular width profile, and $w_0^{(T)}$ is the *unconditioned* width of the microcantilever for a given temperature. In this formulation, the following definitions apply: *soft* conditioning, the microcantilever boundary support end width is less than the free end width with monotonous increasing width, and the conditioning function is given by,

$$\Psi_S(x) = 1 + (\rho_G - 1)x^\beta \tag{2.10}$$

In *rigid* conditioning the microcantilever boundary support end width is greater than the free end width with monotonous decreasing width, and the conditioning function is given by,

$$\Psi_R(x) = 1 + (\rho_G - 1)(1 - x)^\beta \tag{2.11}$$

where the geometry conditioning width ratio, ρ_G, is given by,

$$\rho_G = (w_0^{(T)} + 2\delta)/w_0^{(T)} = w_{max}^{(T)}/w_0^{(T)} \tag{2.12}$$

δ is the amount of *width offset* applied to the unconditioned width, $w_0^{(T)}$, of the microcantilever as shown in Figure 2.1, and β, is the *conditioning factor* and may be varied from zero to infinity. Other geometry conditioning functions, *soft-rigid* (*SORI*) and *rigid-soft* (*RISO*) are given respectively by,

$$\Psi_{SR}(x) = \begin{cases} 1 + (\rho_G - 1)2x^\beta & 0 \le x \le 0.5 \\ 1 + (\rho_G - 1)(2x - 1)^\beta & 0.5 \le x \le 1 \end{cases}$$ (2.13)

$$\Psi_{RS}(x) = \begin{cases} 1 + (\rho_G - 1)(1 - 2x)^\beta & 0 \le x \le 0.5 \\ 1 + (\rho_G - 1)(2x - 1)^\beta & 0.5 \le x \le 1 \end{cases}$$ (2.14)

The cutouts on the microcantilever are modeled in a similar fashion, however two microcantilever geometry conditioning functions, $\Psi(x)$ and $\Psi_C(x)$, are employed, where $\Psi(x)$ represents any of the geometry functions described above, and $\Psi_C(x)$ describes the cutouts, respectively. Hence the microcantilever width is now given by,

$$w(x) = w_0^{(T)} [\Psi(x) - \Psi_C(x)]$$ (2.15)

where,

$$\Psi_C(x) = \alpha_C \Psi(x)$$ (2.16)

Where the value of α_C can be chosen between 0 and 1.

Given in Figure 2.3 is a schematic of single and multiple cutout models as investigated in this work.
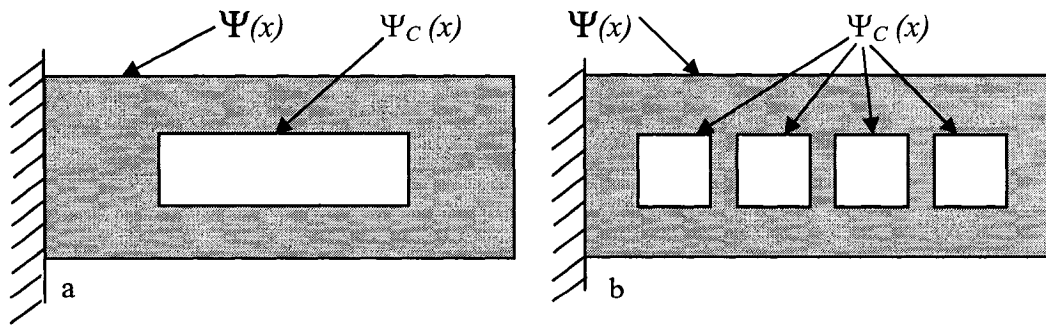
Figure 2.3. Top view of microcantilever cutouts. a) single 500 x 50 μm^2 cutout and b) multiple 50 x 50 μm^2 cutouts.

2.2.4. *Thermal influences*

Thermal influences are modeled by changes to the physical dimensions of the microcantilever through the thermal expansion coefficient of single-crystal-silicon. Shown in Figure 2.4 is the variation of the thermal expansion coefficient as a function of temperature.
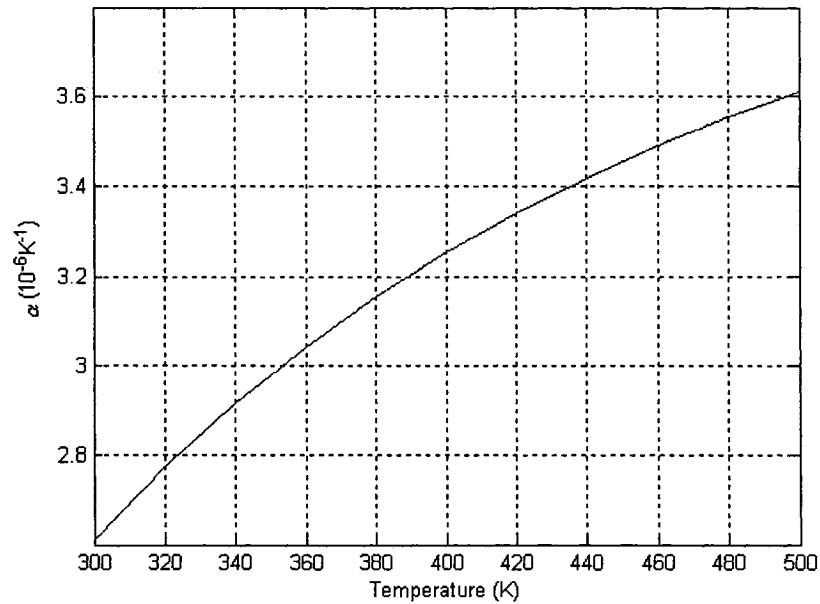
Figure 2.4. Coefficient of thermal expansion data for silicon. Values obtained from [212].

Hence, the change in length is given by

$$\Delta L = \alpha^{(T)} L \tag{2.17}$$

where α is the coefficient of thermal expansion for silicon. The corresponding temperature dependent length is given by,

$$L^{(T)} = L + \Delta L \tag{2.17a}$$

As the influence of temperature on single crystal silicon is isotropic the changes in thickness and in width are given by respectively

$$\Delta h = \alpha^{(T)} h \qquad (2.18)$$

$$h^{(T)} = h + \Delta h \qquad (2.18a)$$

$$\Delta w_0 = \alpha^{(T)} w_0 \qquad (2.19)$$

$$w_0^{(T)} = w_0 + \Delta w_0 \qquad (2.19a)$$

The corresponding change in density is given by

$$\rho^{(T)} = \frac{mass}{L^{(T)} w_0^{(T)} h^{(T)}} \qquad (2.20)$$

The changes to Young's modulus of elasticity as a function of temperature are also included in the theoretical analysis and are obtained from [84, 170] as,

$$E^{(T)} = E(1 + \varepsilon(T - 293)) \qquad (2.21)$$

where ε, the thermal coefficient for Young's modulus, is taken as $- 95e\text{-}6 \ K^{-1}$ for $\{110\}$ single crystal silicon.

2.2.5. Electrostatic influences

For the modeling of the electrostatic influence, the total electrostatic energy must be included in the static and dynamic models. For a simple parallel plate type capacitive system separated by a dielectric gap d_0, as shown in Figure 2.5, the total charge Q, on the microcantilever surface is given by,

$$Q = CV \qquad (2.22)$$

Where, C is the capacitance and, V the electrostatic potential between the plates.

43
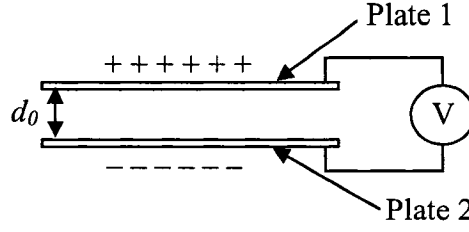
Figure 2.5. A simple parallel plate capacitor.

The electrostatic potential energy is given by,

$$U_E = \int\limits_0^Q V dq = \int\limits_0^Q \frac{q}{C} dq = \frac{Q^2}{2C} = \frac{C^2 V^2}{2C} = \frac{1}{2} C V^2 \tag{2.23}$$

where V is the applied electrostatic potential, and C is the capacitance of the system and is defined as,

$$C = \frac{\varepsilon_0 \varepsilon_r A}{d_0} \tag{2.24}$$

where ε_0 is the permittivity of free space, and ε_r is the relative permittivity of the medium between the two plates, and A is the overlapping surface area of the two plates.

2.2.5.1. *Static analysis under electro-thermo influences*

In the case of an electrostatically actuated thermo-mechanically influenced microcantilever with moving electrode, the applied electrostatic *static* potential energy, $U^{(T)}_{ES}$, is given by,

$$U^{(T)}{}_{ES} = -\frac{\varepsilon_r \varepsilon_0 L^{(T)} V^2}{2} \int_0^1 \frac{w(x)dx}{(d_0 - W_S(x))} = -\frac{\varepsilon_r \varepsilon_0 L^{(T)} V^2}{2d_0} \int_0^1 \frac{w(x)dx}{\left[1 - \dfrac{W_S(x)}{d_0}\right]} \qquad (2.25)$$

The negative sign is given in Equation (2.25) to indicate an opposing force to that of the mechanical restoring force of the microcantilever. A Taylor series expansion is applied to Equation (2.25) in order to linearize it.

$$U^{(T)}{}_{ES} = -\frac{\varepsilon_r \varepsilon_0 L^{(T)} V^2}{2d_0} \int_0^1 w(x)\left(1 + \frac{W_S(x)}{d_0} + \left(\frac{W_S(x)}{d_0}\right)^2 + \ldots + \left(\frac{W_S(x)}{d_0}\right)^n\right)dx \qquad (2.25a)$$

where third order terms and higher are ignored in the modeling.

The static equilibrium position, is obtained from the condition,

$$\frac{\partial}{\partial A_j}\left[U^{(T)}{}_B + U^{(T)}{}_{ES} + U^{(T)}{}_{SP}\right] = 0 \qquad (2.26)$$

wherein $W(x)$ is replaced by $W_S(x)$ in Equations (2.1, 2.6, 2.8).

The static deflection is obtained for a given applied voltage as the particular solution obtained from the following system of simultaneous equations,

$$\sum_j \left[E_{ij}^{22} + K_T^{(T)*}\phi_i(0)\phi_j(0) + K_R^{(T)*}\phi_i'(0)\phi_j'(0) - V_1^{(T)*}E_{ij}^{00}\right]A_j = V_2^{(T)*}\int_0^1 w(x)\phi_i(x)dx$$

$$\forall\ i = 1,\ 2,\ldots,n\quad j = 1,\ 2,\ldots,n \qquad (2.27)$$

where the following definitions are applicable,

$$K_T^{(T)*} = \frac{K_T L^{(T)3}}{E^{(T)}I_0^{(T)}},\ K_R^{(T)*} = \frac{K_R L^{(T)}}{E^{(T)}I_0^{(T)}} \qquad (2.27a)$$

$$V_1^{(T)*} = \frac{\varepsilon_0 \varepsilon_r L^{(T)4}}{E^{(T)}I_0^{(T)}d_0^3},\ V_2^{(T)*} = \frac{\varepsilon_0 \varepsilon_r L^{(T)4}}{2E^{(T)}I_0^{(T)}d_0^2} \qquad (2.27b)$$

45

$$E_{ij}^{00} = \int_0^1 w(x)\phi_i(x)\phi_j(x)dx \qquad (2.27c)$$

$$E_{ij}^{22} = \int_0^1 w(x)\phi_i''(x)\phi_j''(x)dx \qquad (2.27d)$$

$$I_0^{(T)} = \frac{w_0^{(T)}h^{(T)3}}{12} \qquad (2.27e)$$

where I_0 is the moment of inertia of the microcantilever and the * superscript denotes the normalized value for that particular variable.

2.2.5.2. Dynamic analysis under electro-thermo influences

In the context of the *elastic foundation* formulation, the electrostatic *dynamic* potential energy, $U^{(T)}{}_{ED}$, is calculated by introducing an artificial electrostatic spring, $K^{(T)}{}_{E}$, for a given electrostatic potential and thermal load. Beginning with the electrostatic *static* force, $F^{(T)}{}_{ES}(x)$, given by,

$$F^{(T)}{}_{ES}(x) = \frac{dU^{(T)}{}_{ES}}{dW_S(x)} = -\frac{\varepsilon_0\varepsilon_r L^{(T)}V^2}{2}\left[\frac{w(x)}{\left(d_0 - W_S(x)\right)^2}\right] \qquad (2.28)$$

the electrostatic stiffness, $K^{(T)}{}_{E}(x)$, is obtained

$$k^{(T)}{}_{E}(x) = \frac{dF^{(T)}{}_{ES}(x)}{dW_S(x)} = -\varepsilon_0\varepsilon_r L^{(T)}V^2\left[\frac{w(x)}{\left(d_0 - W_S(x)\right)^3}\right] \qquad (2.29)$$

and in normalized form,

$$k^{(T)}{}_{E}^{*}(x) = -\frac{\varepsilon_0\varepsilon_r L^{(T)4}V^2}{E^{(T)}I_0^{(T)}}\left[\frac{w(x)}{\left(d_0 - W_S(x)\right)^3}\right] \qquad (2.29a)$$

46

from which the electrostatic *dynamic* potential energy, $U^{(T)}_{ED}$, may be obtained, and is given by,

$$U^{(T)}_{ED} = \frac{1}{2}\int_0^1 k^{(T)}_E{}^*(x)(W_D(x))^2\,dx \qquad (2.30)$$

The eigensystem defining the flexural motion of the microcantilever for the condition,

$$\frac{\partial}{\partial A_j}\left[U^{(T)}_B + U^{(T)}_{SP} - U^{(T)}_{ED} - T^{(T)}_B\right] = 0 \qquad (2.31)$$

where $U^{(T)}_B$, $U^{(T)}_{SP}$, and $U^{(T)}_{ED}$ are the beam, boundary support springs, and electrostatic *dynamic* potential energies, respectively, and $T^{(T)}_B$ is the beam kinetic energy, is given by,

$$\sum_j\left[E^{22}_{ij} + K^{(T)}_T{}^*\phi_i(0)\phi_j(0) + K^{(T)}_R{}^*\phi_i'(0)\phi_j'(0) - \int_0^1 k^{(T)}_E{}^*\phi_i(x)\phi_j(x)dx - \lambda^{(T)2}E^{00}_{ij}\right]A_j = 0$$

$$\forall\ i = 1,\ 2,...,n\ \ j = 1,\ 2,...,n \qquad (2.32)$$

from which the eigenvalues and natural frequencies of the microsystem are obtained.

$$\lambda^{(T)2}_n = \frac{\omega^{(T)2}_n\rho^{(T)}h^{(T)}L^{(T)4}}{E^{(T)}I_0^{(T)}},\ \ \omega^{(T)}_n = \lambda^{(T)}_n\sqrt{\frac{E^{(T)}I_0^{(T)}}{\rho^{(T)}h^{(T)}L^{(T)4}}} \qquad (2.32a)$$

Shown in Figures 2.6-2.13 are top views of the geometry conditioned microcantilevers *rigid*, *soft*, *SORI* and *RISO*, respectively, as described in section 2.2.3. Given in Figure 2.14 is the cutout model as obtained with the theoretical formulation using Equations (2.15-2.16).
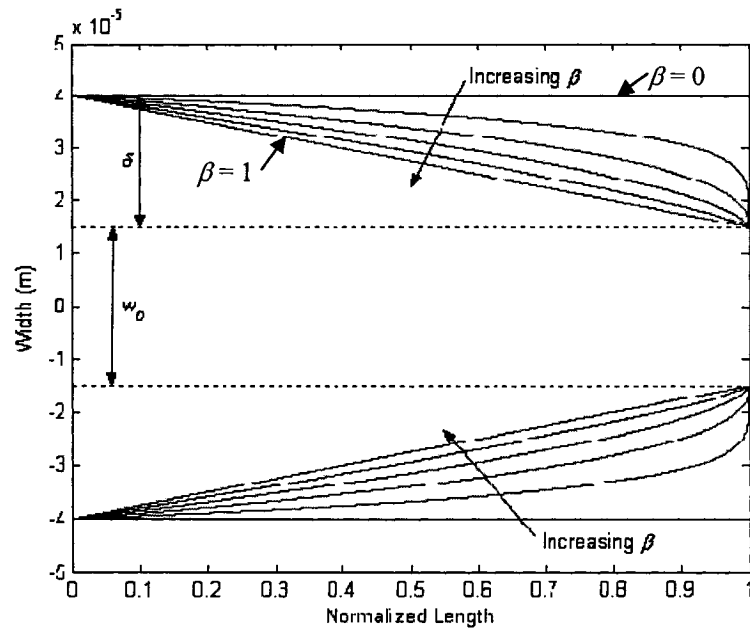
Figure 2.6. *Rigid* configuration for $\beta \leq 1$.
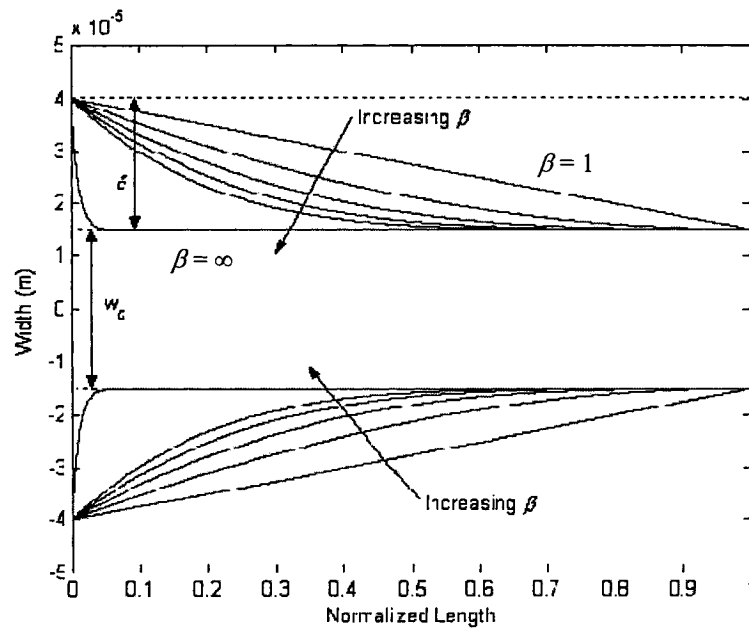
Figure 2.7. *Rigid* configuration for $\beta \geq 1$.

48
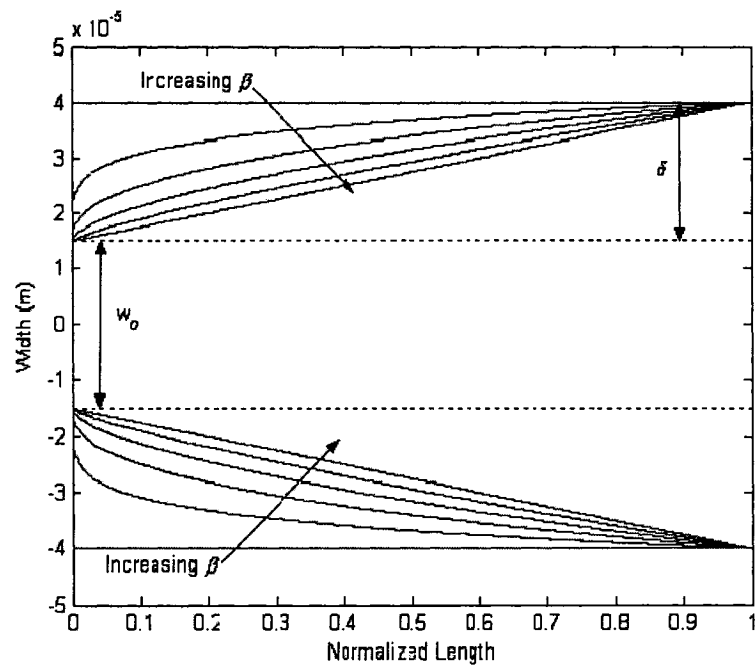
Figure 2.8. *Soft* configuration for $\beta \leq 1$.
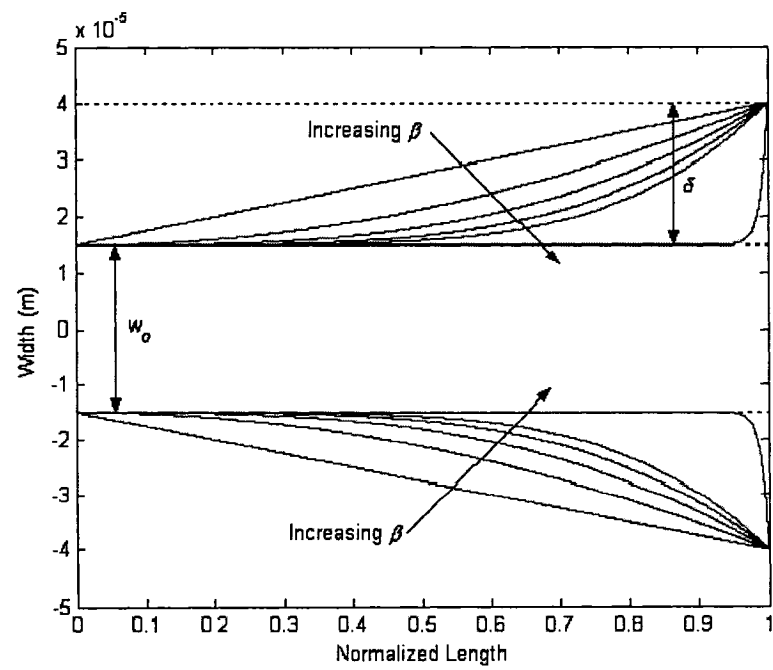
Figure 2.9. *Soft* configuration for $\beta \geq 1$.
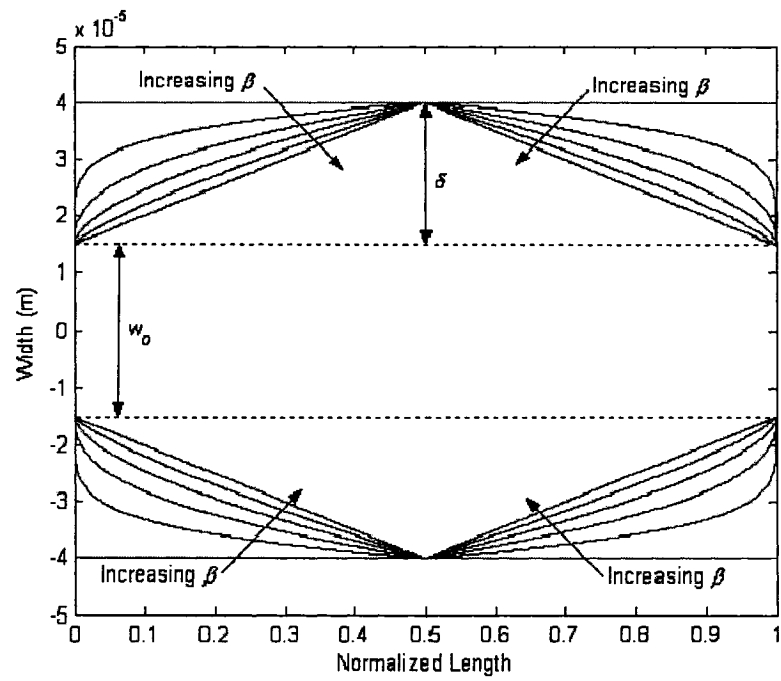
Figure 2.10. *SORI* configuration for $\beta \leq 1$.
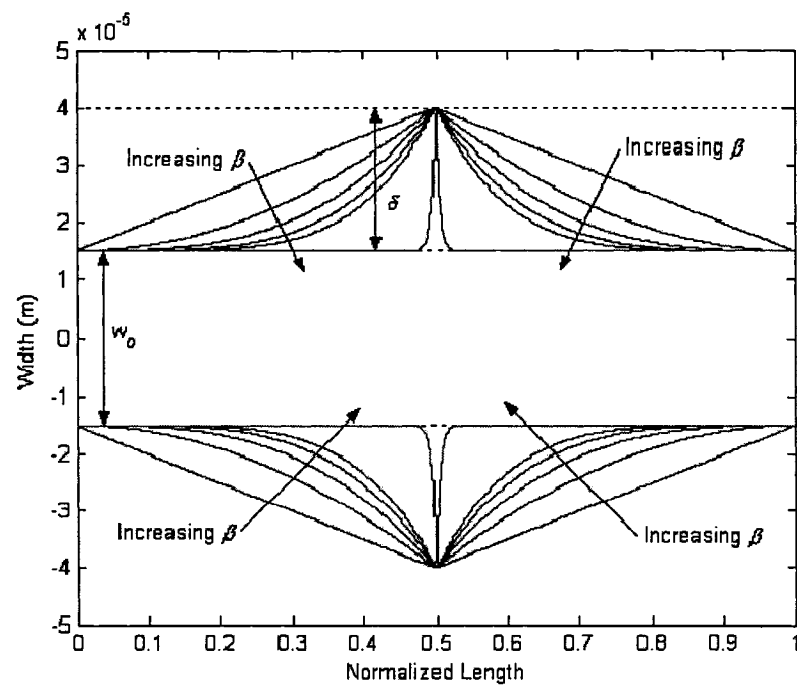
Figure 2.11. *SORI* configuration for $\beta \geq 1$.
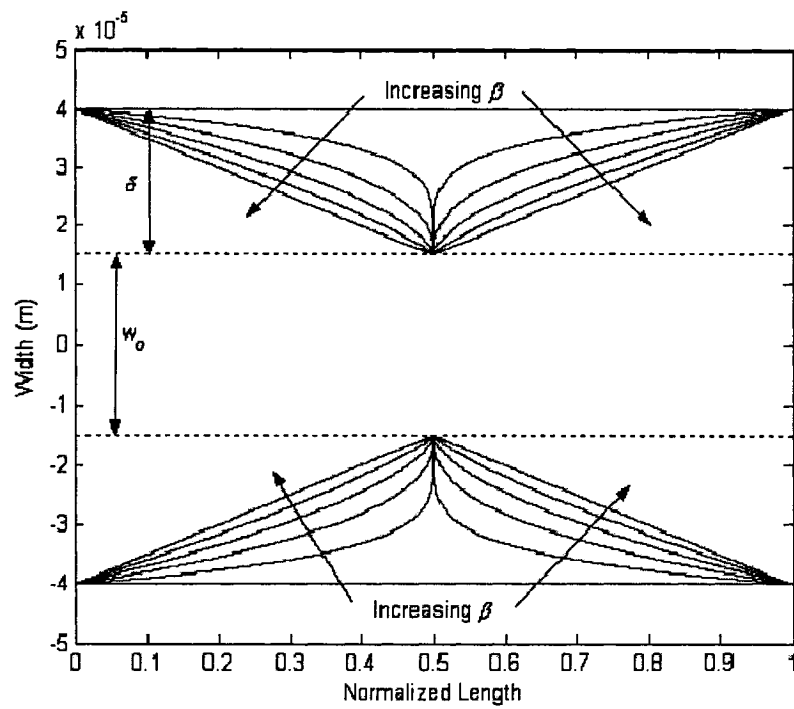
Figure 2.12. *RISO* configuration for $\beta \le 1$.
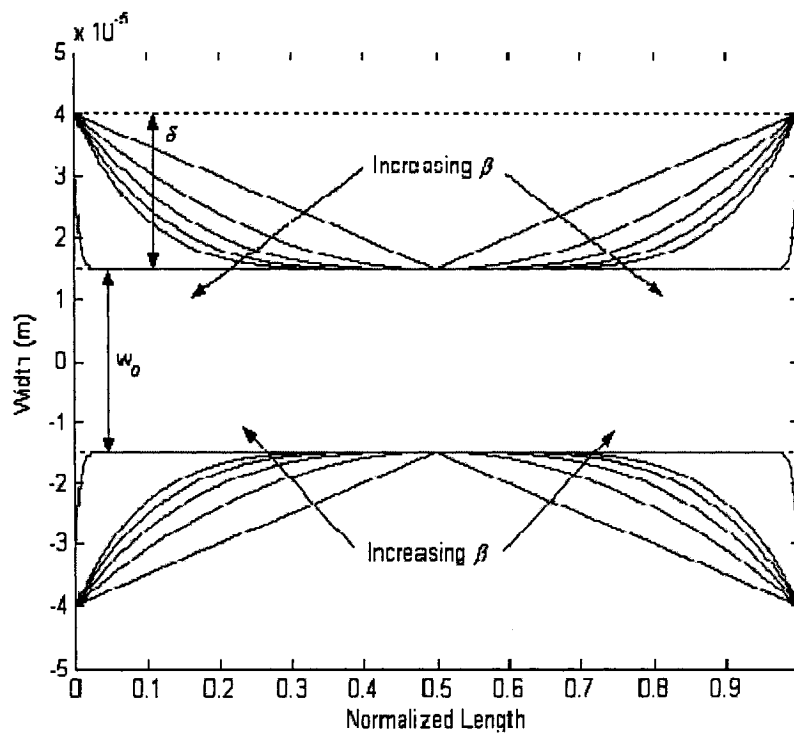
Figure 2.13. *RISO* configuration for $\beta \ge 1$.

51
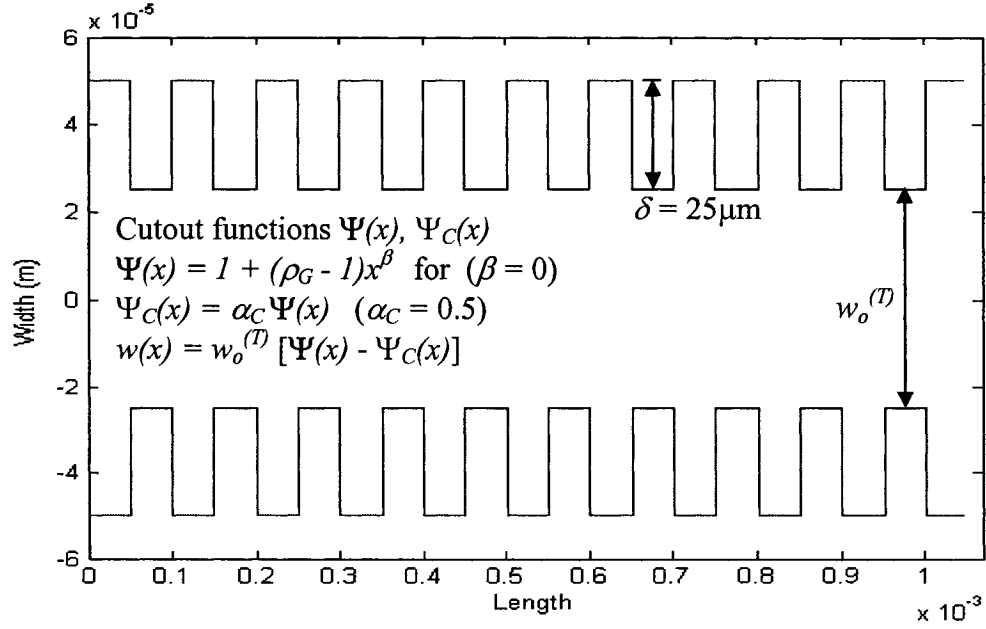
Figure 2.14. Model of microcantilever with cutouts generated using geometry conditioning functions.

2.3. ANALYTICAL RESULTS

Presented here are the results obtained from the theoretical analysis. In the case of boundary suspended microcantilevers, the microfabrication limitations are modeled by changing the boundary support stiffness values of the translational (K_T) and rotational (K_R) springs. Hence, in order to quantify the influence of the microfabrication process on the end support conditions, the dynamic response of a microcantilever beam at different rotational stiffnesses is predicted by solving Equation (2.32) obtained using the Rayleigh-Ritz method. As there is no translation at the support, the boundary is modeled by only varying K_R^* and with a very high value of K_T^*. For the demonstration of the model, the

52

electrostatic, geometry, thermal, and cutouts influences are added sequentially into the model.

2.3.1. *Microfabrication influences*

The solution of the eigensystem of Equation (2.32), gives both the natural frequencies and mode shapes for a given microcantilever with any rotational and translational stiffness values representing non-classical support boundary conditions [207]. In AFM applications, the mode shapes of the beam play a central role in the transmission of topographical details from the surface being probed. However, the non-classical support conditions due to microfabrication limitations will influence the performance of the surface scanning process.

Shown in Figure 2.15 is an SEM image of AFM microcantilevers.
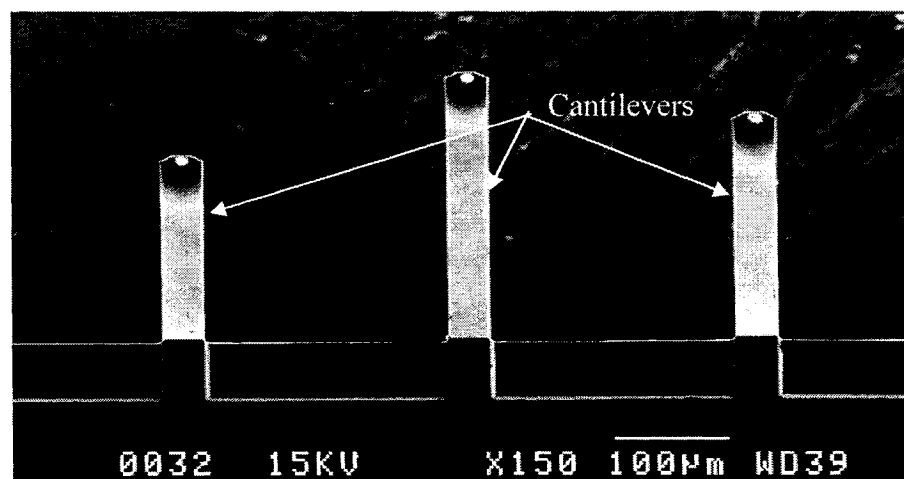
Figure 2.15. SEM image of MikroMasch *Type 'B'* AFM microcantilevers [153].

In this work the frequency response of a commercially available *Type 'B'* AFM microcantilever beam is investigated. In this analysis, the microcantilever beam is assumed to be in non-contact mode. Figure 2.16 is a scheme of a typical *Type 'B'* AFM rectangular probe and pyramidal tip. The mass of the tip is much less than the microcantilever and is neglected in this analysis.

Type 'B' microcantilever
$L = 200\mu m$
$w(x) = 20\mu m$
$h = 0.6\mu m$

Probe tip
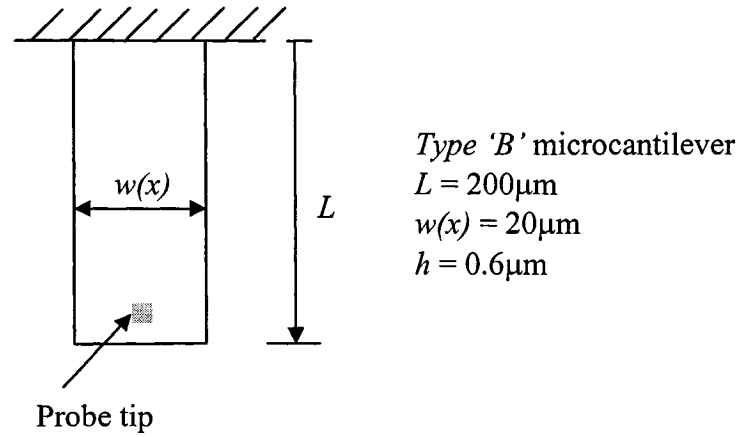
Figure 2.16. Typical dimensions for a *Type 'B'* cantilever probe and pyramidal tip.

The eigenvalues λ_n, obtained for various rotational stiffness values for the *Type 'B'* microcantilever are given in Table 2.1.

Table 2.1. Eigenvalues obtained for various values of the rotational stiffness, with the value of $K_T* = 1 \times 10^{10}$ for the *Type 'B'* microcantilever.

K_R* / λ	0	5	12	17	35	10^5	10^6	10^{10}
1	--	2.61	3.04	3.16	3.33	3.52	3.52	3.52
2	15.42	18.21	19.64	20.15	20.97	22.03	22.03	22.03
3	49.95	53.55	56.06	57.09	58.92	61.68	61.68	61.68
4	104.21	108.16	111.44	112.93	115.85	120.87	120.88	120.88
5	178.19	182.36	186.21	188.10	192.07	199.81	199.81	199.81
6	271.88	276.20	280.49	282.71	287.65	298.46	298.47	298.47

Applying the theoretical formulation of Butt [31] to the experimental results of Lévy [130], the virtual height of the microcantilever, $\bar{z}_n^*$, for the *nth* mode shape, is calculated for each value of rotational stiffness, K_R* by using the following relationship for the optical lever technique [95],

$$\bar{z}_n^{*2} = \left(\frac{2L}{3}\right)^2 \frac{3kT}{K_C \lambda_n^2} \frac{\left(d\Phi_n(\xi)/d\xi\right)^2}{I_n} \tag{2.33}$$

where L is the length, k is Boltzmann's constant, K_C is the cantilever spring stiffness, T is the temperature in the Kelvin scale, and the Φ_n are the mode shapes of the beam, and

$$I_n = \frac{1}{L}\int_0^L \Phi_n^2 d\xi = 1 \tag{2.33a}$$

The average virtual height of the beam, which is the sum of the virtual heights for all of the vibrational modes, is related to the cantilever spring constant in the following way [31],

55

$$\sqrt{\overline{z^{*2}}} = \sqrt{\sum_{n=1}^{\infty} \overline{z_n^{*2}}} = \sqrt{\frac{4kT}{3K}} \qquad (2.34)$$

Therefore, by measuring the virtual height of the beam experimentally, at a given temperature using the optical lever method, and applying Equation (2.34), the spring constant of the microcantilever beam can be calculated. Shown in Figure 2.17 is an overview of the optical lever method in which a laser beam is incident on the reflective surface of the AFM microcantilever. The amount of variation in the deflection is a function of the mode shape for a given temperature.

Laser Diode

Quadrant
Detector
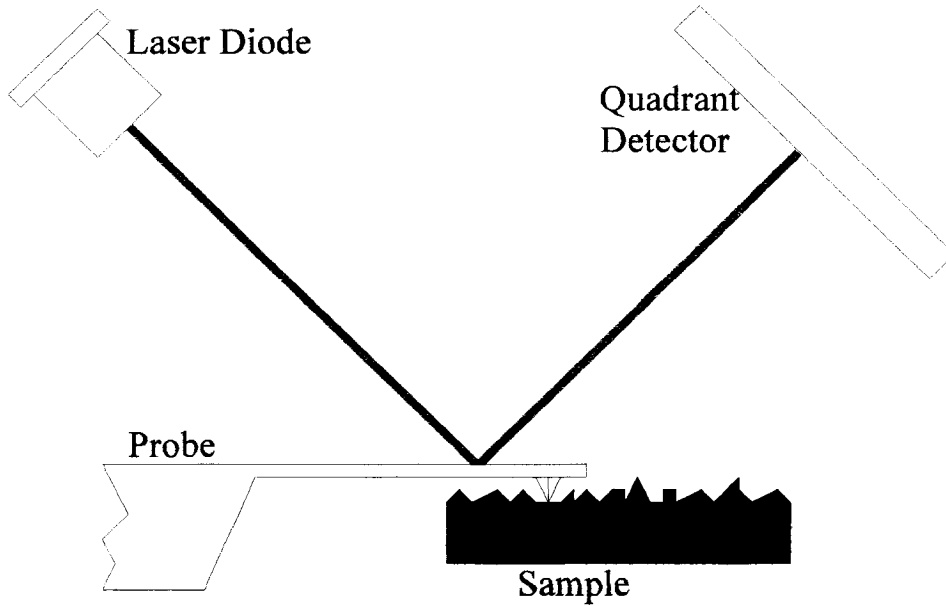
Probe

Sample

Figure 2.17. Overview of the optical lever method. The detector measures the deflection of the *Type 'B'* probe as a function of position on the sample.

By varying the values of the rotational stiffness, it was possible to cause a change in the mode shapes of the beam, and hence a change in the virtual heights as well. Also a

variation in the minima of the virtual height ratio, $\bar{z}_2^{*2} / \bar{z}_1^{*2}$, along the length of the beam was obtained. Only the first two modes, Φ_1 and Φ_2, were considered herein in order to compare the results obtained with those of Lévy [130]. The plotted variation of the normalized eigenvalues, $\Lambda = \lambda_n/\lambda_{n,\,clamped}$, is given in Figure 2.18 and it clearly indicates that care must be taken to include the microfabrication influences when estimating the natural frequencies of the AFM *Type 'B'* cantilevers based only on geometry. Shown in Figure 2.19 are the virtual height ratio for the first two modes where the virtual height is defined as the inclination, dz/dx, along the length of the microcantilever for each mode.
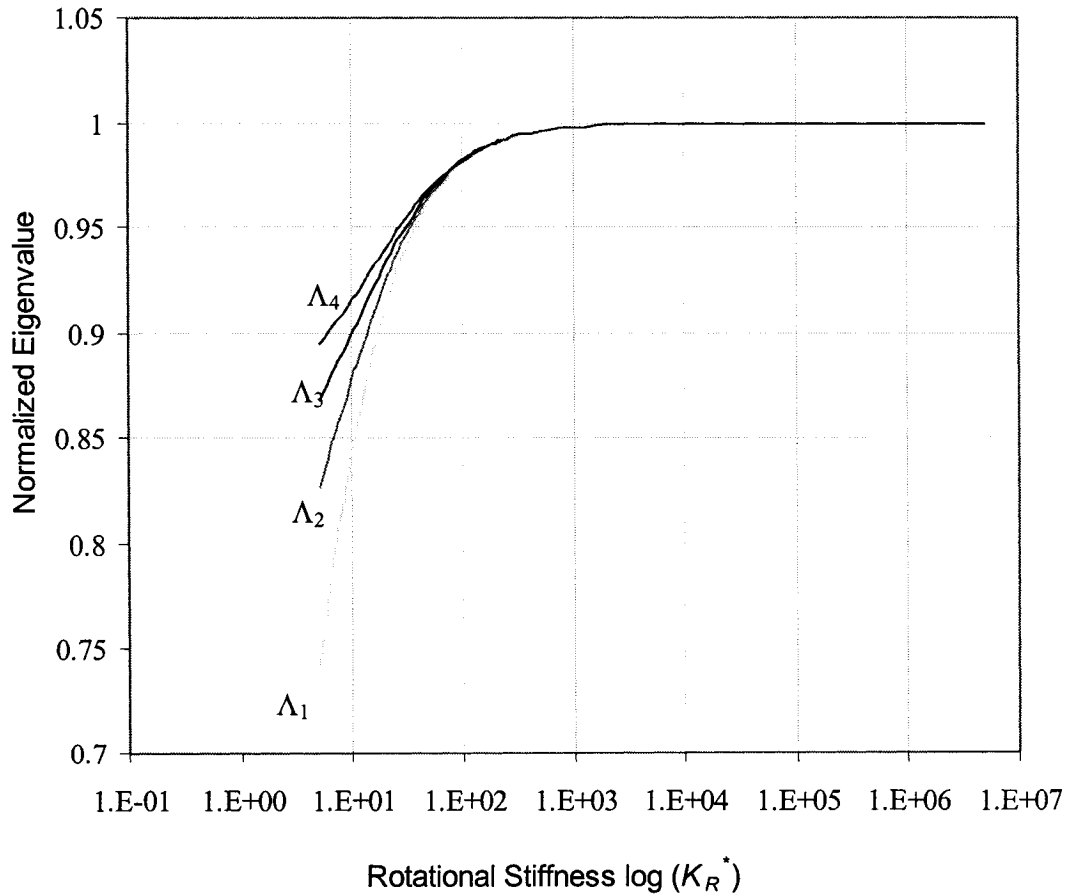
Figure 2.18. The effect of the rotational stiffness on the first four eigenvalues of a *Type 'B'* microcantilever.

The virtual deflections predicted by Butt [31] for a clamped condition and by the present theoretical formulation with $K_R{}^* = 1 \times 10^{10}$, $K_T{}^* = 1 \times 10^{10}$ are compared in Table 2.2.
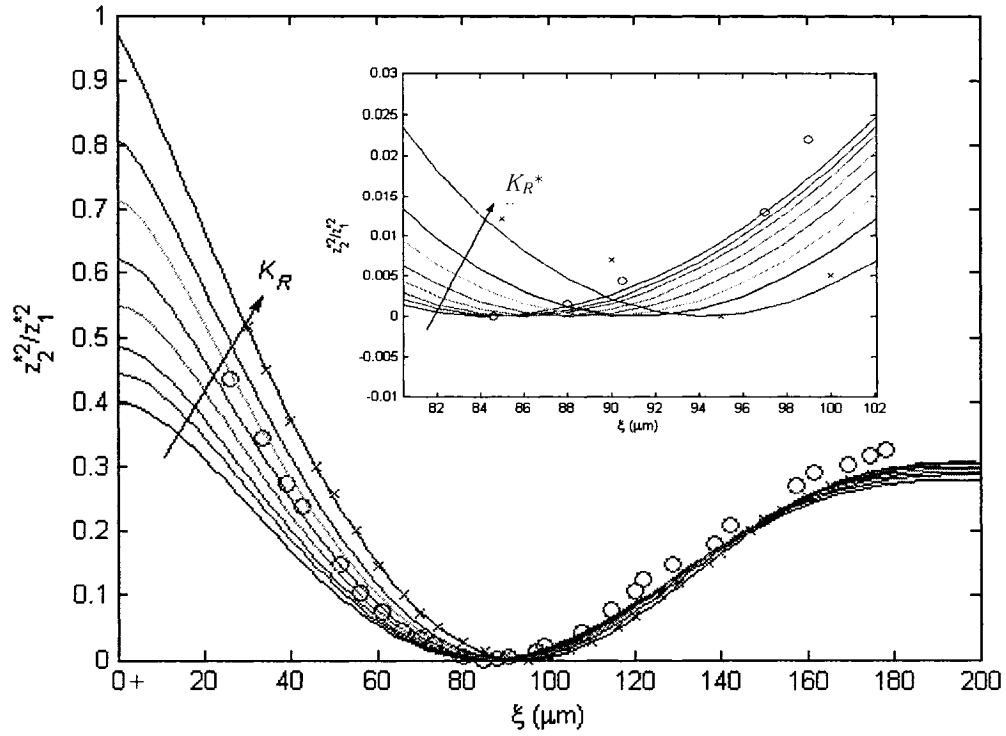
Figure 2.19. The ratios of the virtual displacement for the first two modes as a function of the position on the *Type 'B'* microcantilever for different values of $K_R{}^*$ are shown. The O are the values obtained by [130], the X are those of [31]. The inset is a close up showing the shift in the minimum position to higher values for increasing $K_R{}^*$.

Table 2.2. Comparison of beam eigenfunctions and virtual displacements with the results obtained by Butt [31] for a *Type 'B'* microcantilever.

i	$\sqrt{\lambda_i}$	$\sqrt{\lambda_i}$ [20]	$\sqrt{\bar{z}_i^{*2}}$ (m)	$\sqrt{\bar{z}_i^{*2}}$ (m) [31]
1	1.87	1.88	5.77×10^{-11}	5.77×10^{-11}
2	4.69	4.69	3.20×10^{-11}	3.20×10^{-11}
3	7.85	7.85	1.88×10^{-11}	1.88×10^{-11}
4	10.99	11.00	1.34×10^{-11}	1.34×10^{-11}
5	14.14	14.14	1.04×10^{-11}	1.04×10^{-11}
6	17.27	17.28	8.54×10^{-12}	8.53×10^{-12}

The microfabrication influences and limitations at the *Type 'B'* microcantilever support boundary can be modeled using artificial rotational and translational springs. The micromachined end support conditions are an important factor in the static and dynamic performance of boundary suspended structures such as microcantilevers as can be seen from the variations in the virtual deflections in Figure 2.19. In the model, the micromachining limitations at the boundary support were *lumped* into the rotational stiffness value. The eigenvalues and mode shapes can be obtained for different end support conditions by varying the value of the boundary support rotational stiffness. In this manner the boundary conditioning theory presented aims to quantify the micromachining limitations that are an *intrinsic* part of MEMS manufacturing processes.

2.3.2. *Electrostatic influences*

Electrostatic influences are part of externally applied effects that can be used to actuate a microsystem. The modeling of this influence on microsystems involves an analysis of both the static and dynamic response domains where the static deflection of the microcantilever is a function of an applied DC voltage. The dynamic response is a function of the applied DC bias voltage and amplitude of sinusoidal AC voltage excitation. The analysis presented here is carried out on a *Type 'B'* microcantilever with length L = 350μm, thickness h=1μm and width w = 35μm. The dielectric gap, d_0, is equal to 5μm. The static equilibrium positions of the microcantilever are a function of the applied DC bias voltage and the mechanical restoring force of the microcantilever. Shown in Figure 2.20 is a theoretical representation of the static equilibrium points for a *Type 'B'* microcantilever beam as a function of applied electrostatic potentials [210].
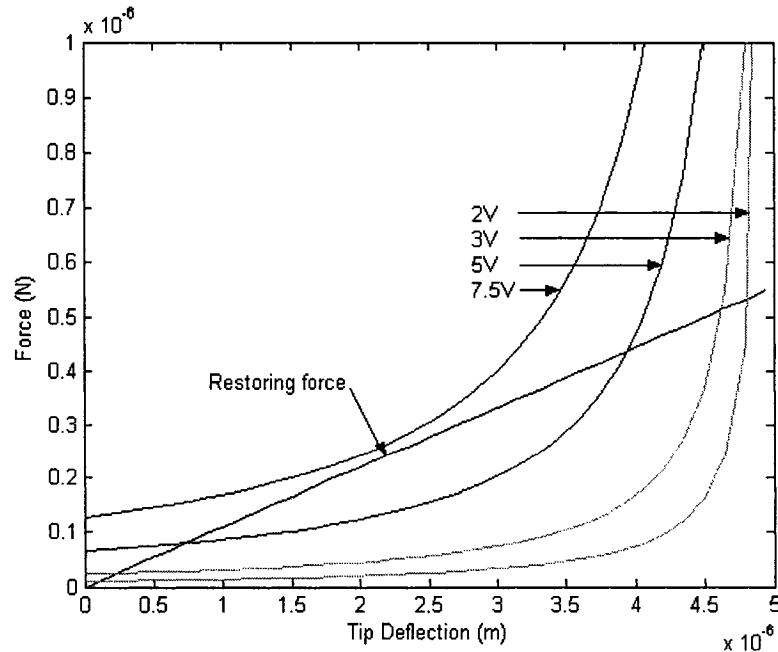
Figure 2.20. Equilibrium between electrostatic and mechanical restoring forces of the microcantilever.

The static equilibrium positions of a microcantilever beam for an applied voltage are estimated using Equation (2.27). Shown in Figure 2.21 are the static deflections of a *Type 'B'* microcantilever as a function of the applied DC voltage.
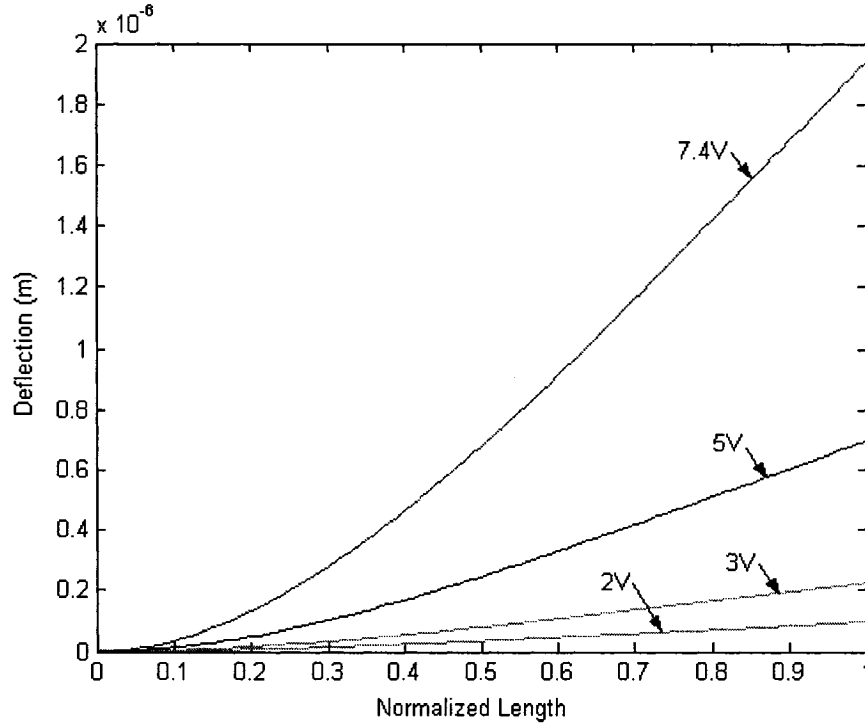
Figure 2.21. *Type 'B'* microcantilever deflections under various applied voltages.

The static deflections may be increased by applying higher DC bias voltages. If the applied electrostatic force is more than mechanical restoring force (for example, 7.5V curve in Figure 2.20) the microcantilever will *snap down* onto the substrate electrode.

The theoretical results for the dynamic characterization are obtained from the solution of Equation (2.32) for a given applied voltage and the *Type 'B'* microcantilever-electrode spacing.

61

Static deflections increase as a function of the applied DC bias voltage and are limited by the *natural* mechanical restoring force of the microcantilever, hence electrostatic forces greater than the mechanical restoring force of the microcantilever result in the microcantilever snapping down onto the substrate. The estimated snap down voltage for this *Type 'B'* microcantilever is ~7.45 volts for a dielectric spacing $d_0 = 5\mu m$.

Given in Table 2.3 are the eigenvalues for different applied voltages. Shown in Figure 2.22 is the variation of resonance frequency as a function of the applied voltage and rotational stiffness K_R^*.

Table 2.3. Eigenvalues obtained for different applied voltages. The * indicates that the microcantilever has touched down.

λ	$V=0$	$V=2$	$V=3$	$V=5$	$V=7$	$V=7.4$	$V=7.5^*$
λ_1	3.52	3.47	3.41	3.12	1.85	0.38	--
λ_2	22.03	22.03	22.02	21.98	21.88	21.83	21.81
λ_3	61.69	61.69	61.69	61.68	61.64	61.63	61.62
λ_4	120.90	120.90	120.90	120.89	120.88	120.87	120.87

Hence, the electrostatic *softening* effect, due to the electrostatic field lowers the eigenvalues as a function of the increasing voltages as given in Table 2.3. In this analysis the electrostatic field varies from 0-1.48 x 10^6 *V/m*. The first eigenvalue is the most affected by the applied electrostatic softening with an overall 89% change within the voltage range 0-7.4V as compared to only 1% for the second eigenvalue.
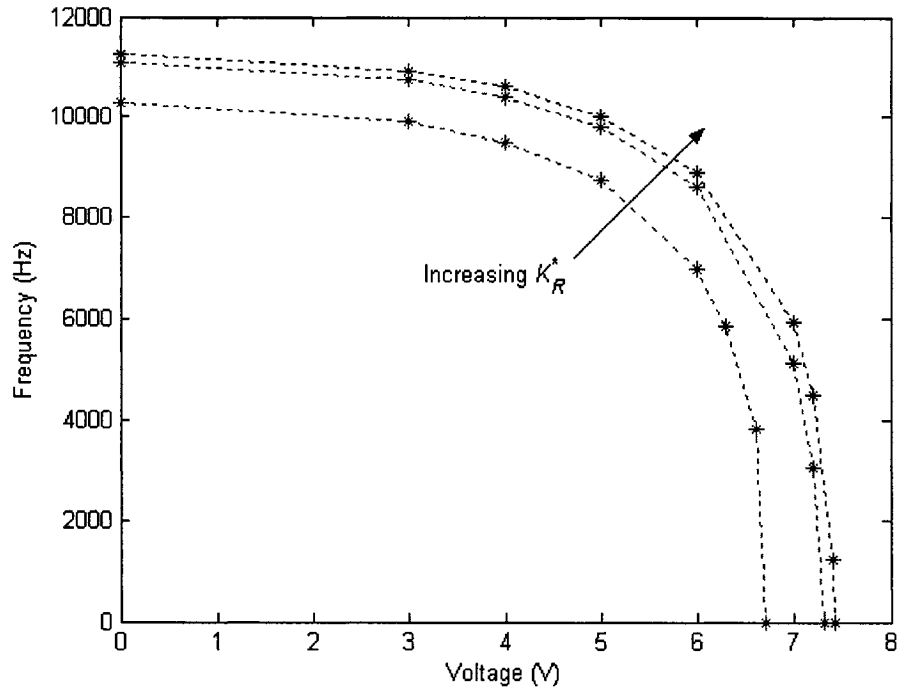
Figure 2.22. The variation to the natural frequency as a function of applied voltage for different rotational stiffness values for *Type* '*B*' AFM microcantilever.

From the results shown in Figure 2.22 it can be seen that the combined effect of *softening* at the boundary due to micromachining influences and *softening* due to electrostatic influences will change the resonance frequency response of a *Type* '*B*' AFM microcantilever and the value of the snap down voltage.

2.3.3. Thermal influences

The modeling takes into account changes to the geometry through Equations (2.17-2.19), changes to the density through Equation (2.20), and variations to Young's modulus through Equation (2.21). All of these individual thermally related parameters will

contribute to alter the mechanical response profile, both static and dynamic, of a given microsystem. Given in Table 2.4 are the changes to the linear dimensions of a single crystal silicon microcantilever *Type 'T'*. Density, and Young's modulus as a function of temperature are also listed in Table 2.4. The silicon density and Young's modulus values are those of MikroMasch. The length L, width w, and thickness h, are not for an actual device and are used only for the theoretical analysis.

Table 2.4. The changes to various physical parameters of a *Type 'T'* microcantilever as a function of thermal load.

T (K)	L (μm)	w (μm)	h (μm)	ρ (kg/m³)	E (GPa)
294	1000.000	30.000	10.000	2330.000	170.000
300	1000.448	30.013	10.004	2326.871	169.888
320	1000.530	30.016	10.005	2326.298	169.567
340	1000.615	30.018	10.006	2325.705	169.246
360	1000.702	30.021	10.007	2325.097	168.924
380	1000.792	30.024	10.008	2324.475	168.603
400	1000.882	30.026	10.009	2323.845	168.282
420	1000.974	30.029	10.010	2323.207	167.961

It can be seen that thermal influences will affect the linear dimensions of the *Type 'T'* microcantilever. There is also a strong thermal dependence of Young's modulus, 1.12% variation over a 120K thermal variation. All of physical changes to these parameters will combine to vary the static and dynamic responses of the microcantilever.

Given in Figure 2.23 is the variation of the resonance frequency as a function of the applied thermal load for an actual Mikromasch *Type 'B'* microcantilever with the following dimensions, measured with an optical microscope and estimates from SEM images, $L = 351\mu m$, $h = 0.94\mu m$, $w = 34.5\mu m$ [208].
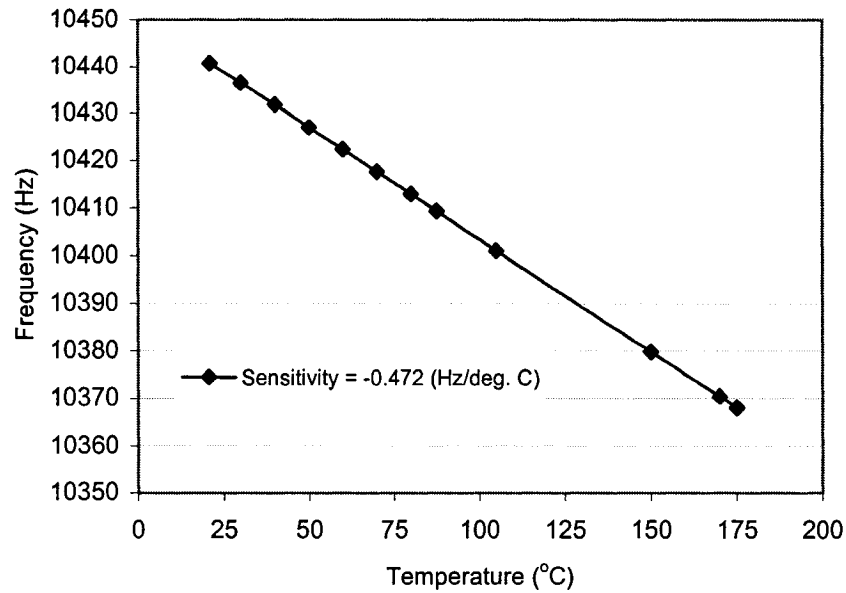
Figure 2.23. The variation of the resonance frequency as a function of the applied thermal load for the *Type 'B'* microcantilever.

The sensitivity is a function of the thermal loading and of the support boundary conditions. It can be seen that the linearity of the change in frequency for the temperature range 25-175 °C can be exploited and used for thermal sensor applications. The changes to the linear dimensions as given in Table 2.4 will influence the capacitance of the microcantilever through the change in the overall surface area of the microcantilever as a function of temperature. Given in Figure 2.24 is the variation to the

capacitance as a function of temperature for a given *Type 'B'* microcantilever-electrode

spacing.
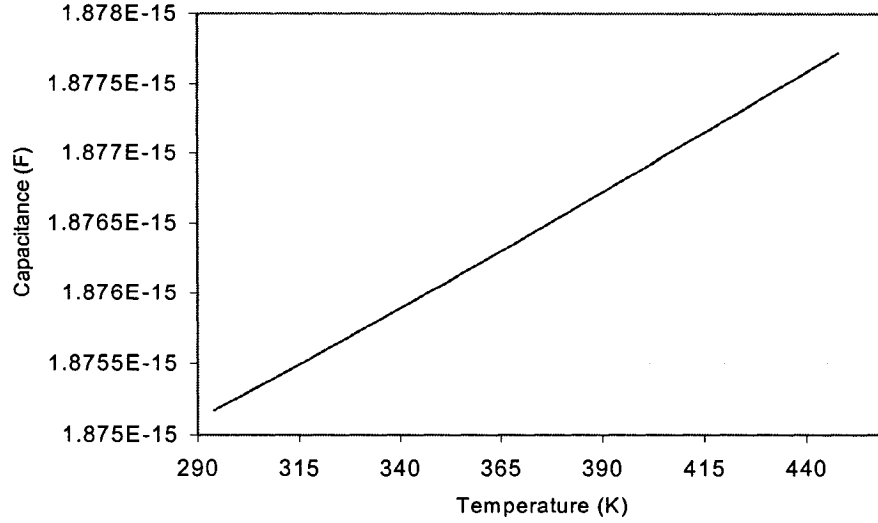
Figure 2.24. Variation to the capacitance as a function of applied thermal load for a *Type 'B'* microcantilever.

.

2.3.4. *Coupled electro-thermo-boundary support influences*

A theoretical analysis using Equation (2.32) for the sensitivity of the *Type 'B'* microcantilever under various applied bias voltages and thermal loads is presented in Figure 2.25 [202]. It can be seen that at low voltages the sensitivity remains linear over the thermal range, however for high voltages the sensitivity becomes non-linear for high temperatures. This is due to the increased electrostatic force as a function of the increased surface area of the *Type 'B'* microcantilever. Hence, the sensitivity can be increased and *optimized* by the application of an appropriate electrostatic DC bias voltage

for a given thermal loading range. Shown in Figure 2.26 are the static deflections for a

Type 'B' microcantilever under a given applied voltage at two different thermal loads.
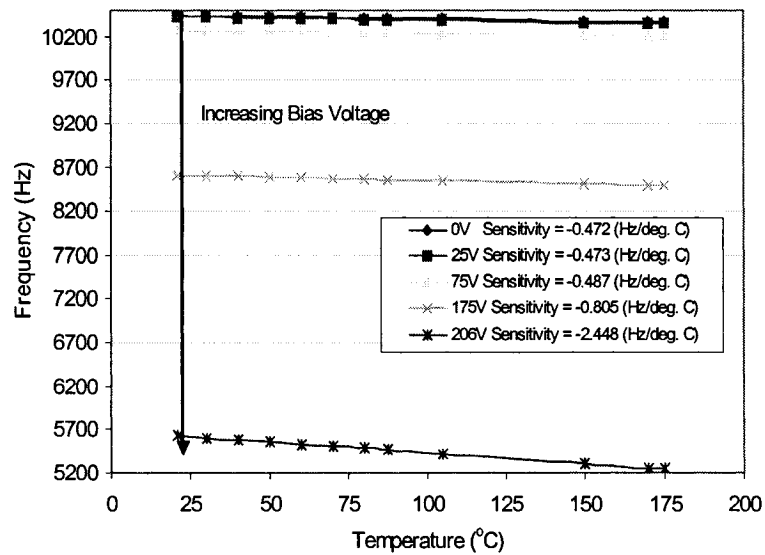
Figure 2.25. Thermal sensitivity curves for various applied bias voltages.
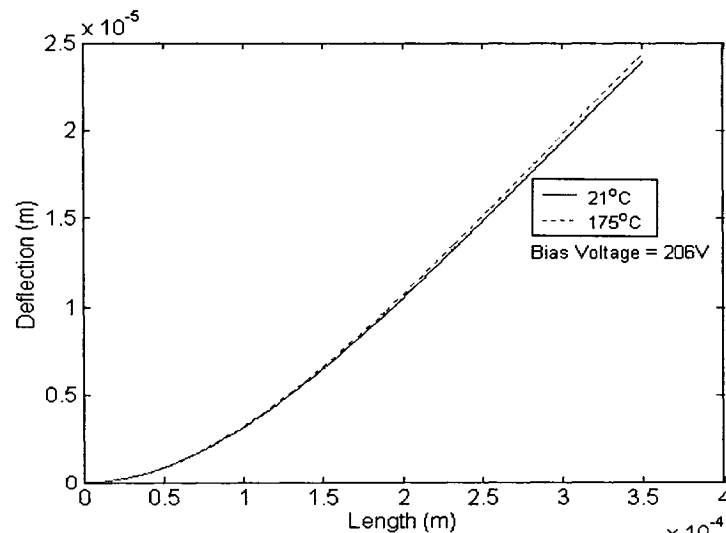
Figure 2.26. Static deflection profiles as a function of applied voltage and thermal loading.

Of the different parameters modeled herein only the microfabrication influence cannot be fully controlled in the manufacturing of microsystems. Hence, it is expected that the sensitivity will also be a function of the support boundary condition of a *Type 'B'* microcantilever. Shown in Figure 2.27 are the sensitivities for various DC bias voltages as a function of thermal loading for classical and non classical boundary conditions, respectively [201].
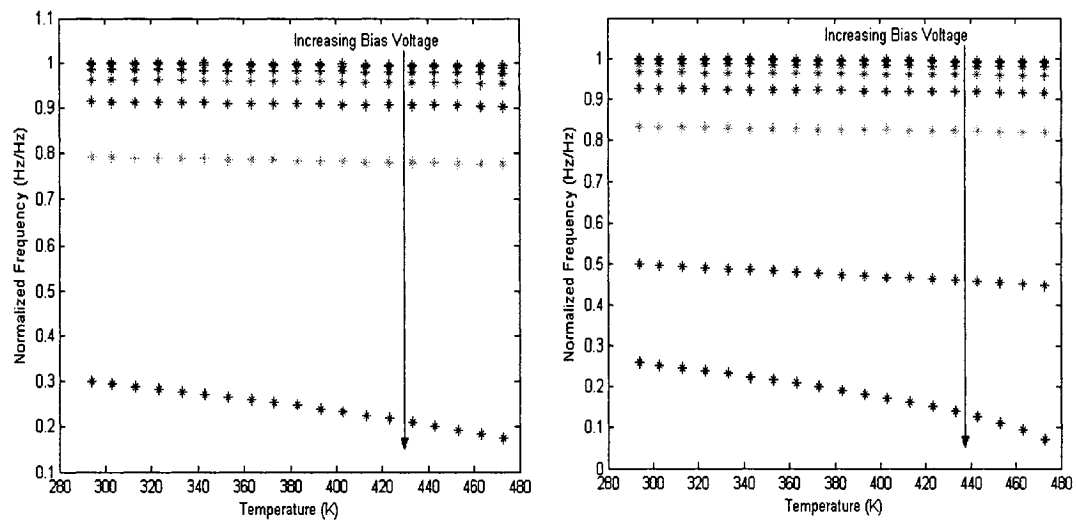
Figure 2.27. The variation of the sensitivity for a *Type 'B'* microcantilever as a function of applied bias voltage and thermal load. Left: Classical boundary support. Right: Non-classical boundary support.

Given in Figures 2.28-2.29 is a comparison of the first and second natural frequency responses for a *Type 'T'* microcantilever under different thermal and electrostatic loading for classical and non classical boundary conditions, respectively. One can note that the combined electro-thermo-boundary support influences can significantly affect the dynamic characteristics of the microcantilever.
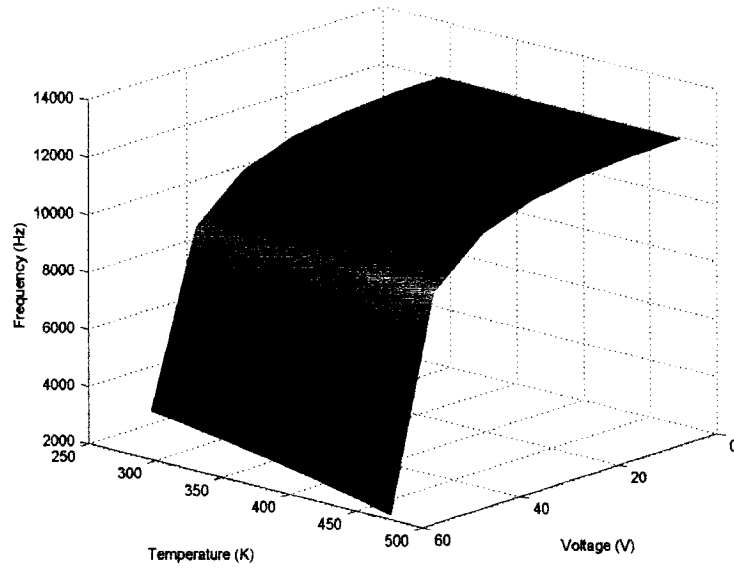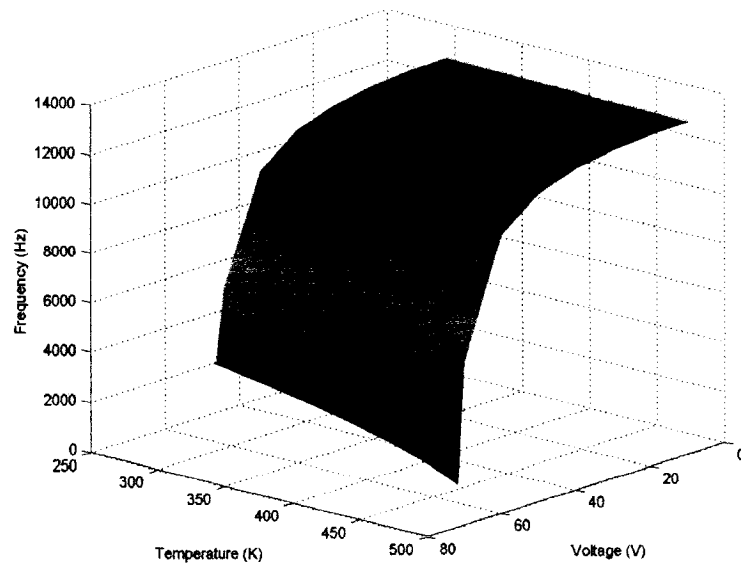
Figure 2.28. Surface plots of the 1st resonance frequency as a function of both applied bias voltage and thermal loading. Top: Classical support boundary conditions. Bottom: Non-classical boundary conditions.
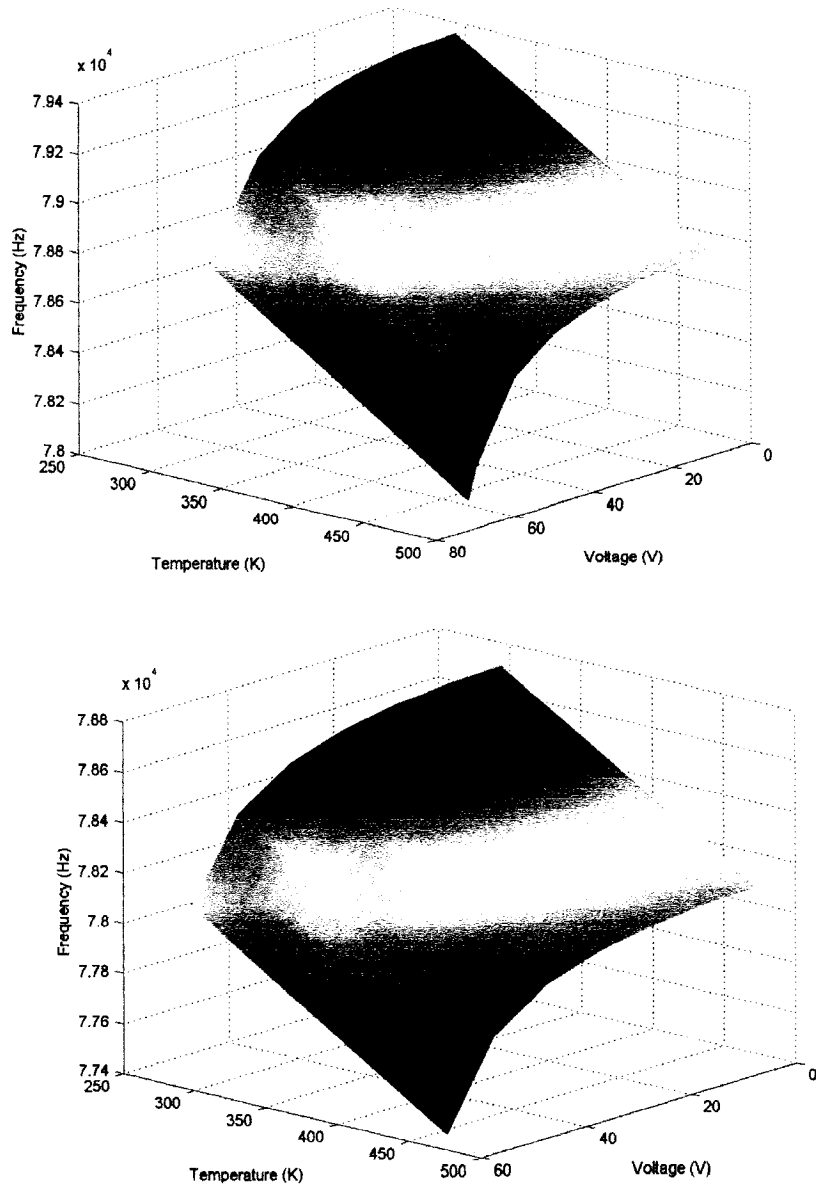
Figure 2.29. Surface plots of the 2nd resonance frequency as a function of both applied bias voltage and thermal loading. Top: Classical support boundary conditions. Bottom: Non-classical boundary conditions.

It can be seen from Figures 2.27-2.29 that silicon microcantilevers for a given microfabricated boundary condition are very sensitive to the applied electrostatic and thermal loading and that the static and dynamic characteristics can be affected in this

regard, hence it is important to predict these characteristics, through theoretical analysis, prior to the manufacturing process for a target operating environment.

2.3.5. *Geometrical influences*

In this section the results of the influence of geometrical contouring on microcantilevers are presented [203, 205]. In the modeling presented here the dynamic response of the microcantilevers are sensitized to the changes in the structural geometries along the length of the microcantilevers.

The changes to the natural frequencies as a function of the taper parameter, β, are presented in Figure 2.30. For this modeling the boundary support springs, K_R^* and K_T^*, are fixed at 1 x 10^{10} in order to simulate classical *Clamped* boundary support conditions for a microcantilever. The offset parameter, δ, is 25μm, the length, $L^{(T)}$, unconditioned width, $w_o^{(T)}$, and thickness, $h^{(T)}$, of the microcantilever are 250μm, 30μm, and 2μm, respectively, and the temperature is taken as 294 Kelvin or 21°C. In this analysis the various microcantilever geometries given in Figures 2.6-2.13 can be used to *trim* or *tune* the natural frequencies through the selection of a particular geometry conditioning function Ψ and tapering parameter β.
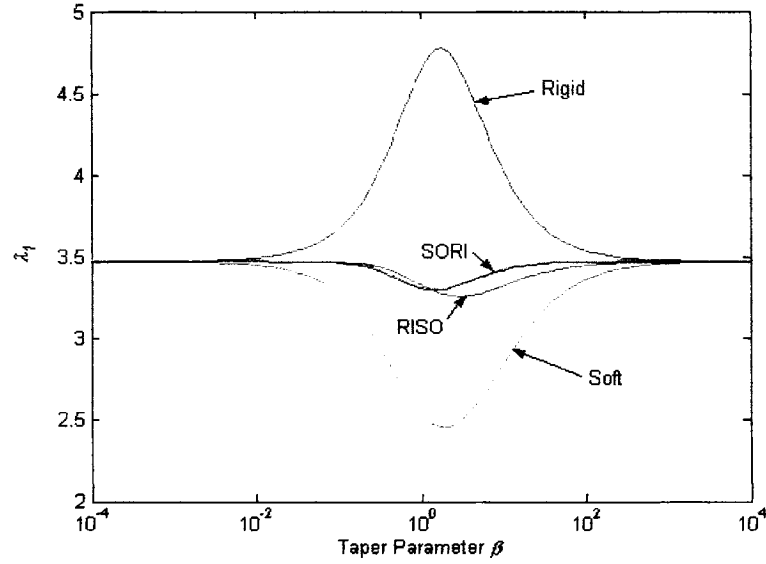
Figure 2.30. The variation of the first eigenvalue as a function of the taper parameter β for the four types of width contouring presented here.

For very low and very high values of β, the eigenvalues are the same for all four types of geometry conditioning. However, for β values between 0.01 and 100 the eigenvalues diverged significantly. This is due to the increased variations in geometry between the four types of conditioning within this β range.

The normalized first and second mode shapes, with respect to the microcantilever tip deflection, as a function of the geometry of the microsystem are presented in Figures 2.31-2.32, respectively, for classical boundary support conditions.
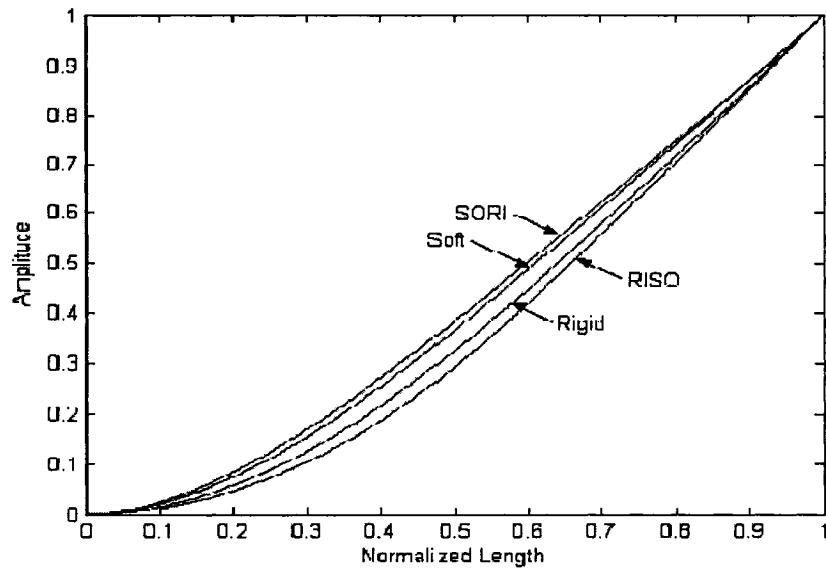
Figure 2.31. Comparing the first mode for the tapered geometries presented in this simulation at *clamped* condition.
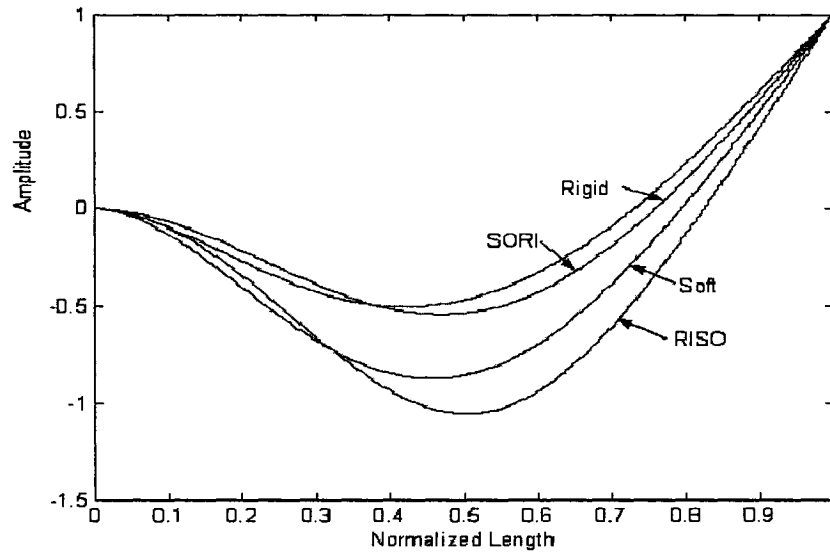
Figure 2.32. Comparing the second mode shapes for the tapered geometries presented in this simulation at *clamped* condition.

The selection of a particular geometry can be used to stiffen or soften a microcantilever response as is seen in Figure 2.30. Hence, the stiffening effect, for example, can be used to overcome softening effect due to thermal and electrostatic influences.

73

2.3.6. *Coupled electro-geometrical influences*

Given here are the theoretical results obtained for electro-geometrical coupling. The geometry conditioned microcantilevers are deflected by applying an electrostatic potential [205]. Due to the different geometries the microcantilevers will experience differing electrostatic stiffnesses, and hence have different static equilibrium positions. For the analysis presented the following data was used: $d_0 = 3\mu m$, voltage = 5V, $\delta = 25\mu m$, $L^{(T)} = 250\mu m$, $w_0^{(T)} = 30\mu m$, $h^{(T)} = 2\mu m$ and $T = 294$ Kelvin. Shown in Figure 2.33 is a comparison of the microcantilever tip deflections as a function of geometry and applied voltage.
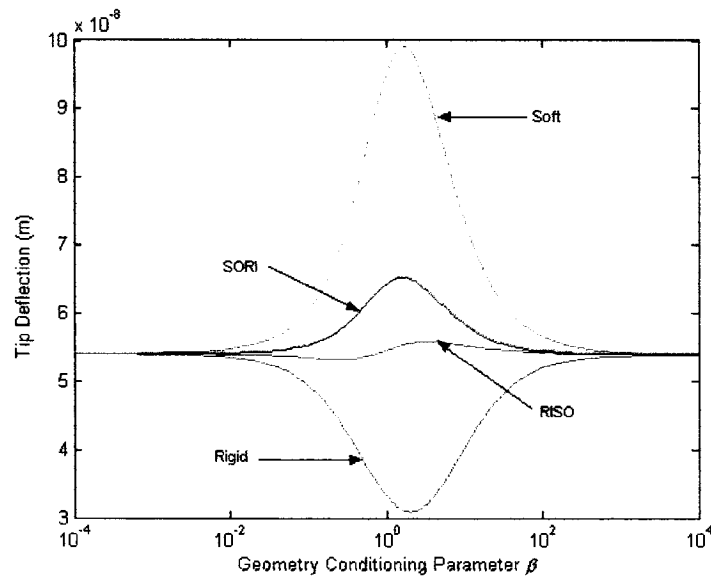
Figure 2.33. The microcantilever tip deflections for the geometry conditioning functions presented here and an applied 5V electrostatic potential.

As the geometrical conditioning can be used to *tune* the dynamic property of a given microcantilever it is of interest to investigate the *influence* of a particular geometry to an applied stimulus such as electrostatic. Given in Figures 2.34-2.37 are the comparison of the first eigenvalue and the static deflections for *soft*, *rigid*, *SORI* and *RISO* conditioning functions, respectively. The two small figures on top are given to illustrate the corresponding geometries within that particular β range. It is the aim of this analysis to determine which geometry conditioning results in a minimal variation in the eigenvalue under the applied electrostatic load. It is expected that, through the various geometries, that the microcantilevers will demonstrate varying static and dynamic performances. In this analysis the static and dynamic profiles are presented together in order predict the stability of a particular dynamic response for a particular conditioning parameter.
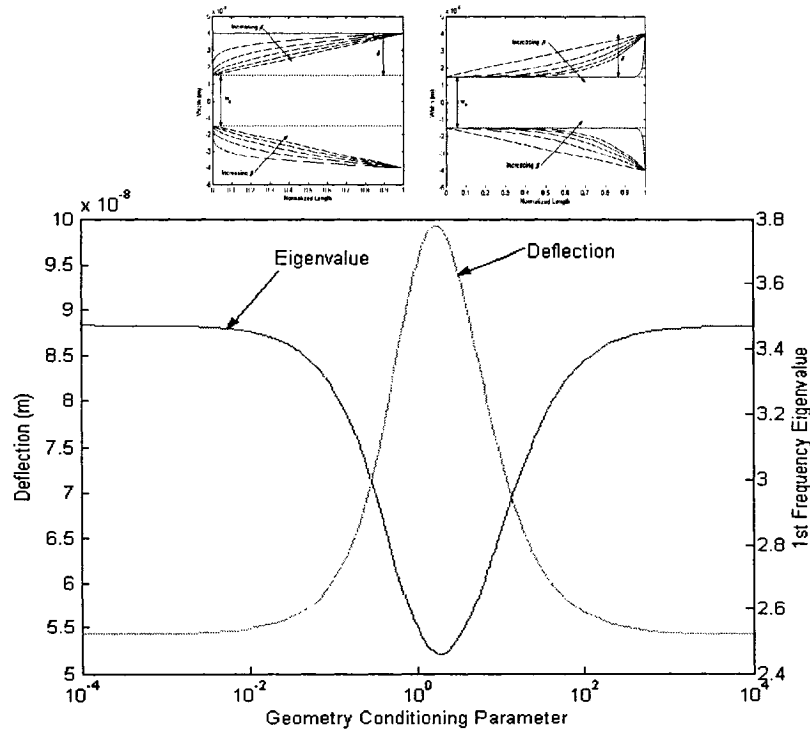
Figure 2.34. Effect of the conditioning parameter on the tip deflection and first eigenvalue for *soft* geometry configuration.

75
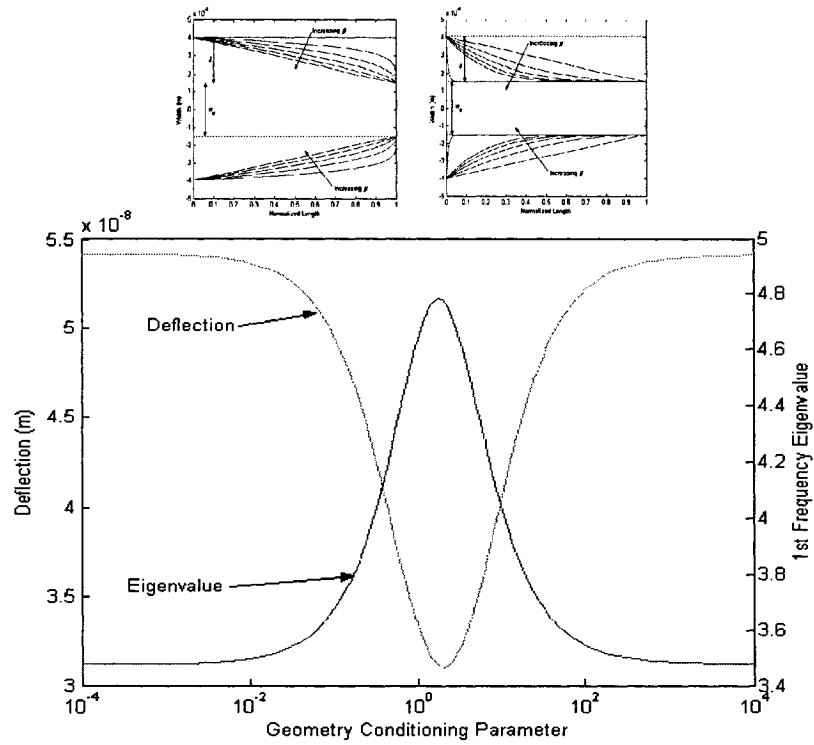
Figure 2.35. Effect of the conditioning parameter on the tip deflection and first eigenvalue for *rigid* geometry configuration.
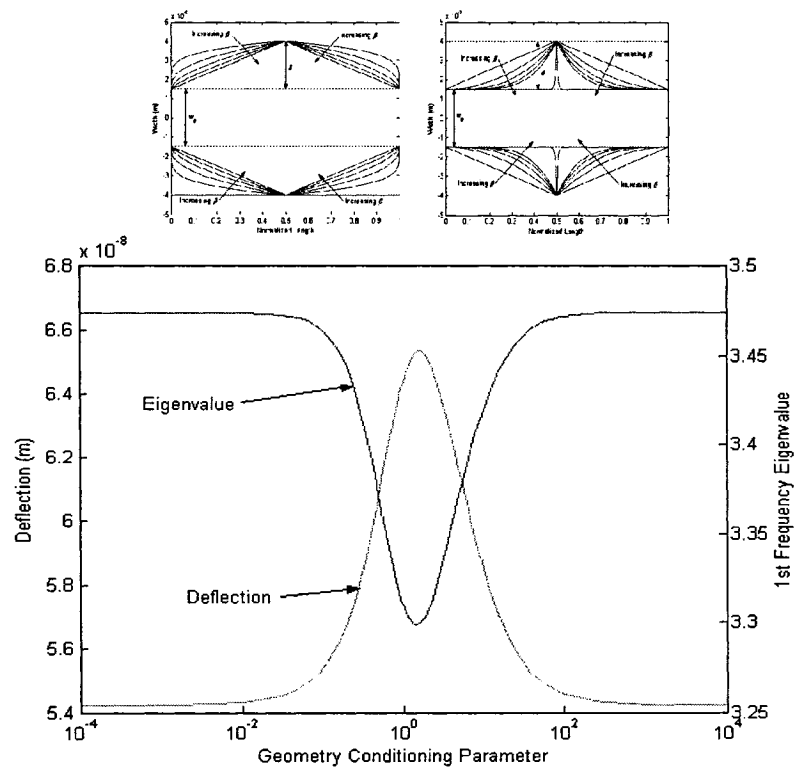
Figure 2.36. Effect of the conditioning parameter on the tip deflection and first eigenvalue for *SORI* geometry configuration.

76
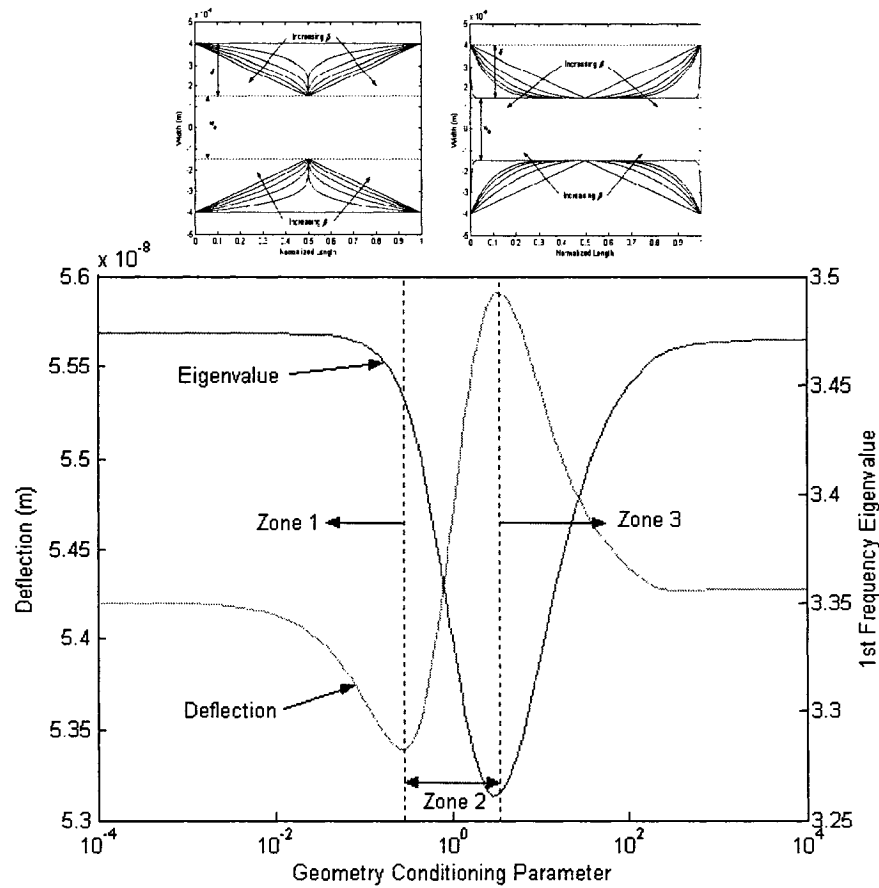
Figure 2.37. Effect of the conditioning parameter on the tip deflection and first eigenvalue for *RISO* geometry configuration.

The *soft* configuration resulted in a 45% change in the tip deflection compared to a 29% change in frequency eigenvalue. For the *rigid* geometry configuration there is a 43% change in deflection and a 27% change in frequency eigenvalue. The *SORI* configuration gives a 17% change in deflection and a 5% change in frequency eigenvalue, while the *RISO* configuration results in, Zone 1: 1.5% change in deflection and a 0.7% change in frequency eigenvalue. Zone 2: 4.5% change in deflection and a 5.5% change in frequency eigenvalue. Zone 3: 3% change in deflection and a 6% change in frequency

eigenvalue. The *rigid* geometry configuration is less affected by the applied electrostatic load, whereas the *soft* conditioning was significantly influenced due to the wider free end width as compared to the *rigid* geometry. For applications where a relatively *invariant* frequency response is required the *RISO* geometry configuration demonstrates good mechanical characteristics in this regard.

2.3.7. *Cutout influences*

Presented here is an investigation on the influence of selective cutout tiling on the dynamic performance of silicon microcantilevers. Surface microfabrication limitations of the MUMPs technology requires etch holes to access underlying sacrificial layers. These are unavoidable in this particular silicon foundry process. Shown in Figure 2.38 are some examples of MUMPs technology structures with cutouts (etch holes).
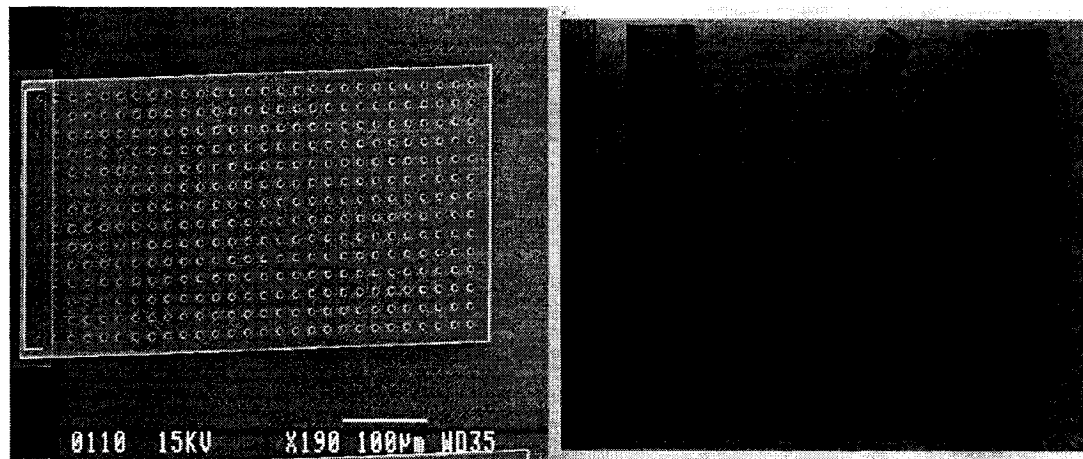
Figure 2.38. MUMPs technology requires cutouts for passage of etchant. Left: microcantilever. Right: Capacitive diaphragm.

The mechanical properties of microcantilevers are dependant upon the physical parameters of the device. In other situations, the cutouts can also be introduced deliberately to tune the elastic behaviour. In this regard, the cutouts can be used to influence either the *stiffness domain* or the *mass domain* of the microcantilever depending upon where the cutouts are placed along the length of the microcantilever [204, 206]. The cutouts could be implemented in both surface micromachining and in bulk micromachining processes. Shown in Figure 2.39 is a schematic of cutouts placed along a microcantilever for left-to-right tiling and right-to-left tiling, respectively.
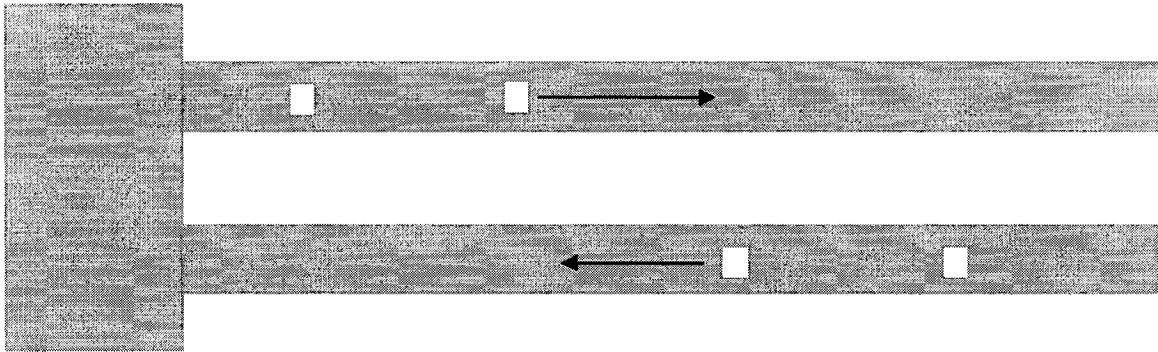
Figure 2.39. Schematic overview of examples of cutouts placed along a microcantilever. For the microcantilever pairs, in the top one has the cutouts placed *left-to-right* while in the lower one they are placed *right-to-left*.

The microcantilever dimensions investigated here are length $L = 1050\mu m$, width $w = 100\mu m$, and thickness $h = 10\mu m$.

Given in Figure 2.40 are the variations in the first eigenvalue as a function of cutout placement for left-to-right and right-to-left cutout tiling respectively. The results are compared with a finite element model using FEMLAB [43].
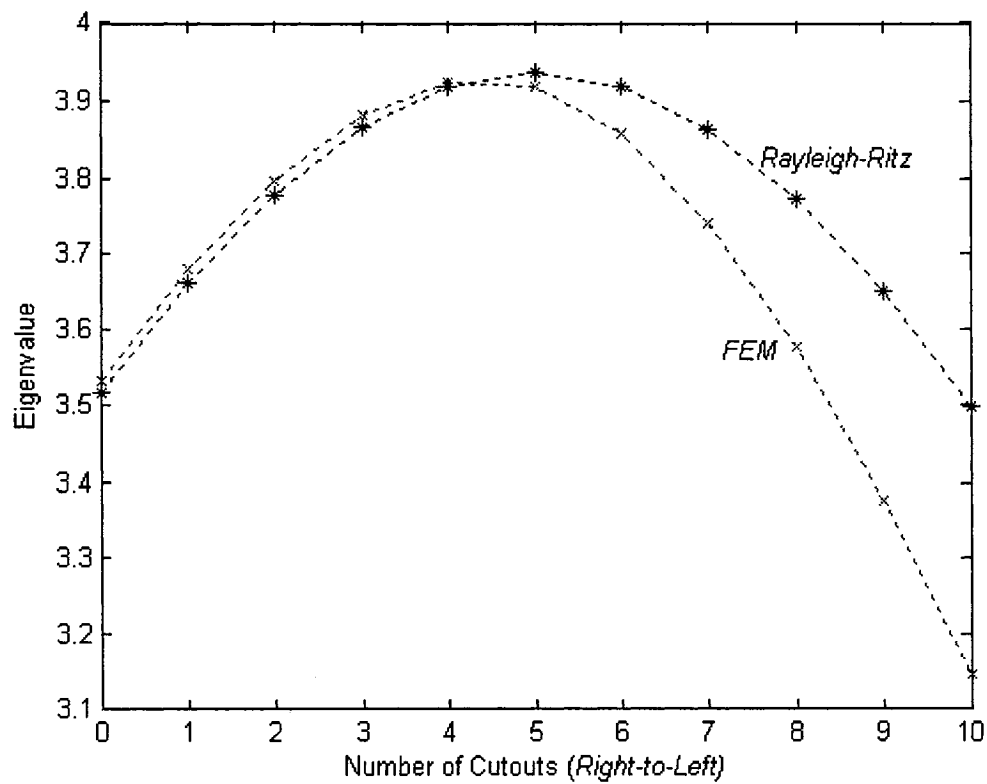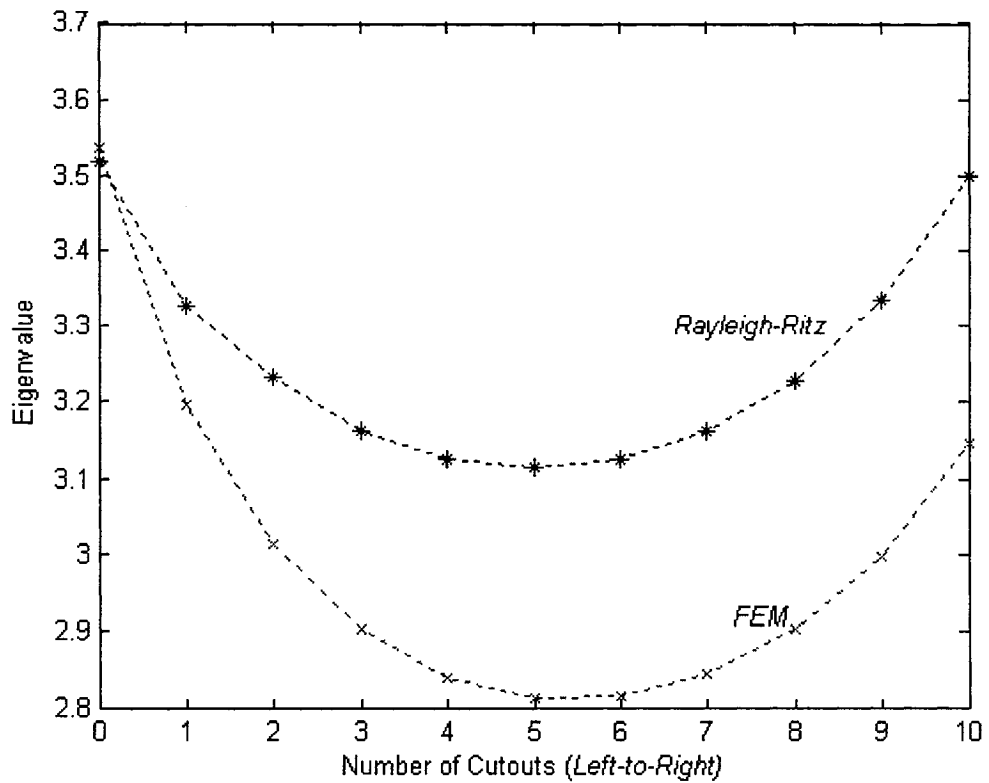
Figure 2.40. A comparison of the 1ˢᵗ eignevalue as a function of the number of cutouts using the Rayleigh-Ritz and FEM methods. Top: *left-to-right* tiling. Bottom: *Right-to-left* tiling.

The *left-to-right* tiling has a greater initial influence on the mechanical stiffness of the microcantilever as can be seen from the reduction in the eigenvalue. As the cutouts are moved to the right the frequency increases as the mechanical stiffness is *restored* and mass is removed form the microcantilever. In this regard the mass and stiffness domains can be defined; for *left-to-right* tiling the mass domain is for points to the right of the minimum of the curve, and the stiffness domain as points to the left of the minimum. Similarly for *right-to-left* tiling the mass domain is to the left of the apex and the stiffness domain is to the right.

It can be seen from these plots that the theoretical formulation in its present format is limited in modeling microcantilevers with cutouts. This is especially true for cutouts located in the *stiffness* domain of the microcantilever. Hence, a *new* approach is required in order to improve upon the theoretical model. This new method, called the *segment Rayleigh-Ritz method*, will be introduced in Chapter 3.

2.4. SUMMARY

A theoretical analysis of microfabrication, electrostatic, thermal, geometry and cutout influences on the static and dynamic properties of microcantilevers was presented. The microfabrication influences and limitations at the microcantilever support boundary were modeled using artificial rotational and translational springs. The eigenvalues and mode shapes were obtained for different end support conditions by varying the value of the rotational stiffness. In this manner the boundary characterization theory presented aims

to quantify the limitations and limitations that are an *intrinsic* part of MEMS manufacturing processes. The electrostatic modeling incorporated the applied voltage through an electrostatic softness in the dynamic regime. Both the static and dynamic performances were simulated for a given applied voltage. Thermal influences took into account the changes to geometrical properties of the microcantilever. It was shown that the influence of thermal loading can affect the frequency response of a microcantilever through the changes to the linear dimensions of the device. Coupled electro-thermo-boundary support influences were also presented. It was shown that the combined effect can significantly alter the performance characteristics of a microcantilever. The sensitivity of the microcantilever to a thermal load was increased as the applied voltage was increased. Four width tapered profiles were presented. The geometry conditioning is a method in which either stiffening or softening attributes may be obtained through the selection of an appropriate contour geometry. The coupled effect of electrostatic and width tapering was also analyzed. Another method to influence the geometry is through cutouts incorporated into the microcantilever. The dependence of the eigenvalues on the number of cutouts for *left-to-right* and *right-to-left* tiling patterns was demonstrated. Through an interpretation of the graphed results a respective mass and stiffness domains have been defined. The modeling of the cutouts was compared to an FEM method and the results showed significant differences. Therefore, in order to better analyze the effect of etch holes and cutouts on the static and dynamic characteristics of microcantilevers, a new theoretical formulation based on a *segment* Rayleigh-Ritz approach is presented in the following chapter.

Chapter 3

SEGMENT RAYLEIGH-RITZ METHOD

Presented in this chapter is an improved method for predicting the static and dynamic characteristics of microcantilevers with cutouts. The theoretical formulation is based on a segment Rayleigh-Ritz approach. The theoretical analysis includes a comparison of the results obtained with non-segmented, finite element and segmented approaches.

3.1. INTRODUCTION

The results obtained for the *normal* Rayleigh-Ritz method in Chapter 2 for microcantilevers with cutouts showed a significant variation from FEM models. This is due to the requirement that the deflection functions, in this case the orthogonal polynomials, be continuous over the microcantilever length and satisfying the outer edge boundary conditions as well as those at the cutouts [126, 157]. A direct result of this is a lower reduction in the strain energy (stiffness) of the microcantilever in the cutout region as compared to its kinetic energy (mass) [157]. Hence, this will lead to generally higher eigenvalues as seen in Figure 2.40, especially, in the stiffness domain.

3.2. *SEGMENT* RAYLEIGH-RITZ METHOD

In this approach, the microcantilever beam is modeled by a series of interconnected segments of various lengths as shown in Figure 3.1. The beam segments are joined together by *inter-segmental* artificial rotational and translational springs. By using this method cutouts of a given length and width in the microcantilever can be modeled as a single segment.

The theoretical formulation presented here is based on the work given in Chapter 2. However, the microcantilever is divided into a number of n_{sg} segments that is a function of the number of cutouts, n_c. For example, a microcantilever with one cutout will be divided into three segments, a microcantilever with two cutouts will be divided into five segments, and so on. Hence, the number of segments for a given number of cutouts is given by,

$$n_{sg} = 2n_c + 1 \tag{3.1}$$

In this approach the individual segments are connected by rotational and translational springs. Given in Figure 3.1 is the enumeration method used to identify the microcantilever beam segments and spring elements. This is illustrated in Figure 3.2 for a microcantilever with one cutout, for example.
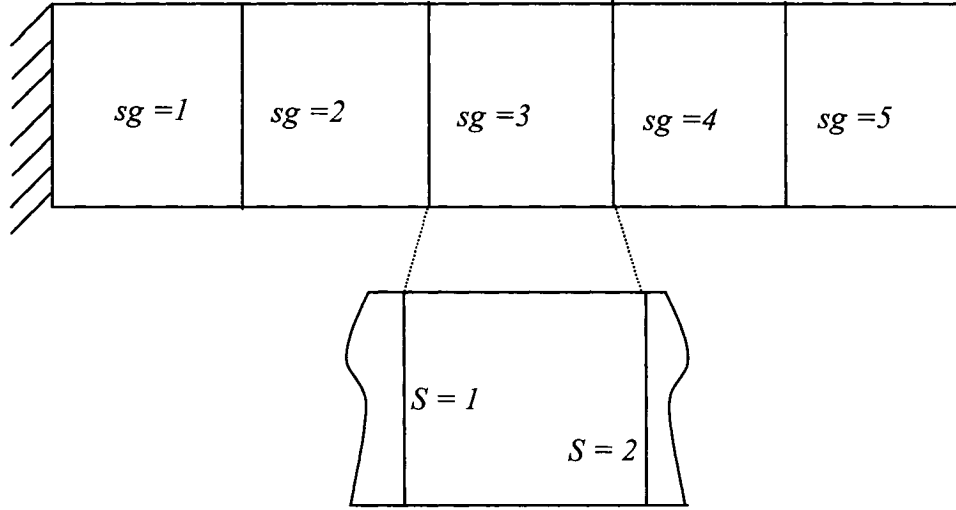
Figure 3.1. Top: A microcantilever divided into 5 segments. Bottom: A close up of one segment and the numbering scheme employed to define the sides for each segment.

Hence, the inter-segmental springs are numbered in the following manner, for the rotational, K_{RsgS}, for example, sg refers to the segment, and S refers to the side, either 1 or 2, of the segment. The same notation is used for the inter-segmental translational springs. An illustration of a microcantilever with one cutout is given in Figure 3.2. This enumeration concept is illustrated in Figure 3.3. The boundary support springs, K_T and K_R, remain as they were defined in Chapter 2.
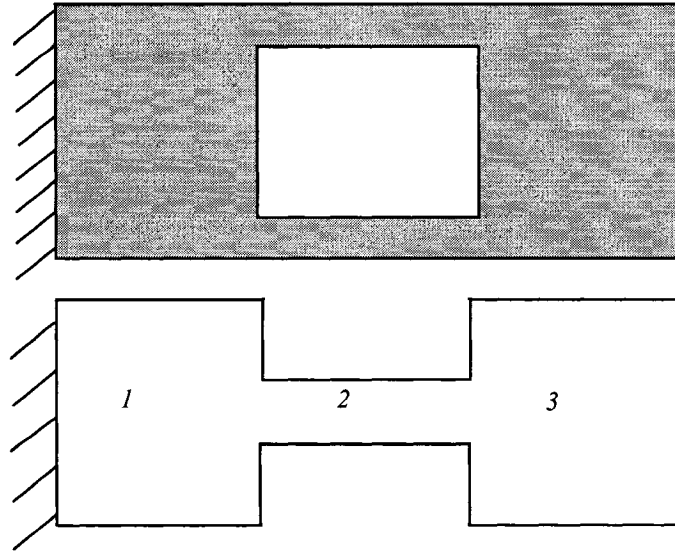
Figure 3.2. Top: Microcantilever with a single cutout. Bottom: The microcantilever is divided into three segments for modeling (Top view).
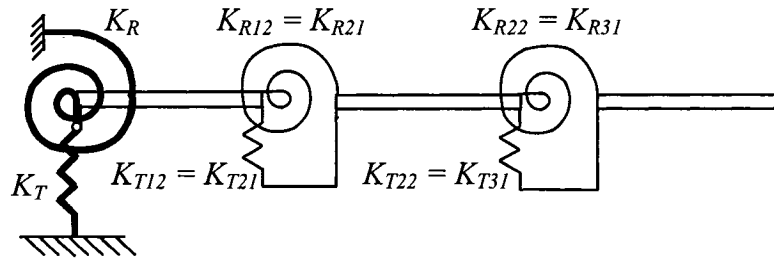
Figure 3.3. An illustration of the segment approach. The individual segments are joined by artificial rotational and translational springs (Side view).

The *problem* of the discontinuity of the shape functions at the cutout boundaries of the microcantilever is overcome in this approach as each segment is allocated its own set of orthogonal polynomials as shown in Figure 3.4 for three segments, based on *free-free* boundary conditions.
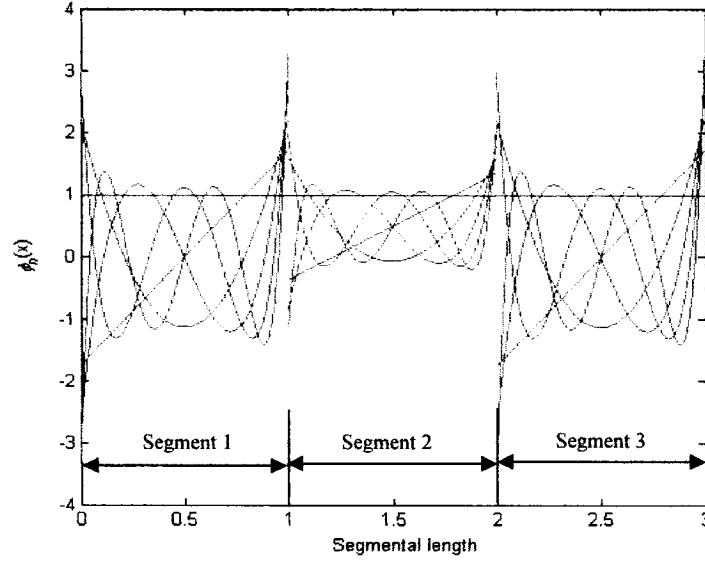
Figure 3.4. Each microcantilever beam segment is allocated its respective set of orthogonal polynomials.

For the segmented microcantilever the strain energy is given by,

$$U^{(T)}{}_B = \sum_{sg=1}^{n_{sg}} \frac{E_{sg}{}^{(T)} h_{sg}{}^{(T)^3} w_{0sg}{}^{(T)}}{24 L_{sg}{}^{(T)^3}} \int_0^1 \Psi_{sg}(x)(W_{sg}''(x))^2 \, dx \tag{3.2}$$

where W_{Ssg} and W_{Dsg} will represent the static and dynamic deflections, respectively.

The segmentized electrostatic *static* potential energy equation becomes,

$$U^{(T)}{}_{ES} = -\sum_{sg=1}^{n_{sg}} \frac{\varepsilon_r \varepsilon_0 L_{sg}{}^{(T)} w_{0sg}{}^{(T)} V_{sg}{}^2}{2 d_{0sg}} \int_0^1 \Psi_{sg}(x)\left(1 + \frac{W_{sg}(x)}{d_{0sg}} + \left(\frac{W_{sg}(x)}{d_{0sg}}\right)^2 + .. + \left(\frac{W_{sg}(x)}{d_{0sg}}\right)^n\right) dx \tag{3.3}$$

where third order terms and higher are ignored. The maximum kinetic energy of the microcantilever is given by,

$$T^{(T)}{}_B = \sum_{sg=1}^{n_{sg}} \frac{1}{2} \omega^2 \rho_{sg}{}^{(T)} h_{sg}{}^{(T)} L_{sg}{}^{(T)} w_{0sg}{}^{(T)} \int_0^1 \Psi_{sg}(x)(W_{sg}(x))^2 \, dx \tag{3.4}$$

Where the following definition applies,

87

$$\Psi_{sg}(x) = \frac{\Psi(x)}{n_{sg}} \qquad (3.5)$$

3.2.1. *Static behaviour under electrostatic influence*

Equation (2.27) for the static equilibrium is now rewritten to take into account the individual segments and is given by,

$$\sum_{sg}\sum_{j} \left(\begin{array}{l} \left[\begin{array}{l} E_{ij}^{22}{}_{sg} + K_{Tsg1}^{(T)}{}^{*}\phi_i'(0)\phi_j'(0) + K_{Rsg1}^{(T)}{}^{*}\phi_i'(0)\phi_j'(0) + K_{Tsg2}^{(T)}{}^{*}\phi_i(1)\phi_j(1) \\ \\ + K_{Rsg2}^{(T)}{}^{*}\phi_i'(1)\phi_j'(1) - V_1^{(T)}{}^{*}{}_{sg}\, E_{ij}^{00}{}_{sg} \end{array} \right] A_{j,sg} \\ \\ - \left[K_{Tsg1}^{(T)}{}^{*}\phi_i(1)\phi_j(0) + K_{Rsg1}^{(T)}{}^{*}\phi_i'(1)\phi_j'(0) \right] A_{j-1,sg} \\ \\ - \left[K_{Tsg2}^{(T)}{}^{*}\phi_i(0)\phi_j(1) + K_{Rsg2}^{(T)}{}^{*}\phi_i'(0)\phi_j'(1) \right] A_{j+1,sg} \\ \\ = V_2^{(T)}{}^{*}{}_{sg} \int_0^1 \Psi_{sg}(x)\phi_i(x)dx \end{array} \right) \qquad (3.6)$$

$$\forall\ i = 1, 2, ..., n \quad j = 1, 2, ..., n \quad sg = 1, 2, ...n_{sg}$$

Where these definitions apply,

$$E_{ij}^{22}{}_{sg} = \int_0^1 \Psi_{sg}(x)\phi_i''(x)\phi_j''(x)dx \qquad (3.6a)$$

$$E_{ij}^{00}{}_{sg} = \int_0^1 \Psi_{sg}(x)\phi_i(x)\phi_j(x)dx \qquad (3.6b)$$

$$K_{TsgS}^{(T)}{}^{*} = \frac{12K_{TsgS}L_1^{(T)3}}{E_1^{(T)}h_1^{(T)3}}, \quad K_{RsgS}^{(T)}{}^{*} = \frac{12K_{RsgS}L_1^{(T)}}{E_1^{(T)}h_1^{(T)3}}, \quad S = 1, 2 \qquad (3.6c)$$

$$V_1^{(T)*}{}_{sg} = \frac{\varepsilon_0 \varepsilon_r W_{0sg}{}^{(T)} L_{sg}{}^{(T)4}}{E_{sg}{}^{(T)} I_{0sg}{}^{(T)} d_{0sg}^3}, \quad V_2^{(T)*}{}_{sg} = \frac{\varepsilon_0 \varepsilon_r W_{0sg}{}^{(T)} L_{sg}{}^{(T)4}}{2E_{sg}{}^{(T)} I_{0sg}{}^{(T)} d_{0sg}^2} \tag{3.6d}$$

In the case of the static analysis, the deflection functions refer to the static deflection.

3.2.2. Dynamic behaviour under electrostatic influence

For the dynamic analysis the segmental electrostatic stiffness now is written as

$$K_E^{(T)*}{}_{sg} = -\frac{\varepsilon_0 \varepsilon_r W_{0sg}{}^{(T)} L_{sg}{}^{(T)4} V^2{}_{sg}}{E_{sg}{}^{(T)} I_{0sg}{}^{(T)}} \left[\frac{\Psi_{sg}(x)}{\left(d_{0sg} - W_{Ssg}(x)\right)^3} \right] \tag{3.7}$$

and the electrostatic potential energy for the dynamic analysis for each segment is given by,

$$U^{(T)}{}_{ED} = \sum_{sg=1}^{n_{sg}} \frac{1}{2} \int_0^1 K_E^{(T)*}{}_{sg}(x) W_{Dsg}(x)^2 \, dx \tag{3.8}$$

where the integrations are carried out over each microcantilever beam segment. The eigensystem is written as,

$$\sum_{sg}\sum_{j} \left(\begin{bmatrix} E_{ij}^{22}{}_{sg} + K_{Tsg1}^{(T)*} \phi_i(0)\phi_j(0) + K_{Rsg1}^{(T)*} \phi_i'(0)\phi_j'(0) + K_{Tsg2}^{(T)*} \phi_i(1)\phi_j(1) \\ + K_{Rsg2}^{(T)*} \phi_i'(1)\phi_j'(1) - \int_0^1 K_E^{(T)*}{}_{sg} \phi_i(x)\phi_j(x) - \lambda_{sg}^{(T)} E_{ij}^{00}{}_{sg} \end{bmatrix} A_{j,sg} \right.$$
$$\left. - \left[K_{Tsg1}^{(T)*} \phi_i(1)\phi_j(0) + K_{Rsg1}^{(T)*} \phi_i'(1)\phi_j'(0) \right] A_{j-1,sg} \right.$$
$$\left. - \left[K_{Tsg2}^{(T)*} \phi_i(0)\phi_j(1) + K_{Rsg2}^{(T)*} \phi_i'(0)\phi_j'(1) \right] A_{j+1,sg} \right.$$
$$\left. = 0 \right) \tag{3.9}$$

$\forall \; i = 1, 2, \dots, n \quad j = 1, 2, \dots, n \quad sg = 1, 2, \dots n_{sg}$

Solution of the eigensystem in Equation (3.9) will give the segmental eigenvalues and natural frequencies.

$$\lambda_n^{(T)^2}{}_{sg} = \frac{\omega_n^{(T)^2}{}_{sg}\rho_{sg}^{(T)}w_{0sg}^{(T)}h_{sg}^{(T)}L_{sg}^{(T)^4}}{E_{sg}^{(T)}I_{0sg}^{(T)}} \tag{3.10}$$

The eigenvalues of the microcantilever are obtained from,

$$\lambda_n^{(T)} = n_{sg}^2 \lambda_n^{(T)}{}_{sg} \tag{3.10a}$$

Given in Figure 3.5 is an example of the strain and kinetic energy matrices for a microcantilever consisting of 3 segments. Although 10 polynomial functions were used in the modeling, the representation given here is limited to 5 for clarity.

With respect to Figure 3.5 the following definitions apply,

$$K_{ij_{sg}} = E_{ij}^{22}{}_{sg} + K_{Tsg1}^{(T)}{}^{*}\phi_i(0)\phi_j(0) + K_{Rsg1}^{(T)}{}^{*}\phi_i'(0)\phi_j'(0) + K_{Tsg2}^{(T)}{}^{*}\phi_i(1)\phi_j(1) + K_{Rsg2}^{(T)}{}^{*}\phi_i'(1)\phi_j'(1)$$

$$- \int_0^1 K_E^{(T)}{}^{*}{}_{sg}\phi_i(x)\phi_j(x)$$

$$k_{ij_{sg}S} = -K_{Tsg1}^{(T)}{}^{*}\phi_i(1)\phi_j(0) - K_{Rsg1}^{(T)}{}^{*}\phi_i'(1)\phi_j'(0) - K_{Tsg2}^{(T)}{}^{*}\phi_i(0)\phi_j(1) - K_{Rsg2}^{(T)}{}^{*}\phi_i'(0)\phi_j'(1)$$

$$M_{ij_{sg}} = \lambda_{sg}^{(T)}E_{ij}^{00}{}_{sg} \tag{3.11}$$

$$\begin{bmatrix}
K_{111} & K_{121} & K_{131} & K_{141} & K_{151} & k_{1121} & k_{1221} & k_{1321} & k_{1421} & k_{1521} & 0 & 0 & 0 & 0 & 0 \\
K_{211} & K_{221} & K_{231} & K_{241} & K_{251} & k_{2121} & k_{2221} & k_{2321} & k_{2421} & k_{2521} & 0 & 0 & 0 & 0 & 0 \\
K_{311} & K_{321} & K_{331} & K_{341} & K_{351} & k_{3121} & k_{3221} & k_{3321} & k_{3421} & k_{3521} & 0 & 0 & 0 & 0 & 0 \\
K_{411} & K_{421} & K_{431} & K_{441} & K_{451} & k_{4121} & k_{4221} & k_{4321} & k_{4421} & k_{4521} & 0 & 0 & 0 & 0 & 0 \\
K_{511} & K_{521} & K_{531} & K_{541} & K_{551} & k_{5121} & k_{5221} & k_{5321} & k_{5421} & k_{5521} & 0 & 0 & 0 & 0 & 0 \\
k_{1112} & k_{1212} & k_{1312} & k_{1412} & k_{1512} & K_{112} & K_{122} & K_{132} & K_{142} & K_{152} & k_{1132} & k_{1232} & k_{1332} & k_{1432} & k_{1532} \\
k_{2112} & k_{2212} & k_{2312} & k_{2412} & k_{2512} & K_{212} & K_{222} & K_{232} & K_{242} & K_{252} & k_{2132} & k_{2232} & k_{2332} & k_{2432} & k_{2532} \\
k_{3112} & k_{3212} & k_{3312} & k_{3412} & k_{3512} & K_{312} & K_{322} & K_{332} & K_{342} & K_{352} & k_{3132} & k_{3232} & k_{3332} & k_{3432} & k_{3532} \\
k_{4112} & k_{4212} & k_{4312} & k_{4412} & k_{4512} & K_{412} & K_{422} & K_{432} & K_{442} & K_{452} & k_{4132} & k_{4232} & k_{4332} & k_{4432} & k_{4532} \\
k_{5112} & k_{5212} & k_{5312} & k_{5412} & k_{5512} & K_{512} & K_{522} & K_{532} & K_{542} & K_{552} & k_{5132} & k_{5232} & k_{5332} & k_{5432} & k_{5532} \\
0 & 0 & 0 & 0 & 0 & k_{1123} & k_{1223} & k_{1323} & k_{1423} & k_{1523} & K_{113} & K_{123} & K_{133} & K_{143} & K_{153} \\
0 & 0 & 0 & 0 & 0 & k_{2123} & k_{2223} & k_{2323} & k_{2423} & k_{2523} & K_{213} & K_{223} & K_{233} & K_{243} & K_{253} \\
0 & 0 & 0 & 0 & 0 & k_{3123} & k_{3223} & k_{3323} & k_{3423} & k_{3523} & K_{313} & K_{323} & K_{333} & K_{343} & K_{353} \\
0 & 0 & 0 & 0 & 0 & k_{4123} & k_{4223} & k_{4323} & k_{4423} & k_{4523} & K_{413} & K_{423} & K_{433} & K_{443} & K_{453} \\
0 & 0 & 0 & 0 & 0 & k_{5123} & k_{5223} & k_{5323} & k_{5423} & k_{5523} & K_{513} & K_{523} & K_{533} & K_{543} & K_{553}
\end{bmatrix}$$

$$\begin{bmatrix}
M_{111} & M_{121} & M_{131} & M_{141} & M_{151} & 0 & 0 & 0 & 0 & 0 & 0 & 0 & 0 & 0 & 0 \\
M_{211} & M_{221} & M_{231} & M_{241} & M_{251} & 0 & 0 & 0 & 0 & 0 & 0 & 0 & 0 & 0 & 0 \\
M_{311} & M_{321} & M_{331} & M_{341} & M_{351} & 0 & 0 & 0 & 0 & 0 & 0 & 0 & 0 & 0 & 0 \\
M_{411} & M_{421} & M_{431} & M_{441} & M_{451} & 0 & 0 & 0 & 0 & 0 & 0 & 0 & 0 & 0 & 0 \\
M_{511} & M_{521} & M_{531} & M_{541} & M_{551} & 0 & 0 & 0 & 0 & 0 & 0 & 0 & 0 & 0 & 0 \\
0 & 0 & 0 & 0 & 0 & M_{112} & M_{122} & M_{132} & M_{142} & M_{152} & 0 & 0 & 0 & 0 & 0 \\
0 & 0 & 0 & 0 & 0 & M_{212} & M_{222} & M_{232} & M_{242} & M_{252} & 0 & 0 & 0 & 0 & 0 \\
0 & 0 & 0 & 0 & 0 & M_{312} & M_{322} & M_{332} & M_{342} & M_{352} & 0 & 0 & 0 & 0 & 0 \\
0 & 0 & 0 & 0 & 0 & M_{412} & M_{422} & M_{432} & M_{442} & M_{452} & 0 & 0 & 0 & 0 & 0 \\
0 & 0 & 0 & 0 & 0 & M_{512} & M_{522} & M_{532} & M_{542} & M_{552} & 0 & 0 & 0 & 0 & 0 \\
0 & 0 & 0 & 0 & 0 & 0 & 0 & 0 & 0 & 0 & M_{113} & M_{123} & M_{133} & M_{143} & M_{153} \\
0 & 0 & 0 & 0 & 0 & 0 & 0 & 0 & 0 & 0 & M_{213} & M_{223} & M_{233} & M_{243} & M_{253} \\
0 & 0 & 0 & 0 & 0 & 0 & 0 & 0 & 0 & 0 & M_{313} & M_{323} & M_{333} & M_{343} & M_{353} \\
0 & 0 & 0 & 0 & 0 & 0 & 0 & 0 & 0 & 0 & M_{413} & M_{423} & M_{433} & M_{443} & M_{453} \\
0 & 0 & 0 & 0 & 0 & 0 & 0 & 0 & 0 & 0 & M_{513} & M_{523} & M_{533} & M_{543} & m_{553}
\end{bmatrix}$$

Figure 3.5. Top: Strain energy matrix. Bottom: Kinetic energy matrix.

3.3. ANALYTICAL RESULTS

The results for the segmental approach are given and compared here. In this analysis the segment Rayleigh-Ritz method is validated firstly by comparing the static deflections,

modes shapes, and virtual deflections for a microcantilever (without cutouts) divided into several segments. This analysis will serve to confirm the theoretical formulation through the invariant results obtained for any number of microcantilever beam segments under a given electro-thermal load. The microcantilever beam has the following dimensions $L = 1000\mu m$, $w = 100\mu m$, $h = 10\mu m$, and operating conditions $T = 400$ Kelvin and $V = 20$ volts. Shown in Figure 3.6 are the normalized first and second mode shapes for 1, 2, 3 and 17 segments, respectively.
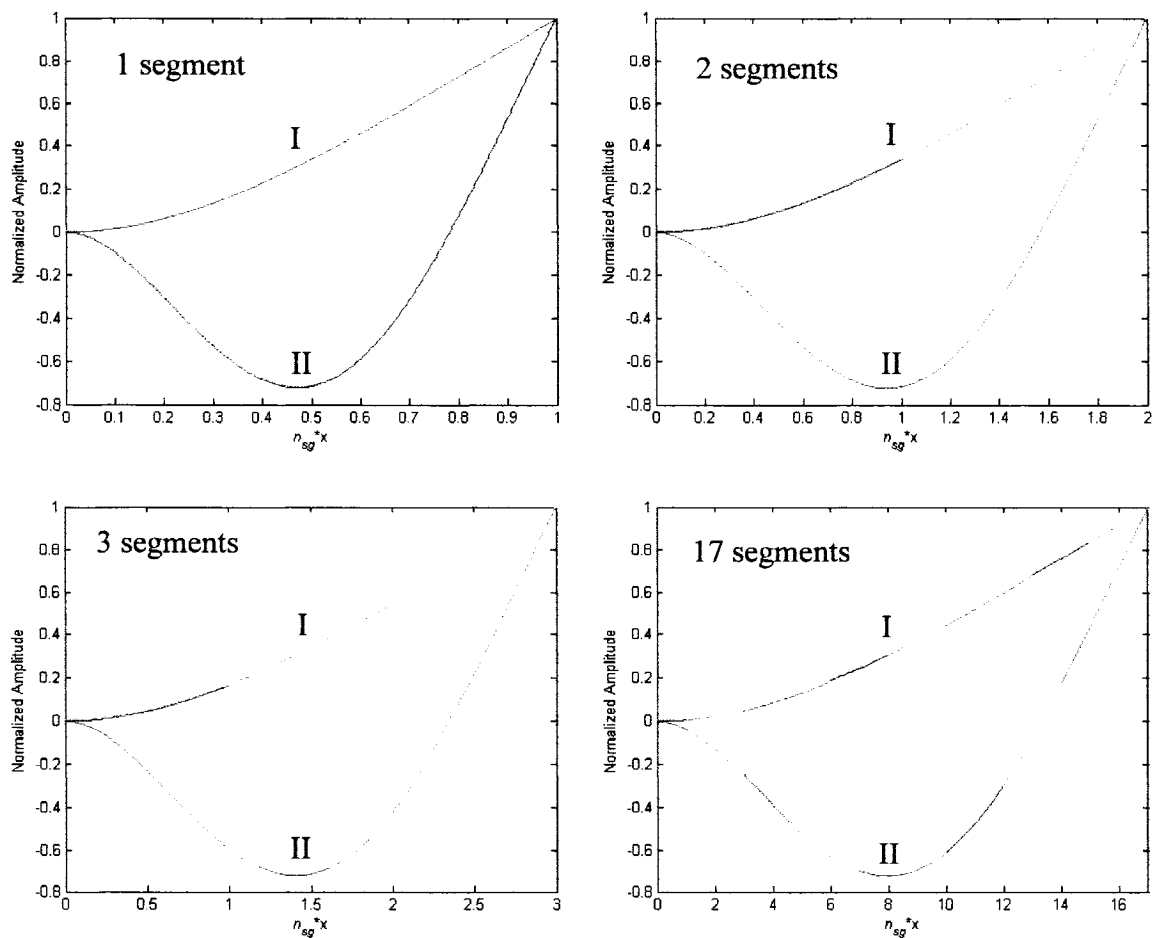
Figure 3.6. A comparison of the first and second mode shapes as a function of the number of segments. Top row: 1 and 2 segments. Bottom row: 3 and 17 segments.

It can be seen from Figure 3.6 that the mode shapes are identical for all the microcantilever models of various segments. Hence, the segmentized eigensystem formulation is validated through these invariant properties.

The static deflection of the microcantilever for a given applied voltage is given in Figure 3.7 for 1, 2, 3 and 17 segments respectively.
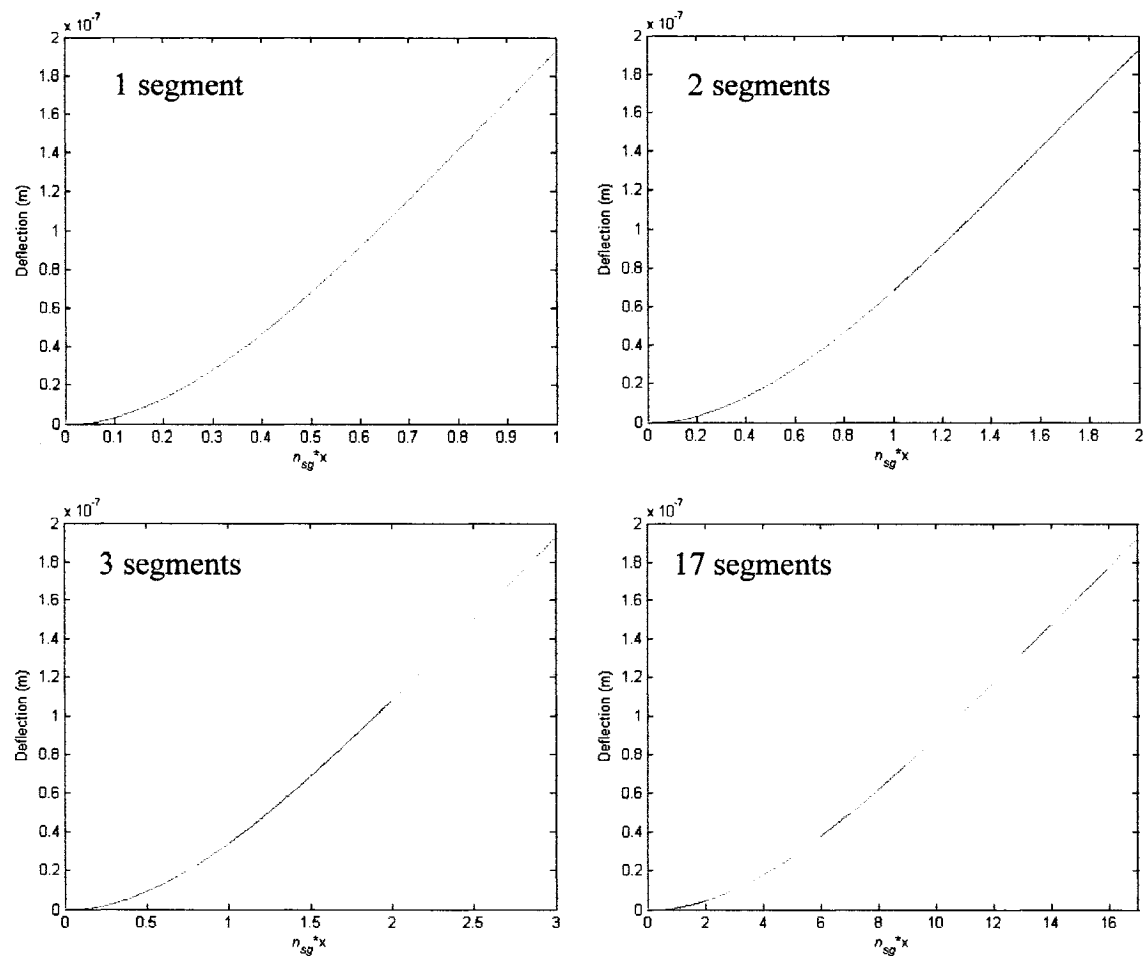
Figure 3.7. A comparison of the static deflections as a function of the number of segments. The bias voltage is 20V. Top row: 1 and 2 segments. Bottom row: 3 and 17 segments.

The virtual deflections [31] are defined as the ratio of the inclinations, dz/dx, of the second mode to the first mode. They are presented in Figure 3.8 for 1, 2, 3 and 17 segments respectively.
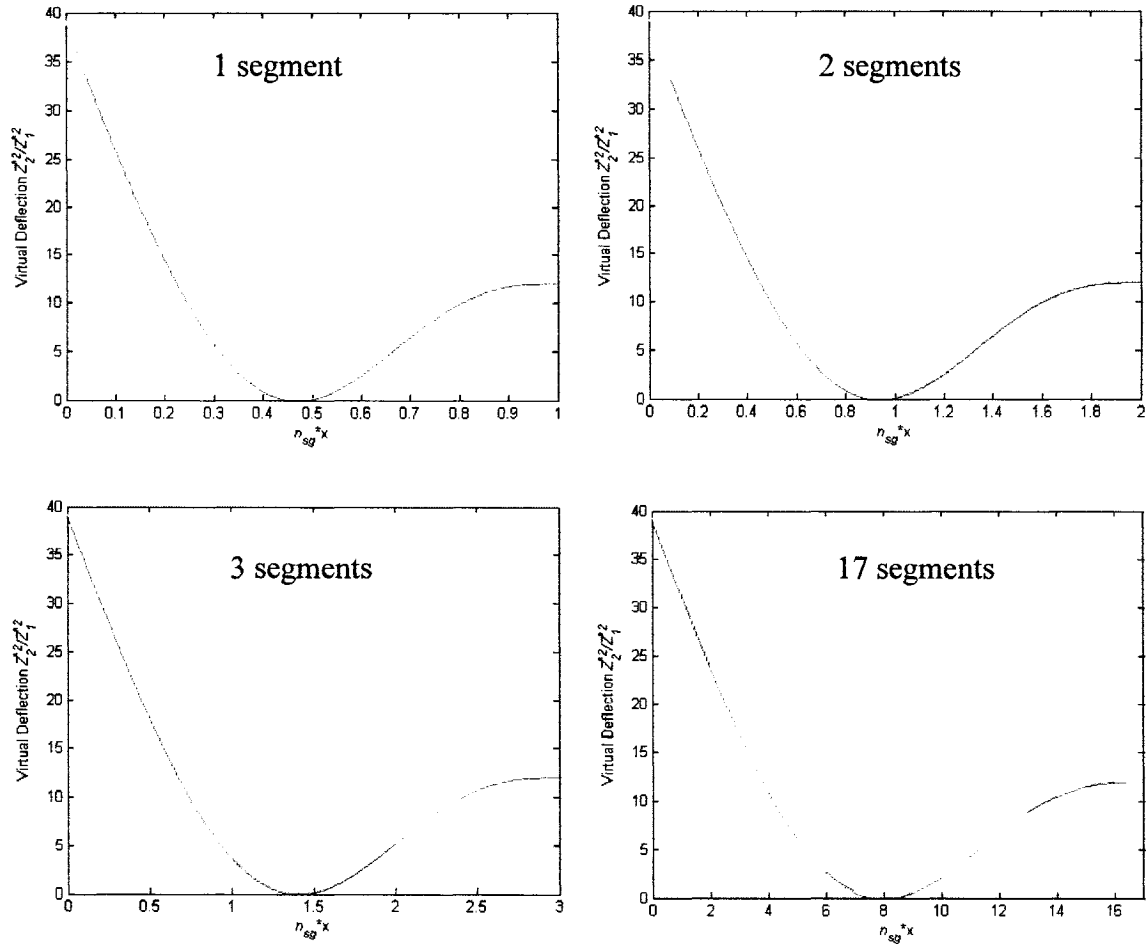
Figure 3.8. A comparison of the virtual deflections as a function of the number of segments. Top row: 1 and 2 segments. Bottom row: 3 and 17 segments.

The 1st and 2nd natural frequencies obtained for this analysis are given in Table 3.1.

Table 3.1. Comparing the first and second natural frequencies of a microcantilever as a function of the number of segments.

Segments	1	2	3	17
1st nat. Freq. (Hz)	12658	12658	12658	12658
2nd nat. Freq. (Hz)	79694	79694	79694	79694

It can be seen from the mode shapes, electrostatic deflections, and virtual deflections obtained for the segmentized Rayleigh-Ritz method that they are all equal regardless of the number of segments incorporated into the microcantilever model. This approach is now compared to an FEM Euler-beam model method using FEMLAB [43] for 1, 3, and 5 segments respectively. In this model there are 1 and 2 cutouts of equal size, respectively, for the 3 and 5 segment analysis. The one segment microcantilever has no cutouts. The results obtained for the first and second natural frequencies are presented in Table 3.2.

Table 3.2. Comparing the first and second natural frequencies of a microcantilever beam using the segmentized Rayleigh-Ritz method and an FEM Euler-beam model.

Number of Segments	Seg. Rayleigh-Ritz (Hz)		FEM (Hz)
1	1st nat. Freq.	13799	13798
	2nd nat. Freq.	86475	86476
3	1st nat. Freq.	12941	12941
	2nd nat. Freq.	88053	88053
5	1st nat. Freq.	13548	13548
	2nd nat. Freq.	85528	85527

The results shown in Table 3.2 indicate that the segment Rayleigh-Ritz method employing orthogonal polynomials as the deflection shape functions can be applied to microcantilevers with cutouts, where each segment is allocated its respective group of shape functions. Hence, these results and the FEM comparison validate this approach as a suitable and precise alternative to the *standard* Rayleigh-Ritz energy method.

It is of interest to compare the standard model with the new formulation to see if there are significant variations between the two approaches to modeling microcantilevers with cutouts. In this analysis a microcantilever of length 1000μm, width 100μm, and thickness 10μm has single 50 x 50 μm² cutouts centered on various locations (125μm, 275μm, 425μm, 575μm, 725μm and 875μm, respectively) along the length of the beam with respect to the fixed end. The results obtained are given in Table 3.3 along with a comparison of the first two natural frequencies of the microcantilever beam as a function of the number of segments.

Table 3.3. A comparison of the natural frequencies of a microcantilever with single cutouts placed at various locations along the beam. Three segments were employed in this analysis.

Center of Cutout (μm)	Ray.-Ritz (Hz)	Seg. Ray.-Ritz (Hz)	FEM (Hz)
No cutout	12070	12070	12067
125	11480	11516	(11516)
275	11755	11748	11748
425	11974	11949	11949
575	12143	12139	12138
725	12333	12359	12359
875	12564	12564	12564

Also the values obtained and shown in graphical form for *left-to-right* cutout tiling in

Figure 2.40 are compared in this approach. They are given in Table 3.4. The

microcantilever beam dimensions used are L =1050μm, w = 100μm, h = 10μm. The

cutouts are 50 x 50μm^2 and are placed 50μm apart with the first cutout centered on 75μm.

Each cutout is added sequentially into the analysis.

Table 3.4. A comparison of the first eigenvalues for the Rayleigh-Ritz, segment Rayleigh-Ritz and FEM methods for *left-to-right* cutout tiling.

Cutouts	Number of Segments	Rayleigh-Ritz	Seg. Rayleig-Ritz	FEM
0	1	3.52	3.52	3.50
1	3	3.33	3.19	(3.19)
2	5	3.23	3.00	3.01
3	7	3.16	2.89	2.90
4	9	3.13	2.85	2.84
5	11	3.12	2.82	2.82
6	13	3.12	2.81	2.82
7	15	3.16	2.86	2.85
8	17	3.23	2.90	2.90
9	19	3.34	3.01	3.00
10	21	3.5	3.15	3.15

From the results obtained it can be seen that the segment Rayleigh-Ritz approach is in

better agreement with the FEM method while the single segment approach provides

higher values. The underlined values in parenthesis in Tables 3.3-3.4 obtained for the

FEM method were included to provide continuity with the values obtained with the segment approach. However, for that particular geometry FEM Euler beam method could not provide an analytical solution.

The combined effect of electrostatic, geometry and cutouts is also investigated using the segmented approach. The static deflection for a given microcantilever width profile and a given applied voltage, and as a function of the cutout size is given in Figure 3.9.
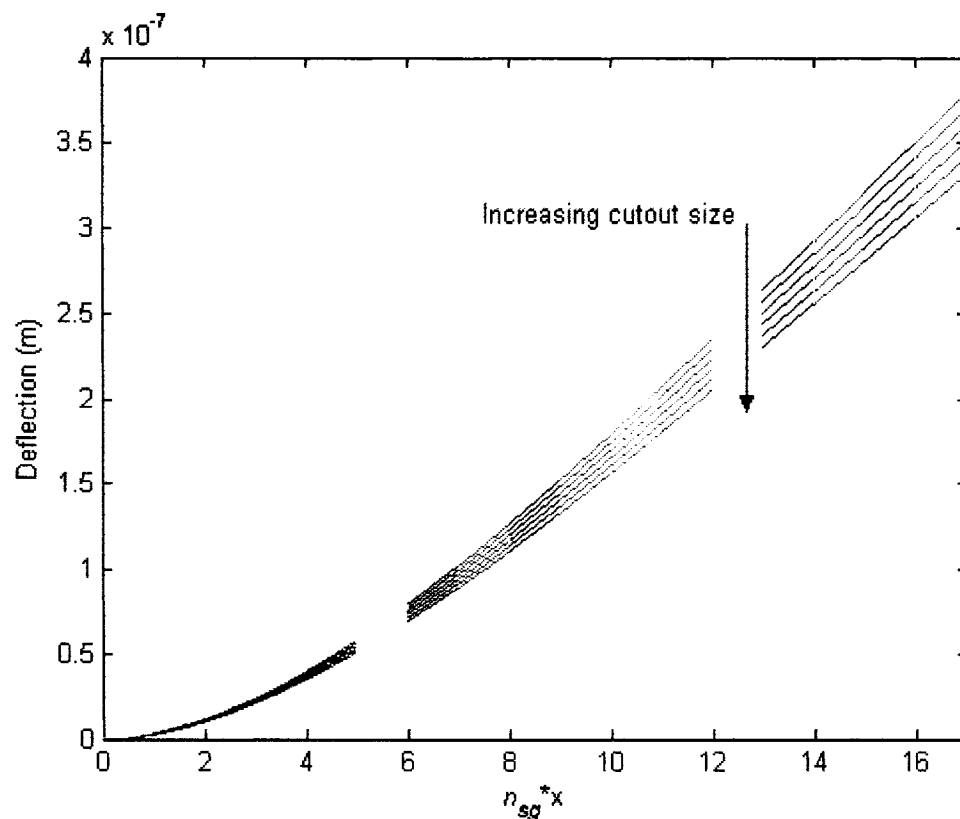
Figure 3.9. The variations to the electrostatic deflections as a function of the microcantilever cutouts.

The deflections decrease as a function of the cutout size due to the reduction in the microcantilever surface area, and hence, a reduction in the electrostatic force acting on the microcantilever.

3.4. SUMMARY

An improved method to predict the static and dynamic characteristics of microcantilevers with cutouts has been demonstrated. This model builds on the theoretical foundation for boundary support, electrostatic, thermal, and geometry influences established in Chapter 2. The method was compared to the *standard* Rayleigh-Ritz and FEM methods, and was found to be in good agreement with the FEM method.

Chapter 4

MICROSYSTEM TESTING METHODS

Presented in this chapter is an overview of MEMS testing methods, and the experimental setup used for the investigation of the static and dynamic characteristics of microscale devices. A detailed experimental procedure is also included along with some sample test results for different microdevices.

4.1. INTRODUCTION

Testing of MEMS devices is one of the important steps in the overall development of microsystems as the commercialization of a given microsystem depends upon the successful validation of the functionality and reliability through experimental testing. Theoretical modeling alone, can only approximate the performance characteristics, hence, a real operational profile can only be obtained through specific testing. Specially designed test equipment and experimentation methods are needed due to the small sizes of the MEMS components. Furthermore, the effect of the microsystem size and microfabrication processes and tolerances makes interpretation of the results very difficult. One of the main considerations is how to perform direct measurements on MEMS devices in a way representing the actual micromechanical elements used in microsystems and the environments under which they will eventually operate. Hence, in

order to obtain accurate data, researchers started to develop their own testing methods specially designed for microscale devices [277].

4.2. TESTING METHODS

The currently available test methods [232, 233] for MEMS can be categorized into two general groups, (i) contact and (ii) non-contact types. Several of the important techniques include: the microtension test where the fracture strengths and Young's modulus can be estimated for non-integrated free standing structures [225, 249, 276]; the axisymmetric plate bend test is primarily used to measure the fracture strengths of relatively thick microstructures [35, 93]; the microbeam bend test where a concentrated load is used to deflect the microstructure and is used for measuring Young's modulus and yield and fracture strength of the microdevice [64, 266]; the M-test where an electrostatic force is applied to bend thin microstructures in order to obtain experimental characteristics for Young's modulus and residual stresses [68, 96]; the wafer curvature measurement method is used primarily for the quantification of residual stresses [72, 257]; dynamic (resonance frequency) tests are suitable for measuring Young's modulus of elasticity and residual stresses in both thick and thin free standing microstructures [99, 187, 188, 280]. These approaches require that the MEMS structure be disturbed in some fashion from its rest position and the changes measured either optically (interferometry, Doppler shift) or electrically (capacitive, resistive), for example. For the contact method, known deflections from the stationary position are applied by a stylus, microprobe or nanoindenter [116, 166, 219], or through some other non-electrical deflection method

such as mass loading [65, 140]. The mechanical properties of the MEMS structure or MEMS material are then deduced from the interpretation of the specific test results under a given applied load. In many cases the use of a contact excitation mechanism will result in the destruction of the MEMS device and hence should only be used sparingly and very selectively.

Hence, after considering all these testing methods and their advantages and disadvantages within the limits of existing test equipment available at the CONCAVE research center, it was decided to setup a non-contacting optical test method. This approach is relatively simple both in terms of equipment types and experimental set up considerations. Also, as it is a non-contacting sensing method the MEMS structures will not be *overly* subjected to handling and other contact forces which could lead to the damage of MEMS chips. Hence, in this regard, non-contact measurement methods can be used quite easily. The excitation and sensing mechanisms are both done in a manner not requiring any direct contact with the MEMS structure. Interferometry, for example, measures the deflections of microcantilever beams by noting the changes to an optically induced fringe pattern before and after the deflection. A monochromatic light source with good reflection characteristics with regards to silicon is generally used and is incorporated onto a Michelson interferometer platform and the deflections are induced through an electrostatic excitation mechanism [102]. The main limitations to the non-contact optical detection methods are the optical alignment of the light source, optics, and microdevice. The scattered light can also pose a problem if it impinges upon secondary structures

resulting in the optical detector analyzing and interpreting multiple signals from various structures.

4.3. LASER DOPPLER VELOCIMETRY (LDV)

The laser Doppler velocimetry approach is especially suitable for microsystems because of the size issues discussed previously. This method measures surface velocity either at a localized point or across a plane defined by a laser light sheet. The configuration adopted here can only measure single point velocities where the out-of-plane motions of the microdevice are detected through the changes in surface velocities as the device is subjected to some base excitations. In this method, a Helium-Neon (HeNe 632.8nm wavelength) laser is used as the light source. The light reflected back from the surface goes through a shift in frequency by an amount proportional to the velocity of the surface. This concept is illustrated in Figure 4.1.
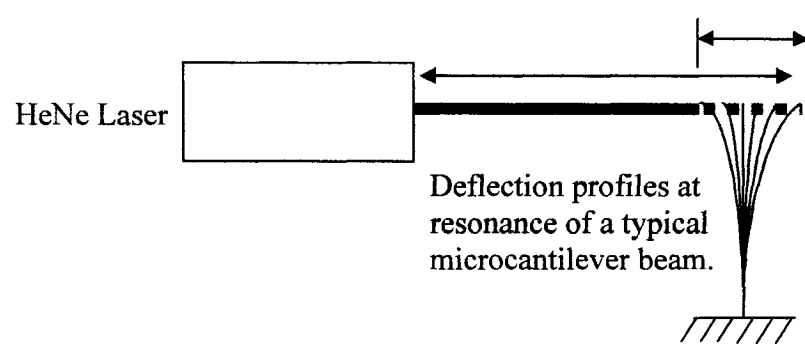
Figure 4.1. This is a typical microcantilever deflection at resonance, and the LDV method to determine the natural frequency. Changes in the beam position with respect to the laser induce a phase shift between the input and output signals.

An LDV detects the Doppler shift, induced by the vibrating surface, of the laser light that is scattered from a small area of the MEMS device. The vibrating MEMS device back scatters light from the laser beam and the Doppler frequency shift is used to measure the surface velocity which lies along the axis of the laser beam. In certain LDV measurement systems a Bragg cell serves to shift the light frequency of the incident laser beam in order to demodulate the frequency of the laser light [246]. The LDV system used for these experiments had a rotating disc in place of the Bragg cell [25] where the optical laser frequency was shifted by 3.456MHz.

4.3.1. *Demodulation of the laser signal*

As laser light has a very high frequency ($\sim 4.74 \times 10^{14}$ Hz), a direct demodulation of the light is not possible. Hence, an optical interferometer is used to mix or *heterodyne* the scattered light with a reference beam of a given reference frequency that is determined by the frequency shift due to the rotational velocity of the disc. In this setup two frequency shifts were possible, 3.456MHz and 0.922MHz, for high and low frequency measurements, respectively. Hence, in this regard the 3.456MHz frequency *replaces* the high optical frequency of the laser source through the heterodyne process. The term heterodyne means to generate new frequencies by mixing two or more signals in a nonlinear device such as a photodiode. The mixing of each pair of frequencies results in the creation of two new frequencies termed *beat* frequencies, of which one is the sum of the two frequencies mixed, and the other their difference. The detection setup used in

these experiments makes use of the frequency difference, $|f_{Laser}-f_{Laser+Disc}|$ for signal demodulation purposes where $f_{Laser+Disc}$ is the frequency shifted laser light.

The frequency modulated signal is a function of the direction of motion of the surface under investigation. For each vibrational cycle the surface motion is zero at two positions of the vibrating microcantilever, hence in order to maintain a signal response at the photodiode the beat frequency, $f_{Disc} = |f_{Laser}-f_{Laser+Disc}|$, output is used for calibrating the 0 voltage level corresponding to these two positions. This principle is shown in Figure 4.2. The photodiode measures the Doppler frequency shift caused by the vibrating microdevice and outputs a voltage signal proportional to the surface velocity of the device.
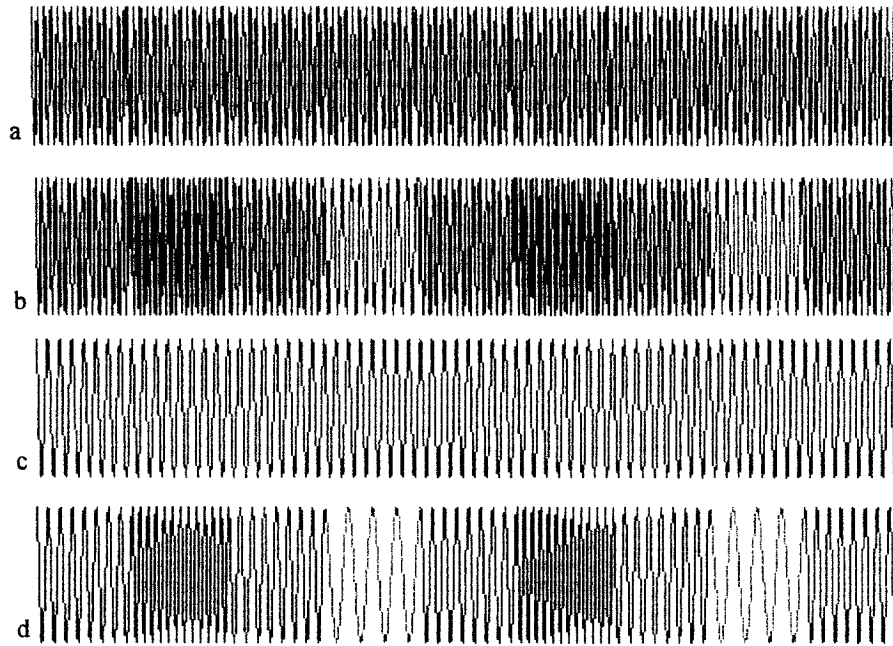
Figure 4.2. Examples of: a) High frequency profile of laser. b) High frequency laser and vibrational response profile. c) Beat frequency, f_{Disc}. d) Beat frequency and vibrational response profile.

As the microcantilever vibrates it repeatedly moves towards and away from the light source as shown in Figure 4.1 above. In this respect the beat frequency is modulated by the back and forth motions of the surface. This results in an increase and decrease in the beat frequency for *to and fro* motions respectively. This is illustrated in Figure 4.3. An overview of the internal optical setup is given in Figure 4.4.
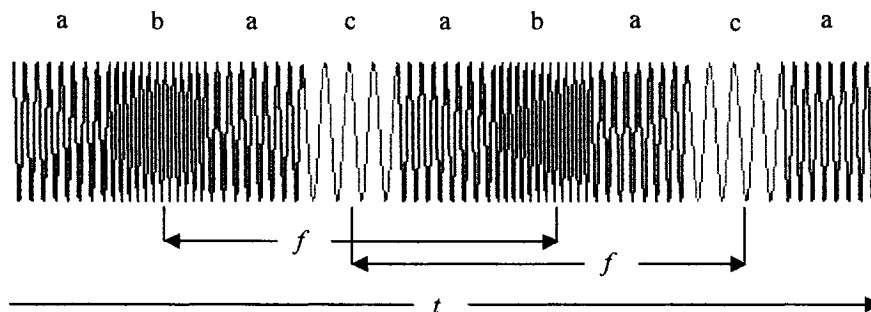
Figure 4.3. The vibrational frequency, *f*, is obtained from the demodulated beat frequency. a) Beat frequency. b) Beat frequency plus Doppler *to* motion. c) Beat frequency minus Doppler *fro* motion.
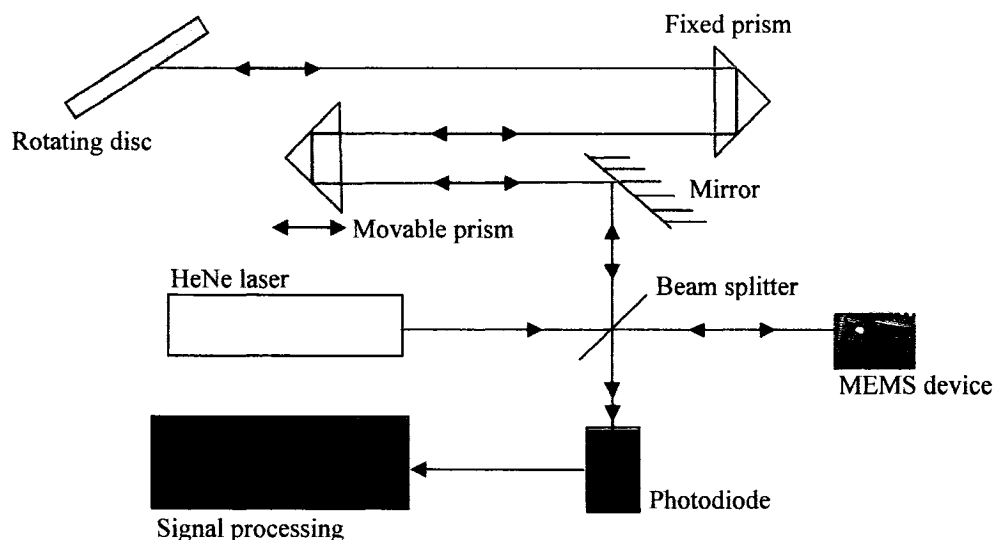
Figure 4.4. A schematic representation of the LDV measuring mechanism using a Michelson (heterodyne) interferometer arrangement.

4.4. TEST SETUP AND PROCEDURE

The experimental setup consisted of a commercially available Brüel & Kjær [25] LDV with HeNe laser and photodiode detector. The nominal beam diameter, as specified by the manufacturer, of the laser at the output is $\approx$ 1mm. The signal detection system consisted of an oscilloscope for the time-domain reference, and a spectrum analyzer for the frequency domain. All the microstructures tested were mounted onto a flat surface for ease of manipulation. The vibration frequency detection limits of the available equipment had an upper limit of $\approx$ 25kHz. Shown in Figure 4.5 is an overview of the optical work bench and experimental setup.
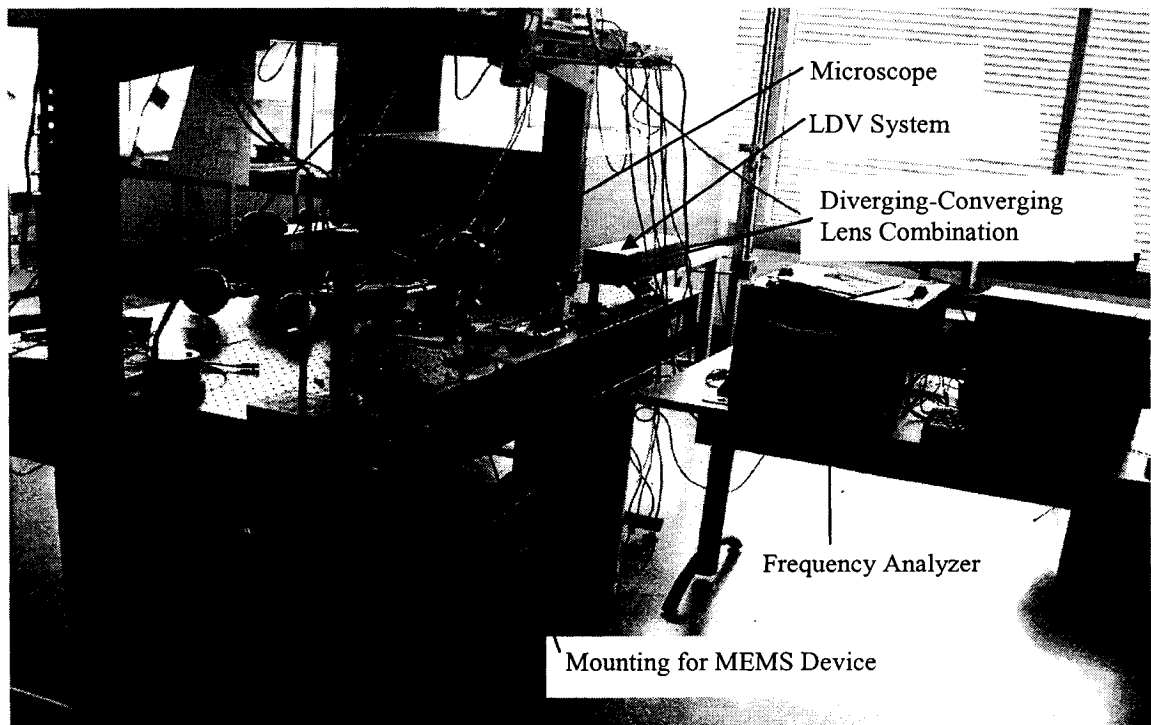
Figure 4.5. The optical bench and test equipment used in the experiments.

Given that the laser beam diameter (1mm) was too large to be used on microscale structures, a diverging-converging lens configuration was used in order to reduce the beam diameter and focus the laser beam onto the microstructure. Different laser spot sizes may be obtained by varying the distance between the lenses in order to test devices of different dimensions [209, 211]. Shown Figure 4.6 is the lens train used in these experiments.

The equipment that was employed for properly focusing the beam consisted of an oscilloscope/frequency analyzer, and micro-positioners. The micro-positioners were used for *fine-tuning* the diverging-converging lenses to optimal positions [151]. By employing this combination of lens separation, oscilloscope signal, and micro-positioners, any desired well focused laser spot size can be achieved.
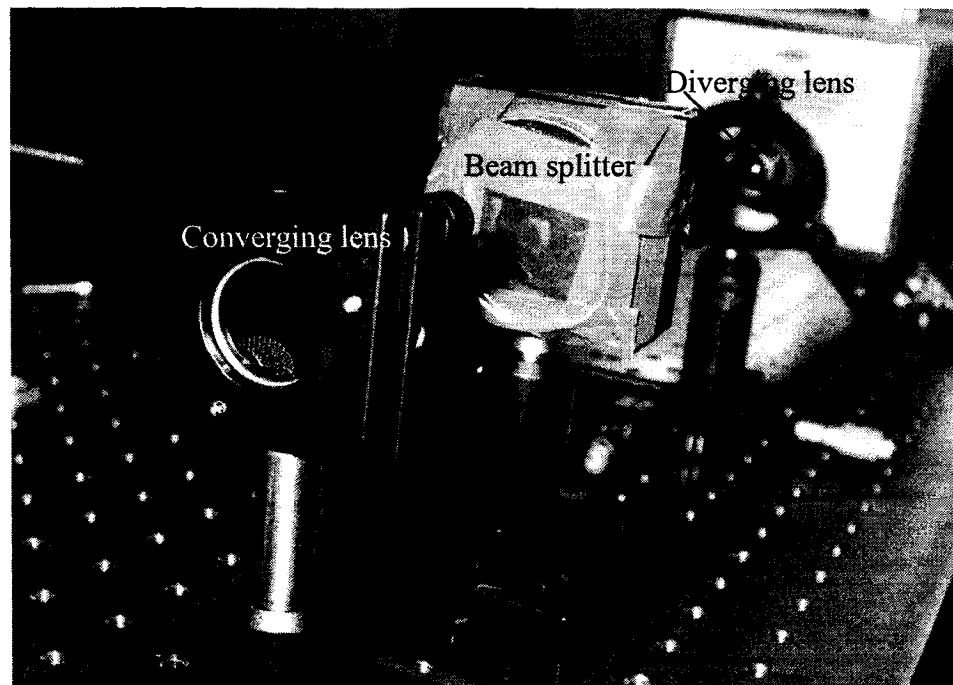
Figure 4.6. The lens train consisting of a diverging-converging lens combination.

A note of caution regarding the laser spot, as the laser beam diameter is reduced the luminous intensity of the beam increases dramatically [151]. In order to reduce the intensity at the detector and to prevent overloading a filter attenuator is positioned between the two lenses (Figure 4.6). Given in Figure 4.7 is a schematic showing the two lenses physical characteristics.

$\phi_L = 21$mm
$f_{L1} = -40$mm

$\phi_L = 25$mm
$f_{L2} = 200$mm
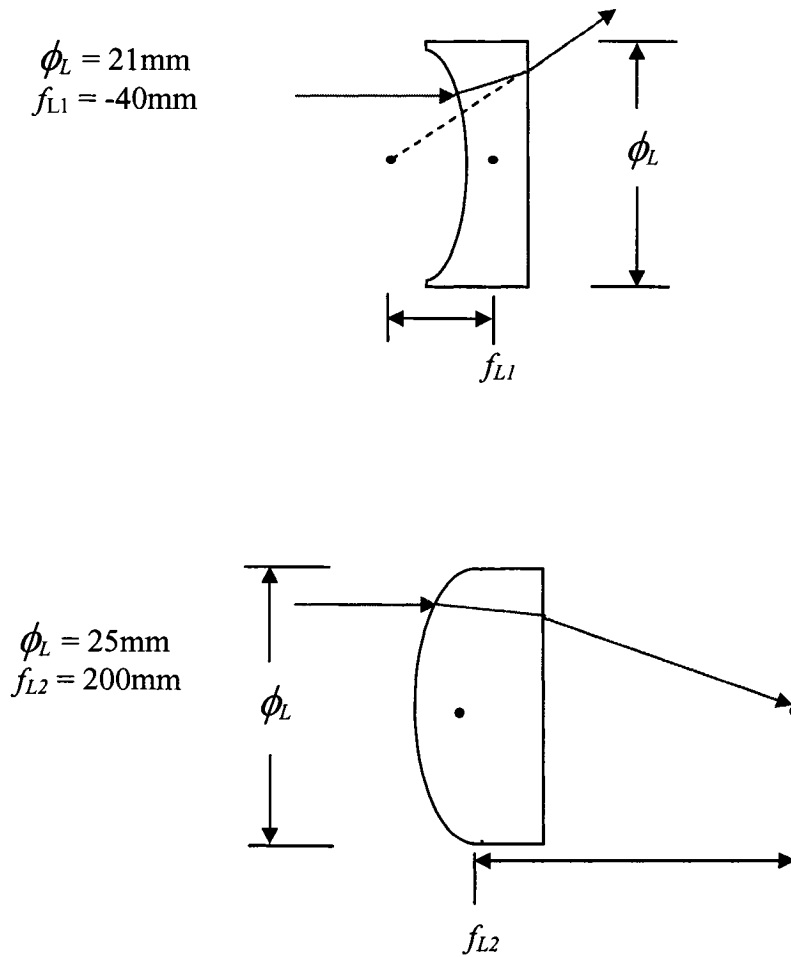
Figure 4.7. The physical characteristics of the laser beam focusing lenses used in the experiments.
Top: Diverging lens ($L1$). Bottom: Converging lens ($L2$).

Some sample calculations for the spot sizes on the converging lens, *L2*, and on the MEMS chip are given here [151]. For a given diverging-converging lens separation $L_{D\text{-}C}$, the spot size, ϕ_{L2}, on *L2*

$$\phi_{L2} = 2\arctan(\theta_{L1})L_{D\text{-}C}$$

(4.1)

Where the following definition applies,

$$\theta_{L1} = \frac{\dfrac{\phi_{Laser}}{2}}{f_{L1}}$$

(4.1a)

ϕ_{Laser} is the laser beam diameter at the output (taken as 1mm [25]), and θ_{L1} is the minimum angular divergence of *L1*.

The spot size on the MEMS surface, ϕ_{MEMS}, is calculated from,

$$\phi_{MEMS} = \frac{4\lambda_{Laser}f_{L2}}{\pi(\phi_{L2})}$$

(4.2)

The results obtained are presented in Figure 4.8.
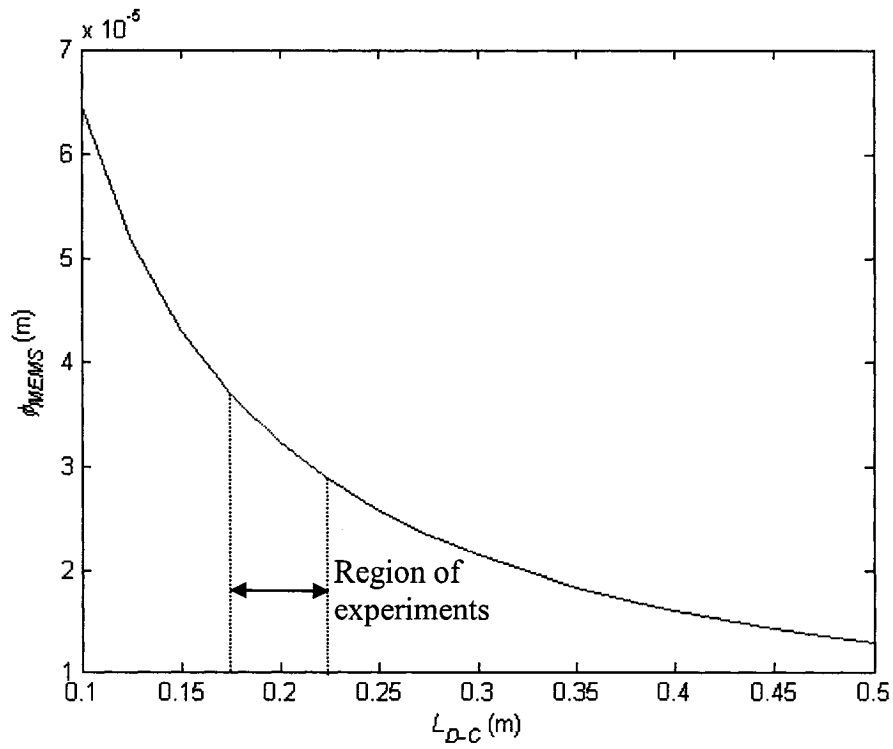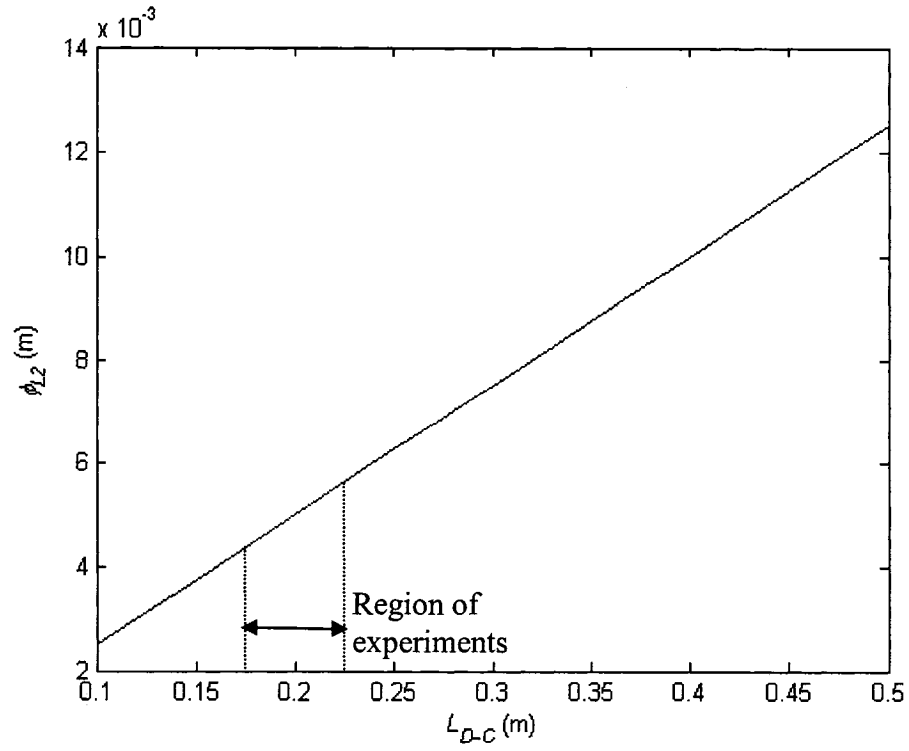
Figure 4.8. Top: Laser spot size on the converging lens, *L2*, as a function of the lens separation. Bottom: Laser spot size on the MEMS surface as a function of the lens separation.

111

The marked portion of the curves presented in Figure 4.8, indicate the nominal lens separation used in the experiments carried out for this work. Some sample values are given Table 4.1.

Table 4.1. Some sample values of the laser spot sizes on *L2* and the MEMS surface for the nominal lens separations used in these experiments.

$L_{D\text{-}C}$ (cm)	ϕ_{L2} (mm)	ϕ_{MEMS} (μm)
15.0	3.75	43.0
17.5	4.37	36.8
20.0	4.99	32.2
22.5	5.62	28.6
25.0	6.25	25.8

By careful analysis and cross-referencing of the time domain and frequency domain to a single frequency signal allowed for proper optical alignment to be used for microscale devices. Shown in Figure 4.9 is a microscope image of several AFM chips with the focused laser spot.
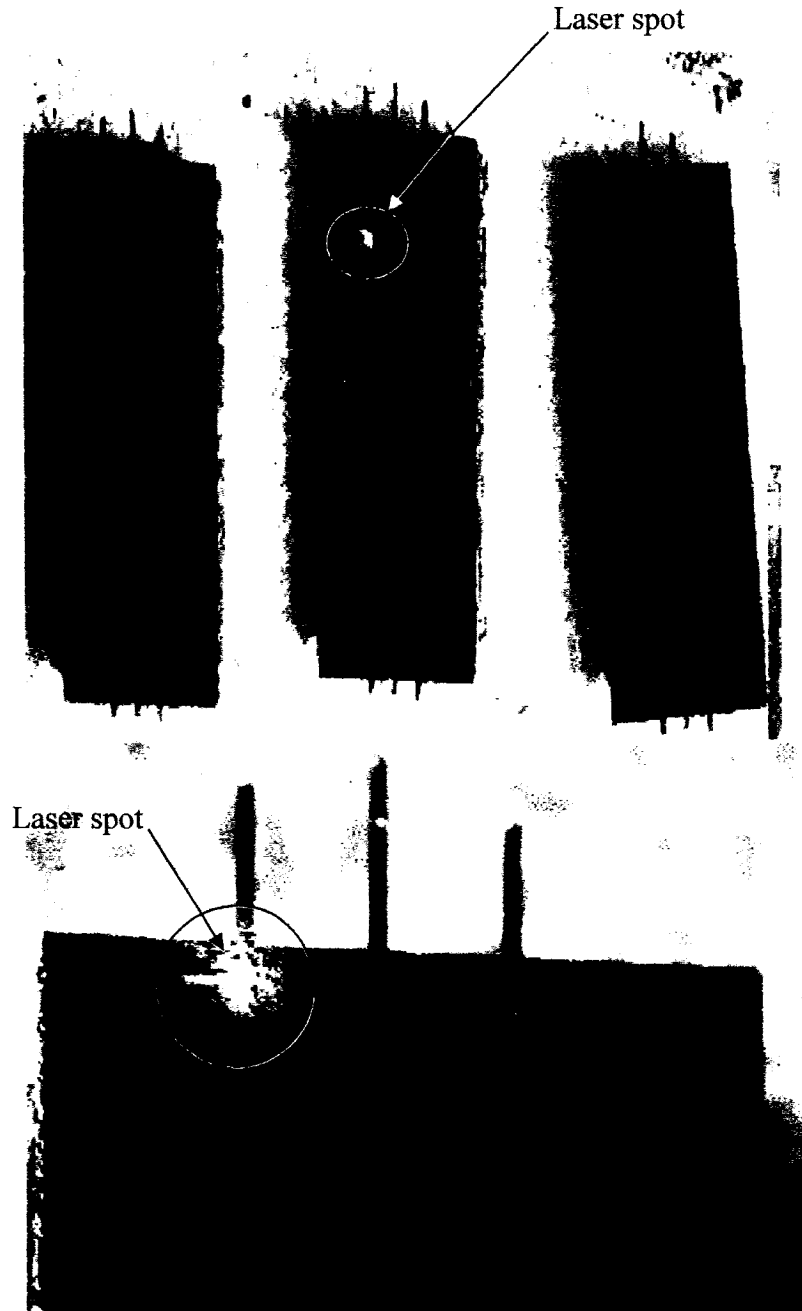
Figure 4.9. Top: A microscope image of several AFM chips with the laser spot on the central one. Bottom: Microscope image showing the laser spot as it approaches one of the microcantilevers. The nominal microcantilever width is 35 microns.

4.4.1. *Experimental setup details*

The HeNe laser was mounted onto a fixed immovable platform. The offset height of the laser housing from the optical table was done so that there would be a degree of motional freedom in the vertical direction in order to properly mount and align the other devices. Initial tests on the limiting detectable range of the laser showed distances in excess of 5 meters (for reflective tape) which was well within the laser-device distances used in these experiments (< 0.3 meter). All the other equipment used for the experimenting was aligned and mounted with respect to the laser position. Each lens was mounted onto individual XY micro-positioners. Here, the XY directions refer to motions along the laser beam axis, and radially outwards, respectively. The bi-directionality of these platforms enabled and facilitated the fine-tuning of the lens positions for signal optimization.

Initial, rough lens positions (with respect to the HeNe laser, and also with respect to each other) were determined by first impinging the laser light onto a piece of reflective tape on a wall 1.5 meters away. A circle of ~2 cm diameter was drawn around the laser spot. Then the diverging lens was inserted into the optical path of the laser beam and adjusted so that the laser spot was still centered on the 2 cm diameter circle. Similarly, the converging lens was inserted into the optical path, with the diverging lens still in place, and also adjusted so that the spot remained centered on the 2 cm diameter circle. Planarity or parallelism of the lenses with respect to each other and, orthogonality with respect to laser beam propagation axis, was determined through a single frequency signal

114

processing and optimization carried out by varying the XY positioner of the respective lens, and by carefully rotating the lenses to optimal positions as determined by the signal response. The beam shaping and orientation with regard to the lenses in the outbound and inbound directions is shown in Figure 4.10.
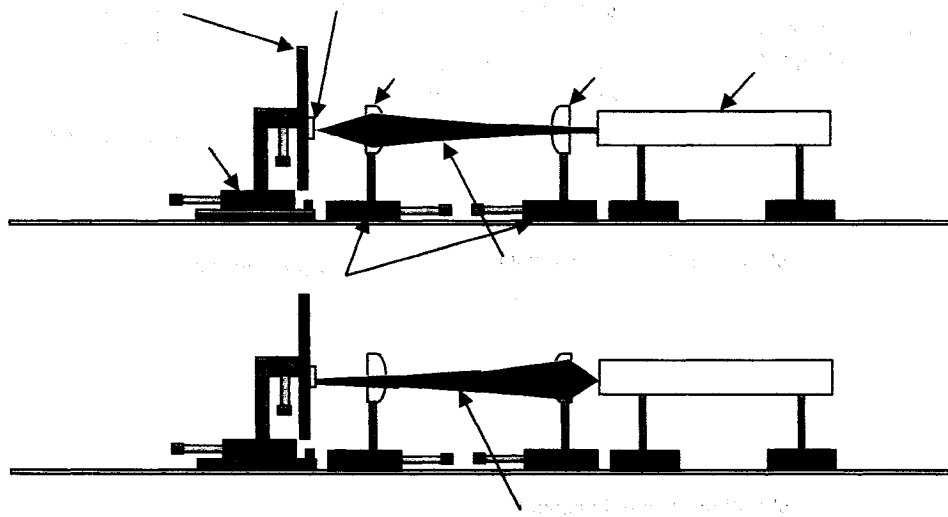
Figure 4.10. A schematic representation of the laser beam profiles.
Top: Outward bound. Bottom: Inward bound with respect to the laser.

As the laser mounting rendered the laser immovable, the MEMS devices were mounted onto a rotational platform for angular alignments and to a pivoting support for pitch control, and the whole fastened onto a XYZ micro-positioner, where the X direction corresponds to the laser beam propagation direction and the Z direction corresponds to radially up/down motions with respect to the laser beam. This allowed the laser beam to be incident on any position on the MEMS device by selectively varying the YZ

positioners. The third directional positioner X, of this platform, allowed for initial tuning of the laser beam (changing laser-device distance while keeping lens positions fixed). The rotational platform was used to maintain the device plane orthogonal to the X direction. The correct directional alignments, rotational and pitch, were obtained by careful monitoring of the output time domain signal to a single frequency input signal, and were done to ensure that the reflected laser beam from the micro device was reflected back to the detector. An overview of the experimental setup and test equipment is shown in Figure 4.11.
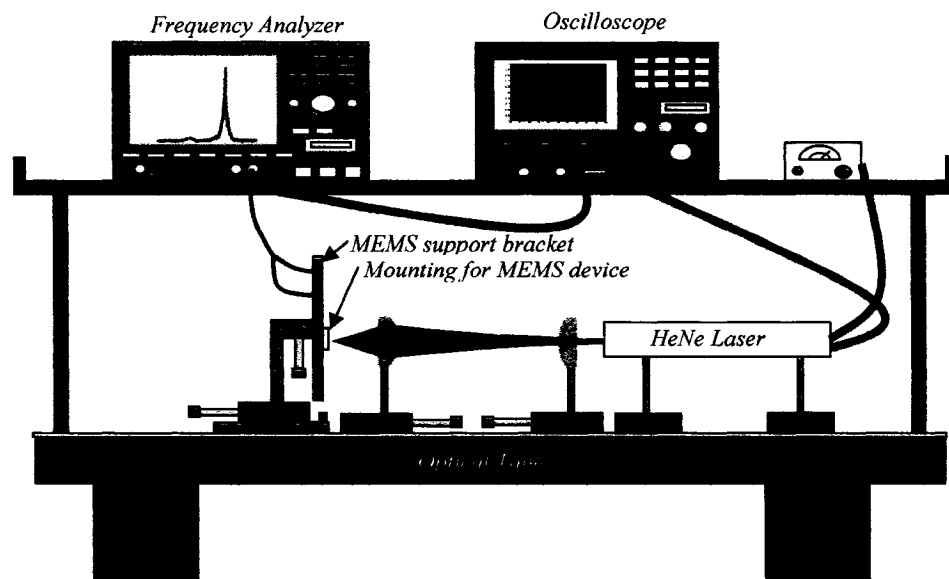
Figure 4.11. Laser based optical test setup developed for the testing of microscale structures.

4.4.2. *Excitation mechanisms*

The microstructures are excited electrostatically by an incorporated electrode assembly and mechanically by shaking with an audio speaker. The electrostatic excitation consisted of a capacitive arrangement where a DC voltage was applied in order to obtain microcantilever static deflections. A swept frequency low amplitude sinusoidal AC voltage was applied to obtain a frequency response of the microcantilever. The mechanical excitation required that the MEMS microcantilever be mounted onto a flat-faced audio speaker. The speaker was used as a mechanical shaker when a sinusoidal swept frequency was applied. No static deflections were possible with the mechanical excitation mechanism.

In the course of the experiments carried out, no appreciable differences were observed in the frequency response of a given MEMS device using either of these two excitation mechanisms. The only differences were in the mounting of the MEMS devices for one or other test setup as the speaker required slightly more clearance from the optical bench than the support for the electrostatic excitation. Also, the speaker employed did not maintain uniform amplitude across the frequency sweep, whereas the electrostatic excitation showed uniform signal amplitude across the entire swept frequency range. Shown in Figure 4.12 is the mechanical excitation mechanism.
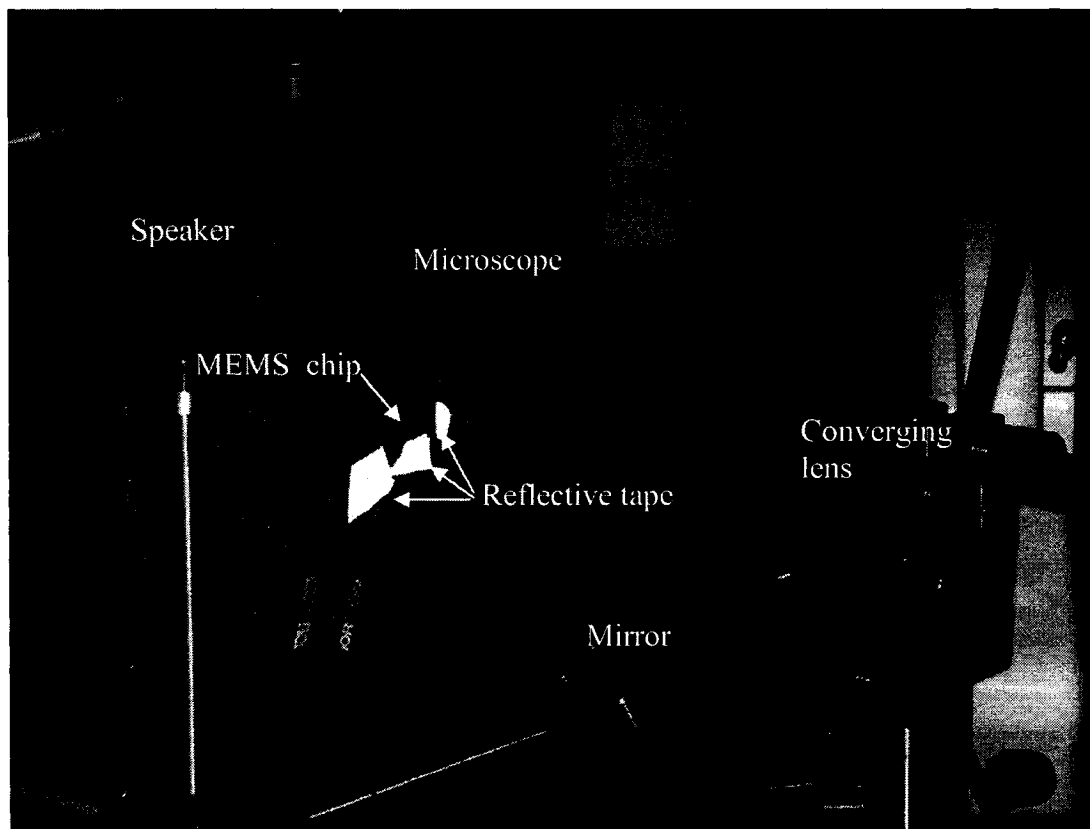
Figure 4.12. A close up image of the flat-faced audio speaker. This type of speaker was selected for the ease of mounting the test structures. The bright regions visible are the highly reflective tape used in the preliminary stages of the experimental set-up and testing.

Shown in Figure 4.13 is the mounting for the electrostatic excitation. Shown in Figure 4.14 is a schematic of the electrostatic excitation mechanism.
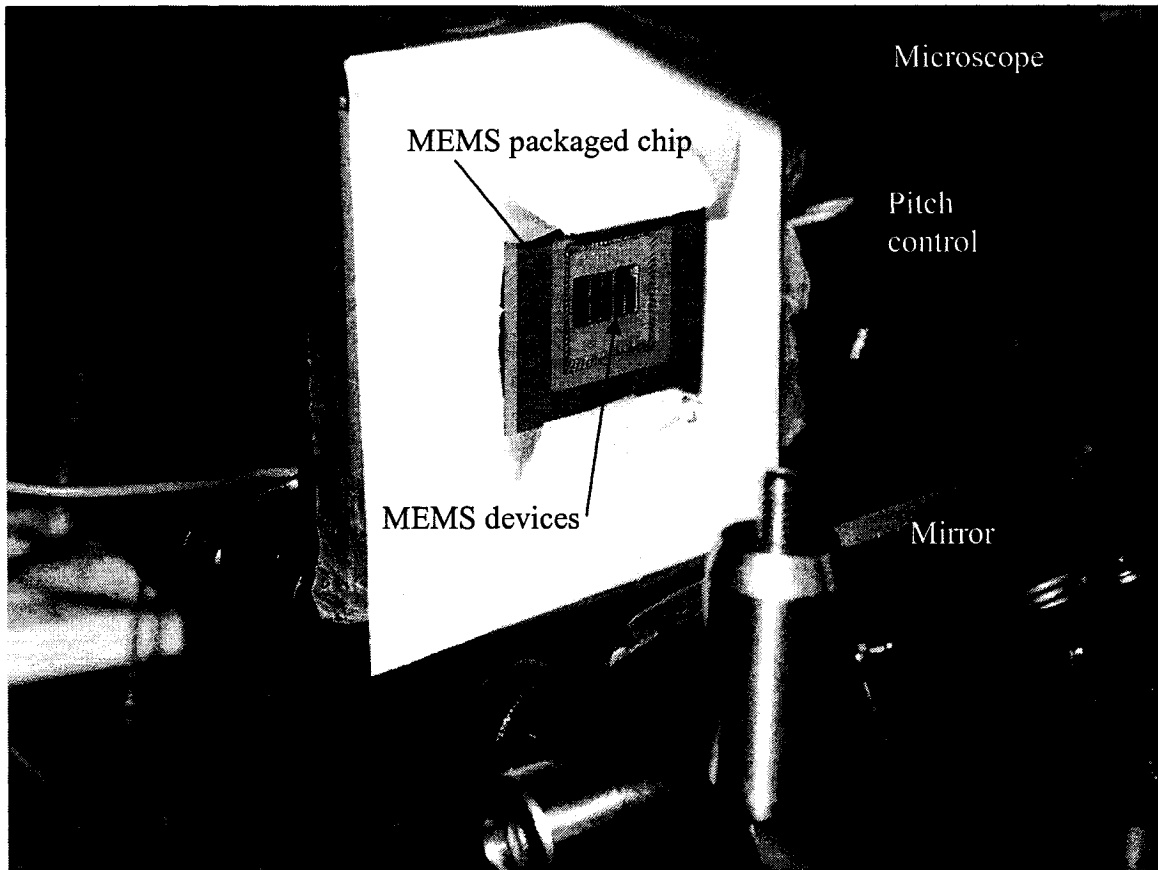
Figure 4.13. The support stand used for the electrostatic excitation of the MEMS devices.
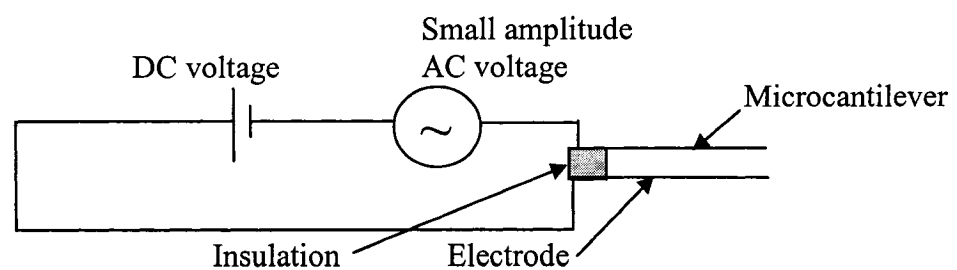
Figure 4.14. Schematic representation for the electrostatic frequency response analysis of a microcantilever.

119

The electrostatic DC voltage static deflections were measured under an optical microscope with a 1000 magnification factor. Given in Figure 4.15 is an overview of the DC static deflection experimental set-up.
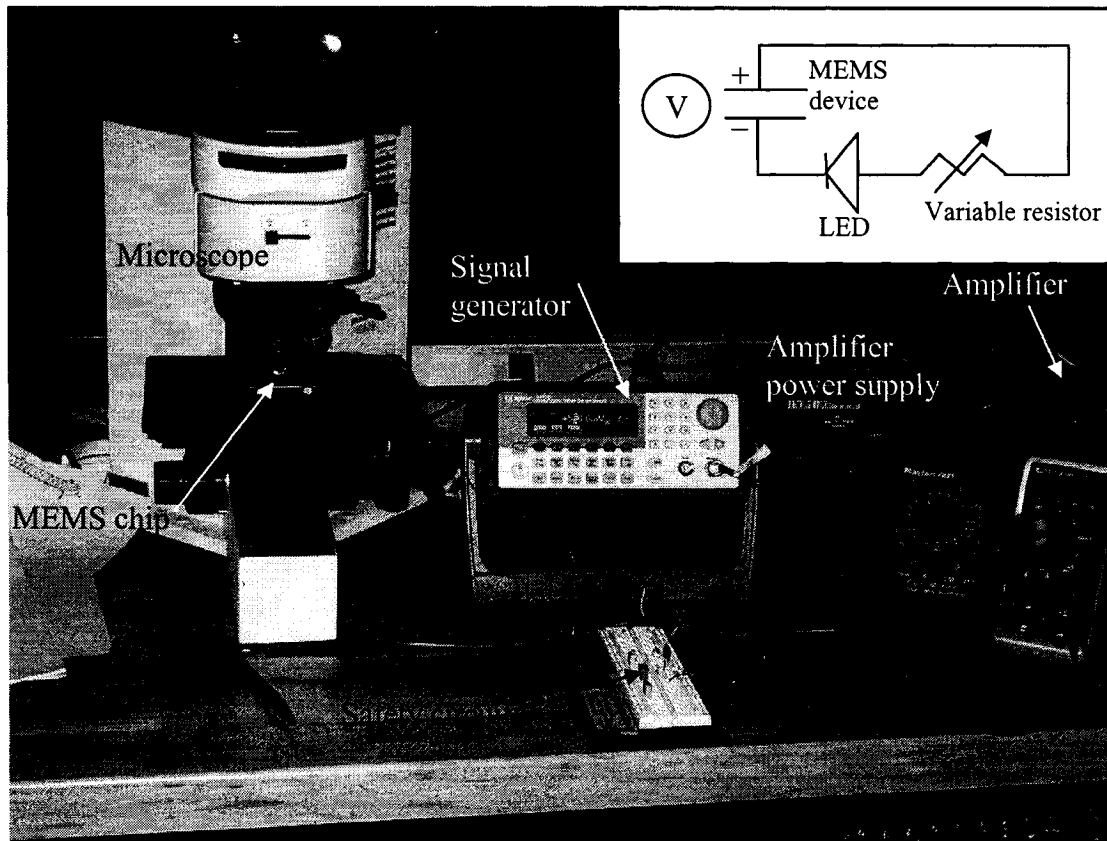
Figure 4.15. An overview of the experimental setup and equipment used for DC static deflections. Inset: A schematic of the safety circuit used to minimize the current in the event of touchdown.

The safety circuit as shown in Figure 4.15 above was included in the electrical circuit shown in Figure 4.14 in order to prevent destruction of the MEMS device in case of short circuiting due to touch down. The safety circuit is illustrated in Figures 4.16-4.17 below and was inserted in parallel with the MEMS chip as a current absorber in the event of touchdown in the microstructure.
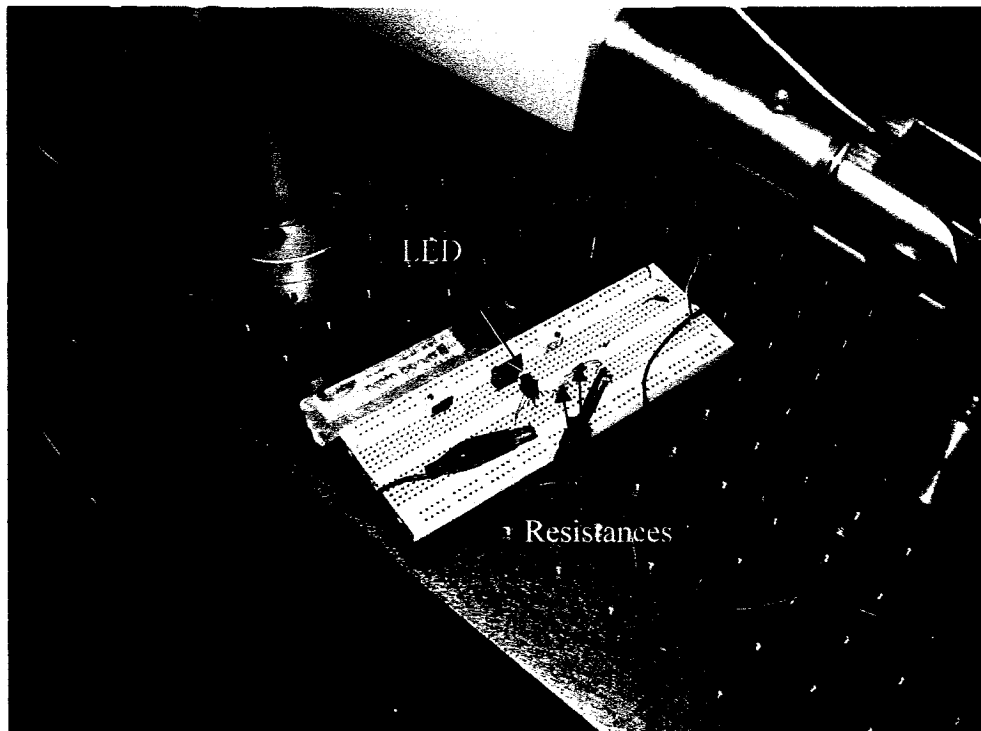
Figure 4.16. An overview of the safety circuit employed in the DC static deflection experiments. It consists of an LED and two megaohm resistances in series.

Figure 4.17. Touchdown! The LED is on, hence current flows through the circuit.

121

The consequences of having one of the microcantilevers touchdown during a DC voltage static deflection testing are quite dramatic. Shown in Figure 4.18 is an SEM image of a MicraGeM [49] technology microcantilever after touchdown.
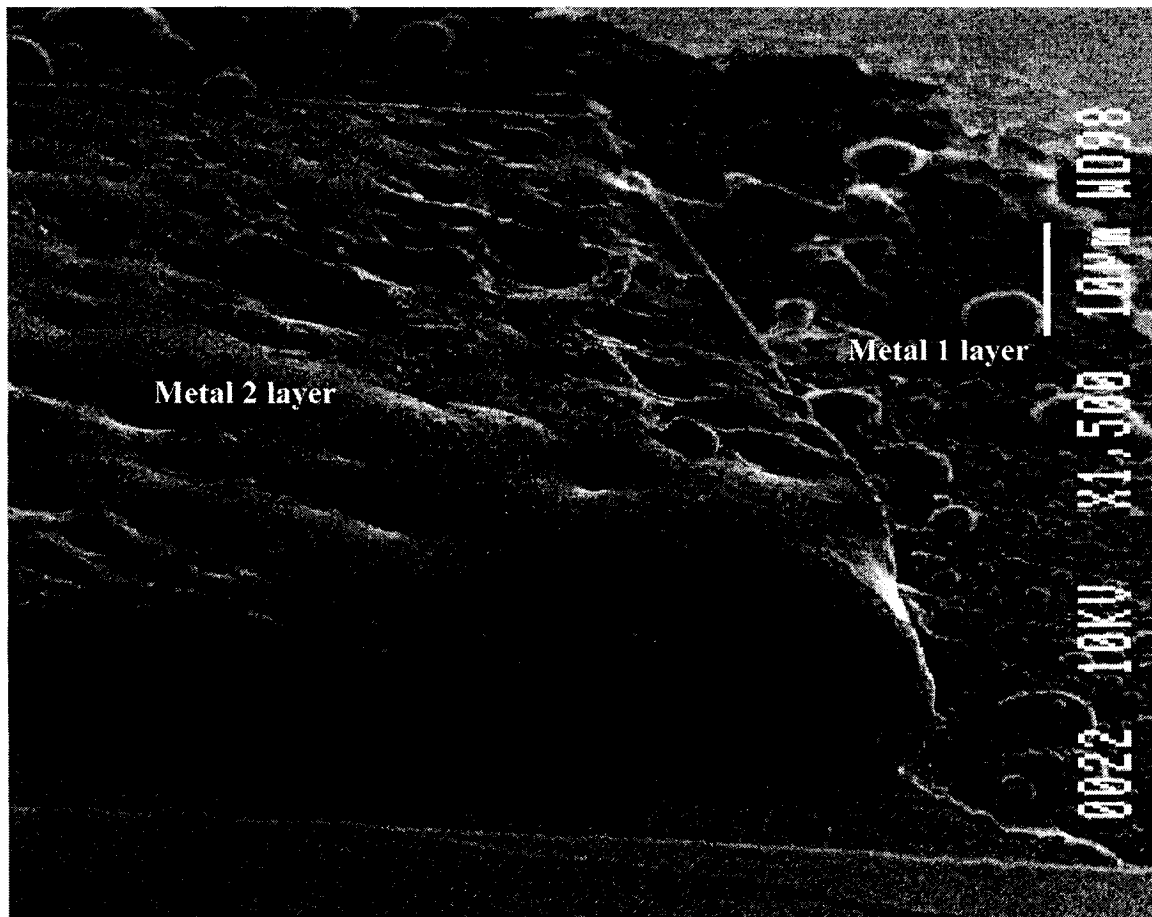
Figure 4.18. The consequences of electrostatic touchdown on a MicraGeM technology microcantilever. The metal 1 and metal 2 layers have melted due to the intense heat generated.

4.4.3. *Frequency response extraction*

The method to determine the resonance frequency of each microcantilever consisted of the following steps. Step one, once the microstructure was securely fastened onto the support, the laser beam was focused onto the substrate and a frequency response of the substrate was obtained by sweeping the input excitation of 0-25kHz with 2.5V amplitude. Step two, the laser spot was then focused onto one of the microcantilevers and swept with a 0-25kHz, 2.5V amplitude signal. In step three, the microcantilever response was deduced using the base response. Hence the resulting spectrum contained only the cantilever resonance(s). In this manner, the resonance frequency of each cantilever was determined. This is shown in Figures 4.19-4.21 for an AFM chip and AFM microcantilevers.
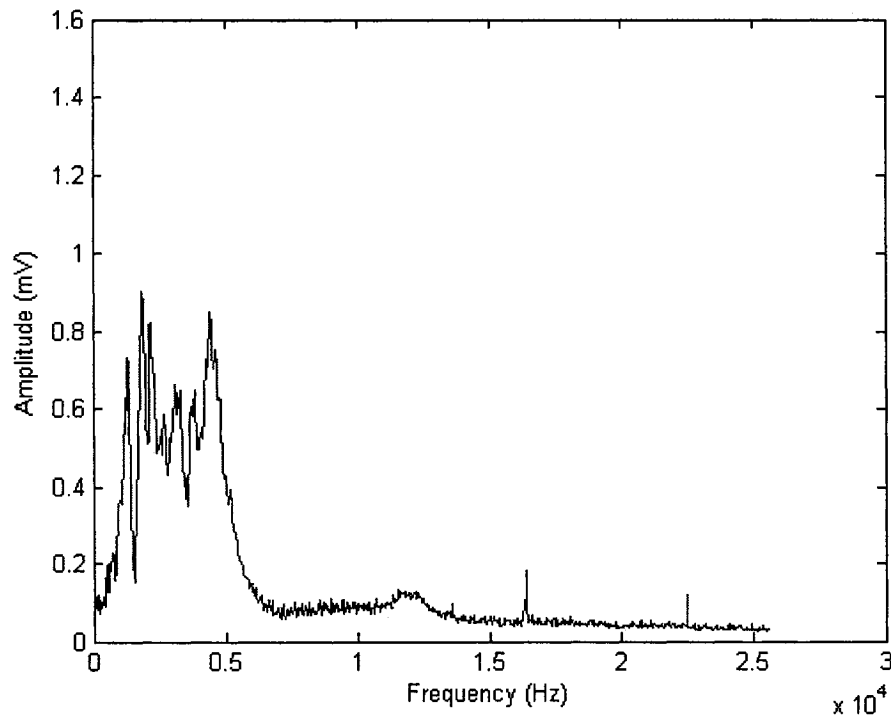
Figure 4.19. Frequency response of the AFM chip substrate generated by a base excitation sweep from 100 Hz to 25 kHz.
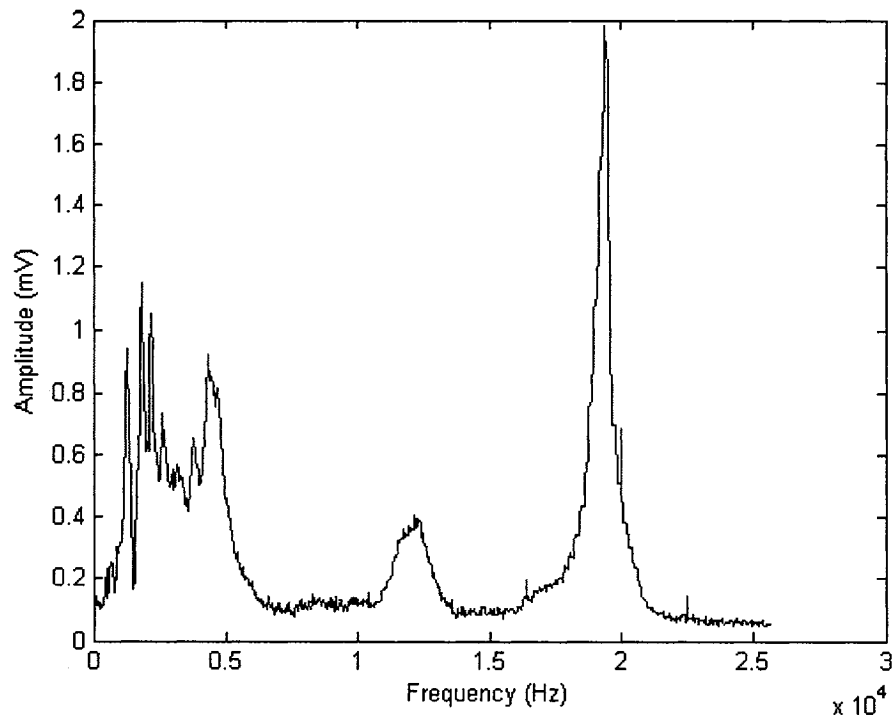
Figure 4.20. The frequency response of the AFM chip and AFM microcantilever.

The AFM microcantilever tested has $L = 353\mu m$, $h = 1.8\mu m$ and $w = 34.5\mu m$ as measured with an optical microscope.
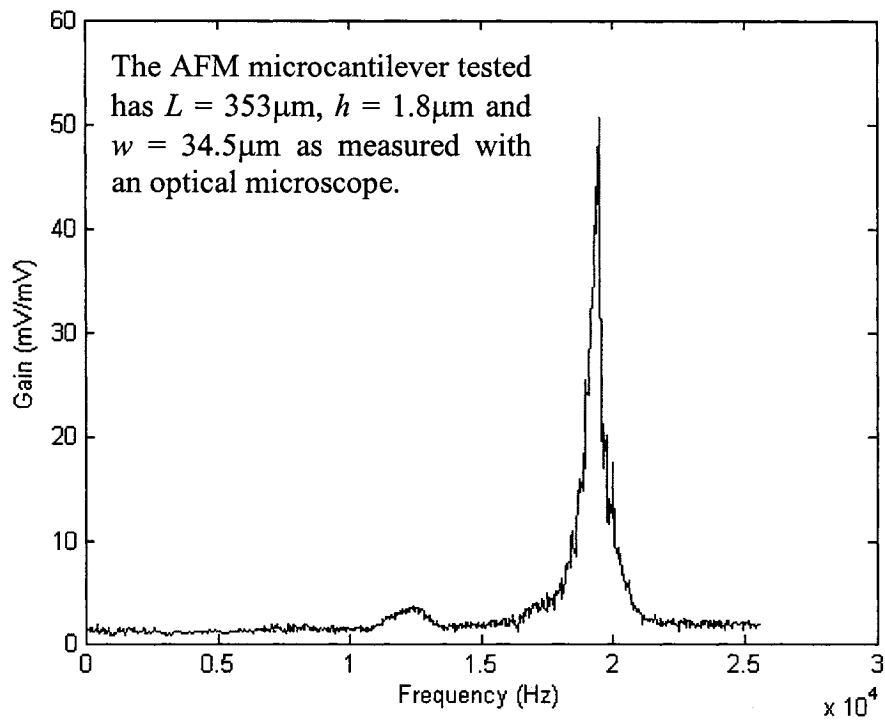
Figure 4.21. The *pure* AFM *Type 'B'* microcantilever resonance after extraction from the global chip substrate response.

4.4.4. Sample test results

The frequency responses shown in Figures 4.19-4.21 were obtained through swept harmonic excitation using the audio speaker. When using his method it is necessary to eliminate the response of the substrate from the final frequency response profile because the mechanical shaking is applied to the entire MEMS chip. On the other hand, for electrostatic excitation no subtraction of the substrate is necessary as only the MEMS structure itself is being excited. Shown in Figures 4.22-4.24 are some sample test results obtained using the LDV system established at Concordia University's CONCAVE research center.
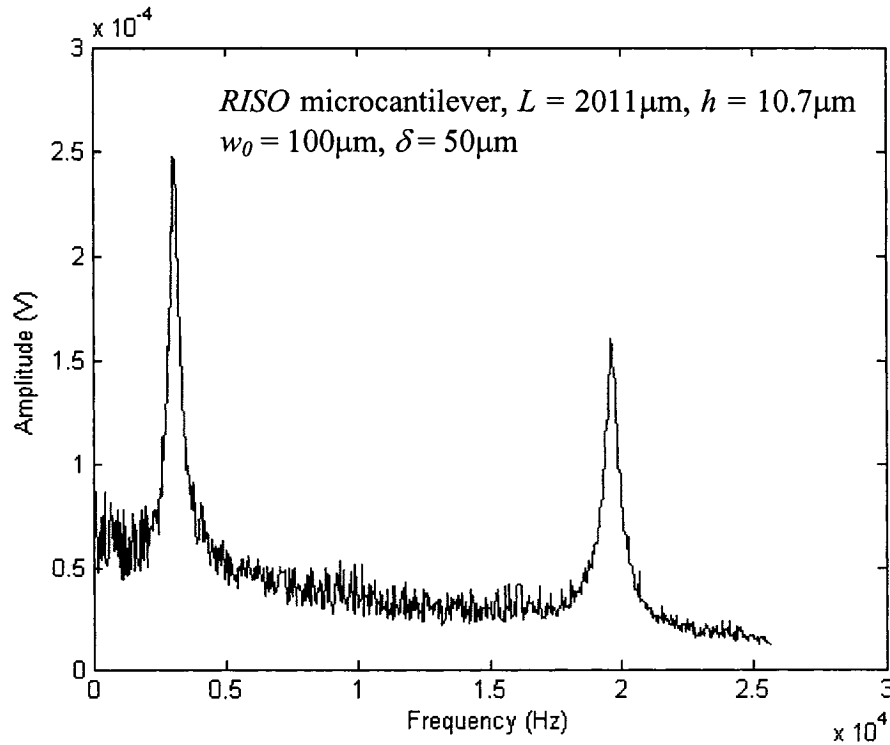
Figure 4.22. The frequency response of a MicraGeM technology microcantilever. Shown are the first and second resonance peaks.
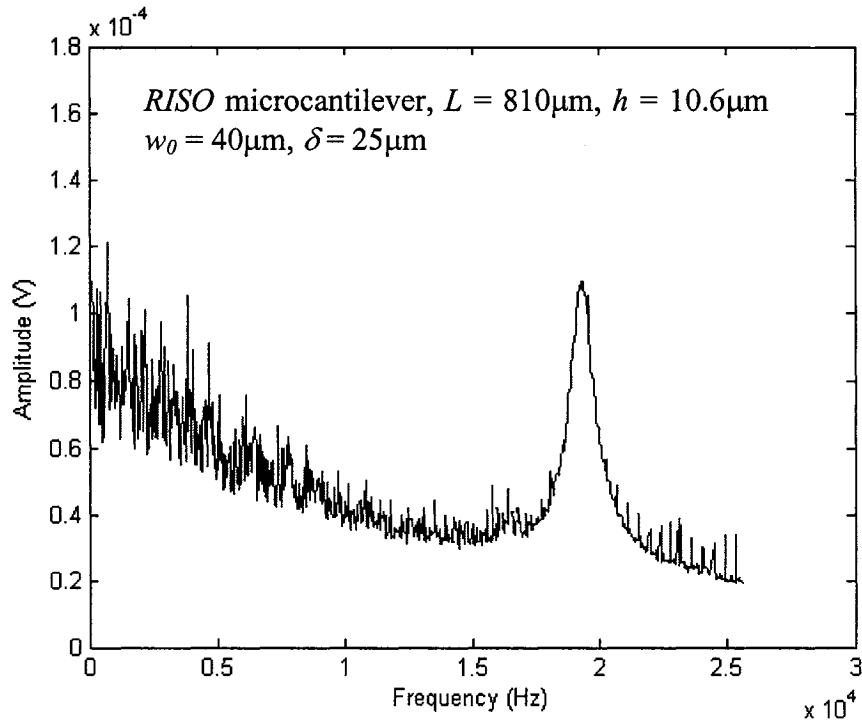
Figure 4.23. The frequency response of a MicraGeM technology microcantilever.
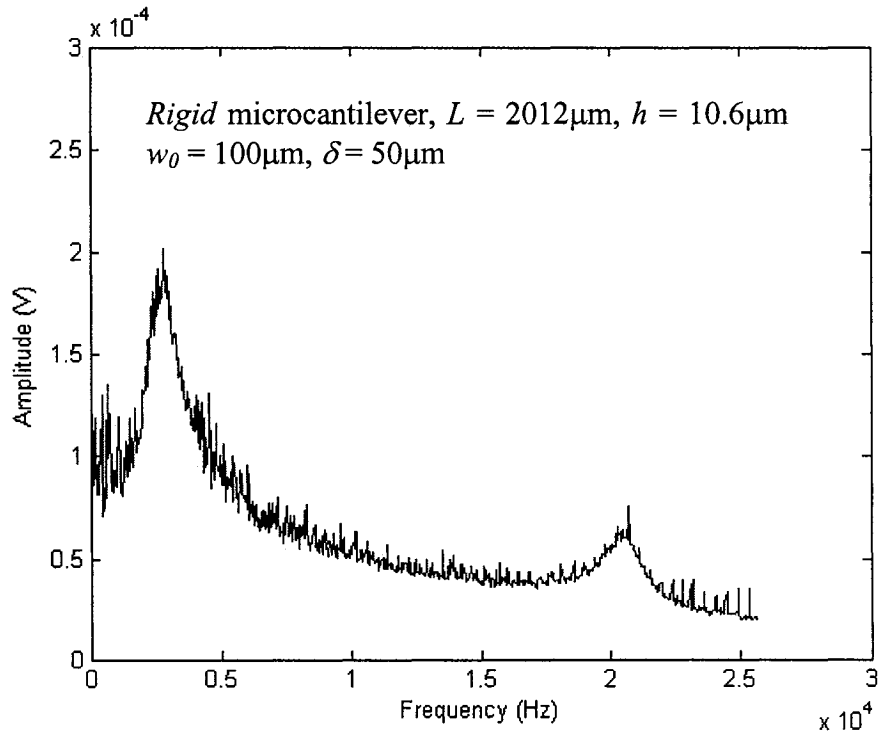
Figure 4.24. The frequency response of a MicraGeM technology microcantilever. Shown are the first and second resonance peaks.

126

4.5. SUMMARY

The testing carried out required that a test setup, using simple test equipment, be established first. This was achieved by using equipment [25] already available at the CONCAVE research center. Once in place the aim of this work was to carry out static and dynamic testing on several different microscale structures. The HeNe laser beam diameter was reduced to a size that would be convenient for measuring the dynamics of microscale devices such as AFM [153] probes, MicraGeM [152] technology, and MUMPs [49] technology microcantilevers by the LDV test method [209, 211]. This was achieved by a combination of a diverging-converging lens combination. Excellent signal-to-noise ratios were obtained by optimizing the lens separations for given devices, and the two excitation mechanisms, mechanical and electrical, showed equally good results. The dynamic response signal was very sensitive to the proper alignment of all the optical components. The rotational platform and pitch control mechanism allowed one to properly orient the MEMS device for testing, and the dynamic testing allowed for the extraction of two resonance frequencies for certain structures, while the static testing, carried out under an optical microscope, measured the tip deflection of the microcantilever as a function of the applied voltage and incorporated a safety circuit to prevent short circuiting and destruction of the MEMS device in case of touchdown. The sample tests carried out on several different structures from varying silicon foundry processes show that the experimental setup is suitable for the static and dynamic testing of microfabricated, microscale, MEMS devices.

Chapter 5

SUPPORT BOUNDARY CHARACTERIZATION

Presented in this chapter is the experimental and theoretical boundary support characterization of AFM and MicraGeM technology microcantilevers. The experiments are done under thermal and electrostatic loading. Using this approach the boundary support condition is quantified with several different thermal and electrical load conditions. The Rayleigh-Ritz energy method, as given in Chapter 2, is used for the simulation.

5.1. INTRODUCTION

The development and integration of microsystems are very closely tied to current microfabrication processes and foundry tolerances and limitations. These microfabrication processes were built based on established silicon IC technology. During the initial period of MEMS development the devices required only simple geometries and were not meant to function in an electro-thermo-mechanical manner where geometry and material properties such as Young's modulus of elasticity influence the static and dynamic characteristics of the microsystem to a great extent [35, 64, 187, 232].

Conventional microfabrication processes limit the fabrication of devices of both low natural frequency and high natural frequency. Low resonance frequency planar devices

would have relatively large surface features leading to high residual stresses, making releasing of such devices difficult due to stiction. In the case of high natural frequency devices the process limitation stems from a decrease in the relative active area [95]. The inherent limitations of the micromachining processes have an influence on the boundary support condition of microstructures [175, 176, 177, 178, 179, 207]. As a result, the non-classical boundary support condition will alter the static and dynamic behaviour of the microstructure by changing the stiffness characteristics due to the end support-microcantilever interface. This problem is amplified as structures are further miniaturized [137].

Theoretical modeling and simulation is necessary so that a performance basis can be established for a particular micro-device. However, the performance characterization of a microsystem through mathematical formulations only is incomplete as it does not take into account the processes outside of the designer's control, such as microfabrication limitations. These processes can only be quantified through experimentation. Hence, the data provided by the testing will not only augment the theoretical model, but also provide feedback in understanding the effect of the micromachining process.

Presented here is the experimental investigation aimed at characterizing the support boundary conditions of micromachined devices through both thermo-mechanical and electro-mechanical testing. These *multiple* tests will provide a profile of the boundary support condition through the invariant rotational stiffness, K_R^* values at different thermal, and electrostatic loads, respectively.

5.2. THERMO-MECHANICAL BOUNDARY CHARACTERIZATION

In this investigation, the boundary characterization of MicraGeM 10μm technology microcantilevers provided in part by Micralyne Generalized MEMS Prototyping Technology and by the Canadian Microelectronics Corporation [42], and AFM microcantilevers probes provided by MikroMasch [153] by thermo-mechanical testing is presented [200]. Through the thermal loading, it is possible to test the same microcantilever under many different stress conditions, and hence, obtain an experimental profile of its dynamic characteristics [208]. The modeling of the microcantilever boundary support is carried out with artificial rotational and translational springs [175, 207], and the mathematical formulation is based on the Rayleigh-Ritz energy method from which the natural frequencies and virtual deflections are obtained [19]. With this approach the influences of the micro-manufacturing processes can be conditioned through the boundary support springs which can be quantified through the frequency response [134].

5.2.1. *Boundary conditioning*

A boundary conditioning approach is used to model and simulate non-classical boundary support conditions, due to microfabrication influences, on the dynamic response of microstructures [177]. In this method it is possible to vary the elastic properties of the microsystem through the boundary support conditions. Shown in Figure 5.1 is the conceptualized non-classical boundary support modeled with a translational spring, K_T,

and rotational spring K_R. ξ is the longitudinal coordinate, and L is the length of the microcantilever.
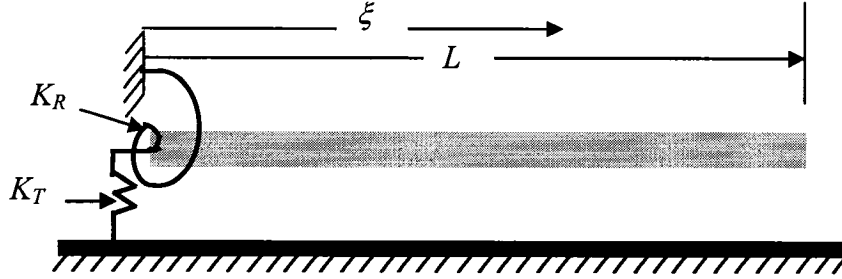
Figure 5.1. Representation of the microstructure with boundary support springs.

In the simulation analysis, the values of K_T and K_R can be varied in order to model a change in the support boundary condition from *Free* to *Clamped*. In the specific configuration of the beam there is no translational motion at the support, and thus, the support is modeled by applying changes to K_R only and maintaining a high K_T value, hence modeling only *Simply Supported* to *Clamped* support end conditions. With this approach it is possible to characterize boundary support conditions in microcantilever structures such as AFM probes. The Rayleigh-Ritz method can estimate the dynamic characteristics of the microcantilever for a given device geometry and rotational stiffness K_R. Shown in Figure 5.2 and Figure 5.3 are schematic representations and SEM images of the AFM boundary support.

The silicon-on-insulator (SOI) MicraGeM 10μm technology consists of anodically bonding an SOI wafer to an etched Pyrex glass substrate and then employing a DRIE etch

131

to pattern the single crystal silicon. The last fabrication step involves coating with a thin metal alloy layer for electrical conduction and reflective properties. Illustrated in Figure 5.4 is a set of SEM images showing the boundary support of an SOI microcantilever. In this process a certain amount of undercutting of the support structure occurred, however, it is not considered significant enough to cause substantial changes to the microfabricated boundary supports as is explained below. A schematic drawing of the undercutting is shown in Figure 5.5.
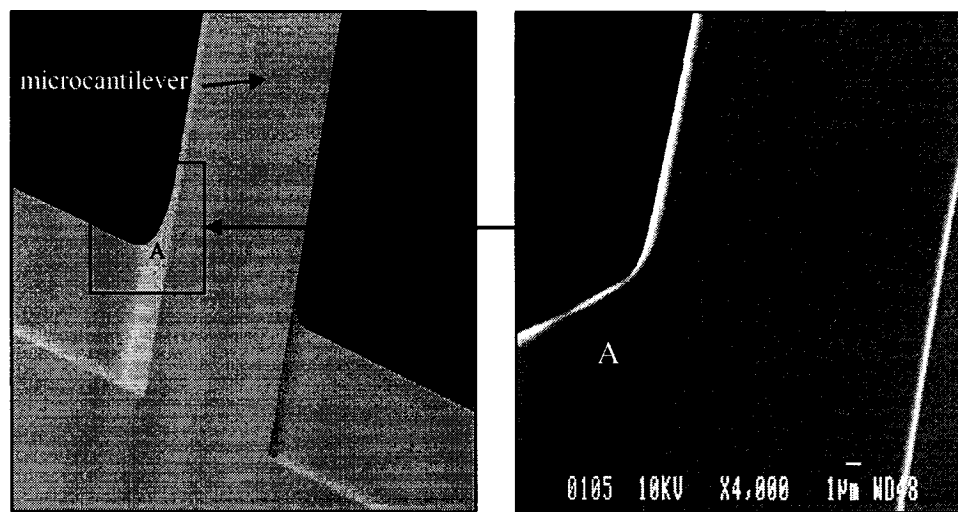
Figure 5.2. AFM boundary support top view. Left: CAD illustration. Right: SEM image. "A" represents the same surface.
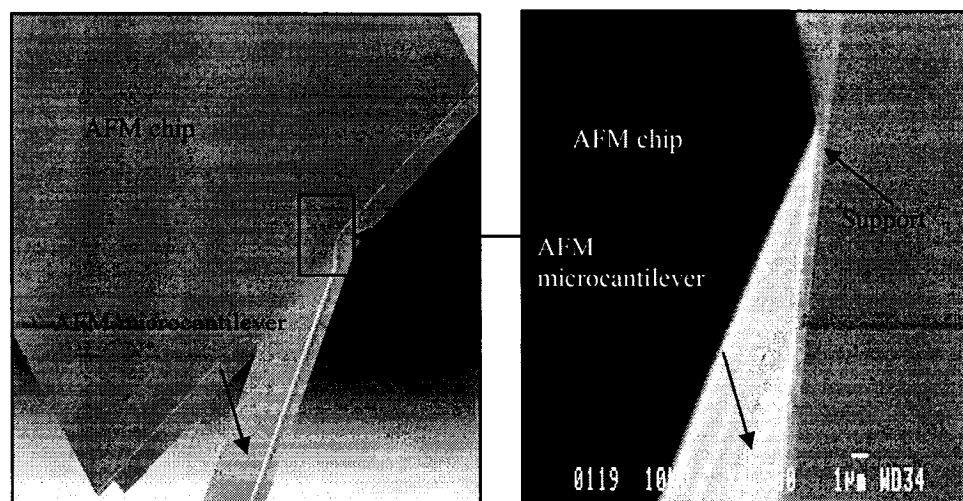
Figure 5.3. AFM boundary support bottom view. Left: CAD illustration. Right: SEM image close up.

132
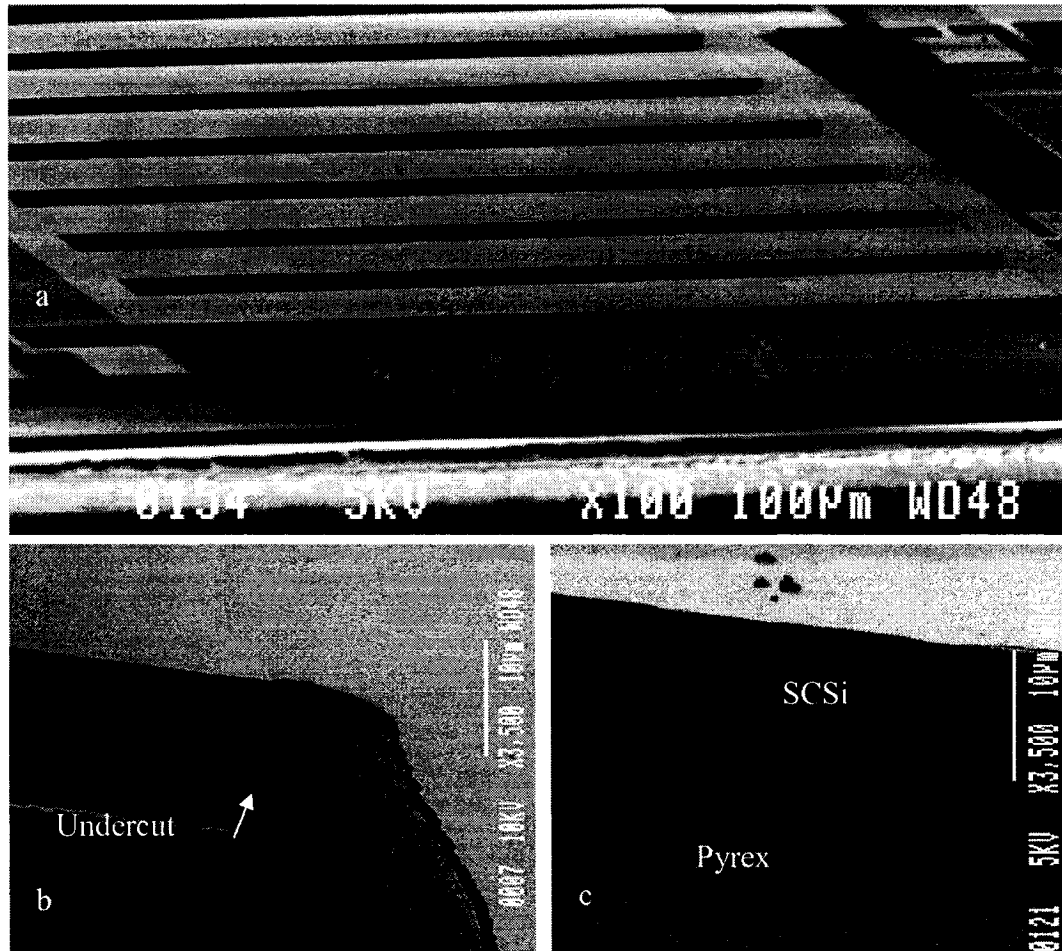
Figure 5.4. a) Overview of an array of cantilevers fabricated using MicraGeM 10μm technology. b) View of boundary support. The undercut is ~1μm. c) View of boundary support at Pyrex-SCSi interface.
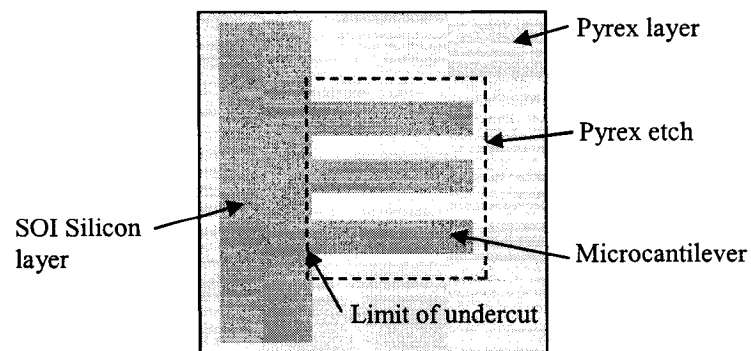
Figure 5.5. A schematic overview of the MicraGeM process layers and the undercutting of the silicon

The elastic properties and geometry of microstructures subjected to a thermo-mechanical environment are strongly dependent on temperature variations. Hence, it is very important to predict the influence of temperature on the strain energy and kinetic energy of the microstructure so that the Rayleigh-Ritz method can be applied for predicting the dynamic behaviour. This research attempts to quantify the non-classical end conditions encountered in micromachined microcantilever beam supports and hence, it is required to create a few different operating conditions that result in different elastic properties but maintaining the same end support conditions. In this way, one would be more confident in identifying the influence of boundary support conditions. In the experimental investigation the microstructures are tested at different thermal conditions. It is also assumed that the end support conditions due to micromachining limitations would not change with thermal environment conditions.

5.3. THERMAL INFLUENCE

The thermal loads applied to the microsystem are modeled by taking into account the changes in dimensions of the microcantilever and material properties such as the dependence of the coefficient of thermal expansion, α, for SCSi on temperature [80, 165, 212, 262]. The other parameter considered for thermal dependence is Young's modulus of elasticity given by Equation (2.21) and as outlined in [74, 84, 170]. The temperature dependent length $L^{(T)}$, width $w^{(T)}$, and thickness $h^{(T)}$ are calculated using thermal expansions due to temperature as given by Equations (2.17-2.19).

The mode shapes and natural frequencies, (Equation (2.32)), depend on the elastic property of the microcantilever. The maximum strain energy of the microsystem includes contributions from the microcantilever and the boundary support springs, and therefore, the temperature dependent maximum strain energy of the microsystem then becomes a function of temperature and is given by Equation (2.5). In this analysis the electrostatic and geometrical factors are not included.

Maintaining the electrical input at zero, the flexural response of the microcantilever is a function of the degree of influence the thermal and mechanical parameters have on the microsystem as a whole. The natural frequencies and mode shapes depend upon the temperature dependent properties and the boundary stiffness values K_R^* and K_T^* that are determined by the type of micromachining foundry process. In order to include the influence of microfabrication processes on the dynamic behaviour, in a simpler way as defined by Equation (2.32), it would be advantageous if the influence is quantified through K_R^*. Hence, it is required to determine the value of K_R^* for any given micromachining process so that the influence of microfabrication processes can be predicted in advance.

The experimental methods and procedures as described in Chapter 4 were adopted for thermal testing [200]. It is assumed that the entire structure is uniformly heated during the thermal testing with the heating pad and IR lamp. Hence, no stress due to thermal gradients is expected. Any thermal effects due to the laser are negligible as compared to the thermal loading. This was verified by calibrating the temperature sensing element at

ambient temperature without the laser light and then again with the laser light. The main requirement for the validation of the experimentation was to obtain an invariant value of K_R^* under varying thermal loads, from which the particular silicon foundry process influence can be extracted and quantified. Hence the multi-parameter conditioning of the microsystem takes into account mechanical, thermal and microfabrication influences on the static and dynamic characteristics of the microsystem.

5.4. EXPERIMENTAL METHODOLOGY

The thermal loading was applied through a MINCO R16.9 [154] heating pad with variable current control and with an integrated resistance-temperature-detector (RTD) temperature sensor. The temperature was automatically maintained and showed good stability during the experimentation to a sensitivity of 0.1°C. The MINCO device was used in conjunction with a 200W IR heating lamp and with this combination temperatures up to 200°C were possible to achieve. Through a comparison of the resonant frequency values obtained experimentally to those of the mathematical model, an understanding into the influence of microfabrication processes and tolerances on the boundary support conditions of microcantilever structures can be obtained.

5.4.1. *Experimental results*

It is known that microfabrication limitations include variations in geometry, material properties and non-classical boundary conditions. In order to focus mainly on the

136

boundary conditions the actual dimensions of the microstructures were used for modeling.

The dimensions of the AFM probes and the MicraGeM 10μm technology SOI

microcantilevers tested in this work were measured using a scanning electron microscope

(SEM) and an optical microscope. The values used in the theoretical analysis and the

material constants supplied by the respective manufacturers, are tabulated in Table 5.1

and Table 5.2 respectively

Table 5.1. The measured physical parameters used in the theoretical modeling of MicraGeM technology microcantilevers. The [##] indicates values as supplied by the manufacturer at room temperature.

MicraGeM	Length (μm)	Width (μm)	Thickness (μm)	Elastic Mod. [##] $(10^9\,\text{Pa})$	Density [##] (kg m^{-3})
# 1	1010	100.1	10.8	129.5	2320
# 2	1008	100	10.9	129.5	2320
# 3	2012	201	10.8	129.5	2320

Table 5.2. The measured physical data of the AFM microcantilevers. The ## indicates values as supplied by the manufacturer, and the * indicates tipless AFM microcantilevers.

AFM	Length (μm)	Width (μm)	Thickness (μm)	Elastic Mod. [##] $(10^9\,\text{Pa})$	Density [##] (kg m^{-3})
# 1	354	35.1	1.7	169.5	2330
# 2	305	35.2	1.71	169.5	2330
# 3*	351	34.5	0.94	169.5	2330
# 4*	299	35	0.96	169.5	2330

The results for the thermo-mechanical testing obtained for the MicraGeM

microcantilevers numbered #1-#3 in Table 5.1, are presented in Figures 5.6-5.8

respectively. Results for the AFM microcantilevers are presented in Figures 5.9-5.12 respectively. Experimental results are shown together with the predicted values for both classical and non-classical end support conditions. The value of K_T^* is maintained at 1 x 10^{10}, and the value of K_R^* is varied in order to match the non-classical theory with the experimental results. For the classical theory both K_T^* and K_R^* have been fixed to a value of 1 x 10^{10} which models a fully clamped boundary support condition. For the condition of $K_T^* = K_R^* = 0$ models a *free-free* cantilever, and $K_T^* = 1$ x 10^{10} and $K_R^* = 0$ models a *pinned-free* cantilever. Evidence of the effect of the changing boundary stiffness K_R^* on the elastic properties of the microsystem are found in the eigenvalues of Equation (2.32a). Hence, the eigenvalues are strictly a function of the boundary support conditions.
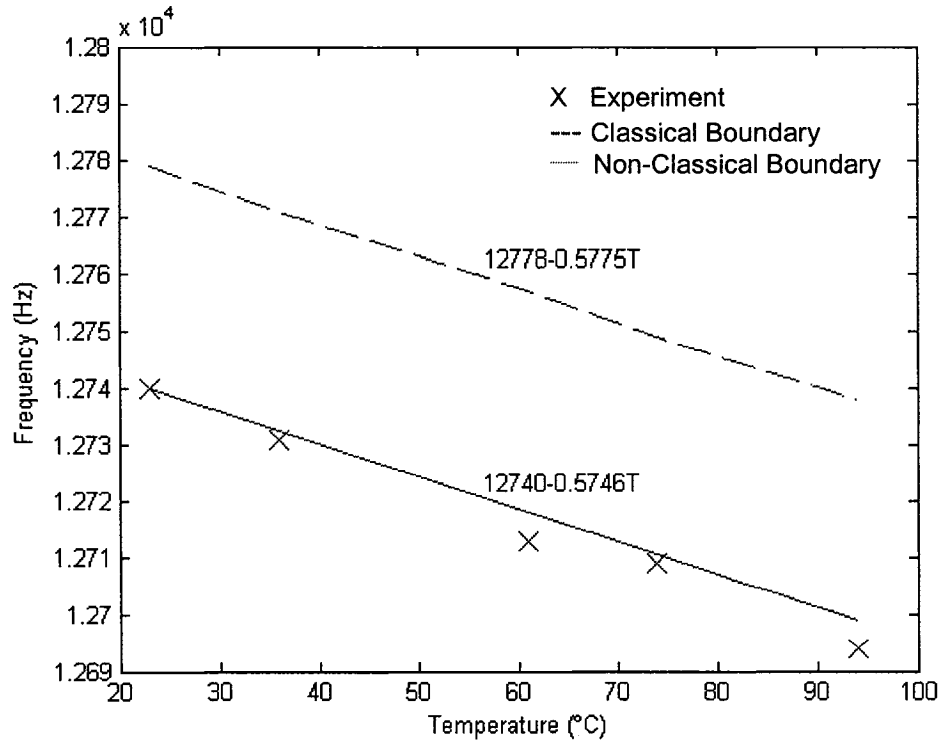
Figure 5.6. The variation of resonance frequency as a function of temperature for MicraGeM microcantilever #1. The difference between classical and non-classical is 0.31%.
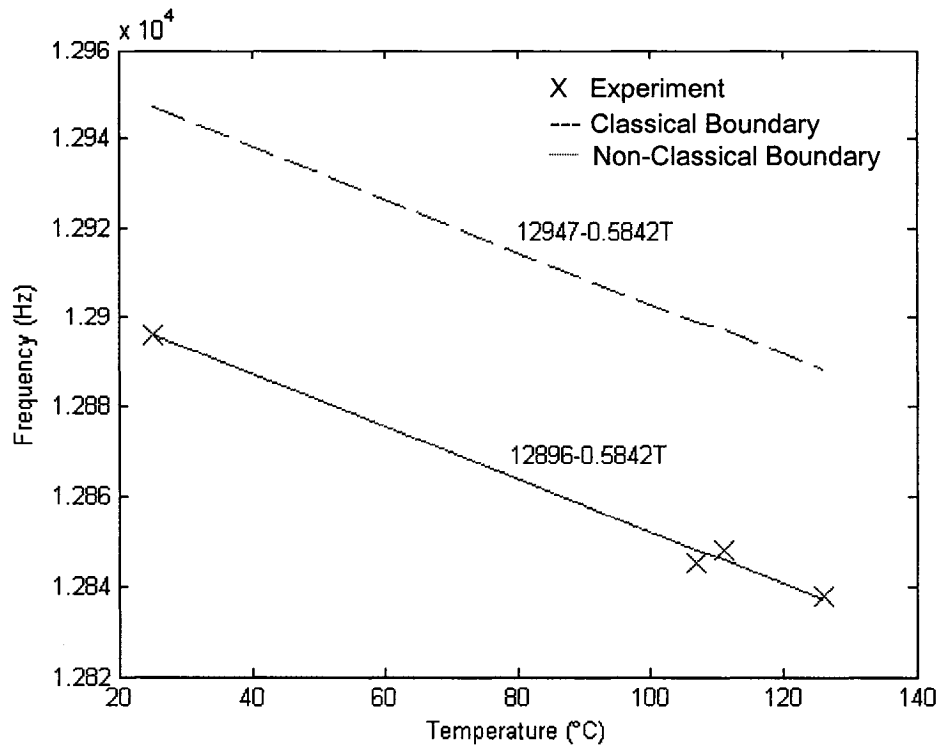
Figure 5.7. The variation of resonance frequency as a function of temperature for MicraGeM microcantilever #2. The difference between classical and non-classical is 0.46%.
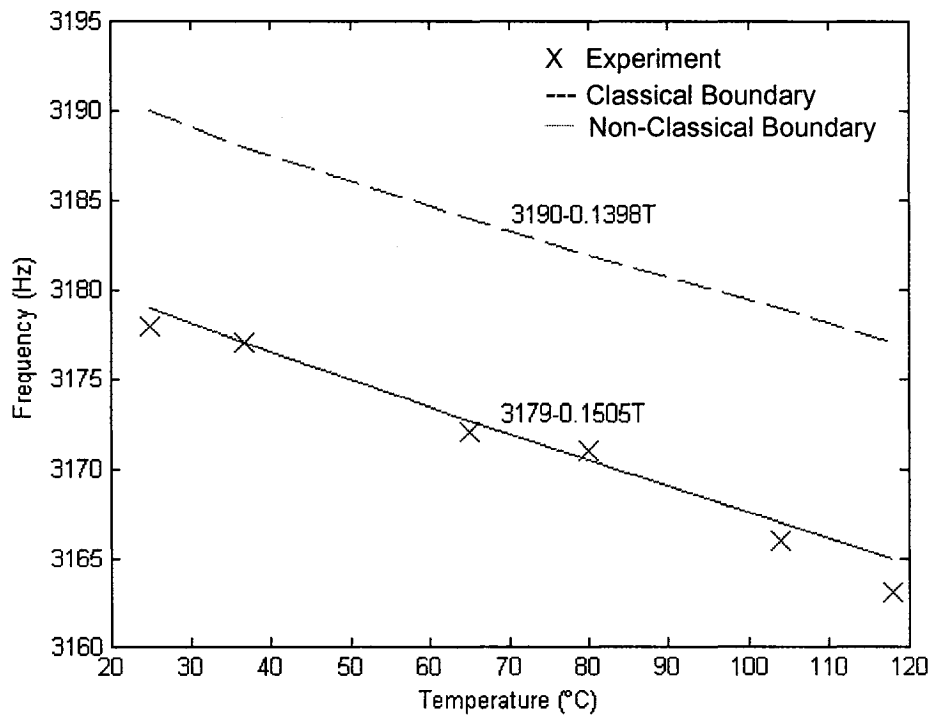
Figure 5.8. The variation of resonance frequency as a function of temperature for MicraGeM microcantilever #3. The difference between classical and non-classical is 0.34%.

139
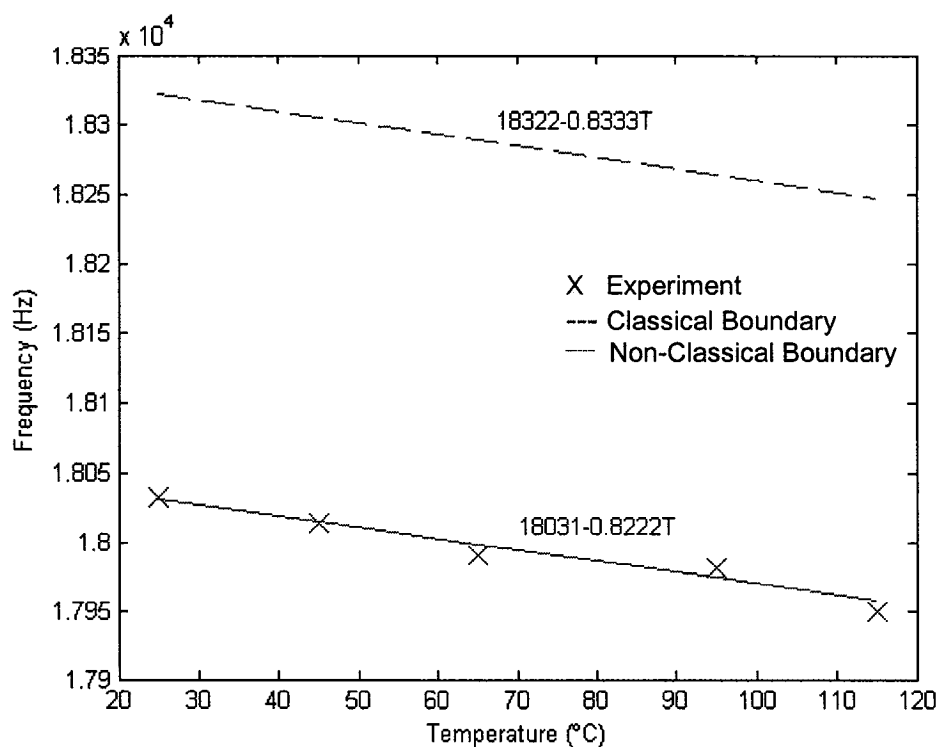
Figure 5.9. The variation of resonance frequency as a function of temperature for the AFM cantilever #1. The difference between classical and non-classical is 1.59%.
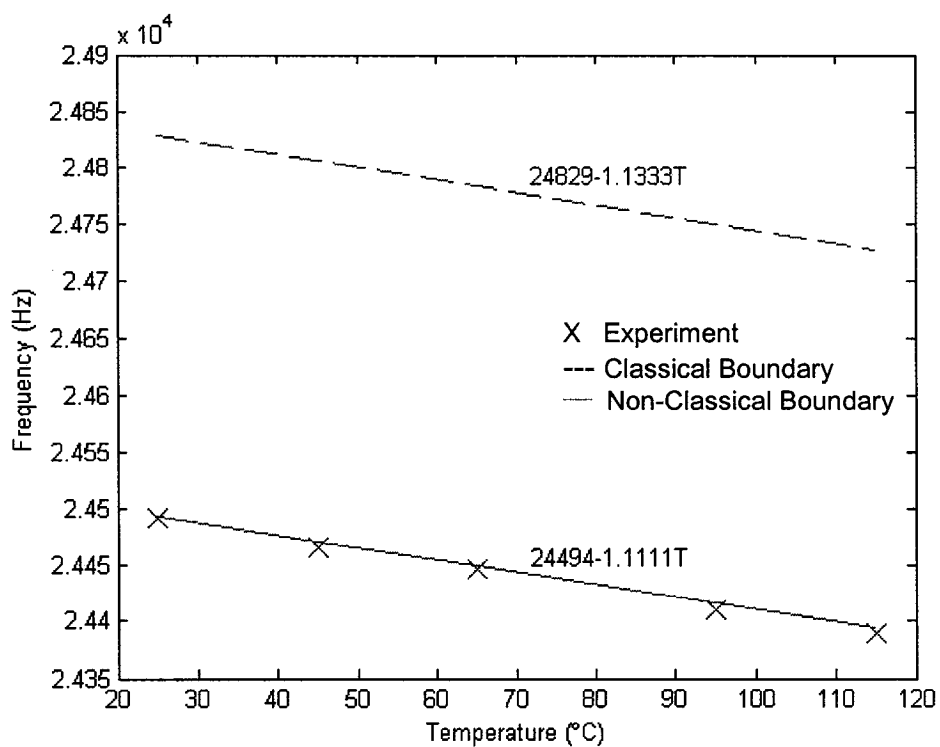
Figure 5.10. The variation of resonance frequency as a function of temperature for the AFM microcantilever #2. The difference between classical and non-classical is 1.35%.

140
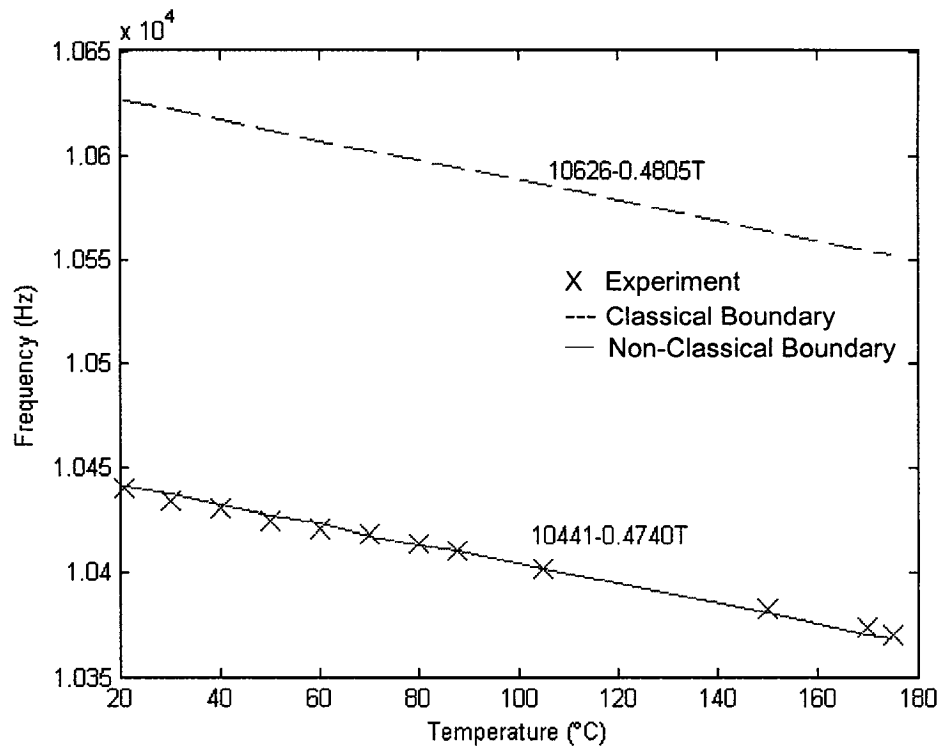
Figure 5.11. The variation of resonance frequency as a function of temperature for the tipless AFM microcantilever #3. The difference between classical and non-classical is 1.74%.
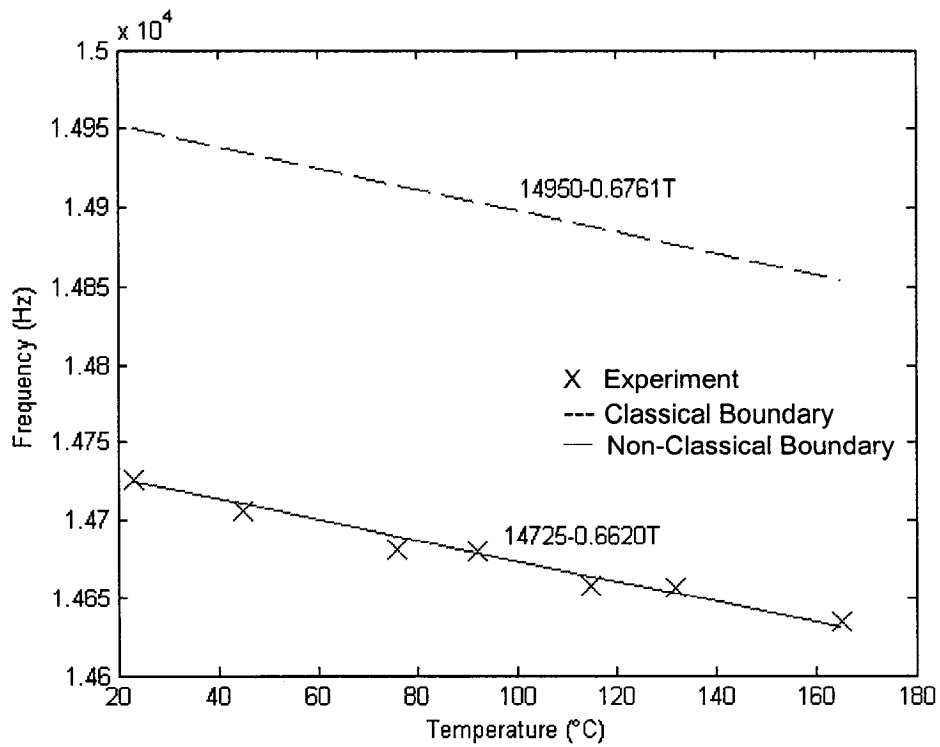
Figure 5.12. The variation of resonance frequency as a function of temperature for the tipless AFM microcantilever #4. The difference between classical and non-classical is 1.51%.

The average difference from the classical boundary support for the MicraGeM and AFM microcantilevers is 0.37% and 1.55%, respectively. The trend in both technologies was consistent for all the devices that were tested. The smaller dimensions of the AFM microcantilevers introduce errors in the measurement of the thickness, for example, and this *margin of error* was maintained for all of the testing.

Given in Table 5.3 are the rotational stiffness values, K_R^*, required to match the experimental values with the theoretical values. From the comparison of the theoretical and experimental results obtained the influence of non-classical boundary conditions can be seen through the K_R^* values, that are a measure of the microfabrication influence for a specific foundry process. Even though only a few devices were tested, they were found to be in good agreement with the theoretical model. Statistical values can be obtained if more devices are tested. One could see different ranges of K_R^* values for different foundry technologies, thereby validating the present boundary characterization technique based on experimental results.

Table 5.3. The rotational stiffness, K_R^*, values estimated that match the experimental values to the non-classical theory.

	MicraGeM	AFM	AFM (Tipless)
	660	124	112
	505	158	130
	558		
Mean	574	141	121

In order to estimate the mass of the tip, the base of the tip was taken as a 9 sided polygon

with circumscribed radius of 5μm as shown in Figure 5.13 and Figure 5.14, with a tip

mass m'.
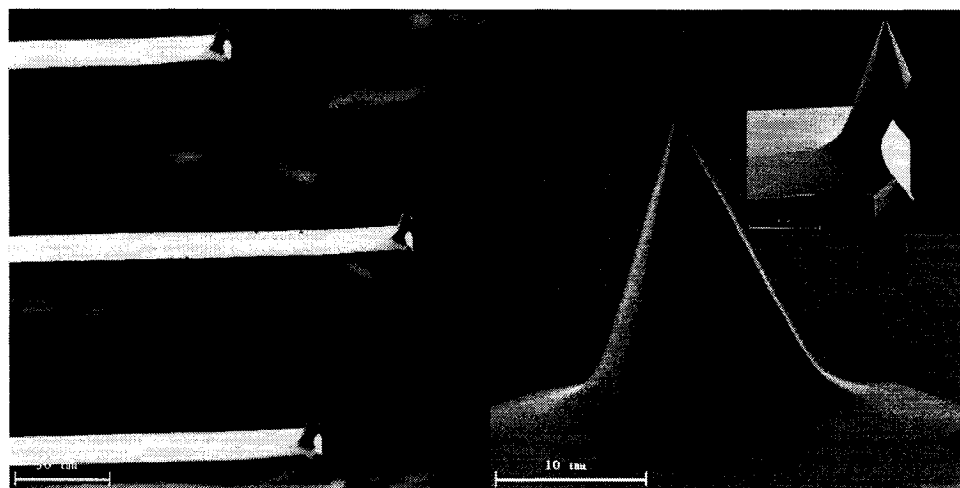
Figure 5.13. Left: AFM microcantilevers. Right: Close up of the tip. Insert: Side view of the tip.
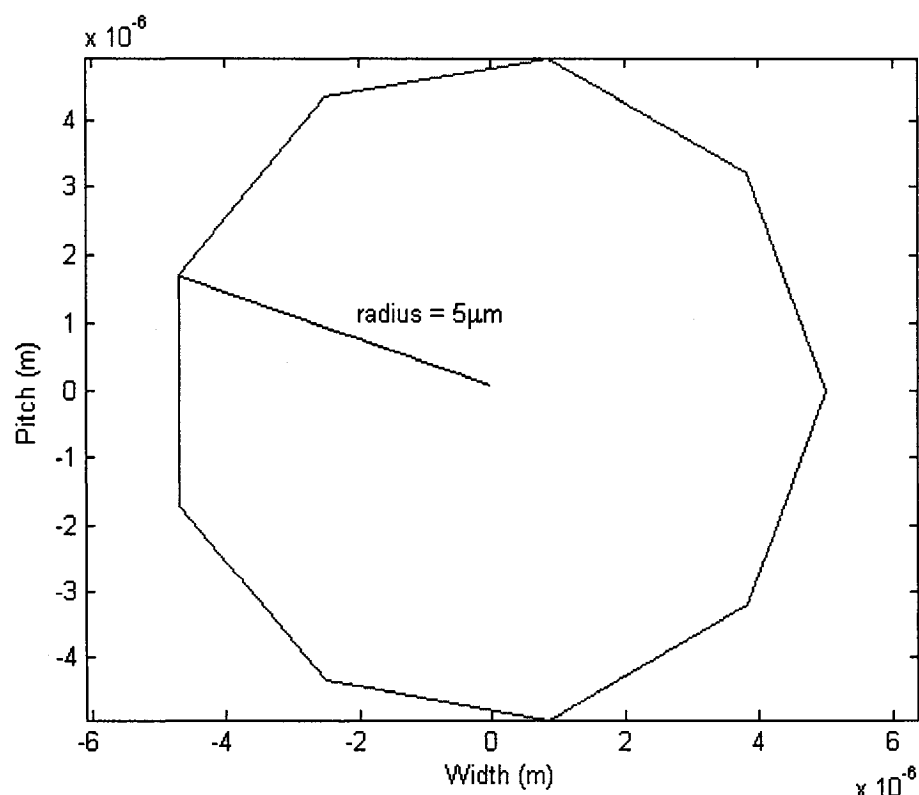
Figure 5.14. The assumed shape of the microcantilever tip base.

The area of the 9 sided polygon base was calculated using

$$A = \frac{9r^2}{2} \sin\left(\frac{360}{9}\right)$$ (5.1)

from which then the volume of a 9 sided conic shape was calculated using

$$Volume = \frac{1}{3} AH$$ (5.2)

where H is the height of the tip and taken as 15μm. The mass was estimated using a single crystal silicon density of 2330 kg m^{-3}, however, as is shown in the insert of Figure 5.13 a substantial amount of mass has been removed from the backside of the tip. Hence an adjustment was made in this regard in the calculations by removing $0.25m'$ from m'. This measurement is an approximation, hence, a calculation removing $0.23m'$ and $0.27m'$ respectively was carried out and resulted in a deviation of 0.14% from the experimental values obtained.

5.5. ELECTRO-MECHANICAL BOUNDARY CHARACTERIZATION

In order to substantiate and validate the boundary characterization it would be of interest to investigate the static and dynamic properties of the microsystems under a different input parameter such as electrostatic [210]. In this way it is expected that the microfabrication influences will manifest themselves in a similar fashion for a given microdevice as was the case for the thermal boundary characterization. This parallel investigation serves two purposes, firstly it enables one to quantify the electrostatic influences in themselves on the microsystem, and secondly when compared to the theoretical model it is possible to extract and reconcile the microfabrication influences with the non-classical mathematical model in a complementary fashion to the thermal loading characterization. Again, an important requirement for the validation of the experimentation was to obtain an unchanging value of K_R^* under several different electrostatic loads. The results will enable one to obtain a *foundry profile* for that particular micromachining process.

The maximum strain energy, Equation (2.5), of the microsystem now has an electrostatic component. Shown in Figure 5.15 is a digital image taken through a microscope of an AFM chip with three microcantilevers suspended over a copper electrode. The AFM chip is mounted onto an insulating material and hard wired to the anode of the power supply, while the copper electrode is wired to the cathode. In this manner it is possible to apply an electrostatic potential between the microcantilevers and the copper electrode.
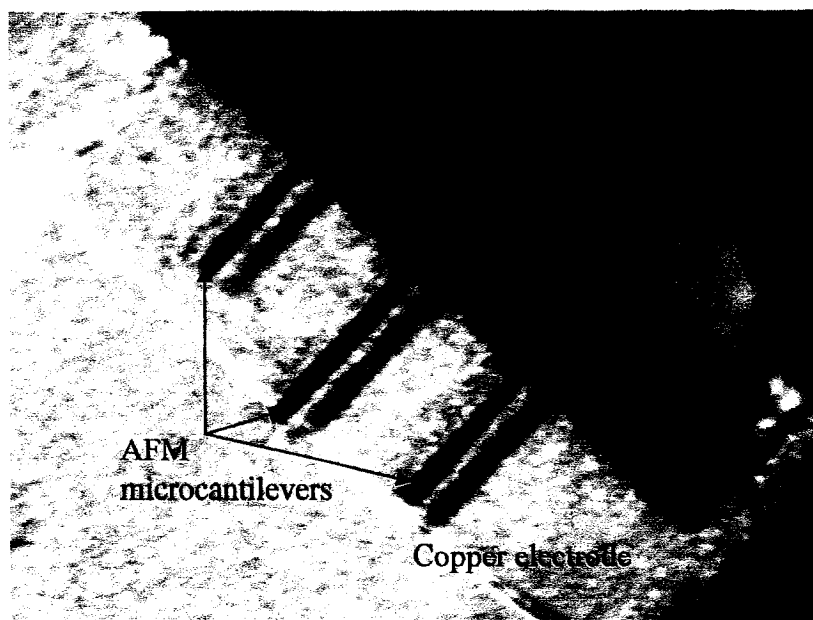
Figure 5.15. A close up image of the AFM chip and three microcantilevers. Also seen are the microcantilevers shadows on the copper electrode surface.

5.5.1. *Experimental results*

The results are again presented in graphical form and include both classical and non-classical modeling curves. The static deflections were measured through an optical microscope by focusing on the microcantilever end. When a potential was applied, the microcantilever would deflect and hence the microcantilever end would be out of focus with respect to the undeflected position. The deflection distance is obtained by noting the difference in the focal point for the undeflected position to that of the new static equilibrium position. Shown in Figure 5.16 are a set of superimposed photographs taken at several different electrostatic potentials showing the changes to the static equilibrium

position of the microcantilever, the theoretical deflections are also calculated using Equation (2.27) and shown for comparison purposes.

Presented in Figures 5.17-5.18 are the static equilibrium position curves for the AFM tipless microcantilevers #3 and #4, respectively, as given in Table 5.2 above. The theoretical classical and non-classical curves are also included so that a comparison can be made with the experimental results. Shown in Figures 5.19-5.20 are the changes to the resonance frequency (experimental, classical theory, non-classical theory) as a function of the applied voltage. The theoretical analysis for the classical and non-classical boundary conditions made use of Equation (2.32).
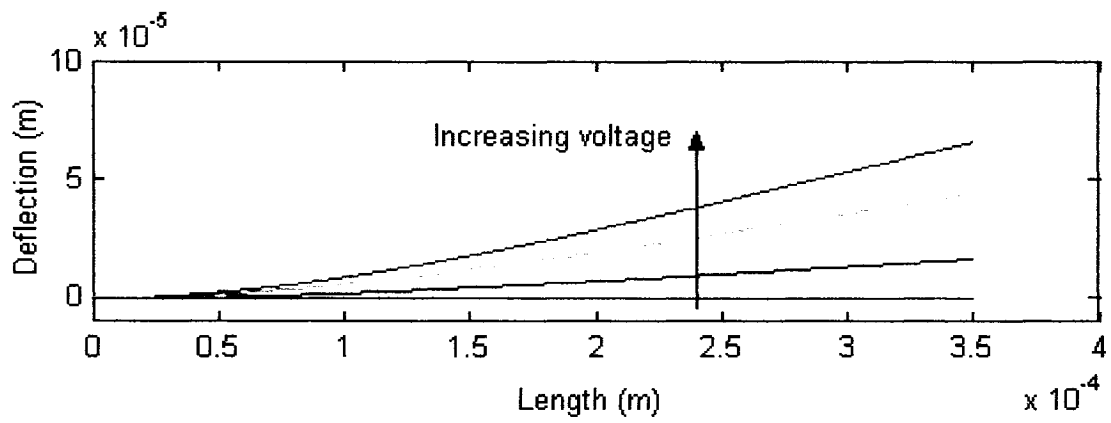
Figure 5.16. The static equilibrium positions for an AFM microcantilever at different applied electrostatic potentials. Top: Experimental. Bottom: Simulation.
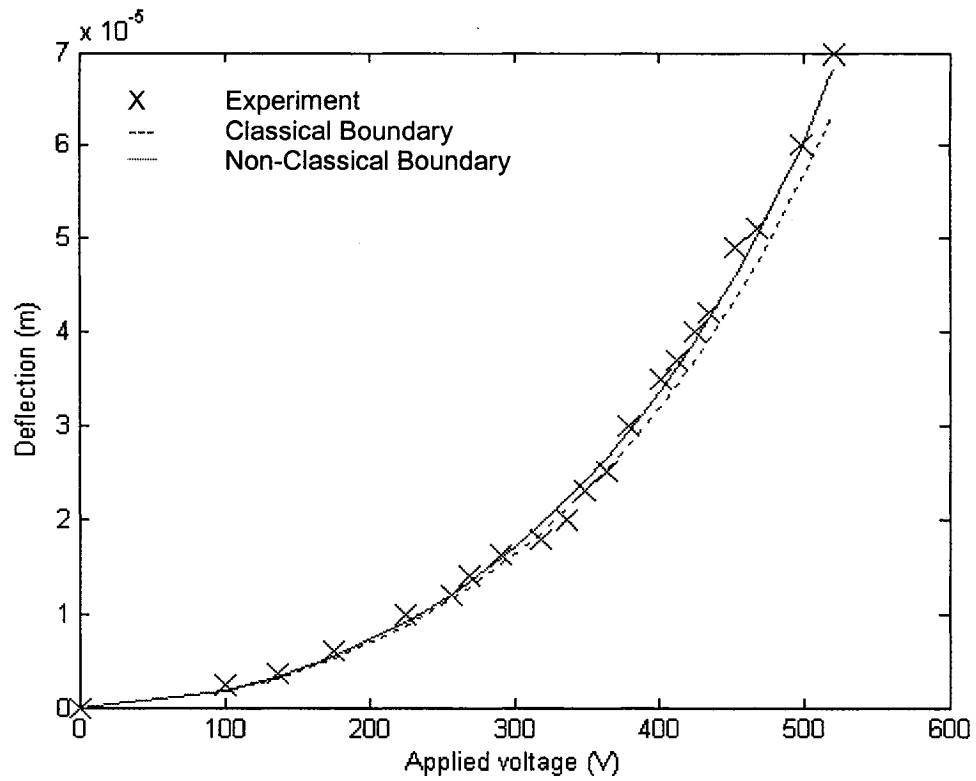
Figure 5.17. The theoretical and experimental static equilibrium tip positions of the tipless microcantilever #3.
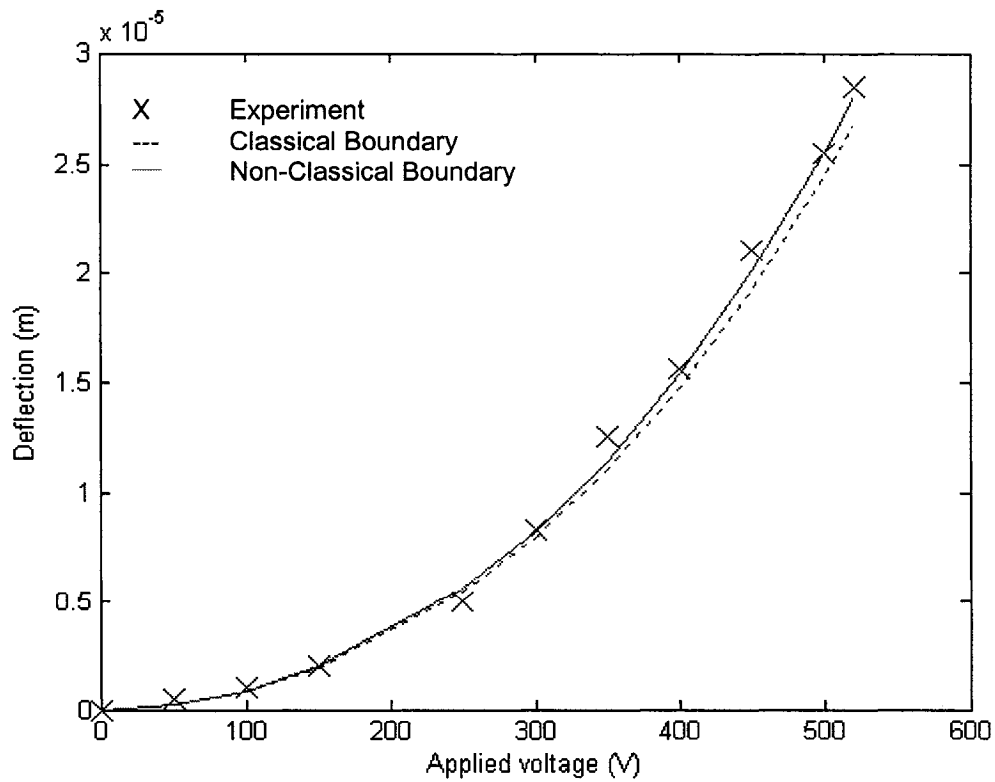
Figure 5.18. The theoretical and experimental static equilibrium tip positions of the tipless microcantilever #4.

149
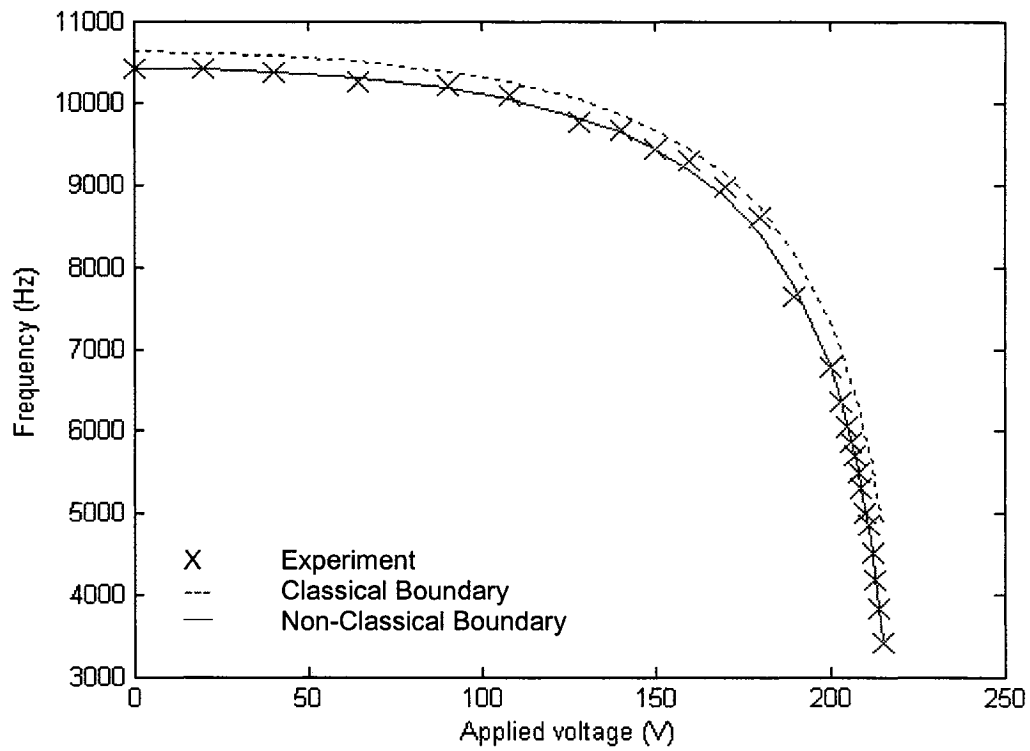
Figure 5.19. The frequency dependence on the applied voltage for the AFM microcantilever #3.
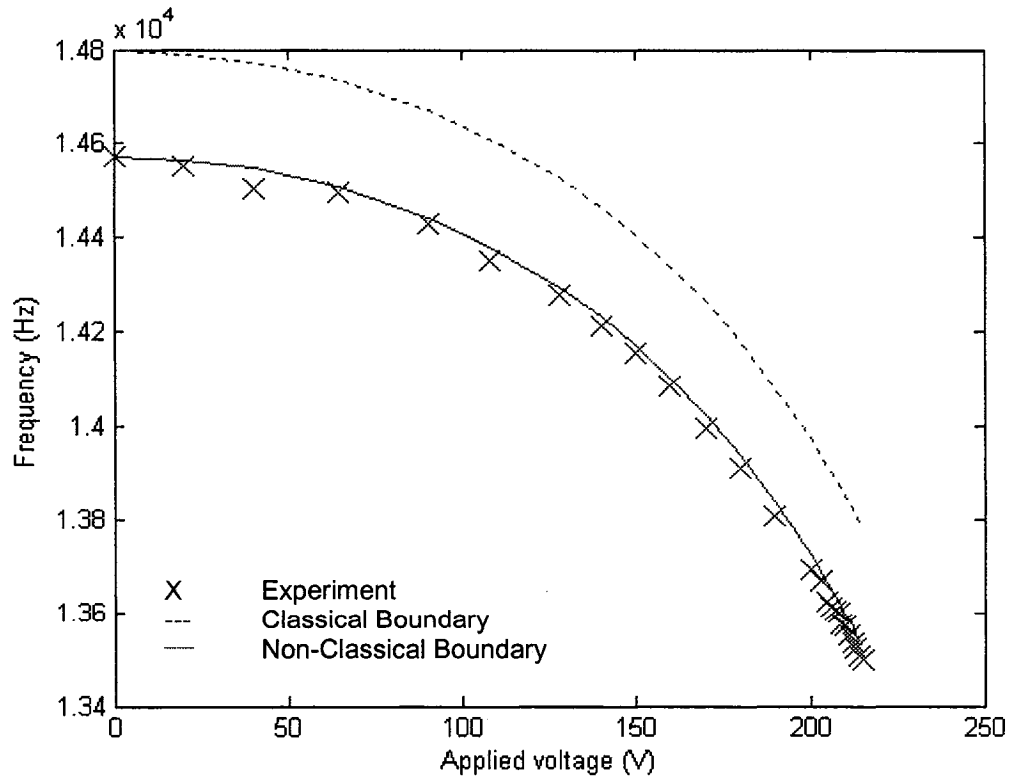
Figure 5.20. The frequency dependence on the applied voltage for the AFM microcantilever #4.

The results shown in Figures 5.17-5.18 are for an estimated dielectric gap d_0 = 88μm, from which a maximum electric field intensity 5.79 x 10^6 V/m was obtained for 510V. For the results shown in Figures 5.19-5.20 the estimated dielectric gap was d_0 = 52μm, from which a maximum electric field intensity 4.04 x 10^6 V/m was obtained for 210V.

Included in the electro-mechanical boundary characterization are the static and dynamic characteristics of two MicraGeM 10μm technology microcantilevers. They have the *RISO* and *SORI* geometry respectively. These two geometries were investigated in order to complement the thermo-mechanical boundary characterization carried out on conventionally shaped MicraGeM technology microcantilevers.

The support boundary characterization of unconventionally shaped microcantilevers such as the *RISO* and *SORI* geometries, will enhance the experimentation already carried out on the MicraGeM technology tolerances and limitations through the thermal and electrical testing. Shown in Figures 5.21-5.22 are the static tip deflections as a function of the applied voltage for *RISO* and *SORI* microcantilevers respectively. Shown in Figures 5.23-5.24 are the resonance variations as a function of the applied voltage for *RISO* and *SORI* microcantilevers respectively.
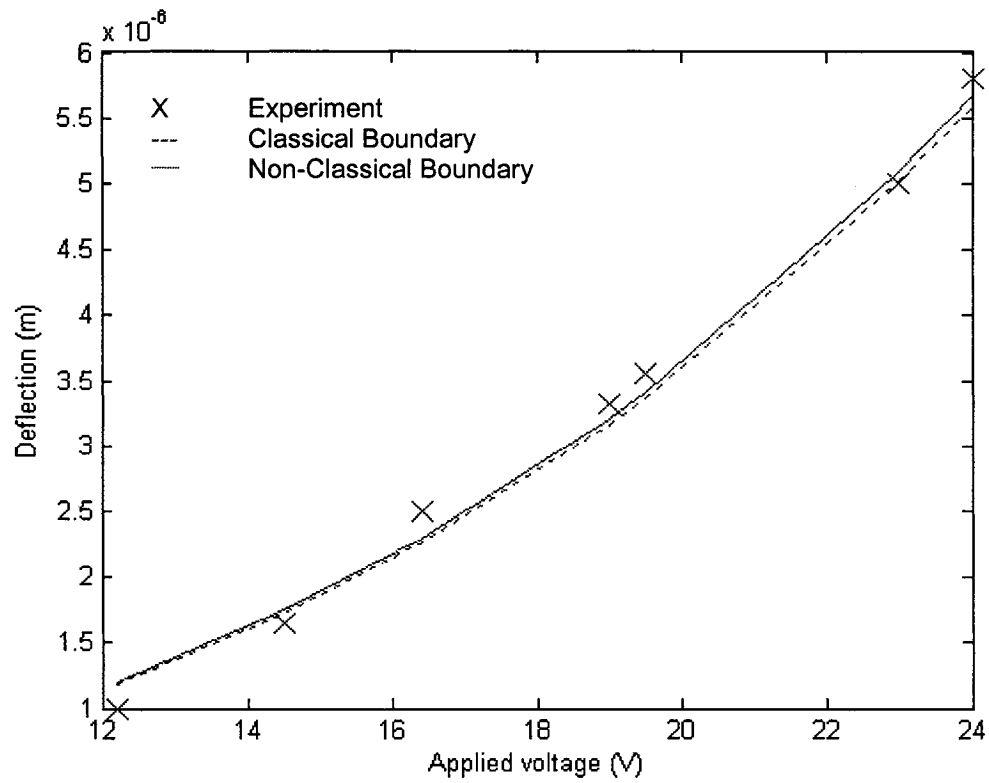
Figure 5.21. *RISO* microcantilever tip deflections as a function of applied voltage.
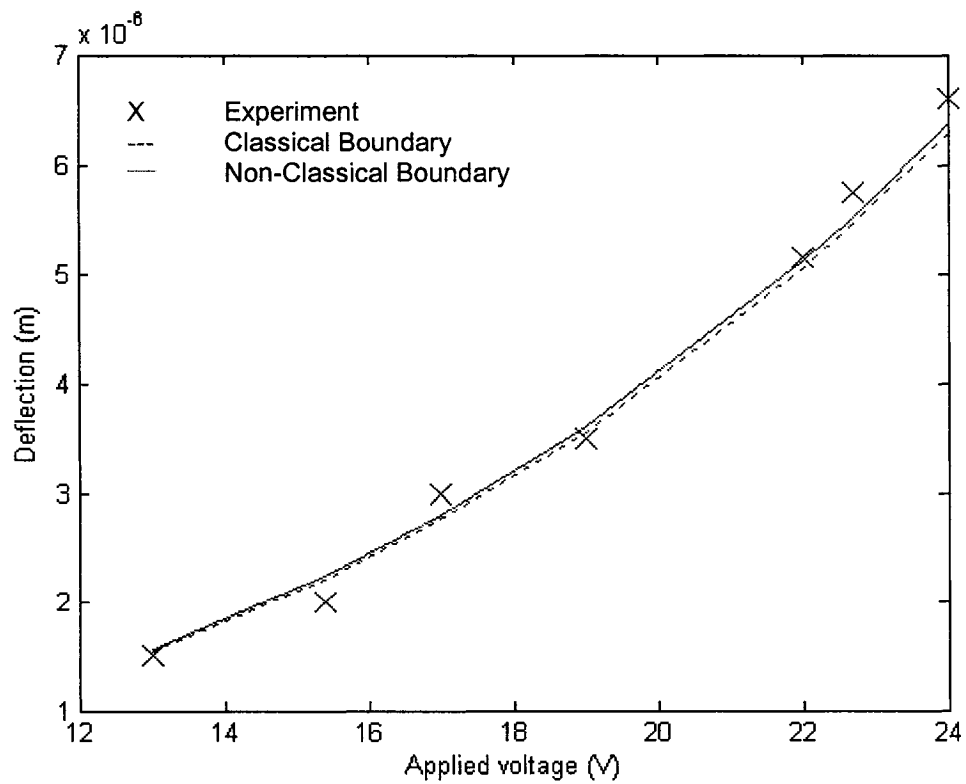
Figure 5.22. *SORI* microcantilever tip deflections as a function of applied voltage.
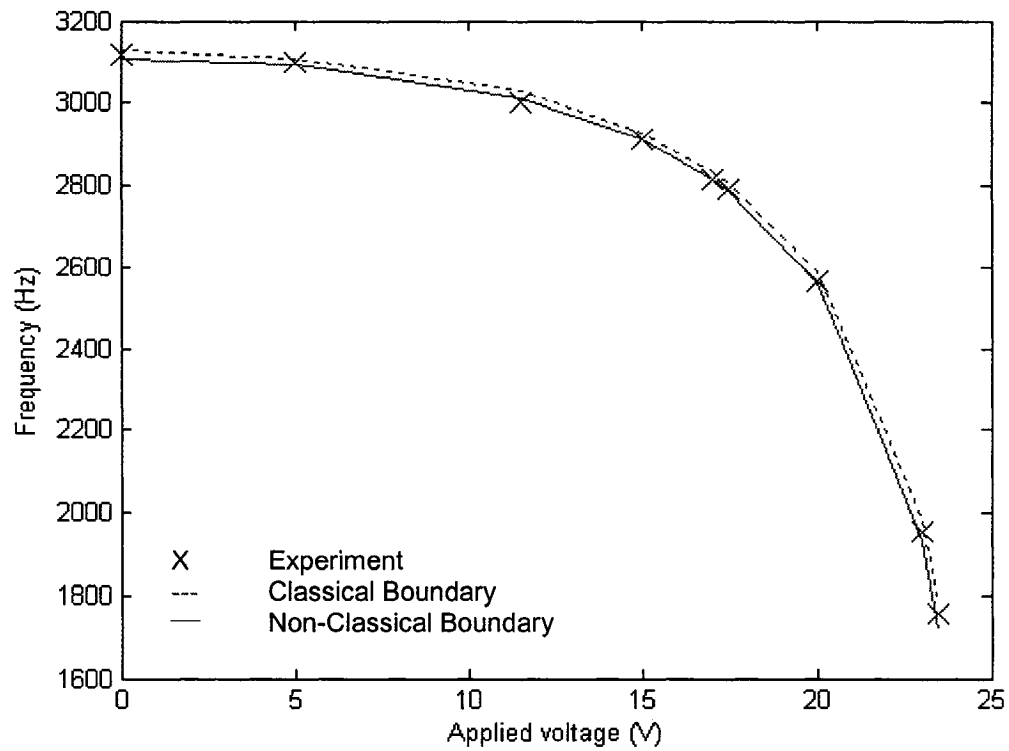
Figure 5.23. The frequency dependence on the applied voltage for the *RISO* microcantilever.
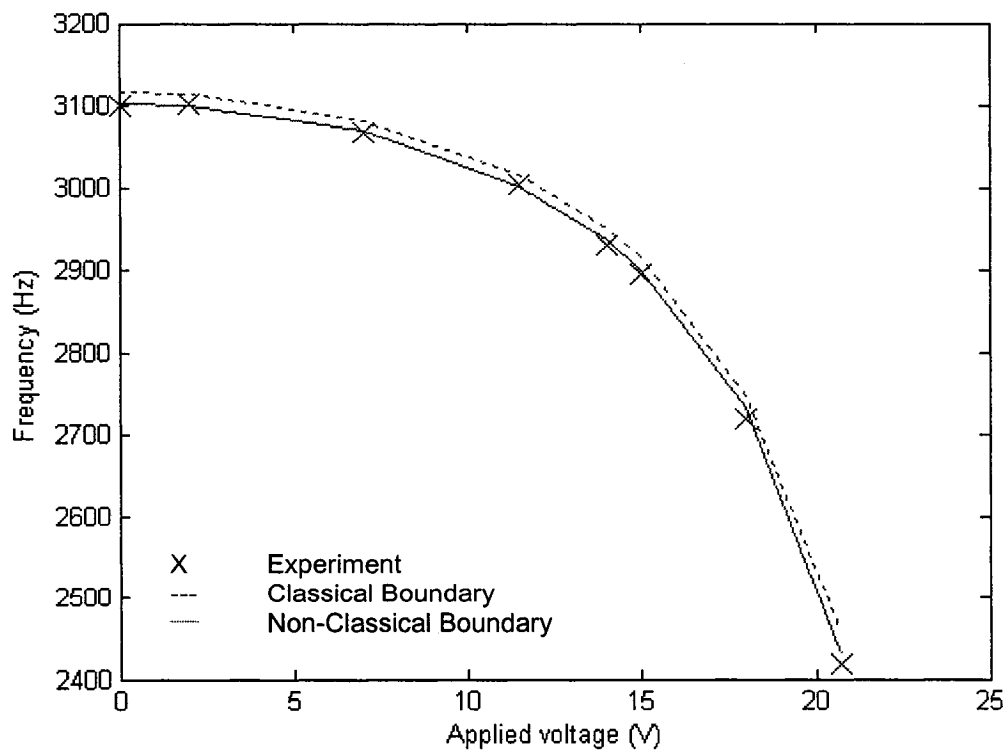
Figure 5.24. The frequency dependence on the applied voltage for the *SORI* microcantilever.

The dielectric gap d_0 for the MicraGeM technology microcantilevers was estimated as 13.3μm resulting in a maximum electric field of 1.8×10^6 V/m.

Presented in Table 5.4 are the $K_R{}^*$ values estimated for the particular microfabrication foundry process. The values obtained for the thermo-mechanical testing are also included. From these results it is possible to establish a *mean* value for the foundry.

Table 5.4. The rotational stiffness, $K_R{}^*$, values estimated that match the experimental values to the non-classical theory for electro-mechanical boundary characterization.

Characterization	*RISO*	*SORI*	AFM #3	AFM #4
Electrostatic *Static*	574	580	110	130
Electrostatic *Dynamic*	586	600	108	128
Mean *Static*	577		120	
Mean *Dynamic*	593		118	
Mean Thermal	574		121	
Mean Foundry	581		120	

The *mean foundry* values in Table 5.4 are an indication of the variation obtainable in the boundary support condition through silicon micromachining processes. The influence of higher value of $K_R{}^*$ obtained for the MicraGeM technology microcantilevers can be seen in Figures 5.23-5.24 where the deviation from classical to non-classical is quite small, whereas by comparison for the AFM microcantilevers the deviation is ~1%. This would

154

indicate that the mechanical characteristics of the MicraGeM are more *predictable* due to the nature of the boundary support condition obtained through the higher $K_R{}^*$ value.

5.6. SUMMARY

The boundary characterization of MicraGeM 10μm technology and AFM microcantilevers probes by thermo-mechanical and electro-mechanical testing has been presented. The process limitations and foundry tolerances of microfabrication technologies result in non-classical support conditions at the structure-support interface. The microcantilever end support modeling was carried out with artificial rotational and translational springs and the mathematical formulation was based on the Rayleigh-Ritz energy method from which the natural frequencies and mode shapes are obtained. Employing this approach, the influences of the micromachining processes can be conditioned through the boundary support springs.

For the thermal influence, changes to both geometry and material properties were incorporated into the model. Through the thermal loading it is possible to test the same microcantilever under many different stress conditions, and hence, obtain a well defined experimental result of its dynamic characteristics through the dynamic non-contact optical testing method. The electro-mechanical characterization served to complement the thermo-mechanical testing and the results obtained with both these testing mechanisms are in very good agreement. For the electro-mechanical testing the frequency

155

responses and the static deflections of the microcantilever tip as a function of the applied voltage were obtained.

The comparison between theoretical and experimental results show a deviation that can be attributable to microfabrication process limitations and foundry tolerances as demonstrated by the stiffness values of the rotational spring. The errors introduced in the measurements of the various microcantilever geometries and dielectric gaps will influence the final results, and therefore for future work, one should investigate the micromachining limitations through K_R^* as a function of the geometry of the clamping zone alone.

Chapter 6

SYNTHESIS OF MICROSYSTEMS

Presented in this chapter are the theoretical and experimental results for the synthesized parameter influence on a microsystem. The analysis includes boundary support, electrostatic, thermal, geometry and cutouts. The natural frequencies obtained are compared to the non-classical boundary support theory as presented in Chapter 5.

6.1. INTRODUCTION

The coupled electro-mechanical influences of MEMS, and the operating conditions they are subjected to, makes it difficult to separate and characterize the discrete mechanical, electrical, thermal and geometrical effects. The *environmental* conditions that can affect the operation of a microsystem are difficult to control. Hence, the establishment of a strong *theoretical-experimental* basis in which all the possible internal and external influences acting on a given microsystem are modeled would accelerate the commercialization of a given product. In this regard, the analytical model takes into account the combined influences and predicts the output of a given microsystem prior to fabrication. The different ways of synthesizing the parameters that influence the behaviour of microsystems are presented in this chapter.

6.2. BOUNDARY SUPPORT-ELECTRO-GEOMETRICAL SYNTHESIS

The analysis presented here begins with an investigation into the frequency responses of several geometry conditioned microcantilevers fabricated through the MicraGeM technology as shown in Figure 6.1. A close up of some of the geometrical features is given in Figure 6.2.

The experimental and theoretical results for non-classical and classical boundary support conditions are given in Figures 6.3-6.5 for microcantilevers #1, #6 and #3, respectively. Given in Table 6.1 are the physical parameters of the microcantilevers as measured with an optical microscope and SEM image estimates. The segment Rayleigh-Ritz method presented in Chapter 3 is used for the analysis.

Table 6.1. The physical parameters used for the boundary support-electro-geometrical modeling of microcantilevers #1, #3 and #6, where $w(0)$ is the microcantilever width at the boundary support.

Microcantilever	L (μm)	h (μm)	w_0 (μm)	$w(0)$ (μm)	δ (μm)	β	d_0 (μm)	n_{sg}
1	810	10.7	40	90	25	0.3	13.3	4
3	810	10.7	40	90	25	3	13.3	6
6	810	10.7	40	69	25	0.5	13.3	6
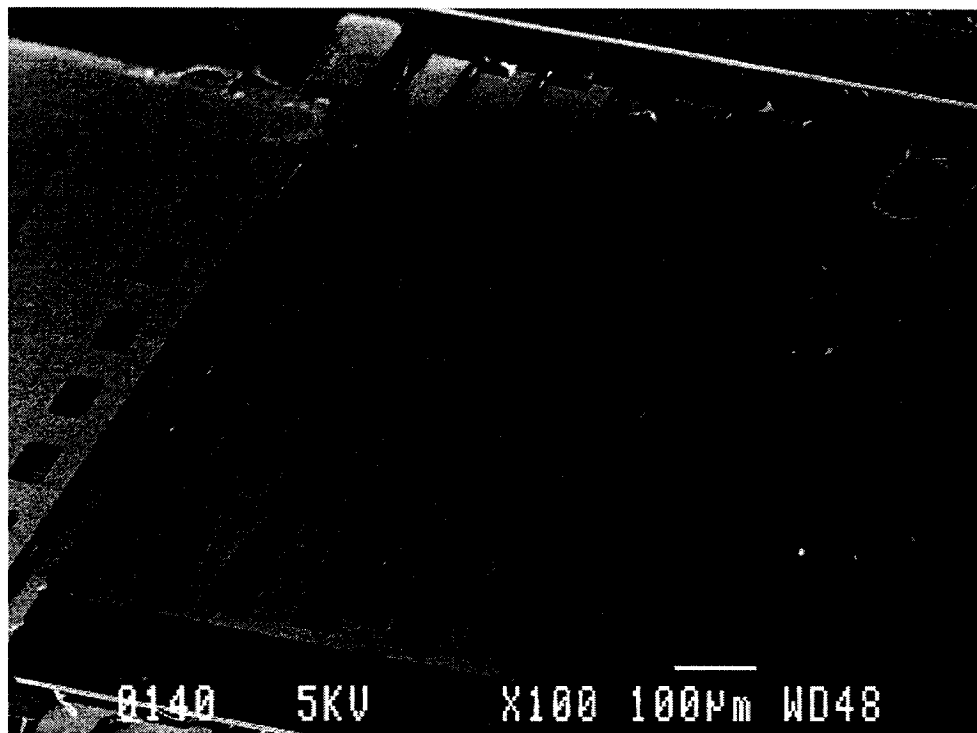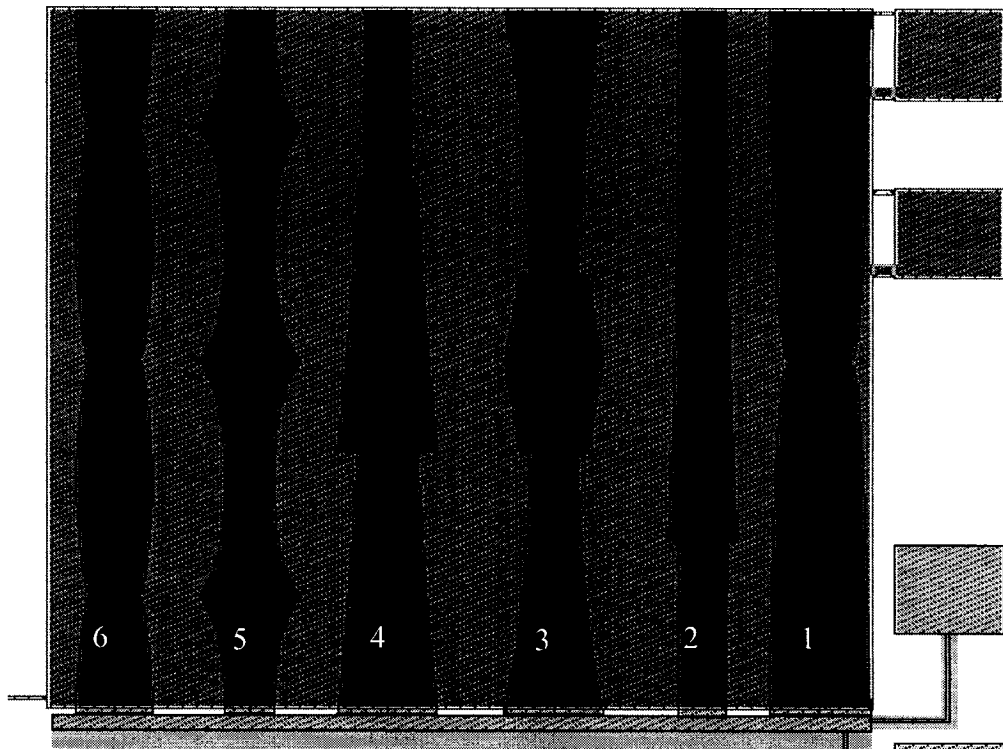
Figure 6.1. Top: MEMSPro layout editor microcantilever design overview. Bottom: SEM image of the microcantilevers fabricated using MicraGeM technology.

0144   5KV   X450   10μm WD48

0145   5KV   X300 100μm WD48
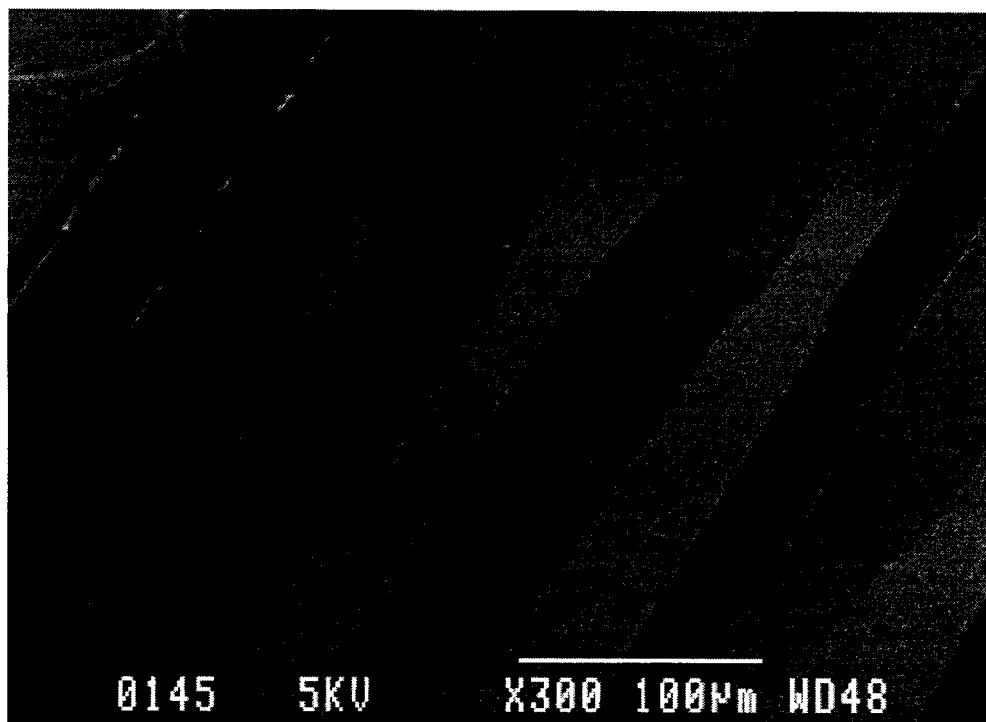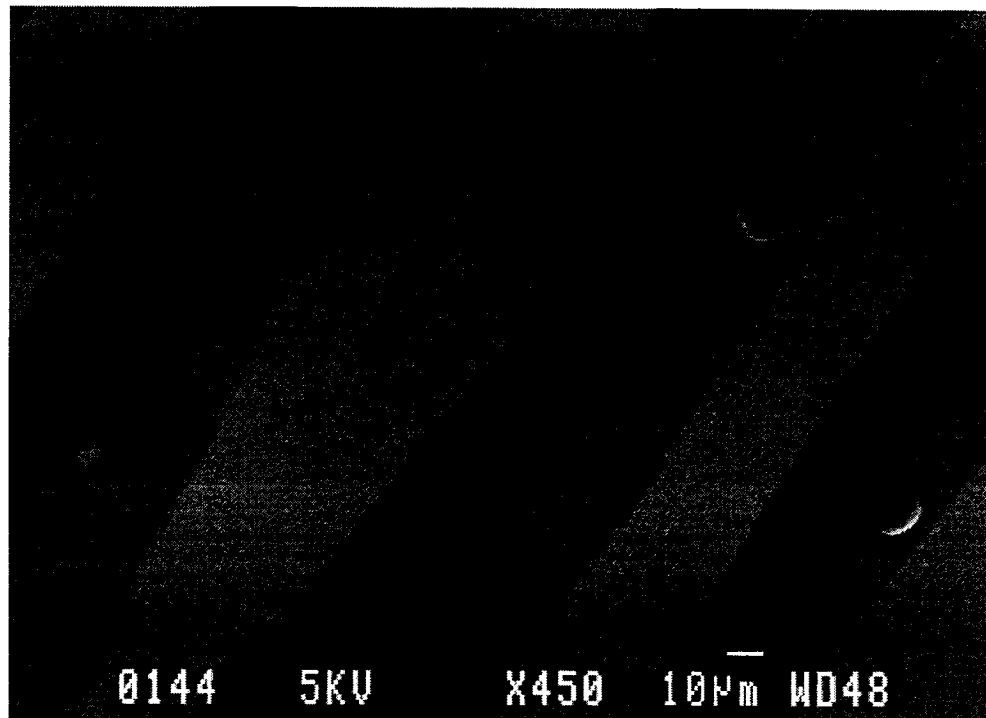
Figure 6.2. Top and Bottom: SEM close up images of some of the geometrical features of the MicraGeM technology microcantilevers.

160
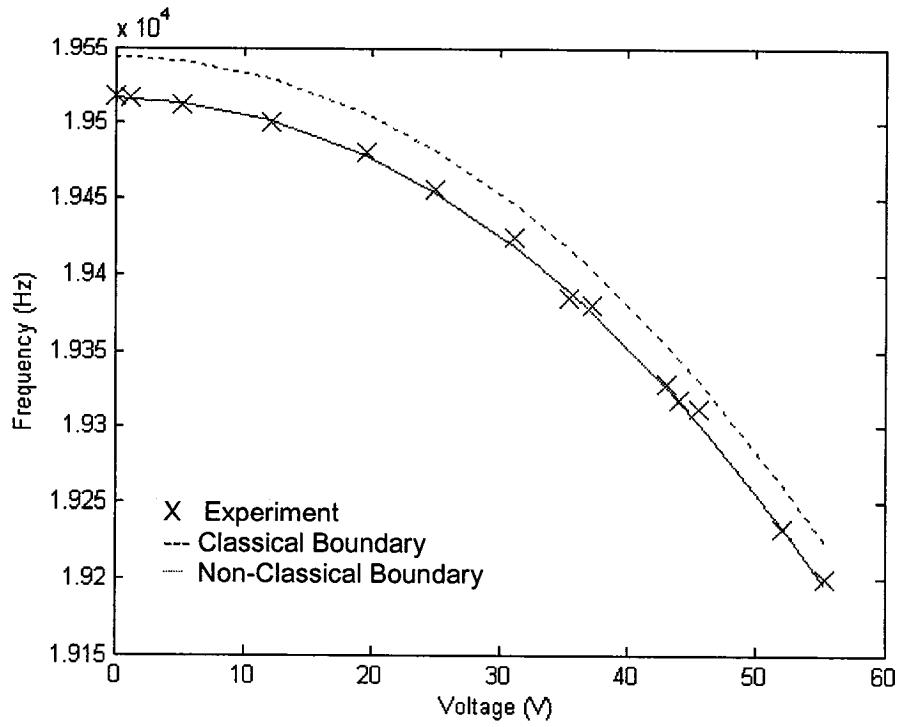
Figure 6.3. The experimental and theoretical frequency responses as a function of the applied voltage for the MicraGeM microcantilever #1.
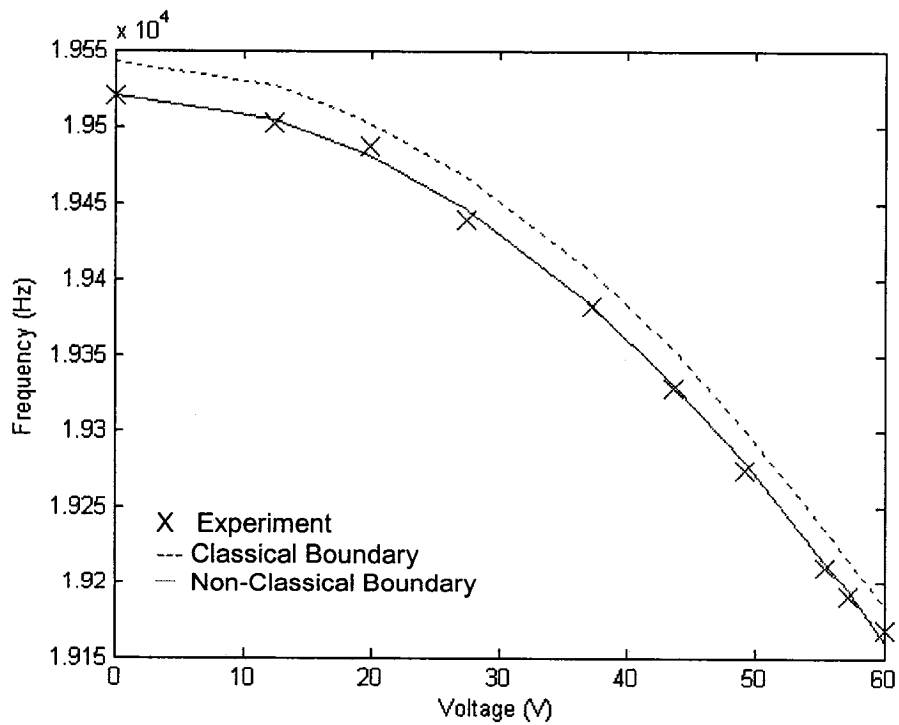
Figure 6.4. The experimental and theoretical frequency responses as a function of the applied voltage for the MicraGeM microcantilever #6.
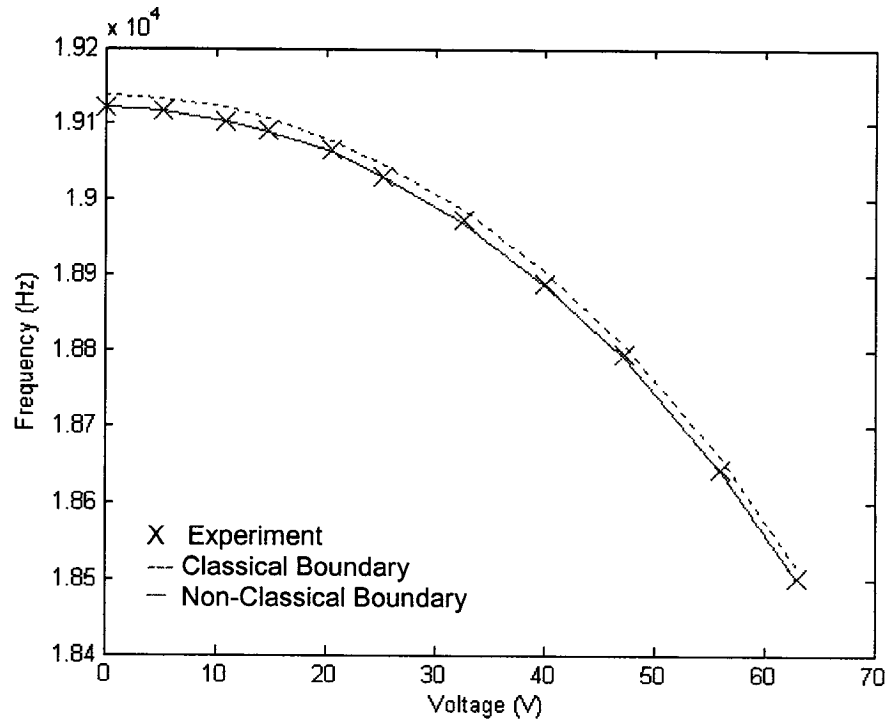
Figure 6.5. The experimental and theoretical frequency responses as a function of the applied voltage for the MicraGeM microcantilever #3.

The experimental results presented in Figures 6.3-6.5 are in very good agreement with the non-classical boundary support analysis, as presented in Chapter 5, using the segment Rayleigh-Ritz method.

The equivalent rotational stiffness, percent deviation from the classical boundary condition and electric field intensities are given in Table 6.2.

Table 6.2. The equivalent rotational stiffness values for MicraGeM microcantilevers #1, #3 and #6, the percentage difference between classical and non-classical theory, and the maximum electric field intensity used in these experiments.

Microcantilever	K_R^*	% Difference	V_{max}/d_0 (10^6 V/m)
1	695	0.14	4.15
3	574	0.08	4.74
6	439	0.11	4.51

The results for the rotational stiffness values for microcantilevers #1, #3 and #6 are consistent with those given in Chapter 5 for the MicraGeM technology process. The theoretical analysis using the segment Rayleigh-Ritz method allows one to minimize and in most cases eliminate the effects of the width discontinuities, such as for microcantilever #3, by dividing the microcantilevers into several segments as outlined in Chapter 3.

6.3. BOUNDARY SUPPORT-ELECTRO-THERMO-GEOMETRICAL SYNTHESIS

The effects of boundary support and electro-thermo influences on microcantilever #3 are presented here. An equivalent rotational stiffness K_R^* of 574 was used for the theoretical analysis as determined from the previous section. Given in Figure 6.6 is the variation in the resonance frequency as a function of the boundary support and thermo-electro influences.
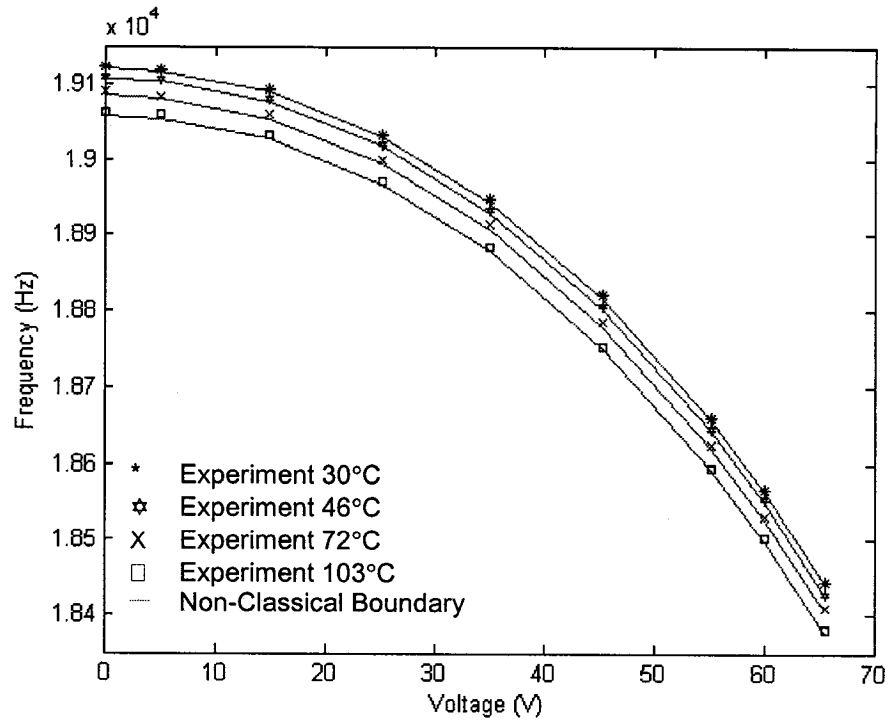
Figure 6.6. The variation of the natural frequency as a function of the boundary support condition and thermo-electro influences for microcantilever #3.

From Figure 6.6 it can be seen that the frequency response of microcantilever #3 is sensitive to both the applied bias voltage and the thermal loading for a given micromachined boundary support. The maximum variation due to the thermal influence at 0 voltage was found to be 0.30%, while at 65.5V it was found to have increased to 0.33%. Further experimentation is required at higher voltages as this deviation is expected to increase even further. For this, a *better* experimental setup is required in which the temperature remains stable for the duration of the experimental sampling.

6.4. Boundary Support-Single Cutout Synthesis

The influence of cutouts on the dynamic characteristics of several microcantilevers is given below. In the first analysis single cutouts are placed at various positions along a microcantilever and a frequency response is taken as a function of the position of the cutout. The mathematical formulation for the cutouts is based on the segment Rayleigh-Ritz approach discussed in Chapter 3. Given in Figure 6.7 is an overview of these microcantilevers along with the MATLAB cutout modeling. The results are also tabulated in Table 6.3 where the segmental lengths, thickness, theoretical and experimental natural frequencies, and the rotational stiffness values obtained for each microcantilever. The dimensions of the microcantilever cutouts are 54 x 54 μm^2 measured with an optical microscope. The width for each microcantilever is 100μm. The thicknesses were estimated from SEM images and from observations using an optical microscope. The lengths were obtained through estimates using an optical microscope.
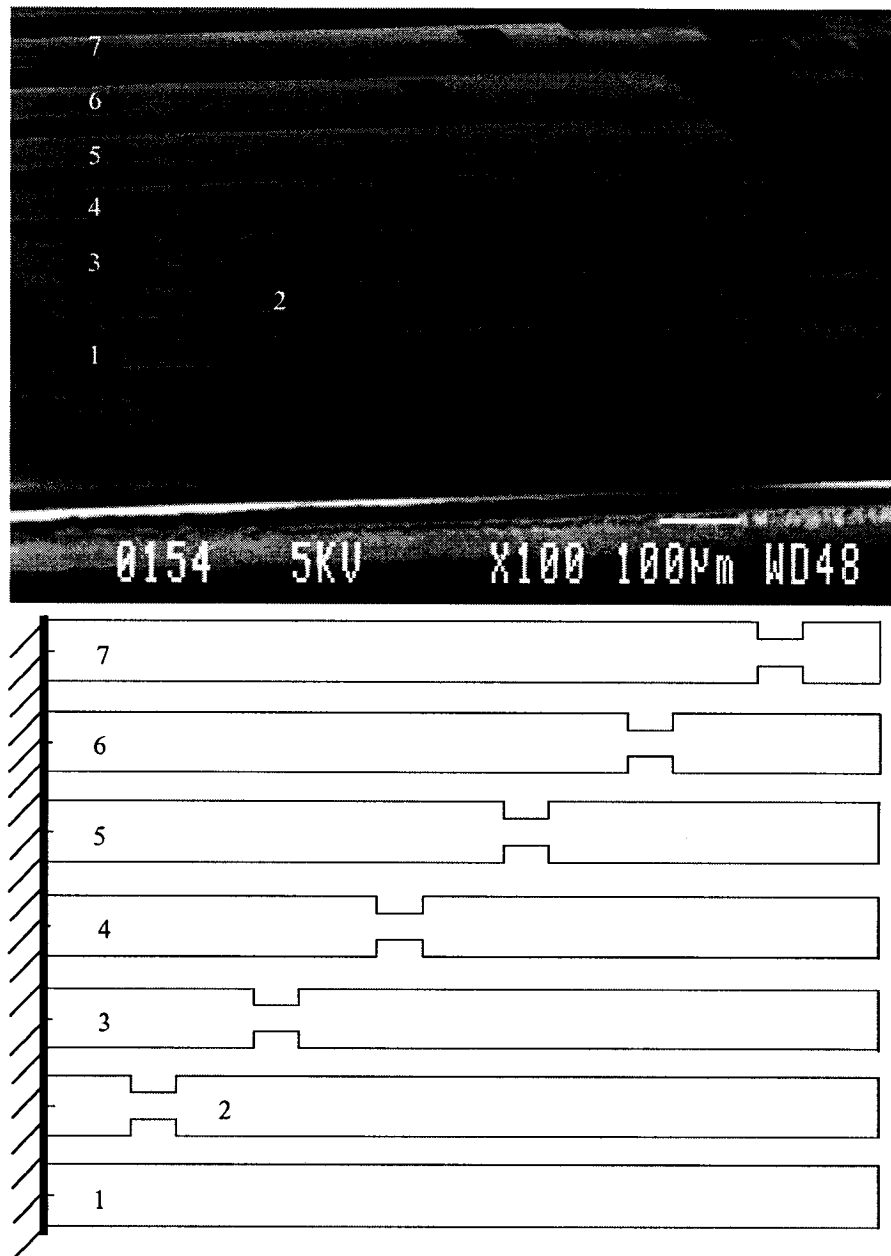
Figure 6.7. MicraGeM technology microcantilevers. Top: SEM image of microcantilevers with single cutout. Bottom: Simulation model.

With reference to Figure 6.7, for the microcantilevers #2 to #7 segment 1 is the segment to the left of the cutout; segment 2 is the cutout portion; segment 3 is the segment to the right of the cutout. Microcantilever #1 is also divided into three segments in order to have segment #2 the same length for all of the theoretical analysis.

166

Table 6.3. The segmental lengths, theoretical and experimental natural frequencies obtained, and the rotational stiffness values used to model the non-classical boundary supports.

Beam	Seg. 1 Length (μm)	Seg. 2 Length (μm)	Seg. 3 Length (μm)	Thickness (μm)	Exp. Freq. (Hz)	Theo. Freq. (Hz)	K_R^*
1	478	54	476	10.6	12576	12575	595
2	100	54	854	10.6	11613	11617	658
3	250	54	704	10.6	11776	11771	508
4	400	54	554	10.6	12167	12170	659
5	550	54	404	10.6	12575	12572	693
6	700	54	254	10.6	12755	12753	724
7	850	54	104	10.6	13099	13096	529
Mean							624

The theoretical results presented in Table 6.3 using the segment Rayleigh-Ritz method are in good agreement with experiment. The variations in the value of K_R^* are an indication of the sensitive nature of micromachining effects at the support boundary. The mean value of K_R^* is in good agreement with previous values obtained for the MicraGeM process. The results given in Table 6.3 indicate that the placement of the cutout on the microcantilever that can be used to influence the response of the microcantilever and hence can be used to tune the response by either *softening* or *stiffening* the elastic characteristics of the microcantilever.

The effect of multiple cutouts on the frequency responses of several microcantilevers is now presented. The analysis is given for microcantilevers with cutouts oriented from either the *clamped* end of the microcantilever or the *free* end of the microcantilever. This is shown in Figure 6.8.
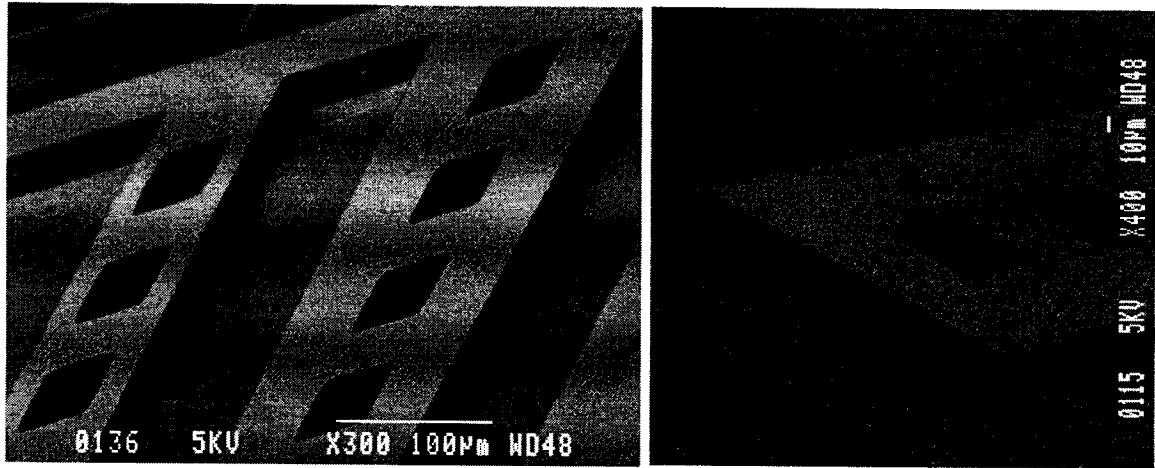
Figure 6.8. Left: Microcantilever beams with cutouts oriented towards the *clamped* end of the beam. Right: An example of microcantilever beam cutouts oriented towards the *free* end of the beam.

The investigation here is divided into two parts consisting of four sets each. Starting with cutouts oriented from the *clamped* end of the beam, the first set consists of 4 equally spaced 54 x 54 μm^2 cutouts on a straight microcantilever, the second set 8, the third 12, and the fourth 16. The cutouts are separated by 47μm. The investigation is carried out for microcantilever cutouts oriented from the *free* end of the beam. The microcantilever cutout models (Equation (3.1)) and the virtual deflections (Equation (2.33)) are presented

168

in Figures 6.9-6.11. Shown in Figure 6.12 is a typical frequency response obtained in the experimental investigation.
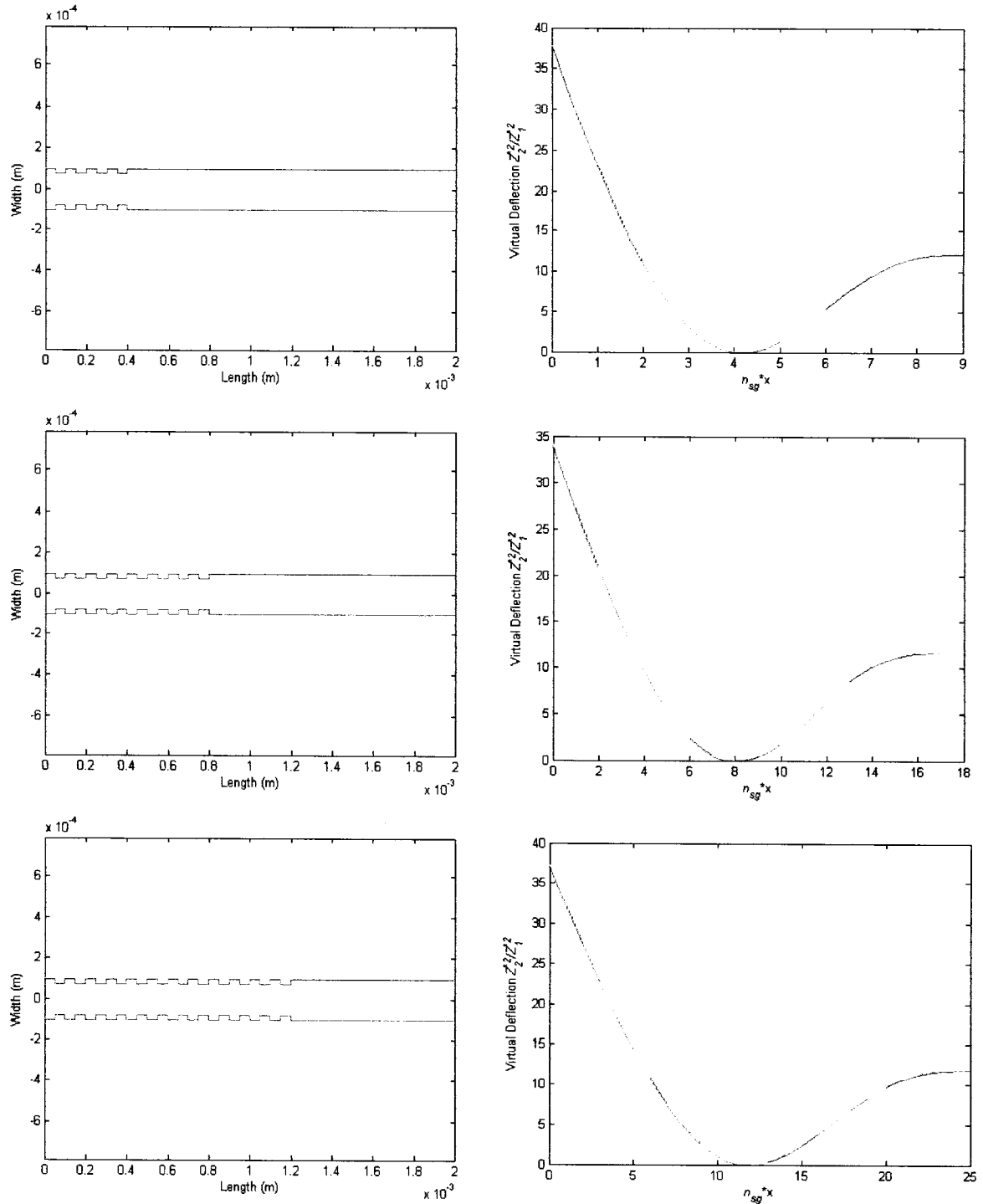
Figure 6.9. Left: MATLAB model for multiple cutouts oriented from the *clamped* end of the microcantilever, for 4, 8, and 12 cutouts respectively. Right: The virtual deflection for each microcantilever as a function of the number of cutouts.
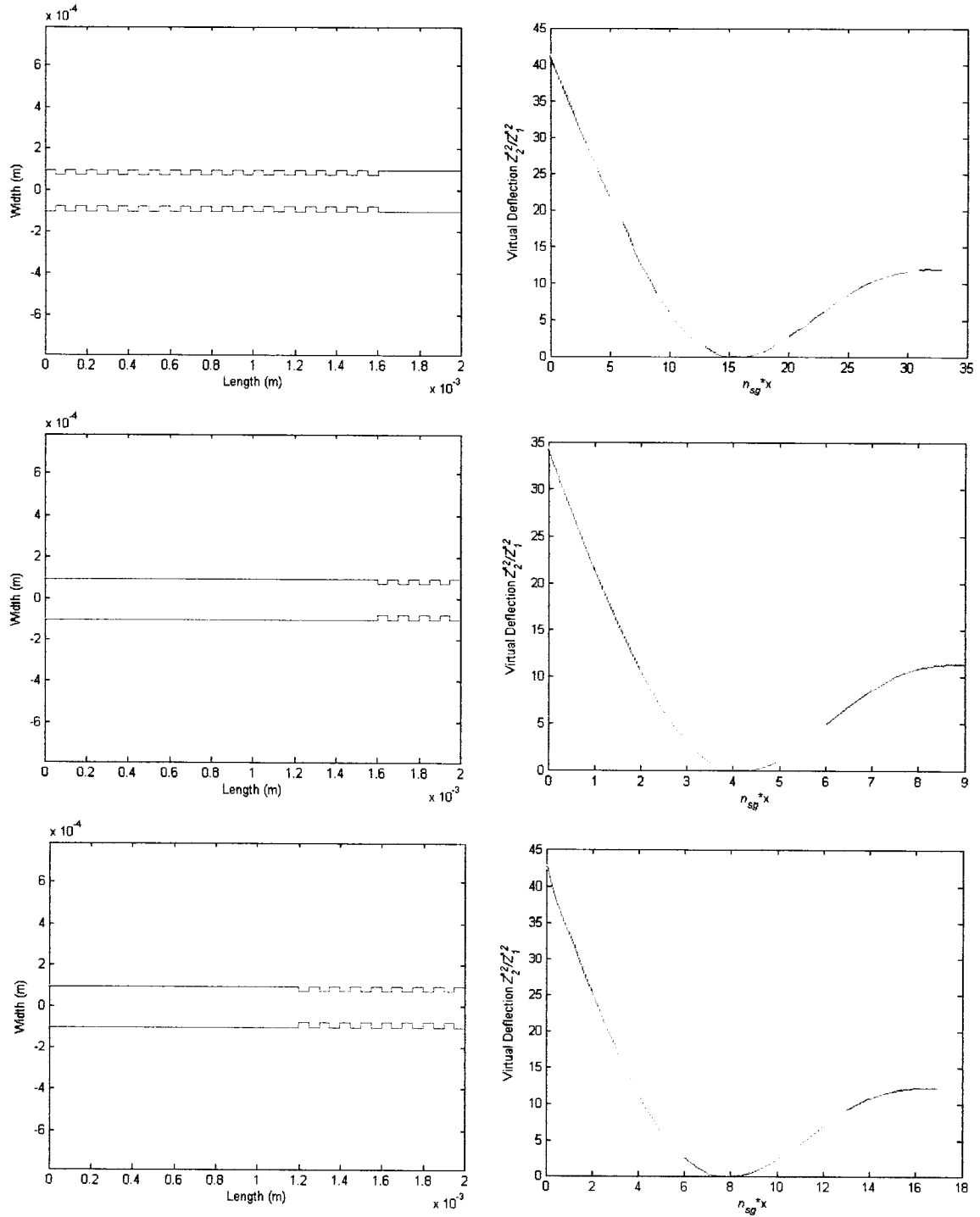
Figure 6.10. Left: Top: MATLAB model for multiple cutouts oriented from the *clamped* end of the microcantilever for 16 cutouts. Middle and Bottom: MATLAB model for multiple cutouts oriented from the *free* end of the microcantilever for 4 and 8 cutouts respectively. Right: The virtual deflection for each microcantilever as a function of the number of cutouts.

170
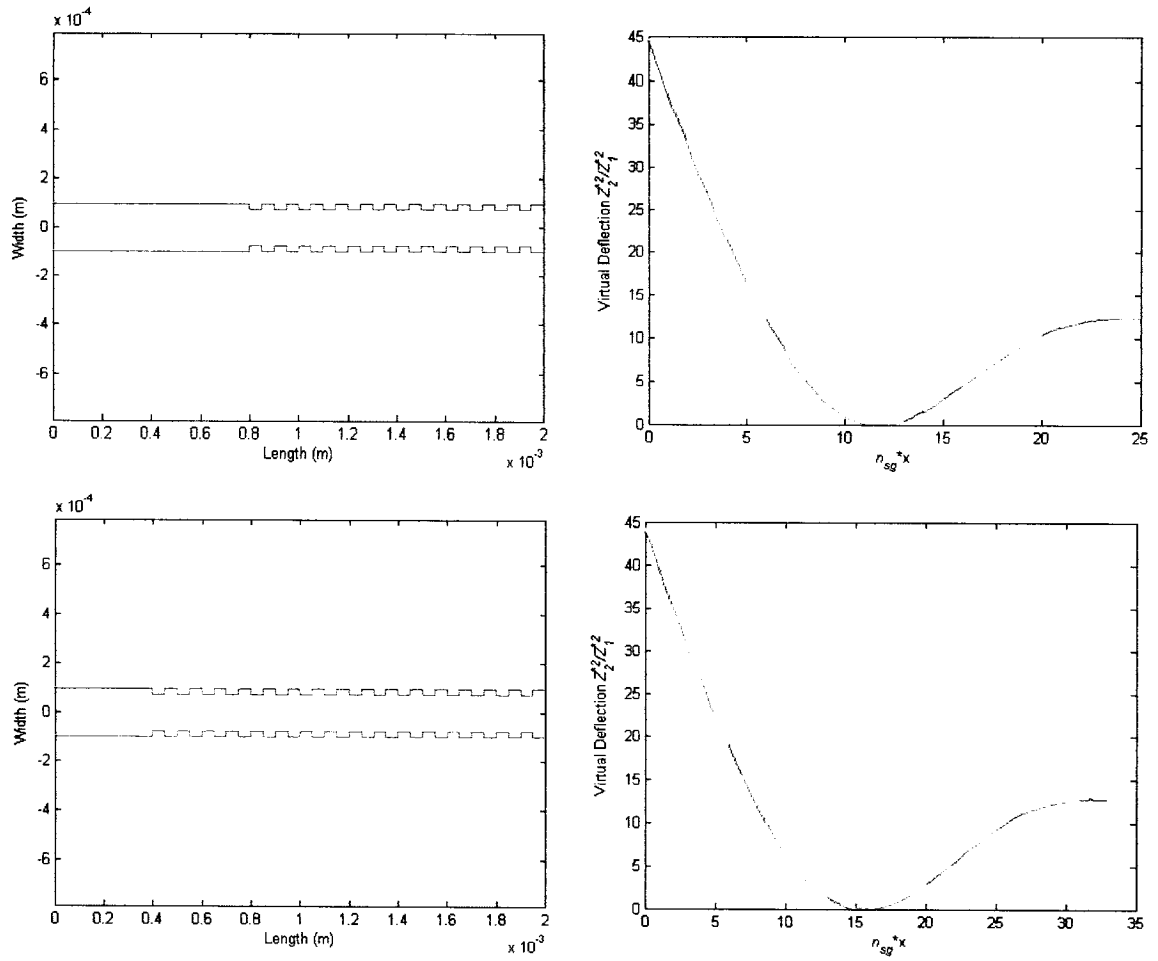
Figure 6.11. Left: MATLAB model for multiple cutouts oriented from the *free* end of the microcantilever 12 and 16 cutouts respectively. Right: The virtual deflection for each microcantilever as a function of the number of cutouts.
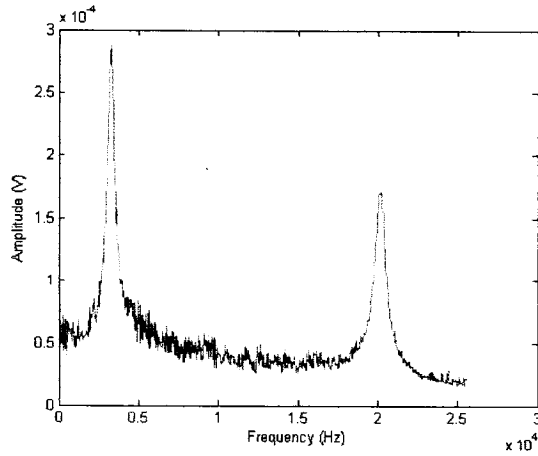
Figure 6.12. A typical frequency response profile as obtained for these experiments.

171

The results obtained for the first and second natural frequencies as a function of the number and orientation of the microcantilever cutouts are presented in Table 6.4. In reading Table 6.4, the following definitions apply: 4C, 8C, 12C, and 16C indicates 4, 8, 12, and 16 cutouts oriented from the *clamped* end of the microcantilever, respectively, and 4F, 8F, 12F, and 16F indicates 4, 8, 12, and 16 cutouts oriented from the *free* end of the microcantilever, respectively.

Table 6.4. The first and second natural frequencies as a function of the number and orientation of microcantilever cutouts. The equivalent non-classical boundary support stiffness is also given for comparison.

Microcantilever	1st nat. Freq. (Hz)	Exp. (Hz)	2nd nat. Freq. (Hz)	Exp. (Hz)	K_R^*
4C	3105	3104	19976	19968	580
8C	3055	3051	20165	20128	598
12C	3045	3043	20083	20032	511
16C	3010	3008	19328	19387	525
4F	3337	3340	20327	20320	612
8F	3423	3439	20350	20327	562
12F	3435	3433	19949	19968	523
16F	3358	3355	19689	19680	614
Mean					565

The first and second natural frequencies given in the table above, are a function of the number and location of cutouts placed on the microcantilevers. It can be seen that the 1st and 2nd natural frequencies do not show the same trends as the modes of vibration are

different, and the cutouts are influencing the vibrational response of these microcantilevers.

6.6. BOUNDARY SUPPORT-MULTIPLE CUTOUT-GEOMETRY SYNTHESIS

The investigation into the multiple cutout influence is continued in this section with the inclusion of microcantilever geometry into the overall analysis. Shown in Figure 6.13 is an SEM overview of a series of MicraGeM technology microcantilevers with varying geometries. In this figure it can be seen that the *SORI* microcantilever has touched down onto the substrate. The MATLAB simulation models and virtual deflections are given in Figures 6.14-6.15, and the results for the first two natural frequencies and the equivalent boundary support rotational stiffness are presented in Table 6.5.
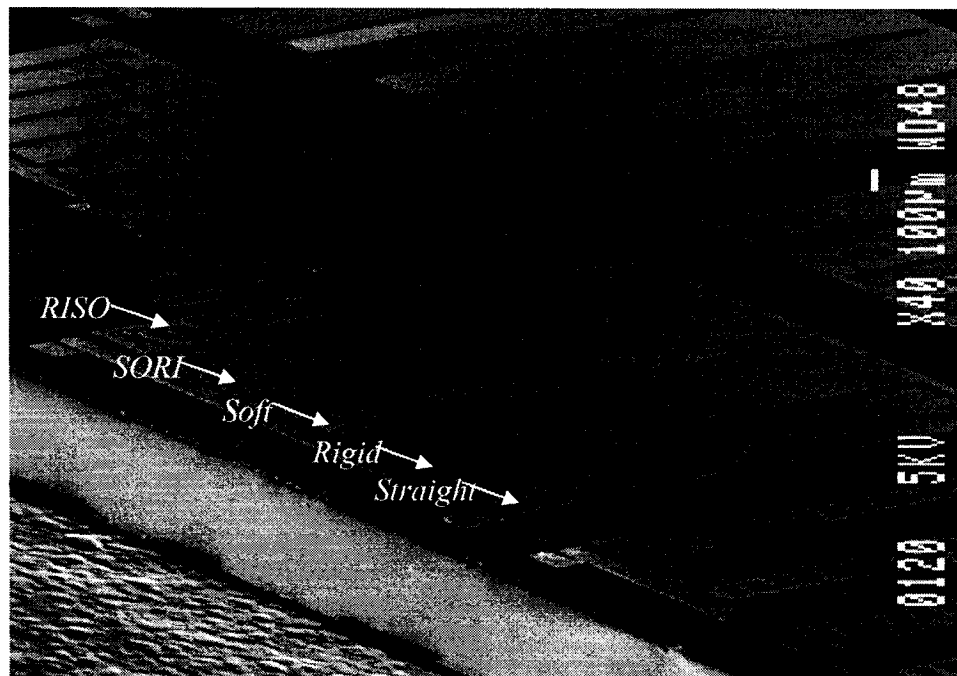
Figure 6.13. SEM image of a microcantilever array of various geometries with multiple cutouts. The microcantilevers were fabricated with the MicraGeM technology.

173
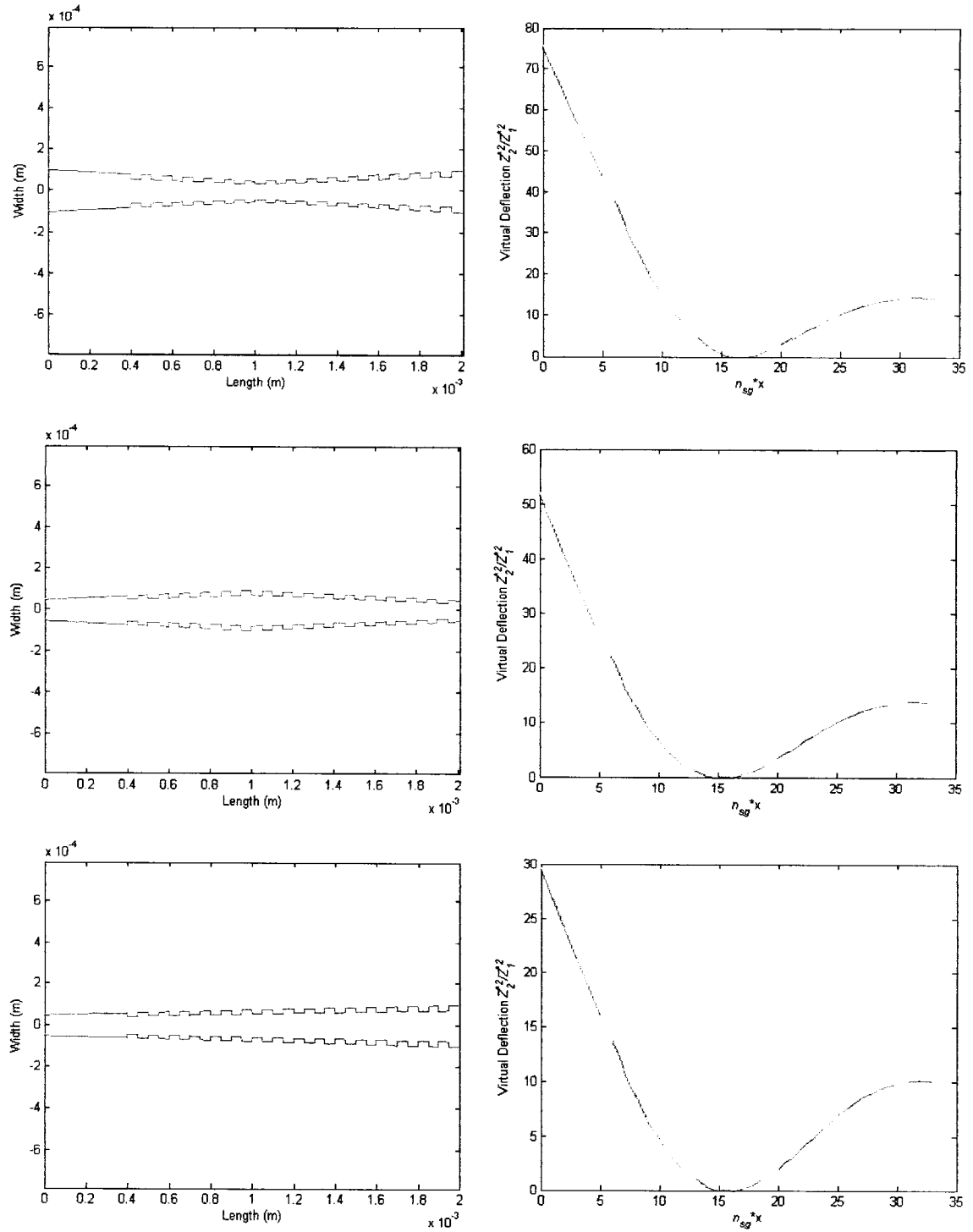
Figure 6.14. Left: MATLAB model for multiple cutouts oriented from the *free* end of the microcantilever for 16 cutouts and for *RISO*, *SORI* and *soft* geometry respectively top to bottom. Right: The virtual deflection for each microcantilever as a function of the cutouts and geometry.

174
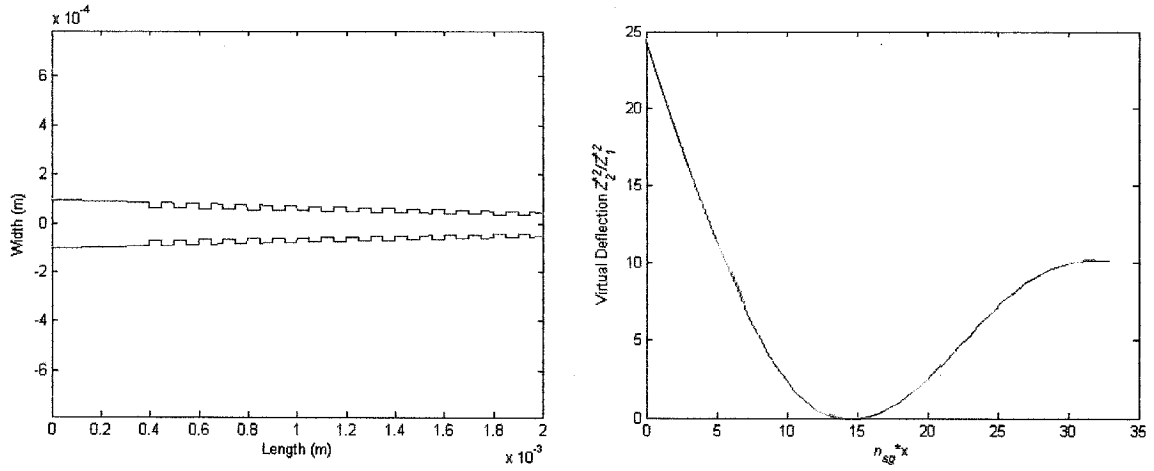
Figure 6.15. Left: MATLAB model for multiple cutouts oriented from the *free* end of the microcantilever for 16 cutouts for *rigid* geometry. Right: The virtual deflection as a function of the cutouts and geometry.

A close up of the microcantilever cutouts for the *SORI* geometry is shown in Figure 6.16.

Figure 6.16. An SEM image showing a close up of the microcantilever cutouts for the *SORI* geometry.

175

Table 6.5. The first and second natural frequencies as a function of the microcantilever cutouts and geometries. The equivalent non-classical boundary support stiffness is also given for comparison. The value for the *straight 16F* microcantilever is taken from Table 6.4 and is reprinted here for comparison.

Microcantilever	1st nat. Freq. (Hz)	Exp. (Hz)	2nd nat. Freq. (Hz)	Exp. (Hz)	K_R^*
RISO 16F	3042	3045	19603	19648	506
SORI 16F	3328	3328	20265	20224	582
Soft 16F	2624	2622	18496	18471	511
Rigid 16F	4224	4225	21216	21257	694
Straight 16F	3358	3355	19689	19680	614
Mean					581

Shown in Figure 6.17 is an SEM image of the *free* end of a type of *SORI* geometry microcantilever beam for the width conditioning parameter β=100.
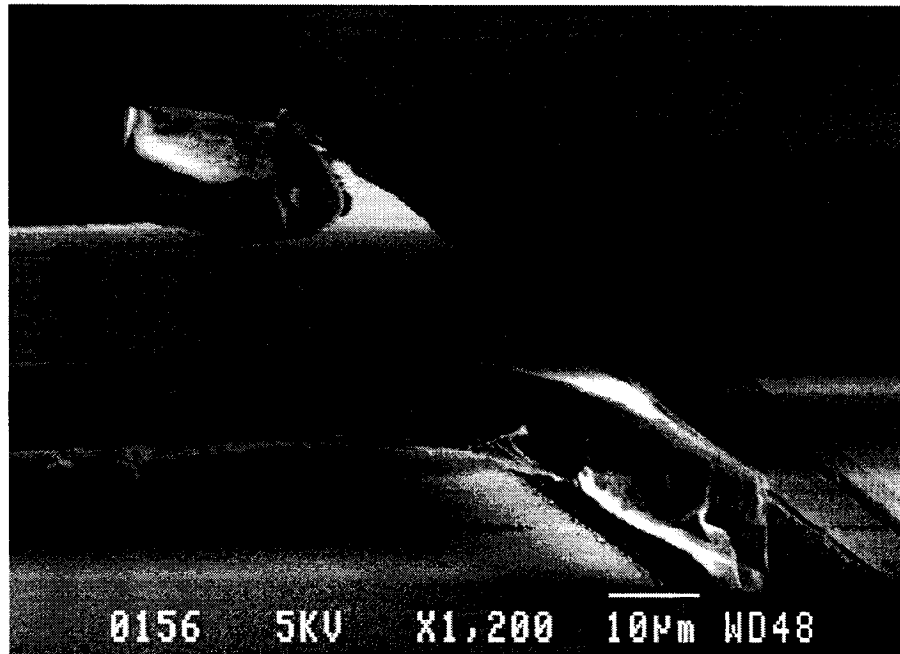
Figure 6.17. An SEM image of a MicraGeM technology microcantilever at the *free* end. This particular beam has *RISO* geometry.

176

The results shown in Table 6.5 are a function of boundary support, cutouts and taper geometry and are in good agreement with the analytical results obtained with the segment Rayleigh-Ritz method. Hence, the taper geometry can be used to further tune the microcantilever either through stiffening with the *rigid* tapering or softening with the *soft* taper.

The comprehensive microsystem synthesis is presented below. In the investigation four different microcantilever beam geometries and with varying numbers of cutouts are analyzed under different electrostatic and thermal loading conditions. In all the cases the boundary support characterization is also included in the modeling.

6.7. SUPPORT BOUNDARY-ELECTROSTATIC-THERMAL-RIGID GEOMETRY-CUTOUTS SYNTHESIS

The multi-parameter synthesis of a *rigid* microcantilever beam geometry with a 16C cutout orientation is given here. Shown in Figure 6.18 are two SEM images of the MicraGeM technology microcantilevers with cutouts. For the analysis presented below the following parameters were used, the measured length $L = 2012\mu m$, thickness $h = 10.6\mu m$, and width $w = 200\mu m$ (where $w_0 = 100\mu m$ and $\delta = 50\mu m$), and the dielectric gap d_0 was estimated as $12.8\mu m$.
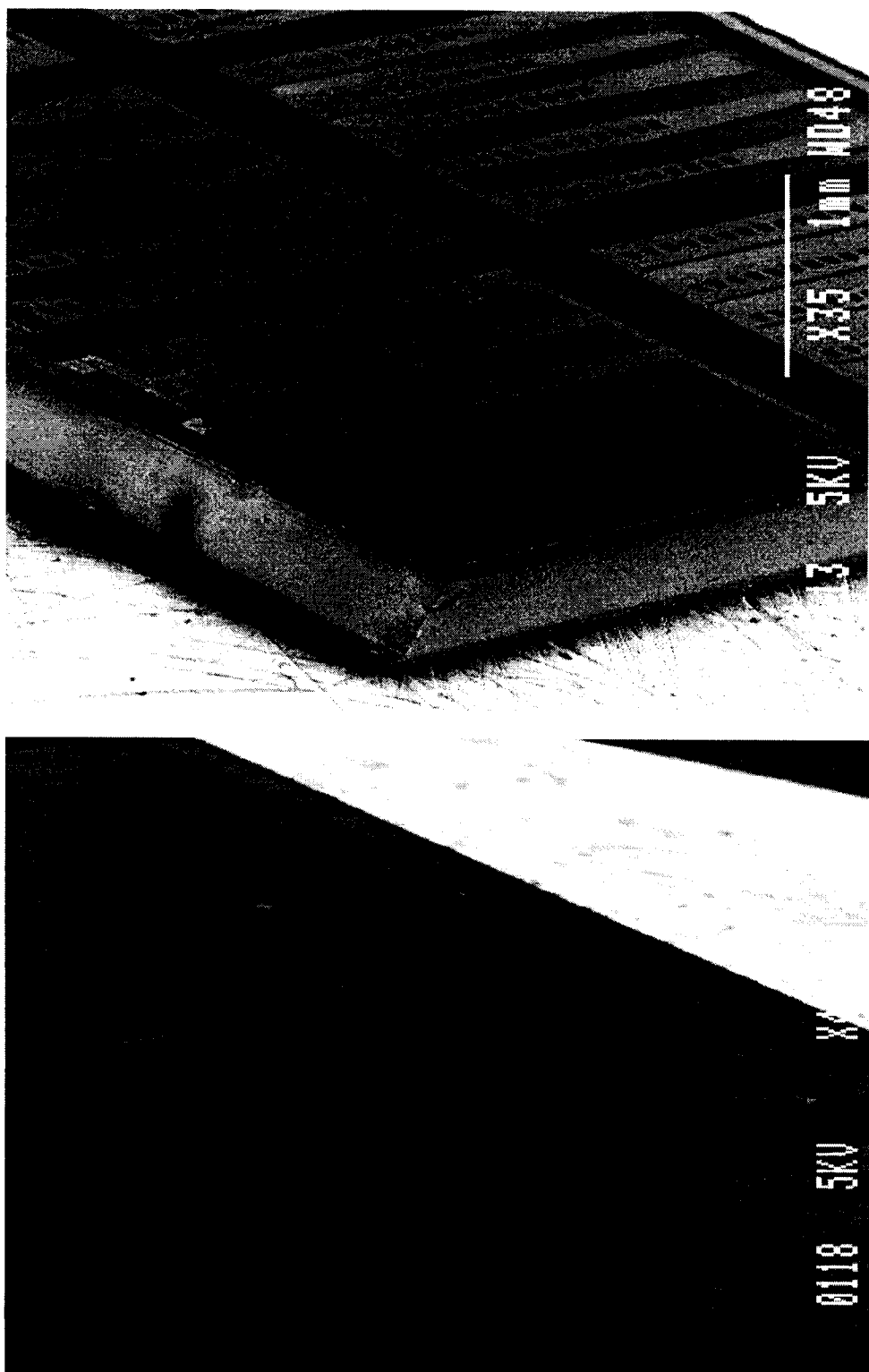
Figure 6.18. Top: An SEM overview of the MicraGeM technology microcantilevers. Bottom: *Clamped* end cutout orientation.

Shown in Figure 6.19 is the MATLAB model representing the *rigid* 16C microcantilever

beam.
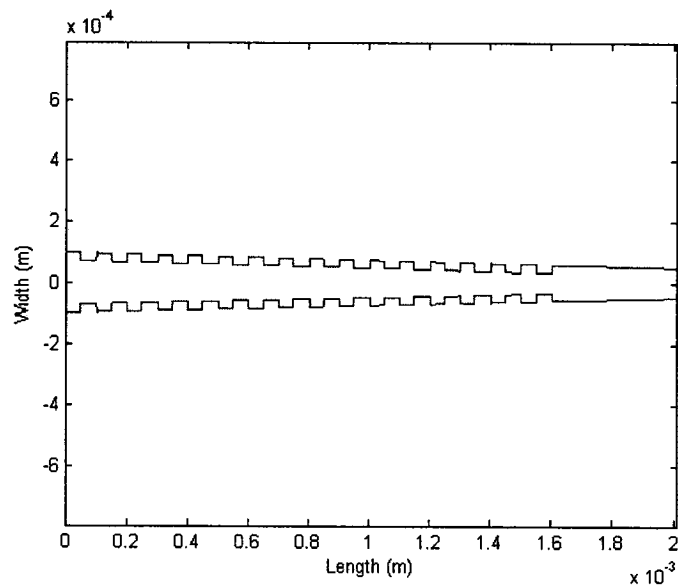
Figure 6.19. *Rigid* 16C microcantilever geometry generated using MATLAB.

Presented in Figures 6.20-6.22 are the variations to the first and second natural

frequencies as a function of the applied voltage, thermal loading, geometry, and cutouts.

The estimated touchdown voltage for this beam is estimated as ~1.2V, hence the

maximum value used for the experiments was 0.8V.
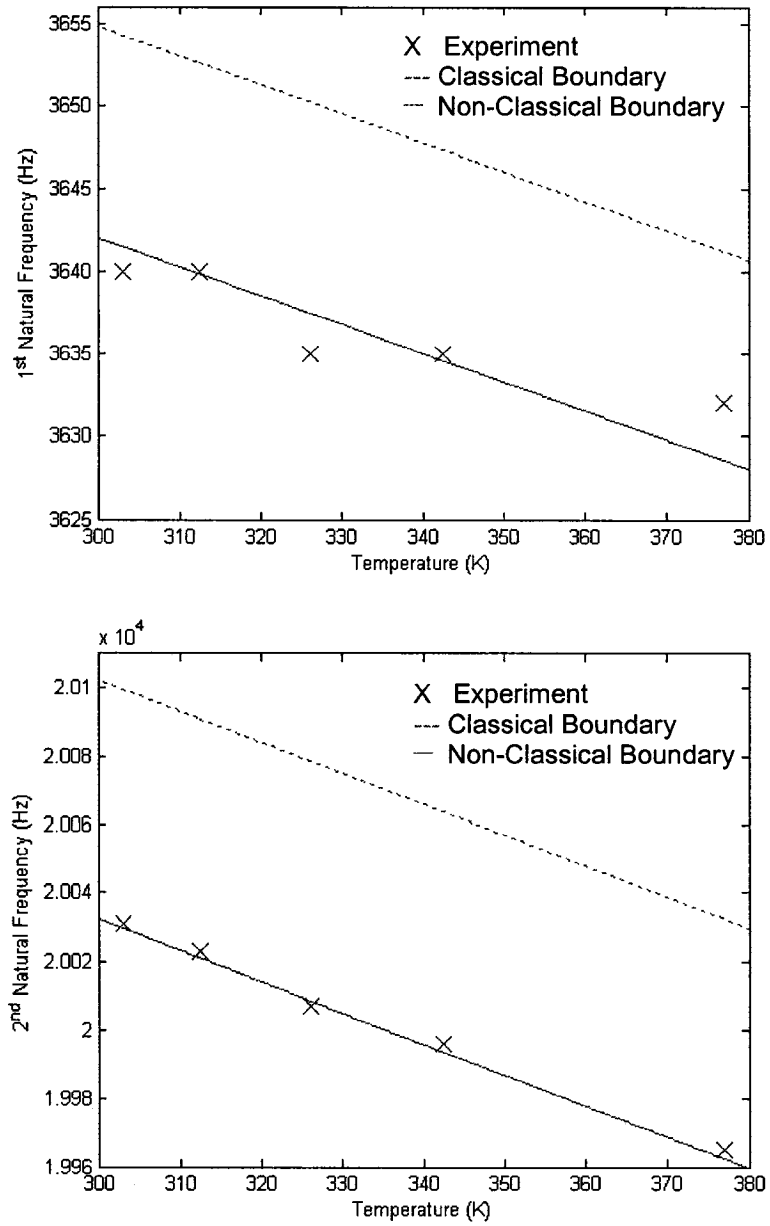
Figure 6.20. Top: The variation of the 1st natural frequency of the *rigid* 16C as a function of an applied 0.5V electrostatic potential and thermal loading. Bottom: The 2nd natural frequency variation.
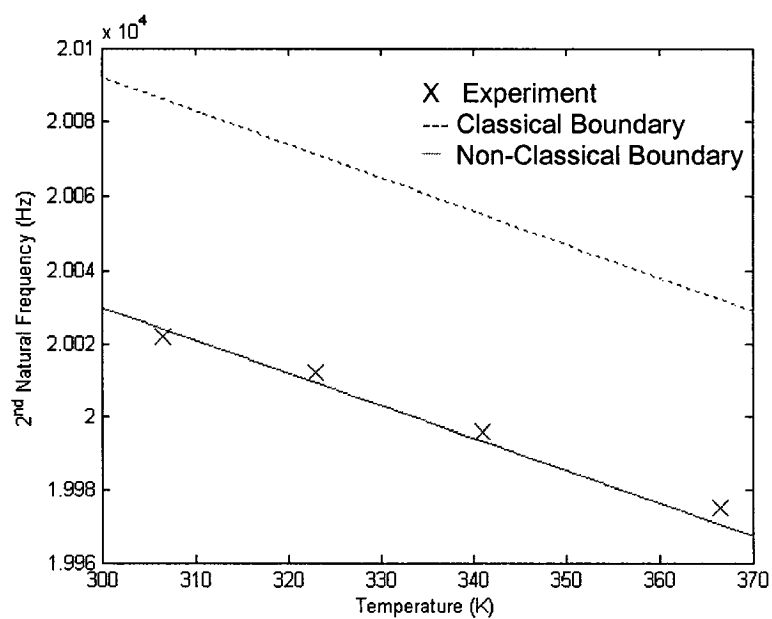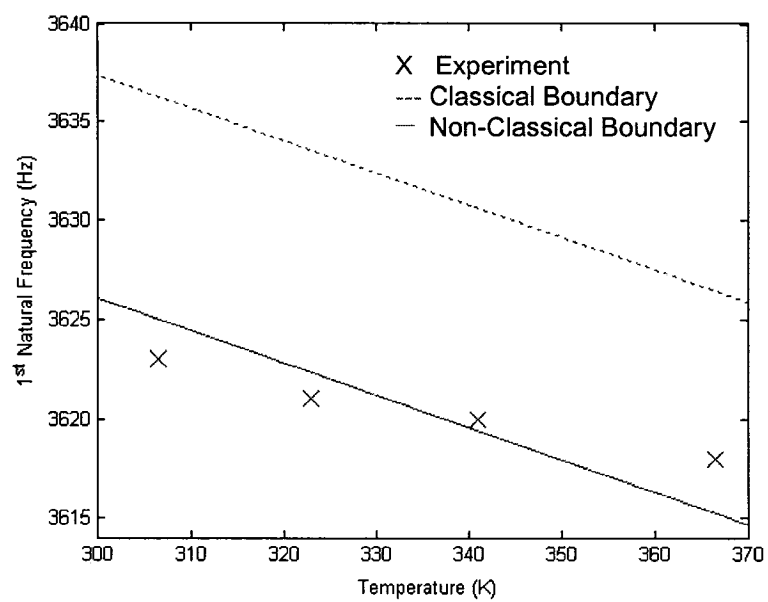
Figure 6.21. Top: The variation of the 1st natural frequency of the *rigid* 16C as a function of an applied 0.6V electrostatic potential and thermal loading. Bottom: The 2nd natural frequency variation.

181
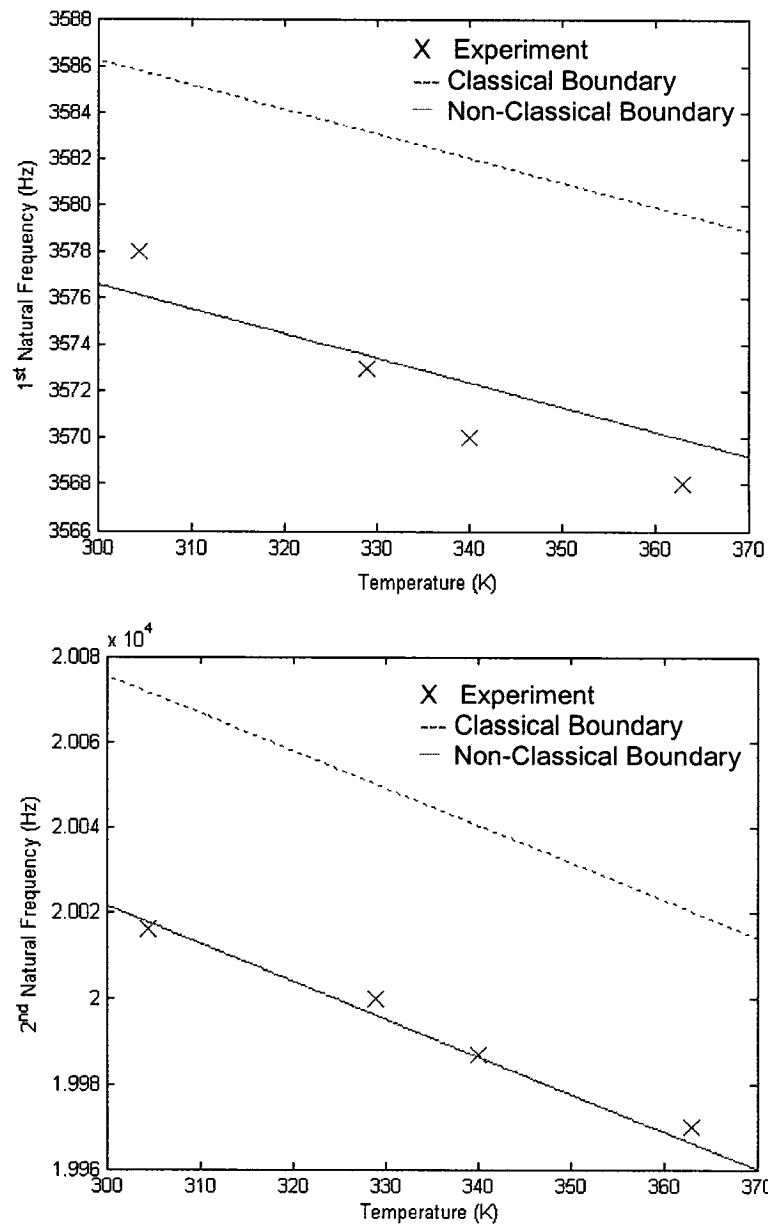
Figure 6.22. Top: The variation of the 1st natural frequency of the *rigid* 16C as a function of an applied 0.8V electrostatic potential and thermal loading. Bottom: The 2nd natural frequency variation.

Given in Table 6.6 are the theoretical and experimental values obtained for the *rigid* 16C microcantilever. The equivalent boundary support stiffness K_R^*, for this microcantilever design is 567 which is in agreement with previous values obtained for MicraGeM microfabrication process.

Table 6.6. The synthesis (boundary support, electrostatic, thermal, geometry, and cutouts) values obtained for the *rigid* 16C microcantilever.

Voltage (V)	Temperature (K)	1st nat. Freq. (Hz)	Exp. Freq. (Hz)	2nd nat. Freq. (Hz)	Exp. Freq. (Hz)
0	294	3676	3677	20035	20042
0.5	303	3642	3640	20029	20034
0.5	312	3640	3640	20021	20029
0.5	326	3637	3635	20009	20013
0.5	342.5	3636	3635	19994	19998
0.5	377	3631	3632	19962	19970
0.6	306.5	3625	3623	20024	20029
0.6	323	3622	3621	20009	20015
0.6	341	3620	3620	19994	20000
0.6	366.5	3615	3618	19970	19981
0.8	304.5	3576	3580	20018	20016
0.8	329	3574	3573	19996	20003
0.8	340	3572	3570	19985	19990
0.8	363	3570	3568	19967	19973

The experimental results presented in Table 6.6 are in good agreement with the theoretical formulation. The natural frequencies decrease as a function of both the applied voltages and thermal loading. The scattered temperatures at the different voltages are due to thermal drifting due to the difficulty in maintaining a stable temperature for the duration of the particular experiment. The individual 5 microcantilever arrays as shown in Figure 6.18 were all fabricated with a common bottom electrode, and hence in this regard the maximum voltage was limited by the snap down voltage of the *soft* microcantilever in each case.

6.8. Support Boundary-Electrostatic-Thermal-SORI Geometry-Cutouts Synthesis

Presented here is the multi-parameter synthesis of a *SORI* microcantilever beam geometry with an 8F cutout orientation. Illustrated in Figure 6.23 is the MATLAB simulation model of this microcantilever.
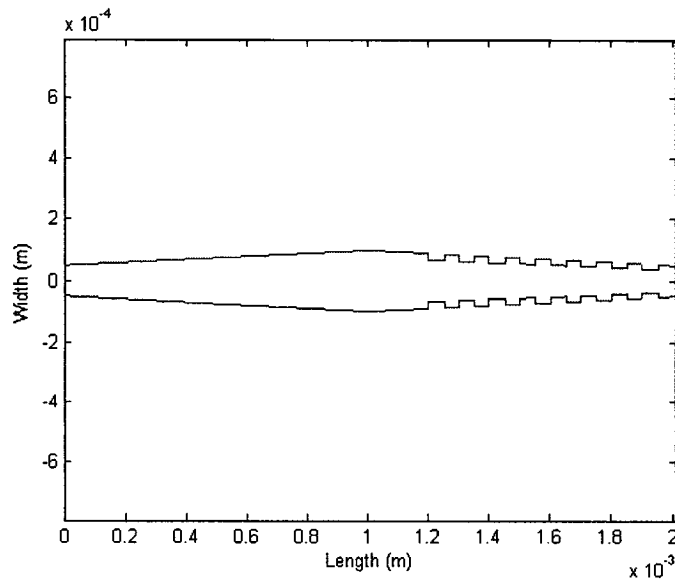
Figure 6.23. *SORI* 8F microcantilever geometry generated using MATLAB.

The results are presented in Figures 6.24-6.26 and the values obtained are tabulated in

Table 6.7 along with the non-classical boundary support stiffness.
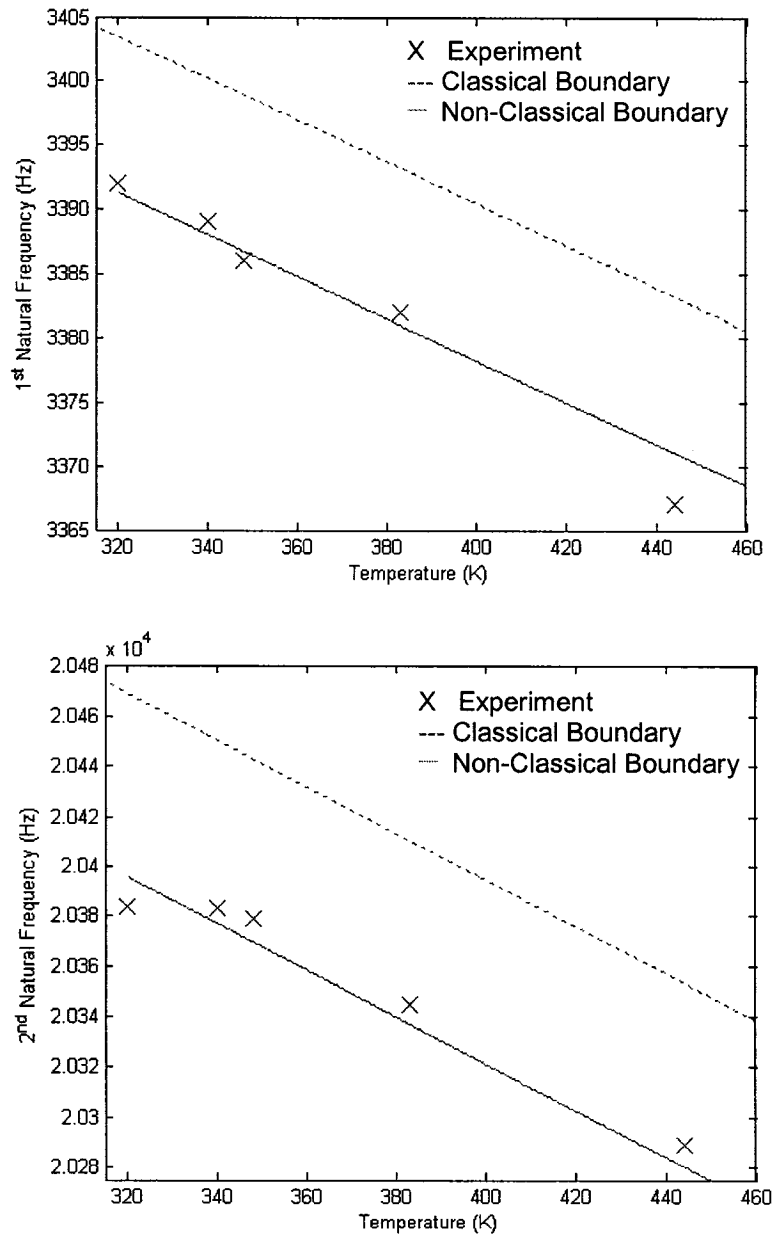
Figure 6.24. Top: The variation of the 1st natural frequency of the *SORI* 8F as a function of an applied 15.6V electrostatic potential and thermal loading. Bottom: The 2nd natural frequency variation.
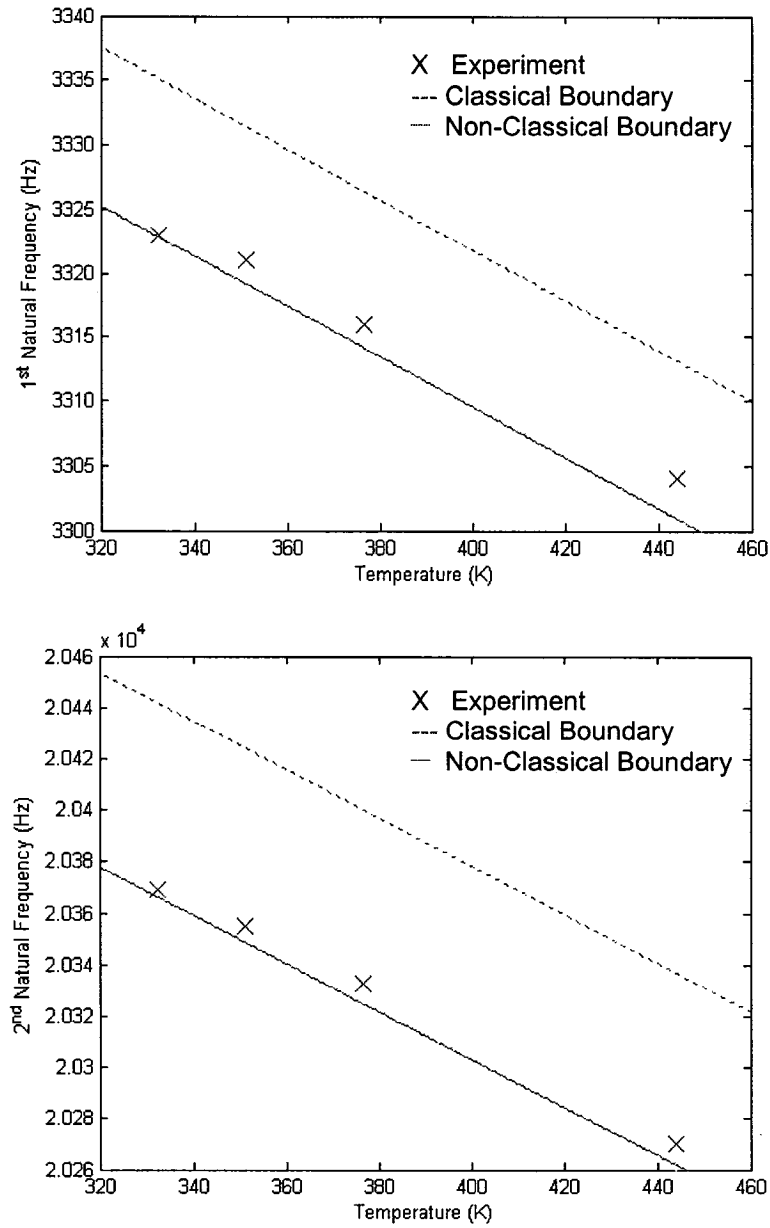
Figure 6.25. Top: The variation of the 1st natural frequency of the *SORI* 8F as a function of an applied 19.2V electrostatic potential and thermal loading. Bottom: The 2nd natural frequency variation.
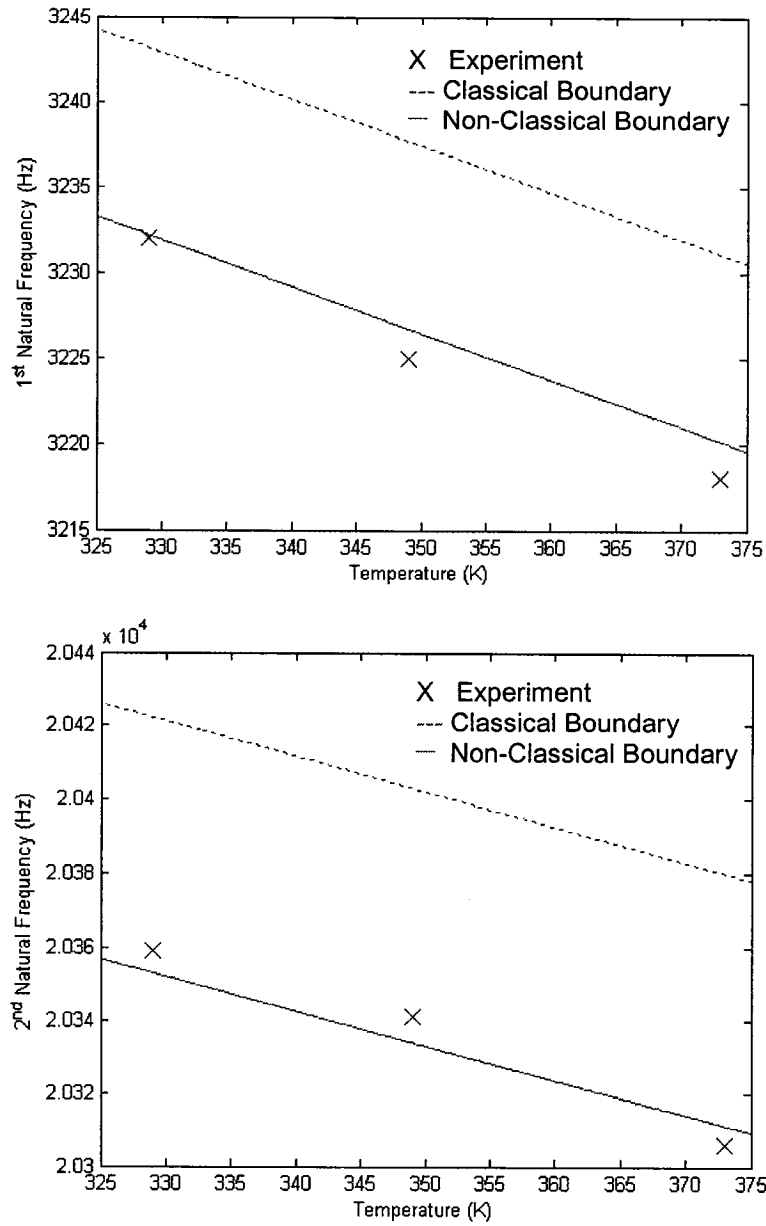
Figure 6.26. Top: The variation of the 1st natural frequency of the *SORI* 8F as a function of an applied 20.4V electrostatic potential and thermal loading. Bottom: The 2nd natural frequency variation.

187

Table 6.7. The synthesis (boundary support, electrostatic, thermal, geometry, and cutouts) values obtained for the *SORI* 8F microcantilever.

Voltage (V)	Temperature (K)	1st nat. Freq. (Hz)	Exp. Freq. (Hz)	2nd nat. Freq. (Hz)	Exp. Freq. (Hz)
0	294	3417	3424	20438	20480
15.6	320	3391	3392	20395	20384
15.6	340	3388	3389	20377	20383
15.6	348	3387	3386	20370	20379
15.6	383	3381	3382	20337	20345
15.6	444.2	3371	3367	20280	20289
19.2	332.5	3323	3323	20366	20369
19.2	351	3319	3321	20349	20355
19.2	376.5	3314	3316	20325	20333
19.2	444	3301	3304	20262	20270
20.4	329	3232	3232	20353	20359
20.4	349	3227	3225	20334	20341
20.4	373	3220	3218	20311	20306

The experimental results obtained for the *SORI* 8F microcantilever configuration show good agreement with the theoretical formulation established in Chapter 3. The estimated touch down voltage for this 5 microcantilever array was ~25volts. The cutouts for this microcantilever serve to reduce the mass and hence an increase in the natural frequency is obtained with respect to a similar microcantilever geometry without cutouts. The

rotational stiffness value is in agreement with previous values estimated for the MicraGeM process. The rotational stiffness value K_R^* was found to be 642.

6.9. SUPPORT BOUNDARY-ELECTROSTATIC-THERMAL-SOFT GEOMETRY-CUTOUTS SYNTHESIS

Presented here is the multi-parameter synthesis of a *soft* microcantilever beam geometry with an 8F cutout orientation. Shown in Figure 6.27 is the simulation model of this microcantilever generated using MATLAB. Shown in Figure 6.28 is a close up of the *free* end of a typical MicraGeM technology microcantilever. The results are presented in Figures 6.29-6.31. The tabulated results and equivalent boundary support stiffness are given in Table 6.8.
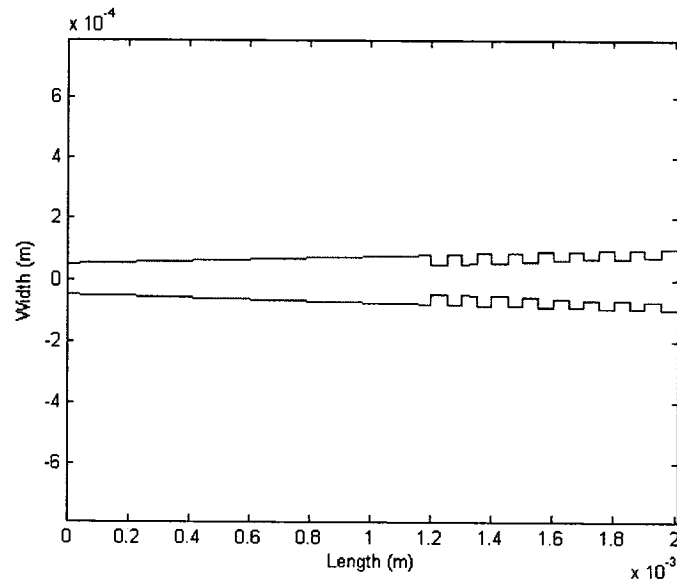
Figure **6.27.** *Soft* 8F microcantilever geometry generated using MATLAB.

Figure **6.28.** An SEM image of a typical MicraGeM technology microcantilever. This image shows the slight variations to the microcantilever thickness.

190
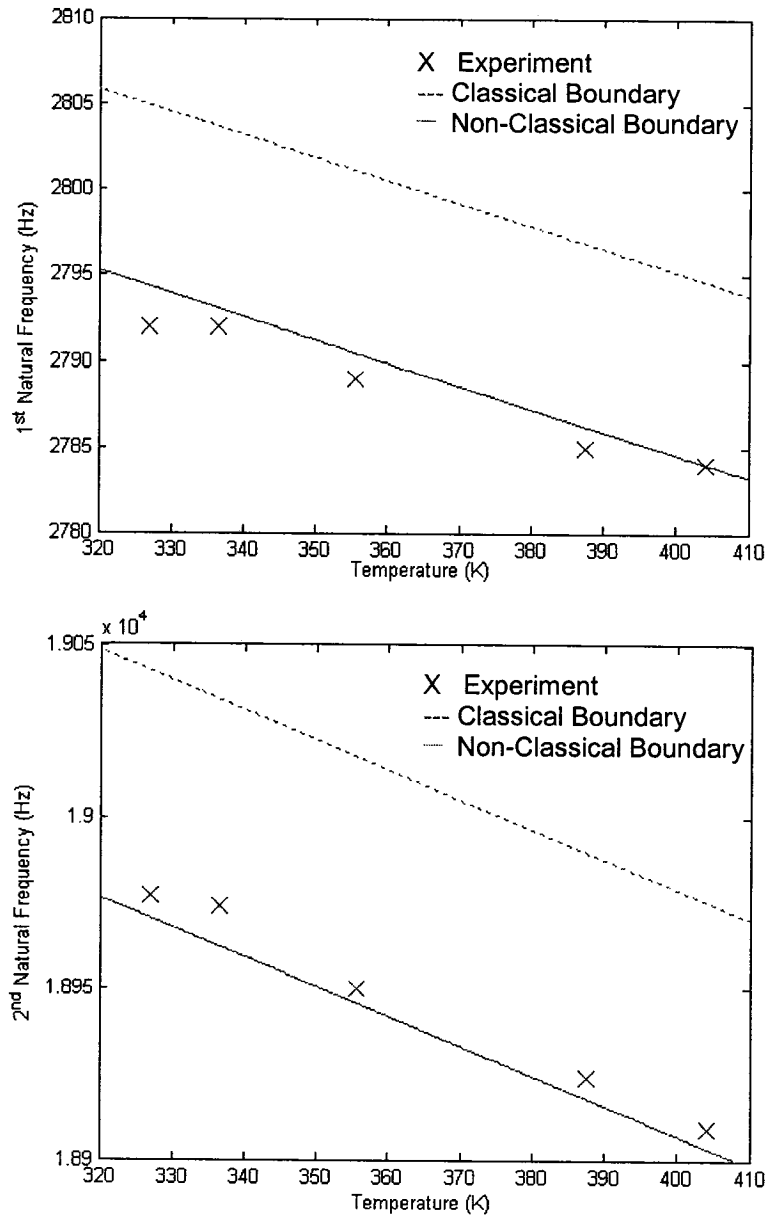
Figure 6.29. Top: The variation of the 1st natural frequency of the *soft* 8F as a function of an applied 8V electrostatic potential and thermal loading. Bottom: The 2nd natural frequency variation.
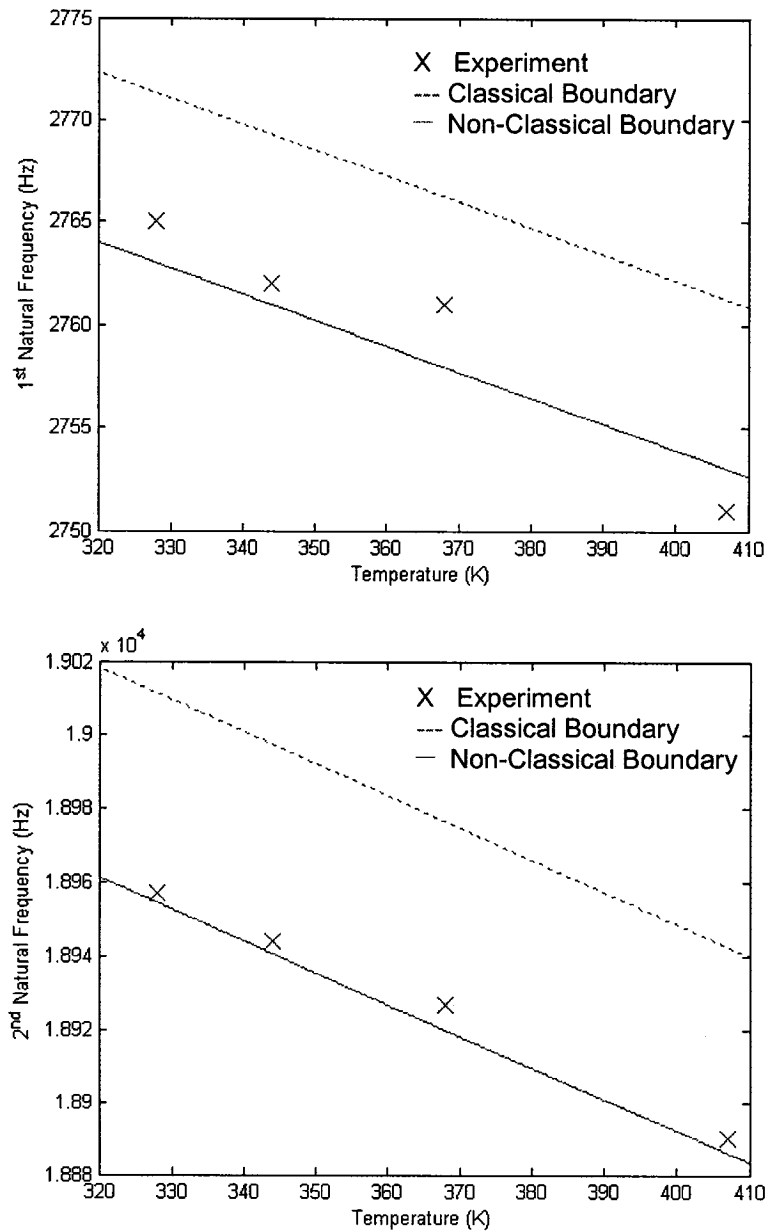
Figure 6.30. Top: The variation of the 1st natural frequency of the *soft* 8F as a function of an applied 16.4V electrostatic potential and thermal loading. Bottom: The 2nd natural frequency variation.
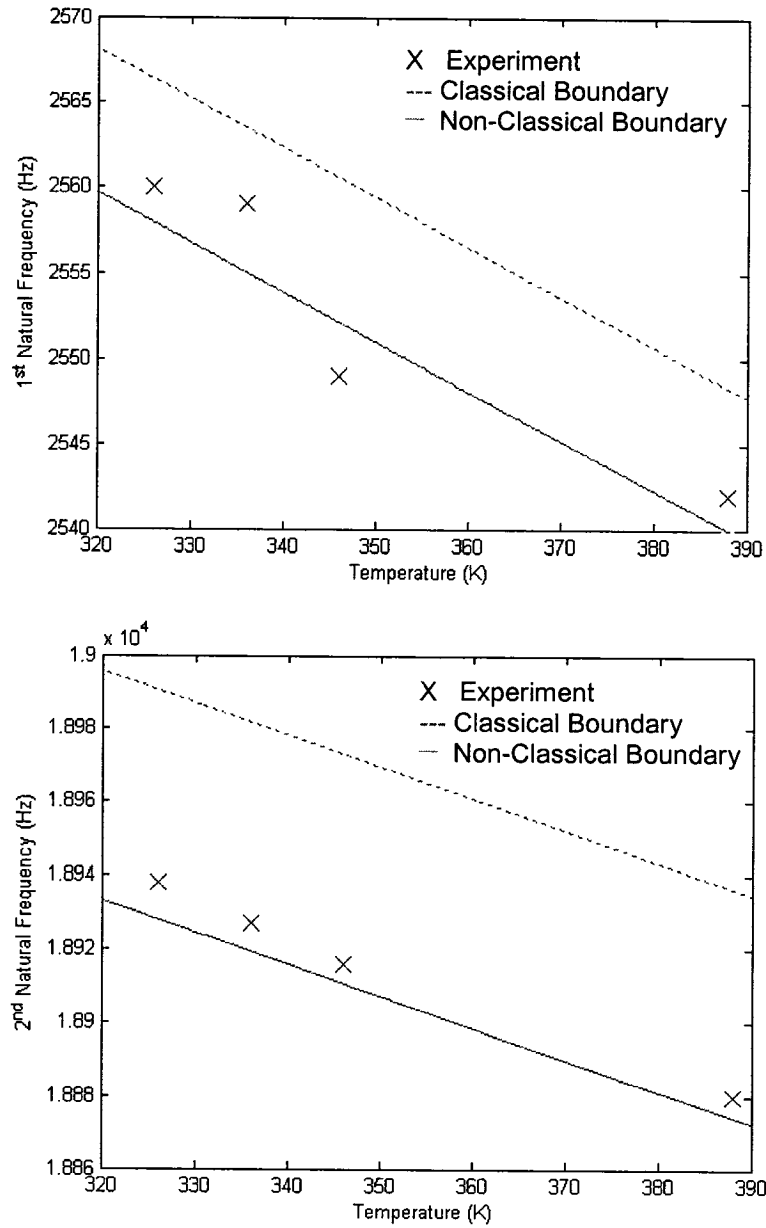
Figure 6.31. Top: The variation of the 1st natural frequency of the *soft* 8F as a function of an applied 20.6V electrostatic potential and thermal loading. Bottom: The 2nd natural frequency variation.

Table 6.8. The synthesis (boundary support, electrostatic, thermal, geometry, and cutouts) values obtained for the *soft* 8F microcantilever.

Voltage (V)	Temperature (K)	1st nat. Freq. (Hz)	Exp. Freq. (Hz)	2nd nat. Freq. (Hz)	Exp. Freq. (Hz)
0	294	2802	2800	19003	19010
8	327	2794	2792	18970	18977
8	336.5	2793	2792	18962	18974
8	355.5	2791	2789	18946	18950
8	387.5	2786	2785	18918	18924
8	404	2784	2784	18903	18909
16.4	328	2763	2765	18955	18963
16.4	344	2761	2762	18940	18944
16.4	368	2758	2761	18920	18927
16.4	407	2753	2751	18886	18894
20.6	326	2558	2560	18928	18938
20.6	336	2555	2559	18919	18927
20.6	346	2552	2549	18911	18916
20.6	388	2540	2542	18874	18880
21.6	417	2194	2196	18818	18826

For experimental results for the *soft* 8F microcantilever configuration are consistent with the theoretical analysis. In comparing the results of Tables 6.7-6.8 the influence of microcantilever width tapering is immediately seen as the resonances for *soft* tapering are substantially lower than for *SORI*. The equivalent rotational stiffness K_R^* was found to be 548 which is in close agreement with earlier results.

6.10. SUPPORT BOUNDARY-ELECTROSTATIC-THERMAL-RISO GEOMETRY-CUTOUTS SYNTHESIS

Presented here is the multi-parameter synthesis of a *RISO* microcantilever beam geometry with an 8F cutout orientation. Shown in Figure 6.32 is the mathematical model of this beam obtained with MATLAB. Shown in Figure 6.33 is a close up of the *clamped* end of a typical MicraGeM technology microcantilever.
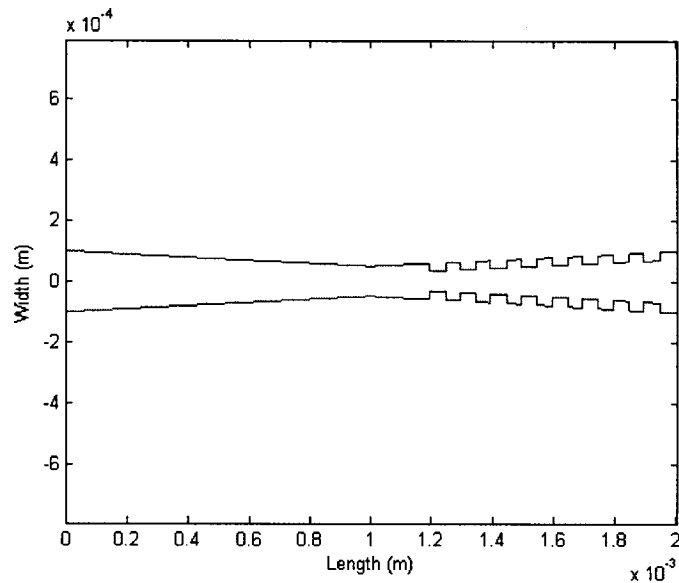
Figure 6.32. *RISO* 8F microcantilever geometry generated using MATLAB.
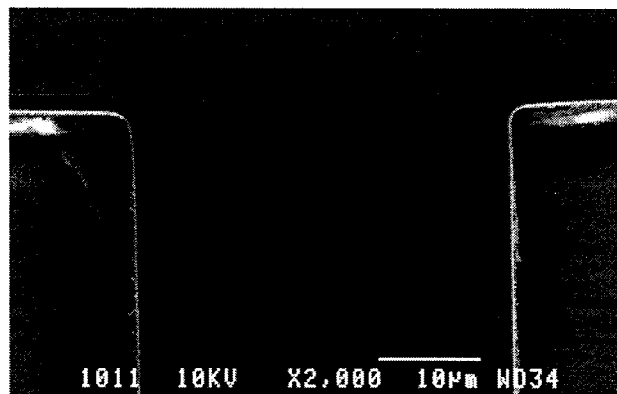
Figure 6.33. The *clamped* end support boundary of a typical MicraGeM technology microcantilever beam.

The results are presented in Figures 6.34-6.35. The tabulated results and equivalent

boundary support stiffness are given in Table 6.9.
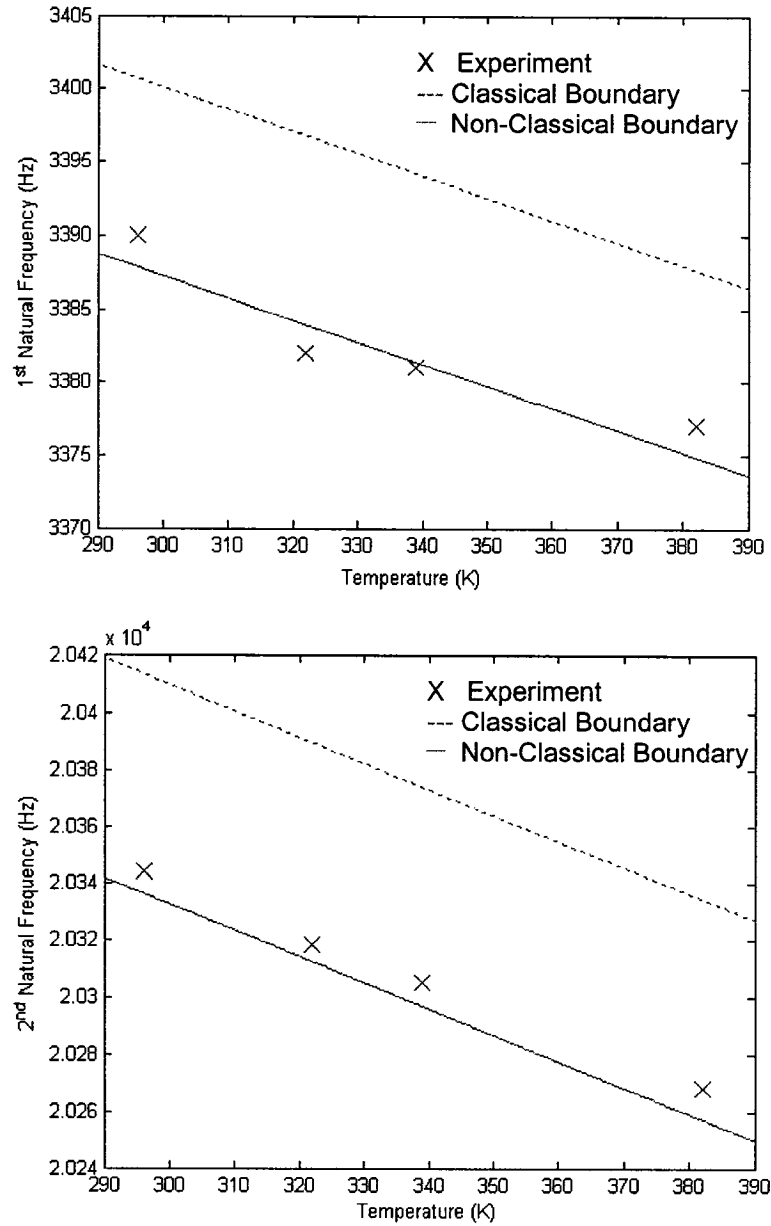
Figure 6.34. Top: The variation of the 1st natural frequency of the *RISO* 8F as a function of an applied 12.9V electrostatic potential and thermal loading. Bottom: The 2nd natural frequency variation.
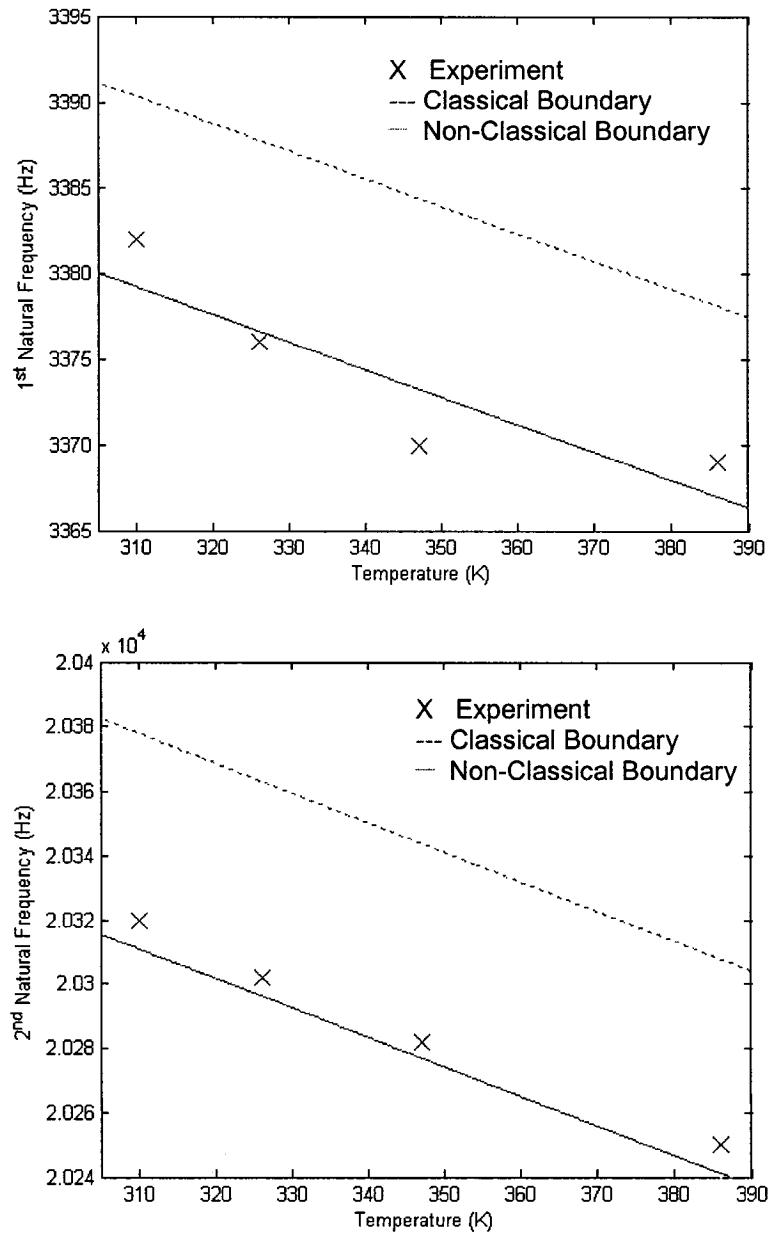
Figure 6.35. Top: The variation of the 1st natural frequency of the *RISO* 8F as a function of an applied 18.5V electrostatic potential and thermal loading. Bottom: The 2nd natural frequency variation.

Table 6.9. The synthesis (boundary support, electrostatic, thermal, geometry, and cutouts) values obtained for the *RISO* 8F microcantilever.

Voltage (V)	Temperature (K)	1st nat. Freq. (Hz)	Exp. Freq. (Hz)	2nd nat. Freq. (Hz)	Exp. Freq. (Hz)
0	294	3394	3395	20349	20360
12.9	296	3388	3390	20336	20344
12.9	322	3384	3382	20312	20318
12.9	339	3381	3381	20297	20305
12.9	382	3375	3377	20257	20268
18.5	310	3379	3382	20311	20320
18.5	326	3377	3376	20296	20302
18.5	347	3373	3370	20277	20282
18.5	386	3367	3369	20241	20250

The experimental results for the *RISO* 8F microcantilever configuration are in good agreement with the segment Rayleigh-Ritz analysis. The rotational stiffness K_R^* value 679 is consistent with the values obtained previously for this microfabrication foundry process. For the analysis presented in Sections 6.7-6.11 a percentage deviation ranging between 0.27%-0.38% was obtained for the differences between the classical and non-classical boundary support models which indicates that the influence of the micromachining limitation at the boundary support is consistent for all the MicraGeM technology devices tested in this research.

6.11. SUMMARY

The synthesis of microsystems was presented in this chapter where boundary support, electrostatic, thermal, geometry, and cutout influences were modeled and characterized. The experimental results indicate that the dynamic qualities of a given microsystem can be tailored through the application of conditioning parameters such as electrostatic, geometry, and cutout orientations. The boundary support influence can not be considered as a known and *controllable* influence as it is intrinsic to the microfabrication process itself. Also, the experimental results reveal that for a given applied voltage and for a specific thermal load one may obtain equivalent dynamic responses. Hence a given microsystem can be activated at lower electrostatic potentials when it is placed in a high thermal environment. Similarly, the microcantilever cutouts can be used to affect either the mass or stiffness domains of the microsystem allowing one to tailor the output based on a set of pre-determined input criteria such as the geometry and the cutout orientation selected.

The experimental results obtained showed good agreement with the mathematical formulation based on the segment Rayleigh-Ritz approach. Also, the equivalent boundary support stiffness values obtained for the MicraGeM technology microcantilevers are all within the same range, thereby confirming the particular microfabrication tolerance for this silicon foundry process. The errors obtained in the experimental results can be in part due to the difficulty in measuring the dimensions of the microcantilevers, especially the thickness of a particular device. In these

199

investigations all dimensional measurements (width, length and thickness) were made using an optical microscope with 1000x magnification. Thickness estimates were also based on SEM images.

The synthesis has been modeled and verified for geometrically contoured cantilevers for the region of temperature and electric field in which the system is expected to behave linearly.

One has to be careful in using this beyond the region of linear assumption, for example, for temperatures above ~225°C and voltages higher than ~60% of pull in.

Chapter 7

CONCLUSIONS AND EXTENSIONS

Presented in this chapter are some final conclusions and applications for the work presented herein.

7.1. CONCLUSIONS

This thesis discussed the synthesis of MEMS microcantilevers by combining the influences of microfabrication limitations at the support boundary, mechanical properties, applied electrostatic fields, and thermal loading. Incorporated within the mechanical properties were the influences of material, width contouring and cutouts. The synthesis was divided into three main subsections. Two theoretical approaches were presented along with experimental results. The Rayleigh-Ritz energy method was used for theoretical modeling of microfabrication, width contouring, cutouts, electrostatic, and thermal influences. The results for microcantilevers with cutouts alone were compared to FEM models and the results obtained showed close agreement. Hence, in order to improve the mathematical formulation regarding the effect of cutouts, a segment Rayleigh-Ritz method was introduced. The results obtained through this approach showed very good agreement with FEM models. In this way the synthesized influence of microfabrication, mechanical, electrostatic, and thermal were analyzed.

The experimental results were given in two main subsections: Firstly, the microfabrication tolerances at the boundary support were investigated through the effect of thermal and through the effect of electrostatic loading. The experimental results obtained showed very good agreement with the non-classical boundary support model. Secondly, the experimental results obtained for synthesized microcantilevers showed very good agreement with the segment Rayleigh-Ritz model for the combined effect of electrostatic and thermal loading.

The testing of micromachined components such as microcantilevers is an important part of the commercialization process for MEMS products and serves to enhance the theoretical model. In this regard, the optical non-contact test method employed was developed at CONCAVE and successfully used by several students for the dynamic characterization of microcantilevers and micromirrors. Two base excitation mechanisms, acousto-mechanical and sinusoidal-electrostatic were used. The sinusoidal-electrostatic excitation was used primarily for packaged MEMS devices and consisted of a small amplitude AC voltage. The acousto-mechanical shaking, of suitable amplitude, was used exclusively for loose die as these are in a non-wire bonded format. Equal frequency response results were obtained for both methods.

There are many factors that influence the final behaviour of microsystems. Several of these were investigated herein in an effort to combine the individual influences into a synthesized behavioural response. A theoretical model based on the Rayleigh-Ritz energy method was employed to capture the effects of microfabrication tolerances,

mechanical influences, electrostatic and thermal loading. Chapter 2 and Chapter 3 laid the foundations for the theoretical modeling for non-segment and segment Rayleigh-Ritz methods, respectively. Given in Chapter 4 was an overview of current MEMS test methods and the experimental procedure and equipment used in the course of the research for this thesis. This experimental approach was used to analyze the effects of micromachining on the microcantilever beam boundary support conditions as described in Chapter 5. Given in Chapter 6 were the experimental results obtained for the synthesized microcantilever response.

The main contributions of the author to the multiparameter analysis and experimental validation of MEMS microcantilevers are drawn from the individual aspects presented in the respective chapters.

7.1.1. *Microsystem modeling*

The theoretical analysis was based on the Rayleigh-Ritz energy method. With this approach the formulation of microfabrication, electrostatic, thermal, geometry and cutout influences were successfully modeled through the concept of an *elastic foundation*. Thermal influences for microcantilevers were modeled through the linear thermal expansion properties of single crystal silicon. The isotropic nature of the thermal expansions for single crystal silicon were exploited and used to redefine the microcantilever length, width and thickness as a function of temperature. The author developed the segment Rayleigh-Ritz method in order to improve the theoretical analysis

of microcantilevers with discontinuities along their length. This new analysis method was successfully used for modeling microcantilevers with geometrical discontinuities such as cutouts and etch holes.

A parametric analysis was conducted and validated with FEM methods and experimental results. The agreement was very good.

The multiparameter influences have been successfully coupled and validated through good agreement with experimental results.

7.1.2. Experimental investigation

The testing carried out required that a test setup, using simple test equipment, be established first. In this regard, the author has pioneered the first successful experimental testing technique for MEMS in Canada. Once in place, the experimental setup was successfully used for the dynamic testing and characterization of microstructures, and was well suited for the integration of electrostatic and thermal influences.

The author has proposed MEMS boundary support characterization through experimental testing using thermo-mechanical and electro-mechanical influences. This enabled the validation of the theoretical model. A comparison of the experimental and theoretical results showed clear agreement. In this regard, microfabrication limitations were clearly

demonstrated through thermo-mechanical and electro-mechanical modeling and experimental validation.

7.1.3. *Microsystem design*

The author has developed a method, using MATLAB, to design and characterize geometrically difficult microstructures. The advantages of this approach are that the design and characterization can be carried out simultaneously without the need for additional analysis tools. This method was successfully used to design and characterize MicraGeM technology microcantilevers of various geometries. In this regard, the author has formulated the design synthesis that has enabled the fine tuning of the static and dynamic behaviour of MEMS microcantilever structures.

7.2. EXTENSIONS

Recently there have been published reports of silicon lasing in SOI silicon technology [121, 182, 213]. This is a very exciting development as it will open up new applications for silicon microphotonic applications especially as integrated systems are *down sized* towards nanoscale dimensions. The main lasing process is obtained through Raman scattering and is described below.

Stimulated Raman scattering (SRS) in SOI waveguides is a way of amplifying optical signals in SOI planar photonic circuits because it does not require the introduction of any

dopants during fabrication of the SOI wafer and the amplified wavelength can be chosen almost freely by simply using *pump light* of an appropriate wavelength [121]. Also, in a *very* recent discovery [120], in which they state that the Raman lasing efficiency can be significantly increased through width tapering of the waveguide along its length. The tapering is applied in order to offset the *free-carrier-absorption* that competes with the optical gain achieved during the amplification process.

If one were now to replace the word tapered *waveguide* with tapered *microcantilever* and apply the synthesis principles described in this work, then it would open a very, very interesting area of research. The combination of silicon lasing and mechanical motion at the microscale has of yet not been explored and the potential areas of applications for silicon-electro-mechanical-tapered-lasers (SEMTLs) would seem to be limitless.

Although a sense of completeness has been achieved in the work carried out herein for the synthesis of microsystems, there remain many areas to explore in order extend and enhance the scope of microsystem synthesis. This task is left for future researchers.

References

1. Abadal, G., Boisen, A., Davis, Z. J., Hansen, O. and Grey, F., (1999) "Combined Laser and Atomic Force Microscope Lithography on Aluminum: Mask Fabrication for Nanoelectromechanical Systems", *Applied Physics Letters*, **74**, 3206-3208

2. Abdel-Rahman, E. M., Younis, M. I. and Nayfeh, A. H., (2002) "Characterization of the Mechanical Behavior of an Electrically Actuated Microbeam", *Journal of Micromechanics and Microengineering*, **12**, 759-766

3. Adams, S. G., Hui, C.-Y. and Macdonald, N. C., (1995) "Simulation of Microelectromechanical Systems using a Hybrid BEM/FEM Code with the Application to the Stability Analysis of a Tunable Oscillator", Proceedings of ASME, Symposium on Micro-Mechanical Systems, San Francisco, California, November 12-17

4. Almeida, V. R., Panepucci, R. R. and Lipson, M., (2003) "Nanotaper for Compact Mode Conversion", *Optics Letters*, **28**, 1302-1304

5. Aluru, N. R., (1999) "A Reproducing Kernel Particle Method for Meshless Analysis of Microelectromechanical Systems" *Computational Mechanics*, **23**, 324–338

6. Aluru, N. R. and White, J., (1997) "An Efficient Numerical Technique for Electrochemical and Simulations of Complicated Microelectromechanical Structures" *Sensors and Actuators A*, **58**, 1–11.

7. Amick, J. A., (1976) "Cleanliness and the Cleaning of Silicon Wafers", *Solid State Technology*, **19**, 47-52

8. Amritsar, J., Stiharu, I. and Packirisamy, M., (2005) "Detection of Acute Myocardial Infarction (AMI) using Bio-MEMS", 4th Canadian Workshop on MEMS: Opportunities and Challenges on the Road to Integration, Ottawa, Ontario, Canada, August 19

9. Ananthakrishnan, V., Sarma, R. and Ananthasuresh, G. K., (2003) "Systematic Mask Synthesis for Surface Micromachined MicroElectroMechanical Systems", *Journal of Micromechanics and Microengineering*, **13**, 927–941

10. ANSYS Inc., 275 Technology Drive, Canonsburg , Pennsylvania, 15317, USA, www.ansys.com

11. ARTWORK Conversion Software Inc., 417 Ingalls Street, Santa Cruz, California, 95060, USA, www.artwork.com

12. AutoDesk Inc, 111 McInnis Parkway, San Rafael, California, 94903, USA, www.autodesk.com

13. Bechtold, T., Rudnyi, B. E. and Korvink, J. G., (2005) "Error Indicators for Fully Automatic Extraction of Heat-Transfer Macromodels for MEMS", *Journal of Micromechanics and Microengineering*, **15**, 430-440

14. Beerschwinger, U., Milne, N. G., Yang, S. J., Reuben, R. L., Sangster, A. J. and Ziad, H., (1994) "Coupled Electrostatic and Mechanical FEA of a Micromotor", *Journal of Microelectromechanical Systems*, **3**, 162-171

15. Benitez, M. A., Plaza, J. A., Sheng, S. Q. and Esteve, J., (1996) "A New Process for Releasing Micromechanical Structures in Surface Micromachining", *Journal of Micromechanics and Microengineering*, **6**, 36-39

16. Bernini, R., Campopiano, S. and Zeni, L., (2002) "Silicon Micromachined Hollow Optical Waveguides for Sensing Applications", *IEEE Journal on Selected Topics in Quantum Electronics*, **8**, 106-110

17. Bhat, R. B., (1997) "Nature of Stationarity of the Natural Frequencies at the Natural Modes in the Rayleigh-Ritz Method", *Journal of Sound and Vibration*, **203**, 251-263

18. Bhat, R. B., (1987) "Flexural Vibration of Polygonal Plates using Characteristic Orthogonal Polynomials in Two Variables" *Journal of Sound and Vibration*, **114**, 65-71

19. Bhat, R. B., (1985) "Natural Frequencies of Rectangular Plates using Characteristic Orthogonal Polynomials in Rayleigh-Ritz Method" *Journal of Sound and Vibration*, **102**, 493-499

20. Bishop, D. J. and Giles, C. R., (1998) "Silicon Micromechanics takes on Light-Wave Networks", *The Industrial Physicist*, 39-42

21. Blum Spahn, O., Sullivan, C., Burkhart, J., Tiggs, C. and Garcia, E., (2000) "GaAs-Based Micromechanical Waveguide Switch", Optical MEMS Conference, Kauai, Hawaii, USA, August 22-24

22. Boisen, A., Birkelund, K., Hansen, O. and Grey, F., (1998) "Fabrication of Submicron Suspended Structures by Laser and Atomic Force Microscopy Lithography on Aluminum Combined with Reactive Ion Etching", *Journal of Vacuum. Science Technology B*, **16**, 2977-2981

23. Brook, A. J., Bending, S. J., Pinto, J., Oral, A., Ritchie, D., Beere, H., Springthorpe, A. and Henini, M., (2003) "Micromachined III-V Cantilevers for AFM Tracking Scanning Hall Microscopy", *Journal of Micromechanics and Microengineering*, **13**, 124-128

24. Brown, K. B., Allegretto, W., Vermeulen, F. E. and Robinson, A. M., (2002) "Simple Resonating Microstructures for Gas Pressure Measurement", *Journal of Micromechanics and Microengineering*, **12**, 204-210

25. Brüel & Kjær S. & V., Skodsborgvej 307, Nærum, 2850, Denmark, www.bksv.com

26. Brugger, J., Jaecklin, V. P., Blanc, N. and Indermühle, P. F., (1993) "Microfabricated Tools for Nanoscience", *Journal of Micromechanics and Microengineering*, **3**, 161-167

27. Brugger, J., Buser, R. A. and de Rooij, N. F., (1992) "Micromachined Atomic Force Microprobe with Integrated Capacitive Read-Out", *Journal of Micromechanics and Microengineering*, **2**, 218-220

28. Burchman, K. E. and Boyd, J. T., (1998) "Freestanding, Micromachined, Multimode Silicon Optical Waveguides at λ = 1.3μm for Microelectromechanical Systems Technology", *Applied Optics*, **37**, 8397-8399

29. Burrer, C., Esteve, J. and Lora-Tomayo, E., (1996) "Resonant Silicon Accelerometer in Bulk-Micromachining Technology", *Journal of Micromechanics and Microengineering*, **5**, 122-130

30. Bütefisch, S., Schoft, A. and Büttgenbach, S., (2000) "Three-Axis Monolithic Silicon Low-G Accelerometer", *Journal of Microelectromechanical Systems*, **9**, 551-556

31. Butt, H.-J. and Jaschke, M., (1995) "Calculation of Thermal Noise in Atomic Force Microscopy", *Nanotechnology*, **6**, 1-7

32. Byun, G., Ölçmen, S. M. and Simpson, R. L., (2004) "A Miniature Laser-Doppler Velocimeter for Simultaneous Three-Velocity-Component Measurements", *Measurement Science and Technology*, **15**, 2075-2082

33. Calleja, M., Tamayo, J., Johansson, A., Rasmussen, P., Lechuga, L. M. and Boisen, A., (2003) "Polymeric Cantilever Arrays for Biosensing Applications", *Sensor Letters*, **1**, 1-5

34. Cheben, P., Xu, D.-X., Janz, S. and Delâge, A., (2003) "Scaling Down Photonic Waveguide Devices on the SOI Platform", International Conference on VLSI Circuits and Systems, Symposium Microtechnologies for the New Millennium, Gran Canaria, Spain, May 19-21

35. Chen, K.-S., Ayon, A. A. and Spearing, S. M., (2000) "Controlling and Testing the Fracture Strength of Silicon on a Mesoscale', *Journal of the American Ceramic Society*, **83**, 1476-1484

36. Chen, L.-Y. and McCluskey, P., (2001) "Microsystem Packaging for High Temperature and Harsh Environments", MST (Microsystems) News, 41-42

37. Chen, S., Yi, X. and Ma, H., (2003) "A Novel Method of Fabrication of Microlens Arrays", *Infrared Physics & Technology*, **44**, 133-135

38. Chen, X., Fox, C. H. J. and Mcwilliam, S., (2004) "Optimization of a Cantilever Microswitch with Piezoelectric Actuation", *Journal of Intelligent Material Systems and Structures*, **15**, 823-834

39. Cheung, D. C. L., Barnes, T. H. and Haskell, T. G., (2003) "Feedback Interferometry with Membrane Mirror for Adaptive Optics", *Optics Communications*, **218**, 33-41

40. Chiao, M. and Lin, L., (2000) "Self-Buckling of Micromachined Beams Under Resisitive Heating", *Journal of Microelectromechanical Systems*, **9**, 146-151

41. Cho, H. J. and Ahn, C. H., (2003) "Magnetically-Driven Bi-Directional Optical Microscanner", *Journal of Micromechanics and Microengineering*, **13**, 383-389

42. CMC Microsytems, 210A Carruthers Hall, Queens's University, Kingston, Ontario, K7L 3N6, Canada, www.cmc.ca

43. COMSOL Inc., 8 New England Executive Park, Burlington, Massachusetts, 01803, USA, www.comsol.com

44. Cong, P. and Young, D. J., (2005) "Single Crystal 6H-SiC MEMS Fabrication Based on Smart-Cut Technique", *Journal of Micromechanics and Microengineering*, **15**, 2243-2248

45. Cong, P., Young, D. J. and Ko, W. H., (2004) "Novel Long-Term Implantable Blood Pressure Monitoring System", IEEE Sensors Conference, Technical Digest, Vienna, Austria, October 24-27

46. Coombe, B., (2006) "A Survey of MEMS-Enabled Optical Devices—Applications and Drivers for Employment", Bechtel Telecommunications Technical Journal, **4**, 1-9

47. Corbeil, J. L., Lavrik N. V., Rajic, S. and Datskos, P. G., (2002) ""Self-Leveling" Uncooled Microcantilever Thermal Detector", *Applied Physics Letters*, **81**, 1306-1308

48. Courtois, B., Mir, S., Charlot, B., and Lubaszewski B., (2000) "From Microelectronics to MEMS Testing", TIMA Labs Research Reports, Grenoble, France 38000, tima.imag.fr

49. Cronos Integrated Microsystems, A JDS Uniphase Company, JDSU, 1768 Automation Parkway, San Jose, California, 95131, USA, www.jdsu.com

50. Datskos, P. G., Sepaniak, M. J., Tipple, C. A. and Lavrik, N., (2001) "Photomechanical Chemical Microsensors", *Sensors and Actuators: B*, **76**, 393-402

51. Datta, M., Pruessner, M. W., Kelly, D. P. and Ghodssi, R., (2004) "Design of MEMS-Tunable Novel Monolithic Optical Filters in InP with Horizontal Bragg Filters", *Solid State Electronics*, **48**, 1959-1963

52. Degoli, E. and Ossicini, S., (2000) "The Electronic and Optical Properties of Si/SiO_2 Superlattices: Role of Confined and Defect States", *Surface Science*, **470**, 32-42

53. Delapierre, G., (1989) "Micromachining: A Survey of the Most Commonly used Processes", *Sensors and Actuators,* **17**, 123-138

54. Desquesnes, M., Rotkin, S. V. and Aluru, N. R., (2002) "Calculation of Pull-in Voltages for Carbon-Nanotube-Based Nanoelectromechanical Switches", *Nanotechnology*, **13**, 120-131

55. DeVoe, D. L., (2003) "Thermal Issues in MEMS and Microscale Systems", IEEE Transactions on Components and Packaging Technologies, **25**, 576-583

56. DiMeo Jr., F., Chen, I.-S., Chen, P., Neuner, J., Rohrl, A., Stawaz, M. and Welch, J., (2003) "Micro-Machined Thin Film H_2 Gas Sensors", *Hydrogen, Fuel Cells, and Infrastructure Technologies*, 1-4

57. Dorsch, J., (2001) "MEMS: Tiny Parts Face Tough Technical Challenges", Semiconductor Magazine, August Issue, 26-34, SEMI Global Headquarters, 3081 Zanker Road, San Jose, California, 95134, USA, dom.semi.org

58. Dotson, N. A., Kim, P. T. and Mason, A., (2004) "Low Cost MEMS Processing Techniques", Proceedings of ASEE, NCS Spring Conference, Kalamazoo, Michigan, USA, April 1-3

59. Dragoman, D. and Dragoman, M., (2003) "Biased Micromechanical Cantilever Arrays as Optical Image Memory", *Applied Optics*, **8**, 1515-1519

60. Drews, D., Noell, W., Ehrfeld, W., Lacher, M., Mayr, K., Marti, O., Serwatzy, C. and Abraham, M., (1998) "Micromachined Aperture Probe for Combined Atomic Force and Near-Field Scanning Optical Microscopy (AFM/NSOM)", Proceedings of SPIE, Materials and Device Characterization in Micromachining, 76-83

61. Duesterhaus, M. A., Bateman, V. I. and Hoke, D. A., (2003) "Shock Testing of Surface Micromachined MEMS Devices, Proceedings of NDIA, 47th Annual FUZE Conference, New Orleans, Louisiana, USA, April 8-10

62. Duffy, S., Bozler, C., Rabe, S., Knecht, J., Travis, L., Wyatt, P., Keast, C. and Gouker, M., (2001) "MEMS Microswitches for Reconfigurable Microwave Circuitry", *IEEE Microwave and Wireless Components Letters*, **11**, 106-108

63. Epstein, A. H., (2003) "Millimeter-Scale, MEMS Gas Turbine Engines", Proceedings of ASME, Turbo Expo, Power for Land, Sea, and Air, Atlanta, Georgia, USA, June 16-19

64. Ericson, F. and Schweitz, J.-A., (1990) "Micromechanical Fracture Strength of Silicon", *Journal of Applied Physics*, **68**, 5840-5844

65. Espinosa, H. D. and Prorok, B. C. (2001) "A Novel Experimental Technique for Testing Thin Films and MEMS Materials", Proceedings of SEM, Annual Conference on Experimental and Applied Mechanics, Portland, Oregon, USA, June 4-6

66. Feuerstein, D. and Werner, F. M., (2004) "Testing MEMS at Wafer Level" *Journal of Evaluation Engineering*, 20-26

67. Feynman, R., (1960) "There's Plenty of Room at the Bottom", California Institute of Technology Engineering and Science Magazine Vol. 23

68. Finot, M., Blech, I. A., Suresh, S. and Fujimoto, H., (1997) "Large Deformation and Geometric Instability of Substrates with Thin-Film Deposits", *Journal of Applied Physics*, **81**, 3457-3464

69. Flores, G. and Mercado, G. A., (2003) "Dynamics and Touchdown in Electrostatic MEMS", Proceedings of IEEE, International Conference on MEMS, NANO and Smart Systems, Banff, Alberta, Canada, July 20-23

70. Ford, J. E., (1999) "Micromachines for Wavelength Multiplexed Telecommunications", Proceedings of MOEMS, Mainz, Germany, August 30

71. Ford, J. E., Walker, J. A., Greywall, D. S. and Goossen, K. W., (1998) "Micromechanical Fiber-Optic Attenuator with 3µs Response", *Journal of Lightwave Technology*, **16**, 1663-1670

72. Freund, L. B., Floro, J. A. and Chason, E., (1999) "Extensions of the Stoney Formula for Substrate Curvature to Configurations with Thin Substrates or Large Deformations", *Applied Physics Letters*, **74**, 1987-1989

73. Frühauf, J., Gärtner, E. and Jänsch, E., (1999) "Silicon as Plastic Material", *Journal of Micromechanics and Microengineering*, **9**, 305-312

74. Fujii, K., Waseda A. and Kuramoto N., (2001) "Development of a Silicon Density Standard and Precision Density Measurements of Solid Materials by Hydrostatic Weighing", *Measurement Science and Technology*, **12**, 2031-2038

75. Fujita, H., (1998) "Microactuators and Micromachines", Proceedings of the IEEE, **86**, 1721-1732

76. Fukazawa, T., Hirano, T., Ohno, F. and Baba, T., (2004) "Low Loss Intersection of Si Photonic Wire Waveguides", *Japanese Journal of Applied Physics*, **43**, 646-647

77. Gehring, G. A., Cooke, M. D., Gregory, I. S., Karl, W. J. and Watts, R., (2000) "Cantilever Unified Theory and Optimization for Sensors and Actuators", *Smart Materials and Structures*, **9**, 918-931

78. Gibson, C. T., Smith, D. A. and Roberts, C. J., (2005) "Calibration of Silicon Atomic Force Microscope Cantilevers", *Nanotechnology*, **16**, 234-238

79. Giurgiutiu, V. and Lyshevski, S. E, (2004) "Micromechatronics: Modeling, Analysis and Design with MATLAB", CRC Press LLC, Boca Raton, Florida, USA 33431

80.   Glazov, V. M. and Pashinkin, A. S., (2001) "The Thermal Properties (Heat Capacity and Thermal Expansion) of Single-Crystal Silicon", *High Temperature*, **39**, 413-419

81.   Gómez, R., Bashir, R., Sarikaya, A., Ladisch, M. R., Sturgis, J, Robinson, J. P., Geng, T., Bhunia, A. K., Apple, H. L. and Wereley, S., (2001) "Microfluidic Biochip for Impedance Spectroscopy of Biological Species", *Biomedical Microdevices*, **3**, 201-209

82.   Goodenough, F., (1991) "Airbags Boom When IC Accelerometer Sees 50G", *Electronic Design*, **8**, 45-56

83.   Greenwood, J. C., (1988) "Silicon in Mechanical Sensors", *Journal of Physics E: Scientific Instruments*, **21**, 1114-1128

84.   Han, J., Zhu, C., Liu, J. and He, Y., (2002) "Dependence of the Resonance Frequency of Thermally Excited Microcantilever Resonators on Temperature", *Sensors and Actuators A*, **101**, 37-41

85.   Han, S. and Browne, T., (2005) "Characterizing Optically Packaged MEMS & MOEMS Devices using Optical Profiling Techniques", Veeco Instruments Inc, Tucson, Arizona, USA 85706, www.veeco.com

86.   Hart, M. R., Conant, R. A., Lau, K. Y. and Muller, R. S., (2000) "Stroboscopic Interferometer System for Dynamic MEMS Characterization", *Journal of Microelectromechanical Systems*, **9**, 409-418

87.   Haug, C., Régnier, and Bidaud, P., (2000) "Compliant Beam Networks Optimization for Microsystems", International Conference on Intelligent Robots and Systems, Takamatsu, Japan, October 30-November 5

88.   Henmi, H., Shoji, S., Shoji, Y., Yoshimi, K. and Esashi, M., (1994) "Vacuum Packaging for Microsensors by Glass-Silicon Anodic Bonding", *Sensors and Actuators: A*, **43**, 243-248

89.   Horenstein, M. N., Pappas, S., Fishov, A. and Bifano, T. G., (2002) "Electrostatic Micromirrors for Subaperturing in an Adaptive Optics System", *Journal of Electrostatics*, **54**, 321-332

90.   Howe, R., (1988) "Surface Micromachining for Microsensors and Microactuators", *Journal of Vacuum Science and Technology: B*, **6**, 1809-1813

91.   Howe, R. T. and Mullen, R. S., (1986) "Resonant-Microbridge Vapor Sensor", IEEE Transactions on Electronic Devices, **33**, 499-506

92. Hsu, T.-R., (2006) "Reliability in MEMS Packaging", 44th International Reliability Physics Symposium, San Jose, California, USA, March 26-30

93. Hu, S. M., (1982) "Critical Stress in Silicon Brittle Fracture, and Effect of Ion-Implantation and Other Surface Treatments", *Journal of Applied Physics*, **53**, 3576-3580

94. Huang, R. S., Abbaspour-Sani, E. and Kwok, C. Y., (1995) "A Novel Accelerometer Using Silicon Micromachined Cantilever Supported Optical Grid and PIN Photodetector", 8th International Conference on Solid-State Sensors and Actuators, Stockholm, Sweden, June 25-29

95. Huang, Y., Ergun, A. S., Hæggström, E., Badi, M. H. and Khuri-Yakub, B. T., (2003) "Fabricating Capacitive Micromachined Ultrasonic Transducers with Wafer-Bonding Technology", *Journal of Microelectromechanical Systems*, **12**, 128-137

96. Hung, E. S. and Senturia, S. D., (1999) "Extending the Travel Range of Analog-Tuned Electrostatic Actuators", *Journal of Microelectromechanical Systems*, **8**, 497-505

97. Hung, E. S. and Senturia, S. D., (1999) "Generating Efficient Dynamical Models for Microelectromechanical Systems from a Few Finite-Element Simulation Runs" *Journal of Microelectromechanical Systems*, **8**, 280-289

98. Hutter, J. L. and Bechhoefer, J., (1994) "Measurement and Manipulation of Van Der Waals Forces in Atomic Force Microscopy", *Journal of Vacuum Science Technology B*, **12**, 2251-2253

99. Ikehara, T., Zwijze, R. A. F. and Ikeda, K., (2001) "New method for an Accurate Determination of Residual Strain in Polycrystalline Silicon Films by Analyzing Resonant Frequencies of Micromachined Beams", *Journal of Micromechanics and Microengineering*, **11**, 55-60

100. Industrial News Room, *Press Release*, (2005) "High-Resolution Laser Micromaching", Thomas Industrial Network, 5 Penn Plaza, 10th Floor, New York, New York, 10001, USA, www.news.thomasnet.com

101 Jensen, B. D., Saitou, K., Volakis, J. L. and Kurabayashi, K., (2003) "Fully Integrated Electrothermal Multidomain Modeling of RF MEMS Switches", *IEEE Microwave and Wireless Components Letters*, **13**, 364-366

102. Jensen, B. D., deBoer, M. P., Masters, N. D. Bitsie, F. and LaVan, D. A., (2001) "Interferometry of Actuated Microcantilevers to Determine Material Properties and Test Structure Nonidealities in MEMS", *Journal of Microelectromechanical Systems*, **10**, 336-346

103. Judy, J. W., (2001) "MicroElectroMechanical Systems (MEMS): Fabrication, Design and Applications", *Smart Materials and Structures*, **10**, 1115-1134

104. Kamalian, R. and Agogino, A. M., (2005) "Improving Evolutionary Synthesis of MEMS through Fabrication and Testing Feedback", IEEE International Conference: Systems, Man, and Cybernetics, Waikoloa, Hawaii, USA, October 10-12

105. Kan, S. C., Eng, T. T., Sin, S. S. Y. and Wong, G. K. L., (1996) "Silicon on Insulator (SOI) Movable Integrated Optical Waveguide Technology", *Sensors and Actuators: A*, **54**, 679-683

106. Kang, J. and Leissa, A. W., (2004) "Three-dimensional Vibration Analysis of Thick, Tapered Rods and Beams with Circular Cross-section", *International Journal of Mechanical Sciences*, **46**, 929-944

107. Kawakatsu, H., Saya, D., Kato A., Fukushima, K., Toshiyoshi, H. and Fujita, H., (2002) "Millions of Cantilevers for Atomic Force Microscopy", *Review of Scientific Instruments*, **73**, 1188-1192

108. Kelly, D. P., Pruessner, M. W., Arnarnath, K., Datta, M., Kanakaruja, S., Calhoun, L. C. and Ghodssi, R., (2004) "Monolithic Suspended Optical Waveguides for InP MEMS", *IEEE Photonics Technology Letters*, **16**, 1298-1300

109. Kendall, D. L., (1990) "A New Theory for the Anisotropic Etching of Silicon and some Underdevelopment Chemical Micromachining Concepts", *Journal of Vacuum Science and Technology: A*, **8**, 3598-3605

110. Keränen, K., Karioja, P., Blomberg, M., Tenhunen, J., Rusanen, O. and Kopola, H., (2001) "Miniaturization and Module Integration of an Infrared Spectrometer", *Optical Engineering*, **40**, 2308-2314

111. Kern, W. and Puotinen, D. A., (1970) "Cleaning Solutions Based on Hydrogen Peroxide for use in Silicon Semiconductor Technology", *RCA Review*, **30**, 187-206

112. Kim, C. S. and Dickinson, S. M., (1992) "The Free Flexural Vibration of Isotropic and Orthotropic General Triangular Shaped Plates", *Journal of Sound and Vibration*, **152**, 383-403

113. Kim, Y.-J. and Allen, M. G., (1999) "In Situ Measurement of Mechanical Properties of Polyimide Films using Micromachined Resonant String Structures", *IEEE Transactions on Components and Packaging Technology*, **22**, 282-290

114. Kinoshita, H. and Jinno, K, (1977) "Anisotropic Etching of Silicon by Gas Plasma", *Japanese Journal of Applied Physics*, **16**, 381-382

115. Kirstein, K.-U., Sedivy, J., Salo, T., Hagleitner, C., Vancura, T. and Hierlemann, A., (2005) "A CMOS-Based Tactile Sensor for Continuous Blood Pressure Monitoring", Proceedings of IEEE, Design, Automation and Test in Europe, **3**, 210-214

116. Knapp, J. A., Follstaedt, D. M., Myers, S. M., Barbour, J. C. and Friedmann, T. A., (1999) "Finite-Element Modeling of Nanoindentation", *Journal of Applied Physics*, **85**, 1460-1474

117. Kolpekwar, A. and Blanton, R. D., (1997) "Development of a MEMs Testing Methodology", IEEE International Test Conference, Washington, District of Columbia, USA, November 3-5

118. Kong, S. H., Wijngaards, D. D. L. and Wolffenbuttel, R. F., (2001) "Infrared Micro-Spectrometer Based on a Diffraction Grating", *Sensors and Actuators: A*, **92**, 88-95

119. Korb, A. R., Dybwad, P., Wadsworth, W. and Salisbury, J. W., (1996) "Portable Fourier Transform Infrared Spectroradiometer for Field Measurements of Radiance and Emissivity", *Applied Optics*, **35**, 1679-1692

120. Krause, M., Renner, H. and Brinkmeyer, E., (2006) "Efficient Raman Lasing in Tapered Silicon Waveguides", *Spectroscopy*, **21**, 26-32

121. Krause, M., Renner, H. and Brinkmeyer, E., (2004) "Analysis of Raman Lasing Characteristics in Silicon-On-Insulator Waveguides", *Optics Express*, **12**, 5703-5710

122. Kretz, A. P. and Styblo, D., (2003) "Towards Continuous Blood Glucose Monitoring", Medical Device & Diagnostic Industry, Feature Article, p. 78

123. Kuehnel, W. and Sherman, S., (1994) "A Surface Micromachined Silicon Accelerometer with On-Chip Detection Circuitry", *Sensors and Actuators: A*, **45**, 7-16

124. Kynch, G. J., (1957), "The Fundamental Modes of Vibration of Uniform Beams for Medium Wavelengths", *British Journal of Applied Physics*, **8**, 64-73

125. Lai, E. and Ananthasuresh, G. K., (2002) "On the Design of Bars and Beams for Desired Mode Shapes", *Journal of Sound and Vibration*, **254**, 393-406

126. Lam, K. Y., Hung, K. C. and Chow, S. T., (1989) "Vibration Analysis of Plates with Cutouts by the Modified Rayleigh-Ritz Method", *Applied Acoustics*, **28**, 49-60

127. Lasky, J. B., (1986) "Wafer Bonding for Silicon-on-Insulator Technologies", *Applied Physics Letters*, **48**, 78-80

128. Lee, D.-W., Wetzel, A., Bennewitz, R., Meyer, E., Despont, M., Vettiger, P. and Gerber, C., (2004) "Switchable Cantilever for a Time-of-Flight Scanning Force Microscope", *Applied Physics Letters*, **84**, 1558-1560

129. Lee, J.-B., English, J., Ahn, C.-H. and Allen, M. G., (1997) "Planarization Techniques for Vertically Integrated Metallic MEMS on Silicon Foundry Circuits", *Journal of Micromechanics and Microengineering*, **7**, 44-54

130. Lévy, R. and Maaloum, M., (2002) "Measuring the Spring Constant of Atomic Force Microscope Cantilevers: Thermal Fluctuations and Other Methods", *Nanotechnology*, **13**, 33-37

131. Li, J., Gao, S. and Liu, Y., (2005) "Feature-Based Process Layer Modeling for Surface Micromachined MEMS", *Journal of Micromechanics and Microengineering*, **15**, 620–63

132. Liang, K., Lin, W. Z., Lee, H. P., Lim, S. P., Lee, K. H. and Feng, D. P., (2001) "A Neural Network Based Method of Model Reduction for the Dynamic Simulation of MEMS" *Journal of Micromechanics and Microengineering*, **11**, 226–233

133. Lin, Q., Jiang, F., Wang, X.-Q., Xu, Y., Han, Z., Tai, Y.-C., Lew, J. and Ho, C.-M., (2004) "Experiments and Simulations of MEMS Thermal Sensors for Wall Shear-Stress Measurements in Aerodynamic Control Applications", *Journal of Micromechanics and Microengineering*, **14**, 1640-1649

134. Lin, T., Turner, K. and Zhang, W., (2003) "Characterization of the Mechanical Properties of Micro-Electro-Mechanical-System (MEMS) Oscillators", Nanotech Nanofabrication Facility, University of California, Santa Barbara, USA

135. LinkCAD, Bay Technology, 9153 Glenmark Drive, Burlington, Iowa, 52601, USA, www.LinkCad.com

136. Liu, A. Q., Zhang, M., Lu, C., Wang F., Lu, C. and Liu Z. S., (2003) "Optical and Mechanical Models for a Variable Optical Attenuator Using a Micromirror Drawbridge", *Journal of Micromechanics and Microengineering*, **13**, 400–411

137. Liu, R., Paden, B. and Turner, K., (2002) "MEMS Resonators that are Robust to Process-Induced Feature Width Variations", *Journal of Microelectromechanical Systems*, **11**, 505-511

138. Livermore, C., Forte, A. R., Lyszczarz, T., Umans, S. D., Ayon, A. A. and Lang, J. H., (2004) "A High-Power MEMS Electric Induction Motor", *Journal of Microelectromechanical Systems*, **13**, 465-471

139. Lu, C., Lemkin, M. and Boser, B., (1995) "A Monolithic Surface Micromachined Accelerometer with Digital Output", *IEEE Journal of Solid-State Circuits*, **30**, 1367-1373

140. Luo, C., Schneider, T. W., White, R. C., Currie, J. and Paranjape, M., (2003) "A Simple Deflection-Testing Method to Determine Poisson's Ratio for MEMS Applications", *Journal of Micromechanics and Microengineering*, **13**, 129–133

141. Macchioni, C. V., (1991) "The Effect of Substrate Temperature and Bias on the Stress, Chemical Etch Rate, and Microstructure of High Deposition Rate Sputtered SiO_2 Films", *Journal of Vacuum Science and Technology: A*, **9**, 2302-2308

142. Madou, M., (1997) "Fundamentals of Microfabrication", CRC Press LLC, Boca Raton, Florida, 33431, USA

143. Mahadevan, R., (1987) "Capacitance Calculations for a Single-Rotor Electrostatic Motor", Proceedings of IEEE, Micro Robots and Teleoperators Workshop, Hyannis, Massachusetts, USA, November 9-11

144. Majumder, S., Lampen, J., Morrison, R. and Maciel, J., (2003) "MEMS Switches", IEEE Instrumentation & Measurement Magazine, March Issue, 12-15

145. Mankame, N. D. and Ananthasuresh, G. K., (2004) "Topology Synthesis of Electrothermal Compliant Mechanisms using Line Elements", *Structural Multidisciplinary Optimization*, **26**, 209-218

146. Marek, J. and Illing, M., (2002) "Micromachined Sensors for Automotive Applications", Proceedings of IEEE, 1st International Conference on Sensors, Orlando, Florida, USA, June 12-14

147. McDonald, G. A., (1990) "A Review of Low Cost Accelerometers for Vehicle Dynamics", *Sensors and Actuators: A*, 21, 303-307

148. McFarland, A. W. and Colton, J. S., (2005) "Chemical Sensing with Micromolded Plastic Microcantilevers", *Journal of Microelectromechanical Systems*, 14, 1375-1385

149. McNamara, S., Basu, A. S., Lee, J.-H. and Gianchandani, Y. B., (2005) "Ultracompliant Thermal Probe Array for Scanning Non-Planar Surfaces without Force Feedback", *Journal of Micromechanics and Microengineering*, 15, 237-243

150. Mehregany, M., Zorman, C. A., Rajan, N. and Wu, C. H., (1998) "Silicon Carbide MEMS for Harsh Environments", Proceedings of the IEEE, 86, 1594-1610

151. Melles Griot, Canadian Office, 18 Antares Drive, Nepean, Ontario, K2E 1A9, Canada, www.mellesgriot.com

152. Micralyne Inc., 1911 94th Street, Edmonton, Alberta, T6N 1E6, Canada, www.micralyne.com

153. MikroMasch, 9755 SW Commerce Cir, Suite B-1 Wilsonville, Oregon, 97070, USA, www.spmtips.com

154. MINCO, 7300 Commerce Lane, Minneapolis, Minnesota, 55432, USA, www.minco.com

155. Mukherjee, T., (2003) "MEMS Design and Verification", Proceedings of IEEE International Test Conference, Charlotte, North Carolina, USA, September 30 - October 2

156. Mullen, R., Mehregany, M., Omar, M. and Ko, W., (1991) "Theoretical Modeling of Boundary Conditions in Microfabricated Beams", Proceedings of IEEE Micro Electro Mechanical Systems, Conference on Micro Structures, Sensors, Actuators, Machines and Robots, Nara, Japan, January 30-February 2

157. Mundkur, G., Bhat, R. B. and Neriya, S., (1994) "Vibration of Plates with Cut-Outs using Boundary Characteristic Orthogonal Polynomial Functions in the Rayleigh-Ritz Method", *Journal of Sound and Vibration*, 176, 136-144

158. Naidu, N. R., Venkateswara Rao, G. and Kanaka Raju, K., (2001) "Free Vibration Behavior of Tapered Beams with Non-Linear Elastic End Rotational Restraints", *Journal of Sound and Vibration*, **240**, 195-202

159. Najar, F., Choura, S., El-Borgi, S., Abdel-Rahman, E. M. and Nayfeh, A. H., (2005) "Modeling and Design of Variable-Geometry Electrostatic Microactuators", *Journal of Micromechanics and Microengineering*, **15**, 419-429

160. Nano Science and Technology Institute, (2005) "Tiny Silicon Chip Developed by Microstaq will Revolutionize Car Technology", NSTI, One Kendall Square, Cambridge, Massachusetts, 02139, USA, www.nsti.org

161. Neugebauer, T. C., Perreault, D. J., Lang, J. H. and Livermore, C., (2004) "A Six-Phase Multilevel Inverter for MEMS Electrostatic Induction Micromotors", IEEE Transactions on Circuits and Systems-II: Express Briefs, **51**, 49-56

162. Neumeister, J. M. and Ducker, W. A., (1994) "Lateral, Normal, and Longitudinal Spring Constants of Atomic Force Microscopy Cantilevers", *Review of Scientific Instruments*, **65**, 2527-2531

163. Ngoi, B., Venkatakrishnan, K., Tan, B., Noel, N., Shen, Z. and Chin, C., (2000) "Two-Axis-Scanning Laser Doppler Vibrometer for Microstructure", *Optics Communications*, **182**, 175–185

164. Numazawa, T., Miura, K., Kawase, K. and Hirata, Y., (2003) "Development of a MEMS Optical Switch Composed of Ribbon-Like Actuator", *SEI Technical Review*, **56**, 37-40

165. Okaji, M. and Imai, H., (1984) "A Practical Measurement System for the Accurate Determination of Linear Thermal Expansion Coefficients", *Journal of Physics E: Scientific Instrument*, **17**, 669-673

166. Oliver, W. C. and Pharr, G. M., (1992) "An Improved Technique for Determining Hardness and Elastic Modulus using Load and Displacement Sensing Indentation Experiments", *Journal of Materials Research*, **7**, 1564-1583

167. Ollier, E., (2002) "Optical MEMS Devices based on Moving Waveguides", *IEEE Journal on Selected Topics in Quantum Electronics*, **8**, 155-162

168. Omar, M. P., Mehregany, M. and Mullen, R. L., (1992) "Electric and Fluid Field Analysis of Side-Drive Micromotors", *Journal of Microelectromechanical Systems*, **1**, 130-140

169. O'Neal, C. B., Malshe, A. P., Singh, S. B., Brown, W. D. and Eaton, W. P., (1999) "Challenges in the Packaging of MEMS", International Symposium on Advanced Packaging Materials, Braselton, Georgia, USA, March 14-17

170. Ono, N., Kitamura, K., Nakajima, K. and Shimanuki Y., (2000) "Measurement of Young's Modulus of Silicon Single Crystal at High Temperature and Its Dependency on Boron Concentration Using the Flexural Vibration Method", Japanese Journal of Applied Physics, 39, 368-371

171. Ouellette, J., (1996) "MEMS: Mega Promise for Micro Devices", The Industrial Physicist, 2, 9-12

172. Osterberg, P. M. and Senturia, S. D., (1997) "M-Test: A Test Chip for MEMS Material Property Measurement using Electrostatically Actuated Test Structures", Journal of Microelectromechanical Systems, 6, 107-118

173. Oxford English Dictionary, Oxford University Press, 198 Madison Avenue, New York, New York, 10016, USA, www.oed.com

174. Packirisamy, M., Stiharu, I, Li, X. and Rinaldi, G., (2005) "A Polyimide based Resistive Humidity Sensor", Sensor Review: Medical Sensors, 25, 271-276

175. Packirisamy, M., Stiharu, I. and Bhat, R. B., (2005) "Influence of Micromachining on Dynamic Behavior of MEMS Structures", Canadian Journal of Electrical and Computer Engineering, 30, 157-162

176. Packirisamy, M., Stiharu, I. and Bhat, R. B., (2002) "Boundary Conditioning of Capacitive MEMS Devices Through Fabrication Methods and Operating Environments", Proceedings of SPIE, International Conference on Smart Materials, Structures and Systems, Bangalore, India, July 17-19

177. Packirisamy, M., Stiharu, I. and Bhat, R. B., (2001) "Application of Boundary Conditioning to the Synthesis of Microsystems", Proceedings of IEEE, Micro Electro Mechanical Systems Conference, Berkeley, California, USA, August 24-26

178. Packirisamy, M., (2000) "Boundary Conditioning Concept Applied to the Synthesis of Microsystems using Fuzzy Logic Approach", Doctoral Thesis, Department of Mechanical and Industrial Engineering, Concordia University, Montreal, Canada

179. Packirisamy, M., Bhat, R. B. and Stiharu, I., (1999) "Boundary Conditioning Technique for Structural Tuning", *Journal of Sound and Vibration*, **220**, 847-859

180. Park, K. Y., Lee, C. W., Jang, H. S., Oh, Y. S. and Ha, B. J., (1998) "Capacitive Sensing Type Surface Micromachined Silicon Accelerometer with Stiffness Tuning Capability", Proceedings of IEEE, The Eleventh Annual International Workshop on Micro Electro Mechanical Systems, Heidelberg, Germany, January 25-29

181. Park, S. R. and O, B.-H., (2001) "Novel Design Concept of Waveguide Mode adapter for Low Loss Mode Conversion", *IEEE Photonics Technology Letters*, **13**, 675-677

182. Pavesi, L., (2005) "Routes Toward Silicon-Based Lasers", *Materials Today*, 18-25

183. Pavesi, L., Gaburro, Z., Dal Negro, L., Bettotti, P., Vijaya Prakash, G., Cazzanelli, M. and Oton, C. J., (2003) "Nanostructured Silicon as a Photonic Material", *Optics and Lasers in Engineering*, **39**, 345-368

184. Pedersen, N.L., (2000) "Design of Cantilever Probes for Atomic Force Microscopy (AFM)", *Engineering Optimization*, **32**, 373-392

185. Peeters, E., (1997) "Challenges in Commercializing MEMS", *Computational Science and Engineering*, **4**, 44-48

186. Petersen, K. E., (1982) "Silicon as a Mechanical Material", Proceedings of the IEEE, **70**, 420-446

187. Petersen, K. E. and Guarnieri, C. R., (1979) "Young's Modulus Measurements of Thin Films using Micromechanics", *Journal of Applied Physics*, **50**, 6761-6766

188. Petersen, K. E., (1978) "Dynamic Micromechanics on Silicon: Techniques and Devices", *IEEE Transactions on Electronic Devices*, **25**, 1241-1250

189. Polytec Inc., 16 Albert Street, Auburn, Massachusetts, 01501, USA, www.polytec.com

190. Povinelli, M. L., Bryant, R. E., Assefa, S., Johnson, S. G., Fan, S., Erchak, A. A., Petrich, G. S., Lidorikis, E., Joannopoulos, J. D., Kolodziejski, L. A. and Ippen, E. P., (2003) "Design of a Nanoelectromechanical High-Index-Contrast Guided-Wave Optical Switch for Single-Mode Operation at 1.55μm", *IEEE Photonics Technology Letters*, **15**, 1207-1209

191. Powell, O., (2002) "Single-Mode Condition for Silicon Rib Waveguides", *Journal of Lightwave Technology*, **20**, 1851-1855

192. Pruessner, M. W., Amarnath, K., Datta, M., Kelly, D. P., Kanakaruja, S., Ho, P. T. and Ghodssi, R., (2004) "Optical and Mechanical Characterization of an Evanescent Coupler Optical Switch", Solid-State Sensor, Actuator and Microsystems Workshop, Hilton Head Island, South Carolina, USA, June 6-10

193. Puigcorbé, J., Vogel, D., Michel, B., Vilà, A., Gràcia, I., Cané, C. and Morante, J. R., (2003) "High Temperature Degradation of Pt/Ti Electrodes in Micro-Hotplate Gas Sensors", *Journal of Micromechanics and Microengineering*, **13**, S119-S124

194. Rabinovich, V. L., Gupta, R. K. and Senturia, S. D., (1997) "The Effect of Release-Etch Holes on the Electromechanical Behavior of MEMS Structures", International Conference on Solid-State Sensors and Actuators, Chicago, Illinois, USA, June 16-19

195. Raiteri, R., Grattarola, M., Butt, H. J. and Skladal, P., (2001) "Micromechanical Cantilever-based Biosensors", *Sensors and Actuators: B*, **79**, 115-126

196. Rayleigh, Lord, J. W., (1892) "On the Influence of Obstacles Arranged in Rectangular Order upon the Properties of a Medium", *Philosophical Magazine*, **34**, 481-502

197. Rembe, C., Muller, L., Muller, R. S., Pisano, A. P. and Howe, R. T., (2001) "Full Three Dimensional Motion Characterization of a Gimbaled Electrostatic Actuator", Proceedings of IEEE, International Reliability Symposium, Orlando, Florida, USA, April 30-May 1

198. Rembe, C., Hart, M., Helmbrecht, M. A., Srinivasan, U., Muller, R. S., Lau, K. Y. and Howe, R. T., (2000) "Stroboscopic Interferometer with Variable Magnification to Measure Dynamics in an Adaptive-Optics Micromirror", Proceedings of IEEE/LEOS, International Conference on Optical MEMS, Kauai, Hawaii, USA, August 21-24

199. Riesenberg, R., Nitzsche, G., Wuttig, A. and Harnisch, B., (2001) "Micro Spectrometer and MEMS for Space", 6th ISU Annual International Symposium, Smaller Satellites: Bigger Business, Strasbourg, France, May 21-23

200. Rinaldi, G., Packirisamy, M. and Stiharu, I., (2006) "Boundary Characterization of Microstructures through Thermo-Mechanical Testing", *Journal of Micromechanics and Microengineering*, **16**, 549-556

201. Rinaldi,G., Packirisamy M. and Stiharu, I., (2005) "Multiparameter Synthesis of Microsystems" Proceedings of SPIE, International Conference on Photonic Devices, Toronto, Ontario, Canada September 12-14

202. Rinaldi,G., Packirisamy M. and Stiharu, I., (2005) "Thermo-Electrical Influence on Static and Dynamic Behaviour of Cantilever Type Silicon Waveguide" Proceedings of SPIE, International Conference on Photonic Devices, Toronto, Ontario, Canada September 12-14

203. Rinaldi, G., Packirisamy, M. and Stiharu, I., (2005) "A Theoretical and Experimental Analysis of Geometry Conditioned Microcantilevers", 4th Canadian Workshop on MEMS: Opportunities and Challenges on the Road to Integration, Ottawa, Ontario, Canada, August 19

204. Rinaldi, G., Packirisamy, M. and Stiharu, I., (2005) "Dynamic Conditioning of MEMS Cantilever Structures by Single Cutout Allocation", 4th Canadian Workshop on MEMS: Opportunities and Challenges on the Road to Integration, Ottawa, Ontario, Canada, August 19

205. Rinaldi, G., Packirisamy, M. and Stiharu, I., (2005) "Geometrical Performance Conditioning of Microstructures", Proceedings of ISSS, International Conference on Smart Materials, Structures and Systems, Bangalore, India, July 28-30

206. Rinaldi, G., Packirisamy, M., Stiharu, I. and Bhat, R. B., (2005) "Influence of Etch Holes on the Behavior of Surface Micromachined Structures", Proceedings of ISSS, International Conference on Smart Materials, Structures and Systems, Bangalore, India, July 28-30

207. Rinaldi, G., Packirisamy, M. and Stiharu, I., (2004) "An Improved Method for Predicting Microfabrication Influence in Atomic Force Microscopy Performances", *International Journal of Nanotechnology*, 1, 292-306

208. Rinaldi, G., Packirisamy, M. and Stiharu, I., (2004) "Optical MEMS Based Bimorph for Thermal Sensing" Proceedings of SPIE, Symposium on Canadian and International Business and Technology Innovations in Optics and Photonics, Ottawa, Ontario, Canada, September 26-29

209. Rinaldi, G., Packirisamy, M. and Stiharu, I., (2004) "Experimental Investigation on the Dynamics of MEMS Structures", Proceedings of SPIE, International Conference on MEMS, MOEMS and Micromachining, Strasbourg, France, April 29-30

210. Rinaldi, G., Packirisamy, M. and Stiharu, I., (2004) "Electrostatic Boundary Conditioning of MEMS Devices", Proceedings of the 8th International Cairo University MDP, Conference on Current Advances in Mechanical Design and Production VIII, Cairo, Egypt, January 4-6

211. Rinaldi, G., Packirisamy M. and Stiharu, I., (2003) "Experimental Investigation on the Dynamics of MEMS Structures", Third Canadian Workshop on MEMS, Applying MEMS in Canada: Challenges and Methods, Ottawa, Ontario, Canada, August 18–22

212. Roberts, R. B., (1981) "Thermal Expansion Reference Data: Silicon 300-850 K", Journal of Physics D: Applied Physics, 14, L163-L166

213. Rong, H., Jones, R., Liu, A., Cohen, O., Hak, D., Fang, A. and Paniccia, M., (2005) "A Continuous-Wave Raman Silicon Laser", Nature, 433, 725-728

214. Rosing, R., Richardson, A., Dorey, A. and Peyton, A., (1999) "Test Support Strategies for MEMS", IEEE International Mixed Signal Test Workshop, Whistler, British Columbia, Canada, June 11-15

215. Ryder, S., Lee, K. B., Meng, X. and Lin, L., (2004) "AFM Characterization of Out-of-Plane High Frequency Microresonators", Sensors and Actuators: A, 114, 135-140

216. Sader, J. E. and White, L., (1995) "Method for the Calibration of Atomic Force Microscope Cantilevers", Review of Scientific Instruments, 66, 3789-3798

217. Sader, J. E. and White, L., (1993) "Theoretical Analysis of the Static Deflection of Plates for Atomic Force Microscope Applications", Journal of Applied Physics, 74, 1-9

218. Sadler, D. J., Garter, M. J., Ahn, C. H., Koh, S. and Cook, A. L., (1997) "Optical Reflectivity of Micromachined {111}-Oriented Silicon Mirrors of Optical Input-Output Couplers", Journal of Micromechanics and Microengineering, 7, 263-269

219. Saha, R. and Nix, W. D., (2002) "Effects of the Substrate on the Determination of Thin Film mechanical Properties by Nanoindentation", Acta Materiala, 50, 23-38

220. Schnitzer, R., Ruemmler, N., Grosser, V. and Michel, B., (1999) "Vibration Measurement of Microstructures by means of Laser Optical Modal Analysis", Proceedings of SPIE, 3825, 72–79

221. Sehr, H., Evans, A. G. R., Brunnschweiler, A., Ensell, G. J. and Niblock, T. E. G., (2001) "Fabrication and Test of Thermal Vertical Bimorph Actuators for Movement in the Wafer Plane", *Journal of Micromechanics and Microengineering*, **11**, 306-310

222. Seidel, H., Csepregi, L., Heuberger, A. and Baumgartel, H., (1990) "Anisotropic Etching of Crystalline Silicon in Alkaline Solutions, I. Orientation Dependence and Behavior of Passivation Layers", *Journal of the Electrochemical Society*, **137**, 3612-3626

223. Seidel, H., Csepregi, L., Heuberger, A. and Baumgartel, H., (1990) "Anisotropic Etching of Crystalline Silicon in Alkaline Solutions, II. Influence of Dopants", *Journal of the Electrochemical Society*, **137**, 3626-3632

224. Setzu, S., Ferrand, P. and Romestain, R., (2000) "Optical Properties of Multilayered Porous Silicon", *Materials Science and Technology*, **B69-70**, 34-42

225. Sharpe, W. N., Yuan, B. and Edwards, R. L., (1997) "A New Technique for Measuring the Mechanical Properties of Thin Films", *Journal of Micromechanical Systems*, **6**, 193-199

226. Shew, B.-Y., Hung, J.-T., Huang, T.-Y., Liu, K.-P. and Chou, C.-P., (2003) "High Resolution X-Ray Micromachining using SU-8 Resist", *Journal of Micromechanics and Microengineering*, **13**, 708-713

227. Shi, F., Palghat, R. and Mukherjee, S., (1996) "Dynamic Analysis of Micro-Electro-Mechanical Systems", *International Journal for Numerical Methods in Engineering*, **39**, 4119-4139

228. Shinshi, T., Kato, F. and Simokohbe, A., (2003) "Light-Driven Microcantilever Actuator based on Photoenhanced Magnetization in a GaAs-Fe Composite Film", *Applied Physics Letters*, **83**, 3425-3427

229. Siebert, P., Petzold, G., Hellenbart, Á. and Müller, J., (1998) "Surface Microstructure/Miniature Mass Spectrometer: Processing and Applications", *Applied Physics A: Materials Science and Processing*, **67**, 155-160

230. Smart, W.H. and Subramanian, K., (2000) "The Use of Silicon Microfabrication Technology in Painless Blood Glucose Monitoring", *Diabetes Technology & Therapeutics*, **2**, 549-559

231. Søndergaard, T., Bjarklev, A., Arentoft, J., Kristensen, M., Erland, J., Broeng, J. and Barkou Libori, S. E., (2001) "Designing Finite Height Photonic Crystal Waveguides: Confinement of Light and Dispersion Relations", *Optics Communications*, **194**, 341-351

232. Srikar, V. T. and Spearing, S. M., (2003) "A Critical Review of Microscale Mechanical Testing Methods used in the Design of Microelectromechanical Systems", *Experimental Mechanics*, **43**, 238-247

233. Srikar, V.T. and Spearing, S. M., (2003) "Mechanical Test Methods for MEMS Devices" *Experimental Mechanics*, **43**, 228-237

234. Strassberg, D., (2001) "Testing MEMS: Don't Reinvent the Wheel—But Take Little Faith", EDN: Voice of the Electronics Engineer, 47-54, Reed Elsevier, 125 Park Avenue, 23rd Floor, New York, New York, 10017, USA, www.edn.com

235. Su, M., Li, S. and Dravid, V. P., (2003) "Microcantilever Resonance-Based DNA Detection with Nanoparticle Probes", *Biochemical and Biophysical Research Communications*, **304**, 98-100

236. Syms, R. R. A., Zou, H., Stagg, J., and Moore, D. F., (2004) "Multistate Latching MEMS Variable Optical Attenuator", *IEEE Photonics Technology Letters*, **16**, 191-193

237. Syms, R. R. A., Zou, H., Yao, J., Uttamchandani, D. and Stagg, J., (2004) "Scalable Electrothermal MEMS Actuator for Optical Fiber Alignment", *Journal of Micromechanics and Microengineering*, **14**, 1633-1639

238. Syms, R. R. A., (2002) "Long-Travel Electrothermally Driven Resonant Cantilever Microactuators", *Journal of Micromechanics and Microengineering*, **12**, 211–218

239. Tabata, O., (1996) "pH-Controlled TMAH Etchants for Silicon Micromachining", *Sensors and Actuators: A*, **53**, 335-339

240. Tadigadapa, S. A. and Najafi, N., (2003) "Developments in MicroElectroMechanical Systems (MEMS): A Manufacturing Perspective", Transactions of the ASME, 125, 816-823

241. Taillaert, D., Bogaerts, W. and Baets, R., (2003) "Efficient Coupling Between Submicron SOI-Waveguides and Single-Mode Fibers", Proceedings of the IEEE/LEOS Benelux Annual Symposium, Enschede, The Netherlands, November 20-21

242. Terry, M., Reiter, J., Böhringer, K. F., Suh, J. W., and Kovacs, G. T. A., (2001) "A Docking System for Microsatellites Based on MEMS Actuator Arrays", *Smart Materials and Structures*, **10**, 1176-1184

243. The MathWorks Inc., 3 Apple Hill Drive, Natick, Massachusetts, 01760-2098, USA, www.mathworks.com

244. Thomson, W. T., (1988) "Theory of Vibration with Applications", Unwin Hyman Ltd., London, England W1V 1FP

245. Thundat, T., Oden, P. I., and Warmack, R. J., (1997) "Chemical, Physical, and Biological Detection using Microcantilevers", Proceedings of the Third International Symposium on Microstructures and Microfabricated Systems, 179-187

246. Torchigin, V. P. and Torchigin A. V., (1998) "Enlarged Shift of Light Frequency in a Modified Bragg Cell", *Pure and Applied Optics*, **7**, 763-782

247. Totsu, K., Haga, Y. and Esashi, M., (2005) "Ultra-Miniature Fiber-Optic Pressure Sensor using White Light Interferometry", *Journal of Micromechanics and Microengineering*, **15**, 71-75

248. Trigg, A., (2003) "Applications of Infrared Microscopy to IC and MEMS Packaging", IEEE Transactions on Electronics Packaging Manufacturing, **26**, 232-238

249. Tsuchiya, T., Tabata, O., Sakata, J. and Taga, Y., (1998) "Specimen Size Effect on Tensile Strength of Surface-Micromachined Polycrystalline Silicon Thin Films", *Journal of Micromechanical Systems*, **7**, 106-113

250. Tucker, R. S., Baney, D. M., Sorin, W. V. and Flory, C. A., (2002) "Thermal Noise and Radiation Pressure in MEMS Fabry-Pérot Tunable Filters and Lasers", *IEEE Journal on Selected Topics in Quantum Electronics*, **8**, 88-97

251. Turner, J. A., Hirsekorn, S., Rabe, U. and Arnold, W., (1997) "High Frequency Response of Atomic-Force Microscope Cantilevers", *Journal of Applied Physics*, **82**, 966-979

252. van Gelder, W. and Hauser, V. E., (1967) "The Etching of Silicon Nitride in Phosphoric Acid with Silicon Dioxide as a Mask", *Journal of the Electrochemical Society*, **114**, 869-872

253. Varadan, V. K. and Varadan, V. V., (2000) "Microsensors, Microelectromechanical Systems (MEMS), and Electronics for Smart Structures and Systems", *Smart Materials and Structures*, **9**, 953-972

254. Veijola, T. and Mattila, T., (2001) "Compact Squeezed-Film Damping Model for Perforated Surface", Proceedings of Transducers, Munich, Germany, June 10-14

255. Vignola, J. F., Liu, X., Morse, S. F., Houston, B. H., Bucaro, J. A., Marcus, M. H., Photiadis, D. M. and Sekaric, L., (2002) "Characterization of Silicon Micro-Oscillators by Scanning Laser Vibrometry", *Review of Scientific Instruments "*, **73**, 3584-3588

256. Vivien, L., Laval, S., Dumont, B., Koster, A. and Cassan, E., (2002) "Polarization-Independent Single-Mode Rib Waveguides on Silicon-On-Insulator for Telecommunication Wavelengths", *Optics Communications*, **210**, 43-49

257. von Preissig, F. J., (1989) "Applicability of the Classical Curvature-Stress Relation for Thin Films on Plate Substrates", *Journal of Applied Physics*, **66**, 4262-4268

258. Walker, J. A., (2000) "The Future of MEMS in Telecommunications Networks", *Journal of Micromechanics and Microengineering*, **10**, R1-R7

259. Walraven, J., (2003) "Future Challenges for MEMS Failure Analysis", IEEE International Test Conference, Charlotte, North Carolina, USA, September 30-October 2

260. Wang, S. H., Quan, C., Tay, C. J., Reading, I. and Fang, Z. P., (2003) "Deformation Measurement of MEMS Components using Optical Interferometry", *Measurement Science and Technology*, **14**, 909-915

261. Wang, W.-C., Fauver, M., Nhut Ho, J., Seibel, E. J. and Reinhall, P. G., (2002) "Development of an Optical Waveguide Cantilever Scanner", Proceedings of SPIE, Opto-Ireland: Optics and Photonics Technologies and Applications, September 5-6

262. Watanabe, H., Yamada, N. and Okaji M., (2004) "Linear Thermal Expansion Coefficient of Silicon from 293 to 1000 K", *International Journal of Thermophysics*, **25**, 221-236

263. Wei, J., Xie, H., Nai, M. L., Wong, C. K. and Lee, L. C., (2003) "Low Temperature Wafer Anodic Boding", *Journal of Micromechanics and Microengineering*, **13**, 217-222

264. Wiley-VCH Verlag GmbH & Company kGaA, P. O. Box 10 11 61, Weinheim, 69451, Germany, LTJ Magazine Article, (2006) January Issue, 62-64, www.laser-journal.de

265. Williams, K. R. and Muller, R. S., (1996) "Etch Rates for Micromachining Process", *Journal of Microelectromechanical Systems*, **5**, 256-269

266. Wilson, C. J., Ormeggi, A. and Narbutovskih, M., (1996) "Fracture Testing of Silicon Microcantilever Beams", *Journal of Applied Physics*, **79**, 2386-2393

267. Windecker, R., Fleischer, M., Körner, K. and Tiziani, H. J., (2001) "Testing Micro Devices with Fringe Projection and White-Light Interferometry", *Optics and Lasers in Engineering*, **36**, 141-154

268. Winters, H. F. and Coburn, J. W., (1979) "The Etching of Silicon with XeF_2", *Applied Physics Letters*, **34**, 70-73

269. Wu, J. and Chiang L., (2004) "Free Vibrations of Solid and Hollow Wedge Beams with Rectangular or Circular Cross-Sections and Carrying any Number of Point Masses", *International Journal for Numerical Methods in Engineering*, **60**, 695-718

270. Yan, J. and Seshia, A. A., (2005) "Effects of Etch Holes in Microelectromechanical Resonators", NSTI Nanotechnology Conference and Trade Show, Anaheim, California, USA, May 8-12

271. Yang, H.-A., Wu, M. and Fang, W., (2005) "Localized Induction Heating Solder Bonding for Wafer Level MEMS Packaging", *Journal of Micromechanics and Microengineering*, **15**, 394-399

272. Yang, M. G. and Koliwad, K. M., (1975) "Auger Electron Spectroscopy of Cleanup-Related Contamination on Silicon Wafers", *Journal of the Electrochemical Society*, **122**, 675-678

273. Yang, Y., Ji, H. F. and Thundat, T., (2003) "Nerve Agents Detection using a Cu^{2+}/L-Cysteine Bilayer-Coated Microcantilever", *Journal of the American Chemical Society*, **125**, 1124-1125

274. Yao, J. J. and MacDonald, N. C., (1996) "A Micromachined, Single-Crystal Silicon, Tunable Resonator", *Journal of Micromechanics and Microengineering*, **6**, 257-264

275. Yao, T., Nanjyo, Y. and Nishino, H., (2001) "Micro-Flow *In Vivo* Analysis of L-Glutamate with an On-Line Enzyme Amplifier based on Substrate Recycling", *Analytical Sciences*, **17**, 703-708

276. Yi, T., Li, L. and Kim, C.-J., (2000) "Microscale Material Testing of Single Crystal Silicon: Process Effects on Surface Morphology and Tensile Strength", *Sensors and Actuators: A*, **83**, 172-178

277. Yi, T. and Kim, C.-J., (1999) "Measurement of Mechanical Properties for MEMS Materials", *Measurement Science and Technology*, **10**, 706-716

278. Young, D., (1950) "Vibration of Rectangular Plates by the Ritz Method", *Journal of Applied Mechanics*, **72**, 448-453

279. Zecchino, M., (2004) "Characterizing MEMS Devices Through Transparent Media", Veeco Instruments Inc, Tucson, Arizona, 85706, USA, www.veeco.com

280. Zhang, L. M., Uttamchandant, D. and Culshaw, B., (1991) "Measurement of the Mechanical Properties of Silicon Microresonators', *Sensors and Actuators: A*, **29**, 79-84

281. Zhang, W., Chen, W., Zhao, X., Li, S. and Jiang, Y., (2005) "A Novel Safety Device with Metal Counter Meshing Gears Discriminator Directly Driven by Axial Flux Permanent Magnet Micromotors Based on MEMS Technology", *Journal of Micromechanics and Microengineering*, **15**, 1601-1606

282. Zhou, D. and Cheung, Y. K., (2000) "The Free Vibration of a Type of Tapered Beam", *Computer Methods in Applied Mechanics and Engineering*, **188**, 203-216

283. Zhou, D. and Cheung, Y. K., (1999) "The Free Vibrations of Tapered Rectangular Plates Using a New Set of Beam Functions with the Rayleigh-Ritz Method", *Journal of Sound and Vibration*, **223**, 703-722

284. Zhu, Y., Barthelat, F., Labossiere, P. E., Moldovan, N. and Espinosa, H. D., (2003) "Nanoscale Displacement and Strain Measurement", Proceedings of the SEM Conference, Experimental and Applied Mechanics, Charlotte, North Carolina, USA, June 2-4

285. Zine-El-Abidine, I., Okoniewski, M. and McRory, J. G., (2005) "Tunable Radio Frequency MEMS Inductors with Thermal Bimorph Actuators", *Journal of Micromechanics and Microengineering*, **15**, 2063-2068

286. Zu, J. W., Cheng, G. and Tang, Q., (2004) "Equilibrium and Stability of Micro-Cantilevers used in Atomic Force Microscopy", Proceedings of the International Conference on MEMS, NANO and Smart Systems, Banff, Alberta, Canada, August 25-27

Appendix I

COMPUTER AIDED DESIGN OF GEOMETRICALLY DIFFICULT MICRO-MECHANICAL STRUCTURES FOR ACADEMIC ENVIRONMENT

Presented in this appendix is a method to generate complex microsystem geometries using MATLAB.

AI.1. INTRODUCTION

The designing of mask layouts for MEMS often involves the incorporation of complex geometries that are not readily drawn using conventional MEMS design software. This process limitation is often due to the difficulty in creating non-linear, overlapped, structured silicon layers in a micro-electro-mechanical domain. The design of randomly curved structures, for example, does not lend itself easily or readily to the MEMS designer, and hence it limits the designer's ability in this regard. One possible solution to this is by approximating curved features with straight lines by carefully positioning straight-line segments *tip-to-tail* at appropriate angles one with respect to the other. This task is monumental when several differing curved structures are envisioned for the microsystem design. This work proposes using MATLAB [243] to design any mask shape for MEMS applications.

MEMS are currently being used in a variety of sensing/actuating applications ranging from inner space: biology and the health sciences, to outer space: satellites and space exploration vehicles etc. The MEMS technology continues to evolve both in the scope of current obtainable miniaturizability and also in the increasing number of applications for MEMS structures, the former as a direct result of mature and well established silicon microfabrication processes, and the latter to the evolution of MEMS CAD design tools which facilitate the designing of microscale structures. Initially MEMS designers used conventional design tool kits established for silicon IC and semiconductor applications. This was due directly to fact that MEMS technology evolved directly from the silicon IC technology. However, the silicon IC structures tend to be very linear and rectangular in shape and hence, the design tools used are simple and when applied to MEMS designing, limit the number of *geometrical options* available to the MEMS engineer.

In many cases the degree of difficulty in designing MEMS devices is directly proportional to the complexity of the intended structure. Complex geometries are handicapped, unfortunately, by the limited availability of adequate CAD based design tools and require careful, painstaking, time intensive designing especially where non-linear geometries are being considered. This *drawback* is further amplified when several complex configurations are incorporated within the same chip layout. This by no means implies that simple micro-scale structures no longer have applications in *micro-markets* on the contrary, humble microcantilever type structures continue to be extensively used in such applications as atomic force microscope probes and photonic waveguides, for example.

The design process involves several equally important considerations such as the choice of material, microfabrication method, feasibility of the design, intended market and cost. The costs involved generally determine whether or not the design has a chance of making it to the production stage. Hence, it would be of great advantage to minimize the overall costs involved, namely the costs involved in the design of the mask layout pattern. It is perhaps the most critical stage in the generation of new types of structures involving non-standard or complex geometries. This is a sensitive issue, and one that unfortunately in many cases, aborts the *idea stage* all together in the *idea-to-device* process. Over the past few years, structured design methods for MEMS have been paid more and more attention. The main limiting issue for achieving such methods is how to automatically generate the layer model and the mask layout [131].

In the process of surface micromachining MEMS device features are *added on* by the deposition of layers of different materials. Each of these layers may then be patterned by the selected removal, through etching, of specific regions of the layer via a photolithographic process. Photolithographic masks determine the regions to be etched [9, 103, 240]. Complex photolithographic mask geometries require intensive time commitments in MEMS CAD designing. Photolithography is the most expensive, complex, and critical process in commercial microsystem fabrication. In addition to mask cost, each of these masks needs to be carefully aligned to prior layers, which is a very complex and time consuming process with feature sizes that are around $0.15 \mu m$ [58].

MEMS designs, in general, are fabricated for high volume applications such as automotive accelerometers, gyroscopes and pressure sensors, or consumer ink-jet print heads. The *batch* microfabrication process and the large final application domain help to offset the initial costs involved in the mask design. Smaller markets for specific types of MEMS devices, and those requiring customized mask designs will drive development cost prohibitively high and are in large part abandoned. Such high start-up design costs are virtually non-recoverable in small market applications. Hence, MEMS applications continue to be dominated by high volume markets [155].

Shown in Figure AI.1 are two examples of intricate geometries generated using conventional IC CAD design tools. These structures, although they appear symmetric, upon closer inspection show variations both in shaping and positioning of the perimeter geometries. Not only will these design errors limit the functionality of these devices, the intensive design-time requirements needed to achieve these types of complicated designs will undoubtedly result in higher than *normal* mask layout design costs, and the errors may not be apparent until the devices are rigorously tested. An important consideration before undertaking time intensive design projects is that the design costs incurred are in general not recoverable. Therefore it would be of great benefit to be able to draw a MEMS chip layout in a simple, accurate, straightforward way, and where complex geometry shaping and structure positioning can be precisely identified and established.
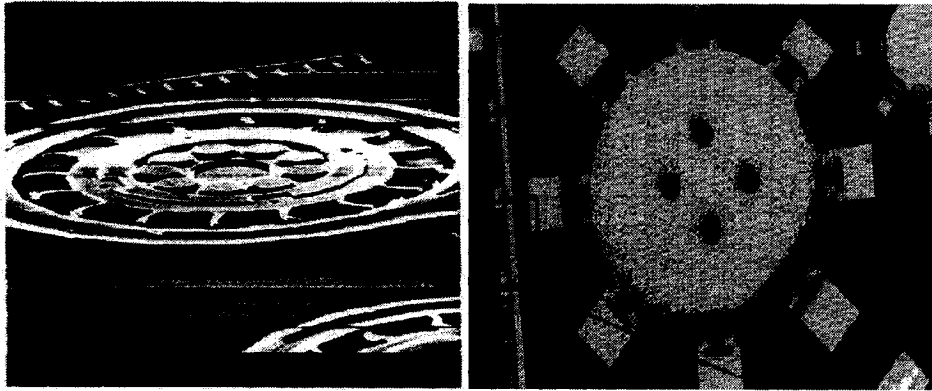
Figure AI.1. Two examples of complex geometries generated using conventional CAD drawing tools.

For many academic institutions, for example, current MEMS design softwares are prohibitively expensive and usually require some form of agreement with industrial partners for software licensing and other considerations. Hence, a MEMS design and analysis tool that is both functional and economical and readily available at university level engineering and science programs will allow academic researchers to fill a *void* by using *in-house* design and analysis tools.

This work proposes using MATLAB programming language as a way of designing MEMS and complex MEMS geometries. One of the main advantages of using MATLAB is that it is readily available at universities and research centers throughout the world, and is a systematic method based on mathematical formulae and equations. The mathematical formulae are used to generate and define the MEMS geometries, and then to generate the photolithographic mask layouts that can be used for a single device design

or for multiple structure designs. By using MATLAB as the *microsystem data* generator it is possible to *draw* and configure an entire MEMS design layout.

AI.2. PROCESS FLOW

The MATLAB based design flow proposed herein is only one of the possible simpler techniques for mask layout designs. It is used here because of the simplicity of the MATLAB coding and also because of the readily available MATLAB software in most university science and engineering programs.

There are three essential steps involved in the design of microsystem structures with the method presented in this paper. After the MATLAB data generation process, the individual MEMS structural layers can be assembled in any conventional MEMS mask layout software such as MEMSPro [49], for example. The ease of this method allows for the design of complex geometries. The process steps are outlined in general form in Figure AI.2.

MATLAB: Create precise geometry such as complex curved structures.

AutoCAD: Generate the MATLAB geometry and save in DXF format.

LINKCAD: Convert DXF files into GDS2 format.

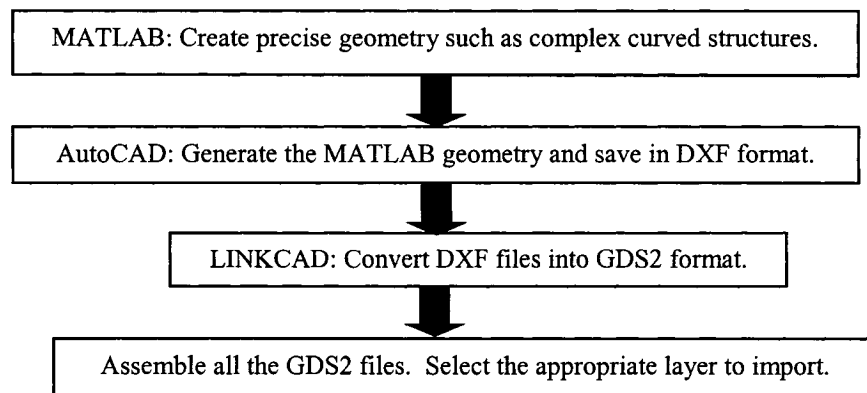| Assemble all the GDS2 files. Select the appropriate layer to import. |
| --- |

Figure AI.2. Four step process flow for the design of microstructures presented in this work.

238

AI.2.1. *MATLAB*

The MATLAB programming language is gaining much importance and recognition in science and engineering applications. Many university undergraduate engineering programs incorporate at least the fundamentals of MATLAB into their curriculum. MATLAB manipulates and generates data matrices, and is a programming tool that is both functional and relatively simple to use with many *built-in* features and toolboxes that allow for graphical analysis, simulation and interpretation, for example. It is not the intent of this work to provide an in depth introduction to MATLAB programming, however, suffice it to say that the importance of using MATLAB for the MEMS mask design is that data can be generated that defines the geometry or shape of the intended device, and that these *data pairs* can be uploaded into AutoCAD [12] in a relatively seamless manner as is discussed below.

By using MATLAB for microsystem mask layout designing, complex and intricate geometries can be defined by relatively simple numerical expressions. Also, this simple approach increases the design flexibility by allowing multiple iterations of the design at various sizes and dimensions, for example, which can be scaled down to micron or submicron levels as is the case for MEMS structures. Another important feature that is not available in conventional microsystem design tools is that MATLAB allows the MEMS designer to carry out parallel performance analysis of the proposed microstructure. Mechanical, electrical, thermal and optical properties, for example, can be specified and evaluated simultaneously within the MATLAB program defining a

specific MEMS device. Similarly, the design iterations discussed above are difficult in conventional MEMS layout editors as resizing of a structure leads to changes in performance and hence must be re-evaluated separately. With MATLAB re-dimensioning of a microstucture can be achieved and the performance evaluation obtained simultaneously for a given set of input criteria (mechanical, electrical, thermal, etc.), therefore a specific MEMS geometry can be optimized for a specific application such as capacitive sensing, for example, where the *sensing component* is a function of both the device geometry and the inter-electrode spacing. Additionally, other important performance characteristics can be analyzed in a similar fashion by using the toolboxes available in MATLAB. These steps have the advantage over other analysis tools such as ANSYS [10], or FEMLAB for example where the sizing of meshes and other factors add complexity to the analysis.

Hence, MATLAB offers several important features for the university environment or graduate level MEMS designing and analysis, it is readily available, it offers a simple method to generate complex geometries, it offers the possibility of parallel performance simulation and analysis of the multi-disciplined MEMS environment, and it offers the flexibility of resizing and varying the mechanical properties (Young's modulus, material properties, etc.) of the structure in a single step process that does not result in added complexity in the analysis process. Shown in Figure AI.3 is a flow chart illustrating the multi-disciplinary nature of microscale devices.

Shown in Figure AI.4 are examples of several *complex* geometries generated using

MATLAB that are not readily *designable* using conventional microsystem CAD mask
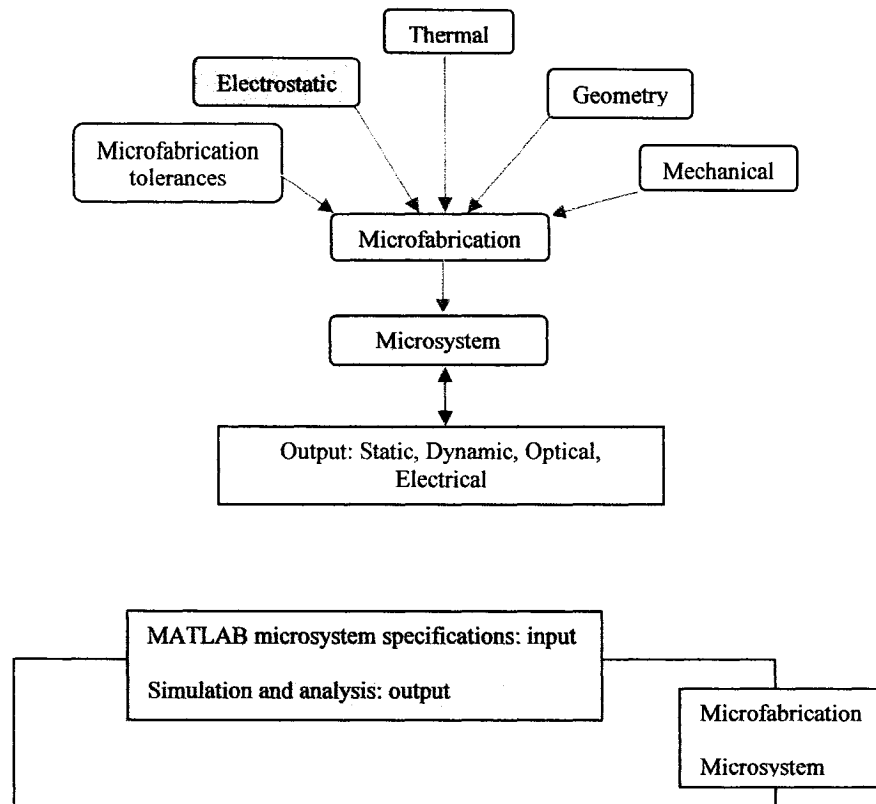
layout tools.

Figure AI.3. A flow chart showing an example of the multi-disciplinary nature of microscale devices. Top: Conventional flow-chart. The double arrow indicates the inverse design dream of MEMS engineers. Bottom: The parallel design-and-analysis capability possible through MATLAB.

Another reason for using MATLAB as the basis for microsystem design is that it can be

used to generate multiple overlapped designs simultaneously, and hence, can be used to

completely fill the design space allocation for a particular microsystem chip. This allows for a great deal of precision in the mask layout especially for intricate structures and especially for overlapping layers. An example of multiple structures in one MATLAB layout is shown in Figure AI.5.
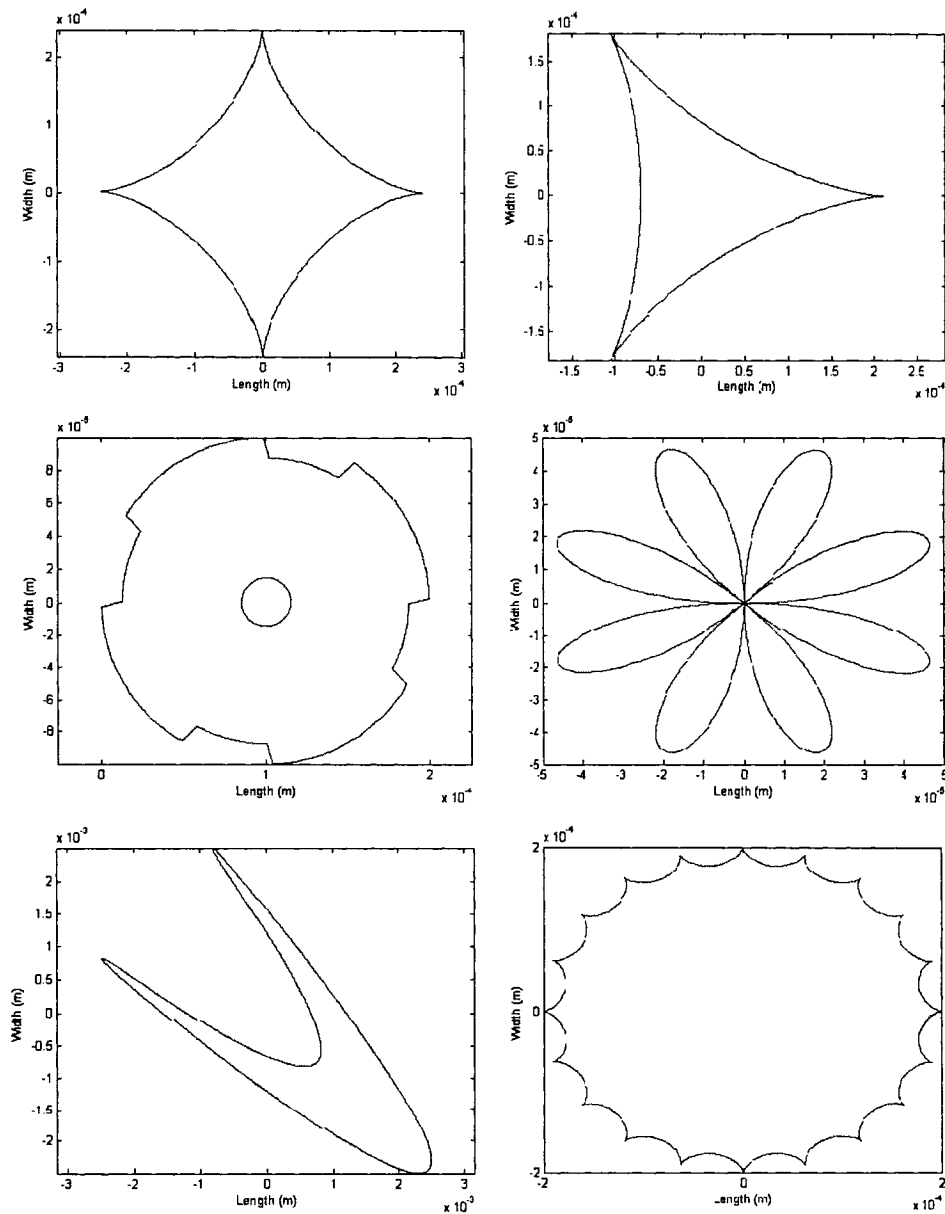

Figure AI.4. Several geometry types generated using MATLAB. Such shapes are often impossible to draw using standard design tools only.
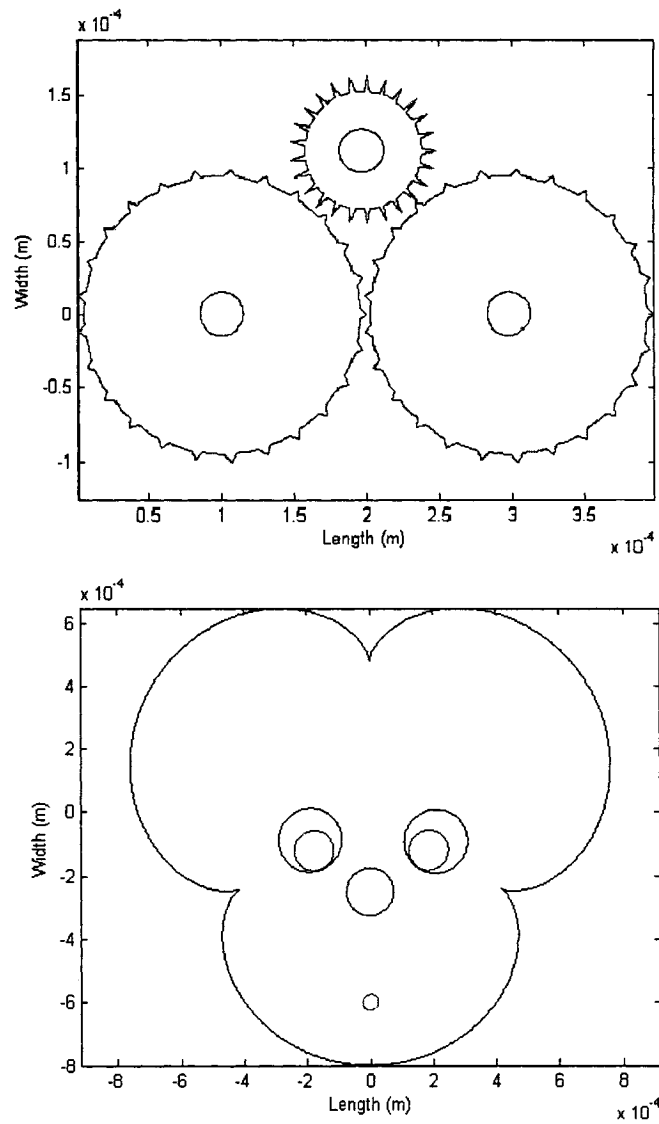
242

Figure AI.5. Examples of multiple overlapping geometries generated and coordinated using MATLAB. Top: Micro-gear train. Bottom: Whimsical micro-mouse.

AI.2.2. *AutoCAD*

The next step in the flow process is to convert the MATLAB data files into a *DXF* file

format. This is achieved by using AutoCAD. The mask data generated in MATLAB is

saved by invoking the *save as CSV* file format in MATLAB. This step ensures that the data pairs generated are saved and separated by a comma and not simply stored as two column vectors. A text editor is used to open the MATLAB stored CSV file and the data is copied into AutoCAD. This will generate the geometry in the AutoCAD window. An example of a converted MATLAB design into AutoCAD is illustrated in Figure AI.6.
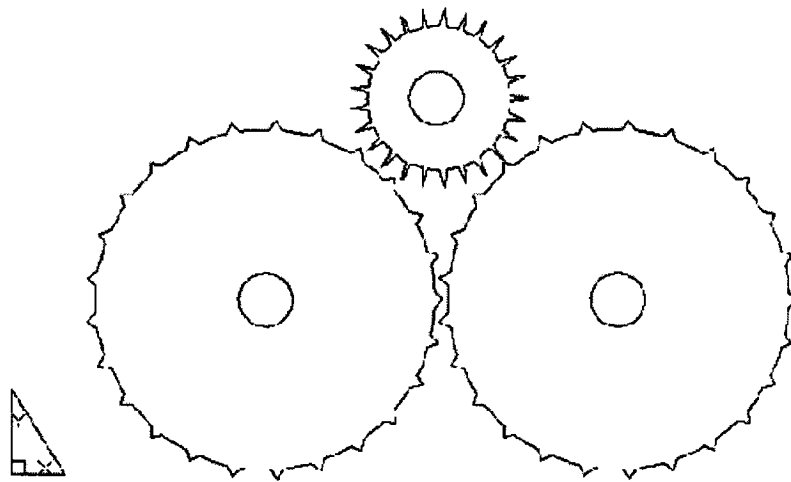

Figure AI.6. The converted MATLAB micro-gear train structures of Figure A.5 as they appear in the AutoCAD environment.

The incorporation of AutoCAD in the layout design steps, as defined in this work, is needed in order to have the mask layout data in *DXF* format. Among the save options

AutoCAD allows for file storage in *DXF* format which may then be converted to *GDS2* format.

AI.2.3. *LinkCAD*

At the current time, most if not all, MEMS type design software can only import/export mask layout data in a *GDS* or *GDS2* format, hence data conversion software is necessary in order to convert the AutoCAD *DXF* type files into a *GDS* or *GDS2* format. The MEMS device mask layers are individually defined by *GDS2* numbers. Each layer is allocated a *GDS* number representing that particular layer such as poly_0 or metal_2, for example. This is true of cutouts or via holes as well. The *GDS2* mask data is then used to generate the eventual photolithographic mask used for the MEMS chip layout.

For the work presented herein LinkCAD [135] software was adopted for the conversion of AutoCAD *DXF* files into *GDS2* format. It should be noted that there exist other conversion software such as ARTWORK [11] that can be employed for *DXF-GDS2* file format conversion. The choice between one or the other is a matter of personal preference. The actual layer definition is left to the last step and is presented below. After this step the final assembly of all the mask layers has to be carried out using a MEMS layout editor.

AI.2.4. *MEMSPro*

The final step is to import the *GDS2* file into the microsystem mask layout design editor. MEMSPro was used to generate the masks. It is at this step that the various structural layers of the MEMS device can be defined. For single structures this is simply a matter of choosing the particular layer to *import* the *GDS2* file to. However, for a multiple component structure layout all the structures will be imported to the same mask layer. In order to change the various layers in multiple structure layouts, the designer must first *ungroup* the structures. Then select the structure whose layer allocation needs to be redefined and select the layer editor to change the layer. Several structures and various layers are shown in Figure AI.7 and Figure AI.8.
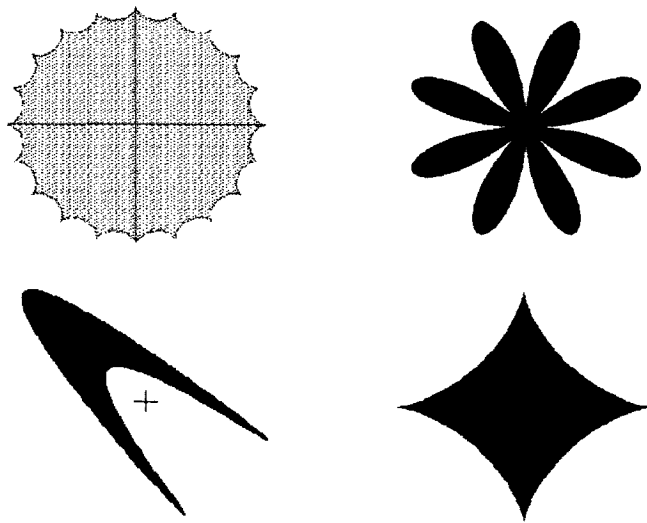
Figure AI.7. The complex geometries of Figure 4 in the MEMSPro layout editor. Each color indicates a distinct layer.
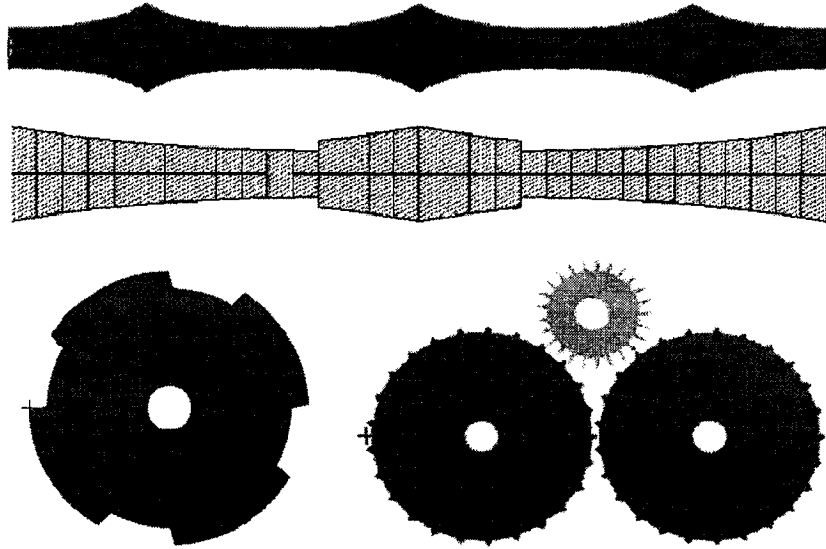
246

Figure AI.8. Examples of complex geometries in the MEMSPro layout editor. Top: microcantilever type waveguides. Bottom left: Single micro-gear. Bottom right: micro-gear train.

AI.3. MICROSYSTEM MASK LAYOUT

The possibility of designing an entire microsystem in MATLAB is very appealing as it allows for precision in shaping, dimensioning, positioning, and theoretical analysis of the microstructures. Whether or not an individual designer would follow these steps is of course a personal choice. Some of the structures presented here are undoubtedly easier to design and implement using a conventional MEMS layout design tool, however this step

is included in order to demonstrate the possibility of using MATLAB to generate an entire MEMS layout within a single MATLAB program.

The example presented here is an illustration of an entire chip layout design following the MATLAB based design method described in this work. Shown in Figures AI.9-AI.11 are the MATLAB, AutoCAD and MEMSPro design layouts respectively. All the geometries are allocated precise shapes and positions on the layout. The dimensions are 5000 x 5000 microns, as specified by the CMC and are typical for microsystem die size allocation.
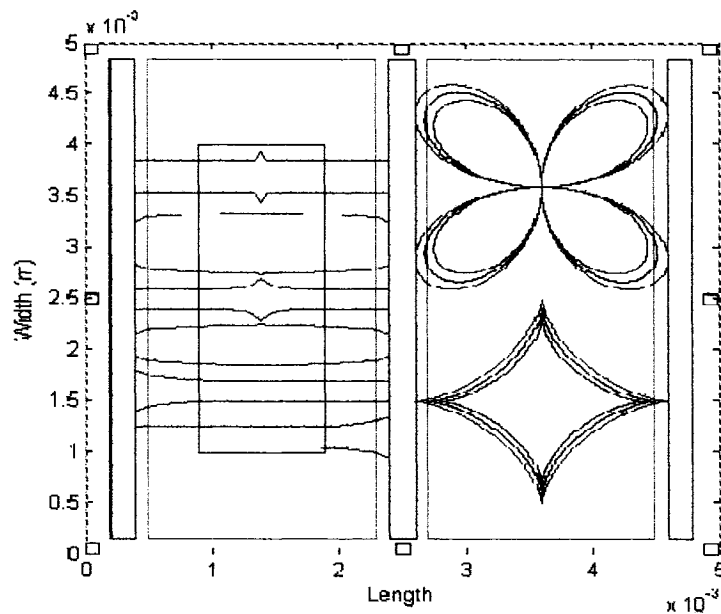

Figure AI.9. A typical microchip layout. The over all die size is 5000 x 5000 microns. The different colors define the various layers involved in the particular microfabrication process.
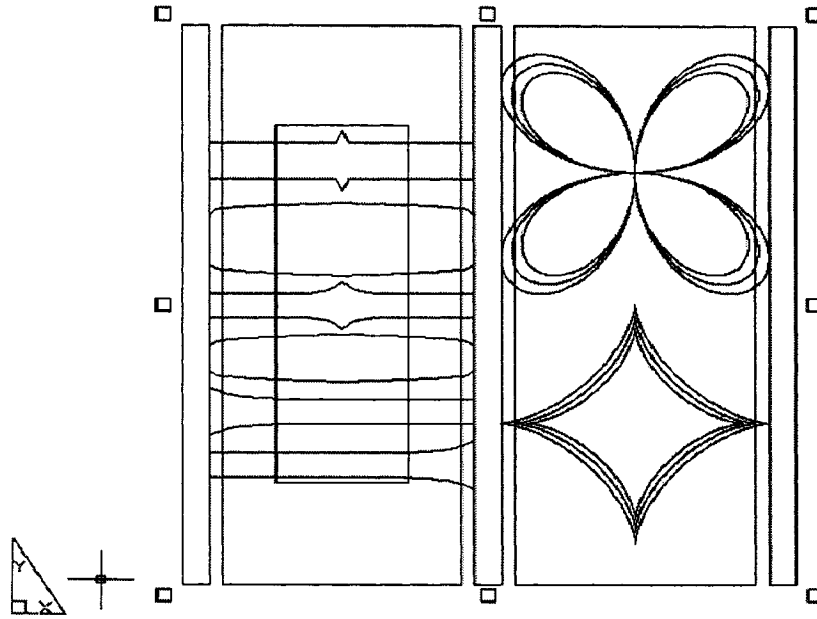
Figure AI.10. AutoCAD design window. The geometries were created from the MATLAB generated data.
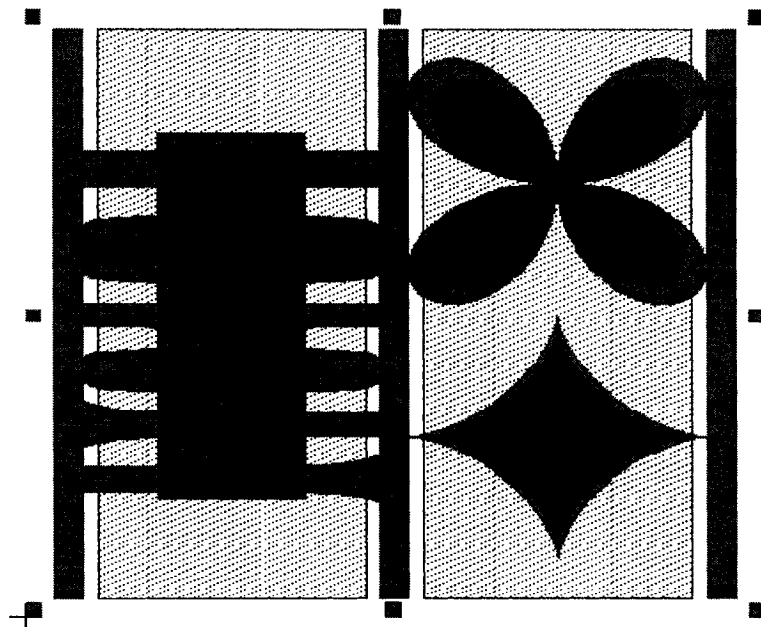

Figure AI.11. The final mask layout in MEMSPro. This mask will be used in the photolithographic process used to fabricate the structures. The various colors correspond to different silicon and metal layers.

249

Shown in Figure AI.12 is a microcantilever array designed using the process steps described in this work. Given in Figure AI.13 is an SEM image of the microcantilever array as fabricated through the MicraGeM microfabrication process. The structural layers in the final design layout in the example presented here are single crystal silicon, etched pyrex cavity of 10μm in the pyrex slide, metal_1 on pyrex and metal_2 on silicon. The metal layers are insulated from each other and have been wire bonded to the appropriate layer defined bonding post. Hence, in this manner the individual microcantilevers can be activated through the application of an electrostatic potential input, for example.
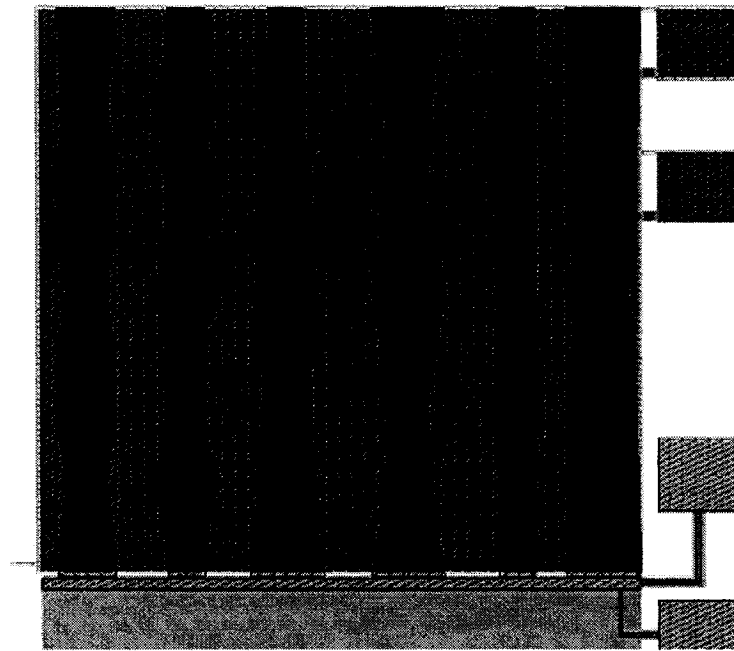

Figure AI.12. An overview of a non-conventional microcantilever array designed using the processes described in this work.
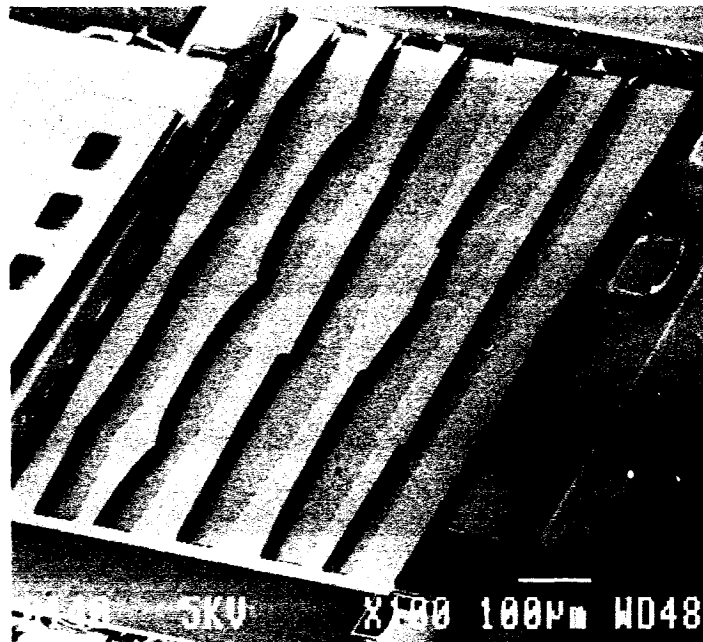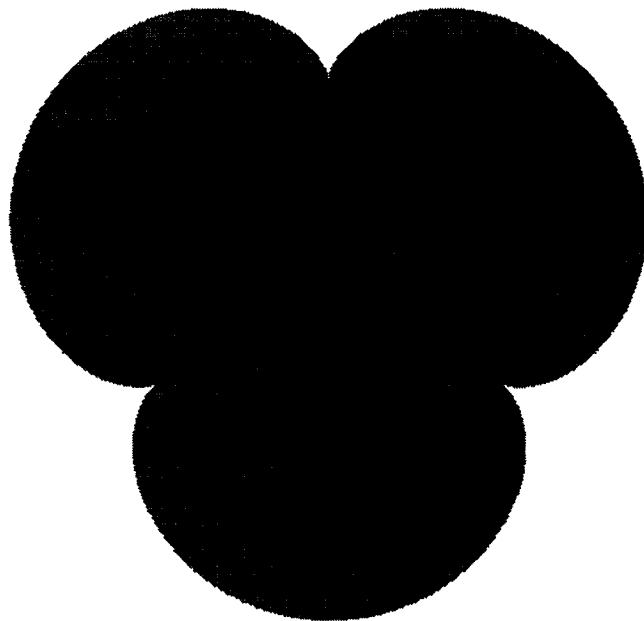
Figure AI.13. An SEM image of the non-conventional microcantilever array fabricated using the MicraGeM foundry process.

AI.4. SUMMARY

The designing of complex MEMS mechanical structures, often with submicron features, is a challenging task for the design engineer. Many CAD MEMS design tools in mask layout editors either do not support the complex geometries or offer only limited design tools to draw to such features. Presented in this paper was a simple, systematic method based on mathematical equations and formulae to define microsystem layout geometries using MATLAB programming language. This approach can be used to generate complex photolithographic mask geometries commonly encountered in microsytem design and microfabrication processes. It was shown that this method may be used for single device design, for multiple and overlapped designs, and for entire microchip layouts. Also, the advantages of using MATLAB include cost effectiveness especially in academic environments where MATLAB is readily available in science and engineering programs, and the possibility to carry out parallel design-and-analysis in a single step process. This relatively simple approach enables the microsystem designer to *draw* the entire microchip layout using MATLAB and to use the incorporated toolboxes to simulate and analyze both the input an output environments of the microsystem. Of course all microsystem simulation should be followed up with rigorous testing in order to obtain a comprehensive performance profile of the microsystem.

Appendix II

MICRAGEM: SILICON-ON-INSULATOR BASED MICROMACHINING PROCESS

An overview of the MicraGeM microfabrication process is given here.

AII.1. INTRODUCTION

MicraGeM (Micralyne Generalized MEMS) [49] is a MEMS prototyping process under development at Micralyne Inc. in conjunction with the Canadian Microelectronics Corporation (CMC). This technology is different from traditional MEMS processes by the materials used in the process, and by its variable geometry. This process enables users to develop fully-suspended MEMS devices with metal electrodes (rather than silicon). Users of the process can select two fabrication options during each production run. This makes the MicraGeM process more versatile and flexible than other MEMS prototyping technologies, enabling designers to develop MEMS devices with varying thickness of layers and gap sizes between layers. Silicon-on-insulator MEMS are found in many microphotonic waveguide [105, 121, 241, 256] applications today, for example.

AII.2. OVERVIEW OF THE MICRAGEM PROCESS

For each fabrication run MEMS designers are given the following process choices regarding the thickness of the silicon layer and etch depth. Option A: A 10μm thick,

single crystal silicon (SCSi) membrane over a 10μm gap. Option B: A 2μm thick, SCSi

over a 2μm gap, or a 10μm thick SCSi layer over a 12μm gap. Each design is allocated a

run space of 10mm x 5mm for each option and designers receive 10 MicraGeM chips for

their submitted designs. Figure AII.1 illustrates the main steps in the fabrication process.

In the first step a 525μm thick pyrex wafer is patterned with Mask_1, or Mask_2 for etch

depths of 2μm or 10μm, respectively. Both masks can be applied concurrently if an etch

depth of 12μm is required by the designer. Through a *lift-off* method using the Mask_3

step, Metal_1 (50nm titanium, 50nm platinum, 200nm gold) is applied to the etched
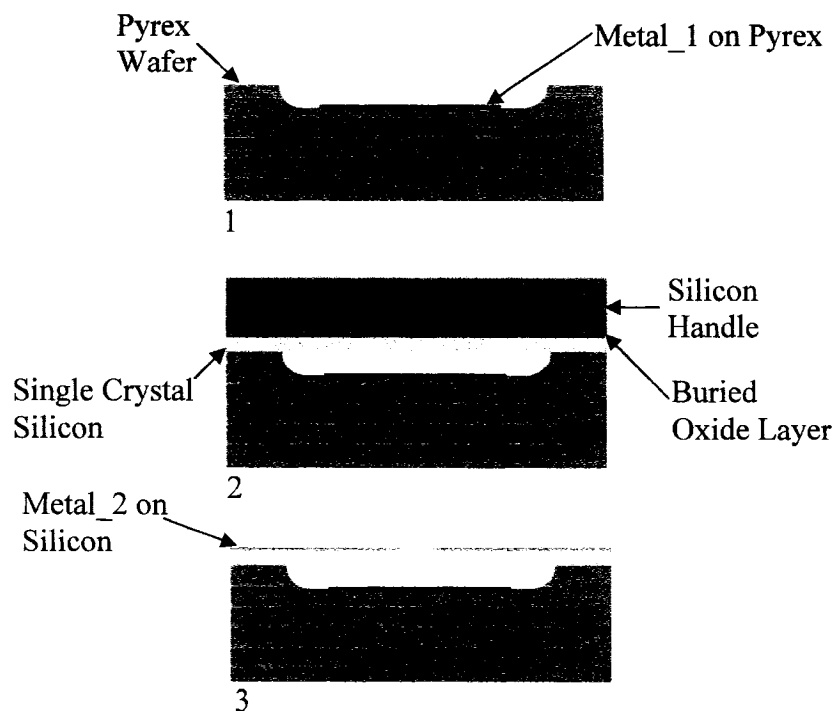
pyrex surface, Figure AII.1. 1.

Figure AII.1. The main steps in the MicraGeM micromachining process.

In step two, an SOI wafer consisting of a 525μm thick silicon handle, oxide layer, and

SCSi is anodically bonded, SCSi side down, to the pyrex layer, Figure AII.1. 2. Anodic

bonding is an electrostatic process in which a high voltage (~1000V) is applied. The applied potential induces a migration of ions across the pyrex-silicon interface and creates an irreversible chemical bond at the boundary [88, 127, 263]. The next process step completely removes the silicon handle and oxide layer leaving only 10μm thick SCSi layer on pyrex. Metal_2 consisting of a 100Å chrome and 750Å gold layer is then deposited onto the SCSi layer, Figure AII.1. 3. Mask_4 is used to pattern the Metal_2 layer. The Metal_2 layer is used mainly for its light reflection properties for applications in micromirrors, for example. In the final process step, Mask_5 is used to pattern the structures on the SCSi as specified by the designers and a plasma etch process is used to release the final structures. The finished wafers are then diced and packaged and sent out to the respective designers. Although not discussed in detail here, there are other design parameters such as minimum separation and sizing of structures, for example, that will require careful consideration during the design process. Shown in Figure AII.2 is an overview of a MicraGeM layout.
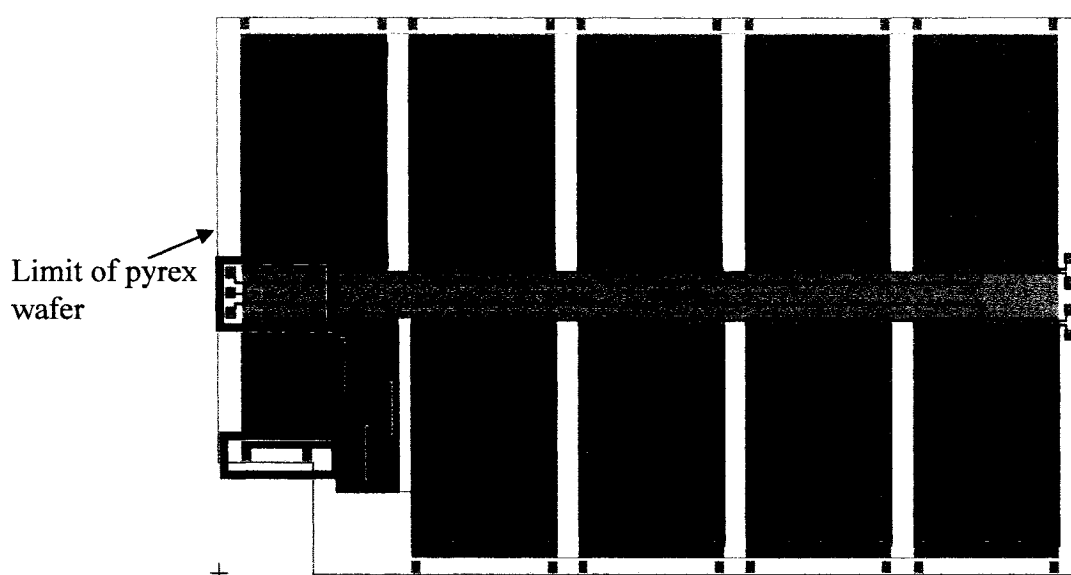

Figure AII.2. An overview of a MicraGeM chip design with SCSi structures. The features enclosed by black boxes are highlighted below.

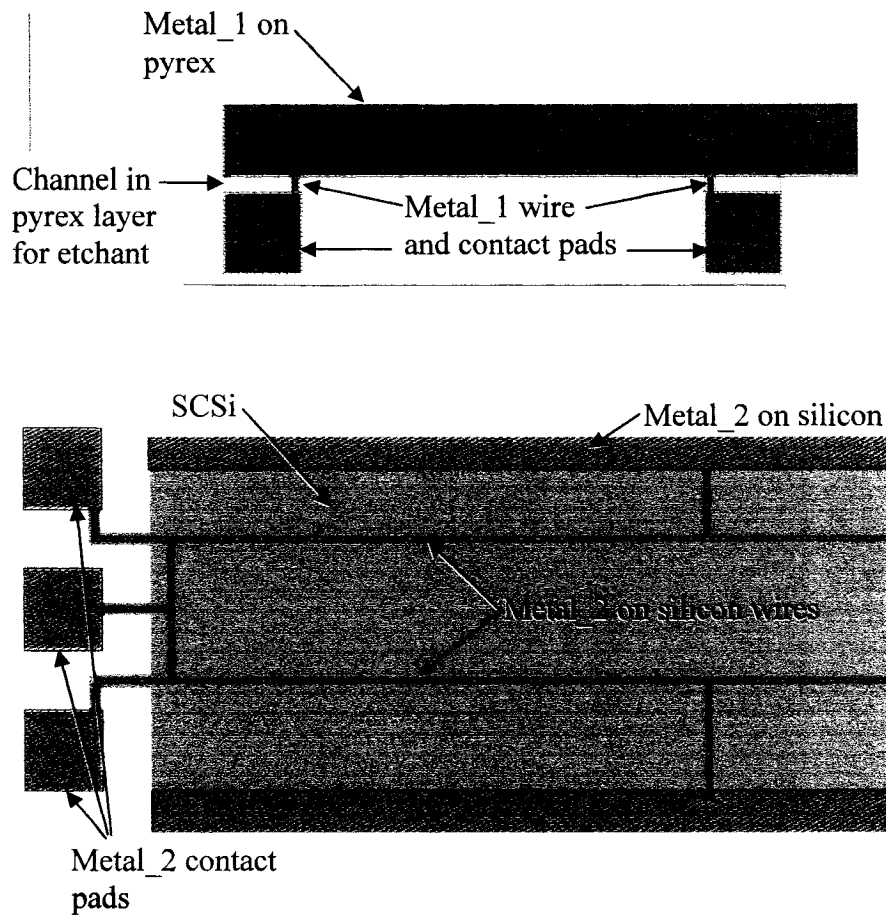Shown in Figure AII.3 are close up images of several features of Figure AII.2.

Figure AII.3. Top: Pyrex etch layer with Metal_1. The electrification is provided through the Metal_1 contact pads. All pyrex etch surfaces must be connected by a channel for passage of the etchant. Bottom: SCSi layer with Metal_2 contact pads and wiring scheme.

256

AII.3. Summary

The MicraGeM microfabrication process consisting of 5 mask steps has been presented. It is based on a silicon-on-insulator platform where a silicon wafer is anodically bonded to an etch patterned pyrex glass wafer consisting of a Metal_1 layer. Sequential lithography mask steps are used to pattern and release the SCSi structure. A Metal_2 layer can be applied to the SCSi layer for either electrical conductivity or optical reflection, for example. This technology is especially suited for structures requiring overhanging portions such as microcantilevers, or moveable mirrors for beam steering applications, for example.